

Thermodynamics of ultracold ^{39}K atomic Bose gases with tuneable interactions

A dissertation submitted to the
University of Cambridge for the
degree of Doctor of Philosophy

Naaman Tammuz
Cavendish Laboratory, November 2011



**UNIVERSITY OF
CAMBRIDGE**

Cavendish Laboratory

© 2011 Naaman Tammuz

Cavendish Laboratory
University of Cambridge
19, J J Thomson Avenue
Cambridge CB3 0HE
UK

Abstract

This thesis can conceptually be divided into two sections. In the first, consisting of chapters 2 and 3, I describe the design and construction of an experimental system for the production of ultracold Bose condensed gases of the isotopes ^{39}K and ^{87}Rb . We work with ^{39}K primarily due to the existence of a very broad Feshbach scattering resonance in its absolute ground state which enables precise and wide tuning of the s-wave scattering length. In order to cool ^{39}K sufficiently it is sympathetically cooled by ^{87}Rb while held in a magnetic trapping potential, after which both species are transferred to a purely optical trap. The ^{87}Rb is removed from the trap and the remaining ^{39}K is evaporated further by gradual lowering of the trap depth. We produce quasi-pure ^{39}K condensates containing over 4×10^5 atoms. The same apparatus can also produce ^{87}Rb condensates of over 8×10^5 atoms.

The second part of the thesis, consisting of the chapters 4 and 5, describes experiments aimed at addressing the influence of interparticle interactions on the thermodynamics of ultracold Bose gases. Firstly, we investigate the saturation of excited states as the driving mechanism behind Bose-Einstein condensation, in accordance with Einstein's original description. We find that real, interacting gases deviate more strongly from this picture than predicted by simple mean-field theories. Extrapolation to the non-interacting limit, however, allows us to recover Einstein's picture. Secondly, we investigate the effect of interaction strength on the shift of the condensation critical point from its ideal-gas value. We reveal for the first time the beyond-mean-field corrections to this quantity, in qualitative agreement with the most recent theoretical predictions, and also observe non-equilibrium effects in the regime of very weak and very strong interactions.

Declaration

I declare that this thesis is my own work and is not substantially the same as any that I have submitted or am currently submitting for a degree, diploma or any other qualification at any other university. No part of this thesis has already been or is being concurrently submitted for any such degree, diploma or any other qualification. This thesis does not exceed the word limit of sixty thousand words, including tables, footnotes, bibliography and appendices, set out by the Faculty of Physics and Chemistry.

Cambridge, *November 2011*

Acknowledgements

It is a pleasure to thank the many people with whom I have had the good fortune of sharing the last four years and who have directly and indirectly contributed to the work described in this thesis. First and foremost, I would like to thank my supervisor, Zoran Hadzibabic, for giving me the precious opportunity to join the group at its inception, despite my minimal experimental background and relatively fresh arrival to the field of cold-atom physics. The freedom given to my colleagues and me during these early days of the project always made us feel trusted, and Zoran did a good job of concealing any fears he might well have harboured. His steady and optimistic hand at the group's helm over the years has helped us overcome many practical and conceptual obstacles and has made our work more rewarding as a result.

There is a great deal of satisfaction and enjoyment to be had from working towards a common goal as part of a team, and I have been very fortunate in the teammates with whom I have had the chance to spend time, both in the lab and out. It requires a delicate balance of personalities to produce a group that is both fun and productive and I feel lucky to have been part of just such a group. Thank you from the bottom of my heart to Rob Smith and Robbie Campbell for all the shared experiences, for the good sense of camaraderie, for their humour and their relaxedness. The same thanks go to Scott Beattie and Stuart Moulder, who arrived two years into our work and immediately became an indispensable source of aid and entertainment. The newest generation of students, Igor Gotlibovych, Tobias Schmidutz, Alex Gaunt and Richard Fletcher are all talented physicists and great individuals and it is very comforting to know that both of the atom-machines are in such capable and skilled hands. Thanks also to Jun-Young Kim and Philip Richman, who have been part of the team along the way. I would also like to greatly thank Rob Smith, Alex Gaunt, Richard Fletcher and Scott Beattie again for their reading of the manuscript of this thesis and for

their helpful comments and suggestions.

Throughout my PhD we were fortunate to have as guests in our group a steady stream of talented undergraduate students, whose work greatly contributed to the overall progress of the lab and whose presence brought to the lab different perspectives and a breath of fresh air. In particular, thanks go to Alexandre Dareau, Nils Engelson, Mehdi Lallouache, and Diana Aude. Alexandre for the fun time spent designing our imaging system, dissecting projectors and playing with SLMs, Nils for his work on our optical dipole trap (amongst other things), Mehdi for his work on our fiberport cluster and Diana for her work on the microwave evaporation system. We also had the distinctly enjoyable privilege of a 3-month visit to our group by Prof. Jean Dalibard from the ENS in Paris. Any time spent in Jean's company is happy, well spent time and I am extremely grateful to have been able to benefit from his presence for such an extended period. I am very grateful for the good neighbourly relations we enjoyed with the friendly and hard-working members of Michael Köhl's hybrid BEC-ion-trapping lab and Fermi gas lab, who were always ready and willing to share from both their experiential and material supplies, as well as their footballing prowess. Our other colleagues in the AMOP group, from the teams of Mete Atatüre and Richard Phillips, were also a source of help and encouragement. I wish them all success and happiness in all their future endeavours.

We also occasionally had to venture outside the lab, and when we did so we were lucky enough to find ourselves in the friendly, safe and competent hands of the staff of the Cavendish laboratory. Our first port of call for anything not directly related to a cold atom is Pam, the most wonderful group administrator in the world, who was always ready to help with any issue and often went to extra lengths to ensure things got done right. A PhD devoted in large part to the construction of an experiment from scratch, should not and can not be considered complete without abundant thanks to the technical staff who make such a labour-intensive task manageable. Special thanks go to the head of the student workshop, Nigel Palfrey, with whom I spent many days milling, lathing, drilling and shooting the breeze. Thanks also to Peter Norman and Chris Summerfield from the main workshop for their expert and friendly handling of any machining request we threw at them. Thank you to the staff of the Cavendish stores for providing us with all the wires, tubes, pens, lab books, jubilee clips, resistors, capacitors and op-amps we could have dreamt of and a big thank you to Luis and his team in the big-ass burrito van for making Thursday lunchtimes extra special.

Thank you to my friends. Orr, Aharon and Adam, Allon and Roohia, Lail, Roi, Jesper, Safi, and everyone else who is dear to my heart - thank you for everything that has been and that is yet to come. Thank you to my family. My unbelievably supportive and caring parents, my beautiful and gifted sister, my loving and cheerful grandparents, my cool relatives across the pond(s) and Gretha and Victor, who have sent so much goodness and wisdom my way.

Last but not most, all day and every day, thank you to Petra, who makes my heart explode.

Contents

1	Introduction	1
1.1	Background	1
1.2	Temperature, density and length scales	3
1.3	Why ^{39}K ?	4
1.4	Thesis outline	6
2	Theoretical background	9
2.1	Laser cooling and trapping	10
2.2	Optical pumping	25
2.3	Magnetic trapping	26
2.4	Evaporative and sympathetic cooling	30
2.5	Optical trapping	37
2.6	Feshbach resonances	39
2.7	Bose-Einstein Condensation	44
2.8	Absorption imaging	48
3	Design, assembly and performance of our ^{39}K-^{87}Rb apparatus	53
3.1	Sequence overview	54
3.2	Vacuum system	55
3.3	Laser System	69
3.4	Magneto-optical trap (MOT)	75
3.5	Quadrupole and compensation coils	77
3.6	Optical pumping and magnetic capture	80
3.7	Transport	81

3.8	QUIC trap	83
3.9	Sympathetic cooling	89
3.10	Crossed dipole trap (CDT)	94
3.11	Feshbach field and Feshbach resonance	100
3.12	Onset of BEC in ^{39}K	108
3.13	Sequence summary	108
3.14	Imaging setup and procedure	108
3.15	Image analysis	115
3.16	Timing control	119
4	The role of saturation in Bose-Einstein condensation	123
4.1	Introduction and motivation	124
4.2	Experimental procedure for investigating saturation	126
4.3	Observation of non-saturation	129
4.4	Varying interaction strength and temperature	130
4.5	Mean-field theories of interacting gases	131
4.6	Comparing experiment and theory	140
4.7	Discussion and Conclusions	146
5	Interaction-dependence of the BEC transition temperature	151
5.1	Introduction and theory	152
5.2	Previous experimental studies	158
5.3	Experimental method	161
5.4	Extracting the T_c shift	164
5.5	Non-equilibrium measurements	166
5.6	Conclusions	169
6	Summary and Outlook	171
	Appendices	177
A	^{87}Rb and ^{39}K properties	177
B	A compact system for the rapid production of ^{87}Rb BECs	181
B.1	Vacuum chamber	182
B.2	Lasers and coils	184
B.3	Optical Plug	186

B.4 Performance	189
C Using Spatial Light Modulators for versatile creation of optical potentials	193
C.1 Spatial Light Modulators	194
C.2 Experimental setup	195
C.3 Trial 1: Laguerre-Gauss modes	197
C.4 Trial 2: 2D confinement and the 2D-3D crossover	200
C.5 Trial 3: Arbitrary potentials	201
C.6 Home-made SLM	203
C.7 Current status and future plans	205
D MOT and science cell properties	207
E Magnetic fields produced by current-carrying coils	211
E.1 Fields from circular coils	211
E.2 Fields from rectangular coils	214
F A tightly confining potential for studies of two-dimensional Bose gases	217
F.1 Introduction	217
F.2 The $0-\pi$ phaseplate	219
F.3 Estimating the trapping frequency and depth	221
F.4 Experimental setup	222

“In the eighteenth century it was often convenient to regard man as a clockwork automaton. In the nineteenth century, with Newtonian physics pretty well assimilated and a lot of work in thermodynamics going on, man was looked on as a heat engine, about 40 per cent efficient. Now in the twentieth century, with nuclear and subatomic physics a going thing, man had become something which absorbs X-rays, gamma rays and neutrons.”

Thomas Pynchon (b. 1937), *V*.

1

Introduction

“The general public has long been divided into two parts; those who think that science can do anything and those who are afraid it will.”

Thomas Pynchon, *Mason & Dixon*

1.1 Background

The basic dichotomy of the elementary particles of nature by now requires little retelling: fermions, the fundamental constituents of matter possessing half-integer spin, are prohibited from simultaneously occupying the same quantum state while bosons - elementary or composite particles possessing integer spin - are sociable and prefer to aggregate in the same state. In this thesis we concern ourselves only with the latter class of particles and can encapsulate the aims of the reported experiments as exploring the consequences of inter-particle interactions on different aspects of their gregarious behaviour.

Central to the understanding of the properties of bosonic systems¹ is the concept of the Bose-Einstein condensation (BEC) phase transition, which occurs when the wave-like nature of indistinguishable particles begins to dominate their behaviour. In this “quantum-degenerate” regime, a macroscopic fraction of the particles occupies the confining potential’s single-particle ground state. The BEC transition plays a key role in the explanation of experimental signatures observed in many disparate systems. Manifestations of this bosonic quantum degeneracy include the behaviour of Cooper pairs in superconductors (1911) [1], the superfluid properties of ⁴He (1938) [2, 3, 4, 5, 6] and ³He (1972) [7, 8, 9], the condensation of magnons in antiferromagnets (2000) and ferrimagnets (2006) [10, 11], fermionic pair condensates in dilute Fermi gases (2004) [12] and condensation of microcavity polaritons (2006) [13, 14].

Perhaps the most striking and clear demonstration of this phenomenon, however, has been provided by the field of ultracold atomic Bose gases. This burgeoning field with its newly-developed experimental techniques, recognized by the Physics Nobel prizes of 1997, 2001 and 2005 [15, 16, 17], has provided the means for cooling trapped atomic ensembles down to unprecedented temperatures - on the order of tens of nanokelvin - allowing us to perform extremely sensitive measurements on the quantum nature of these versatile and highly-controllable systems. Magnetic trapping of neutral atoms was first reported in [18] and the first demonstration of the magneto-optical trap was reported two years later [19]. The concurrent introduction and development of evaporative cooling [20, 21, 22] lead to the first experimental observations of BEC in dilute atomic Bose gases in 1995 [23, 24, 25] and quantum degeneracy in fermi gases a few years later [26, 27]. To date, fifteen atomic species have been condensed in ultracold atom groups around the world (see table 1.1).

1995	1995	1995	1998	2000	2001
⁸⁷ Rb [23]	²³ Na [24]	⁷ Li [25]	H [28]	⁸⁵ Rb [29]	⁴ He* [30, 31]
2001	2003	2003	2005	2007	2009
⁴¹ K [32]	¹³³ Cs [33]	¹⁷⁴ Yb [34]	⁵² Cr [35]	³⁹ K [36]	⁴⁰ Ca [37]
2009	2010	2011			
⁸⁴ Sr [38, 39]	⁸⁶ Sr [40]	¹⁶⁴ Dy [41]			

Table 1.1: Atomic species to have been condensed at the time of writing.

¹ An even number of constituent elementary fermions (electrons, protons, neutrons) makes an atom bosonic, while an odd number make it a fermion.

Our understanding of these systems' properties has grown in parallel with our experimental ability to manipulate their external and internal degrees of freedom. Novel magnetic and optical trapping methods enable samples to be loaded into periodic, lower-dimensional and dynamically reconfigurable potentials, while the discovery of Feshbach scattering resonances [42] has provided the ability to tune the strength and nature of interatomic interactions. This has enabled investigation of the delicate interplay between interparticle interactions and external potentials in determining the thermodynamic behaviour of these systems. Experiment and theory continue to yield valuable insights into the underlying many-body physical effects as well as opening the way to new technological applications of these systems in fields such as high-precision metrology and quantum information processing. Reviews of the history of this field can be found in [43, 44] and a discussion of more recent experimental and theoretical results can be found in [45, 46].

The experiments described in this thesis investigate the effects of interactions on the thermodynamic behaviour of a Bose gas, both well within the regime of quantum degeneracy (chapter 4) as well as on its threshold (chapter 5). Below is a summary of the relevant temperature, density and length scales as well as a discussion of our motivations for working with ^{39}K . This is intended to serve as an overview, with the technical elements introduced here to be explained more rigorously in chapters 2 and 3.

1.2 Temperature, density and length scales

Broadly speaking, the effects of quantum statistics become significant when the number of thermally accessible states becomes comparable to the number of particles in the system, such that the average occupancy of a state below the system's thermal energy becomes of order one. In terms of macroscopic parameters, namely temperature and number density, the onset of quantum degeneracy occurs when the characteristic spatial extension of a particle, as given by its thermal de Broglie wavelength

$$\lambda_{\text{dB}} = \frac{h}{\sqrt{2\pi m k_B T}} \quad (1.1)$$

becomes comparable to the mean inter-particle spacing $\ell \sim n^{-1/3}$, where n is the particle number density, h is Planck's constant, m is the mass, k_B is Boltzmann's constant and T is the temperature.

This is quantified by the *phase-space density* of the gas

$$\rho = n\lambda_{\text{dB}}^3 \quad (1.2)$$

which measures the number of particles within a ‘de Broglie volume’, λ_{dB}^3 . BEC therefore occurs when $\rho \sim 1$. A property shared by all cold-atom experiments is the extreme diluteness of the trapped samples, which is required in order to keep them in their metastable, weakly-interacting, gaseous phase. The weak-interactions also make the system more amenable to theoretical treatment, which is otherwise complicated by the strong interactions present in solids or quantum liquids such as the helium superfluids. Densities on the order of 10^{13}cm^{-3} - roughly ten orders of magnitude below those of a typical solid - are required in order to avoid prohibitive molecule formation rates via three-body recombination. Table 1.2 shows some typical densities for comparison.

nucleus	white dwarf	lead	water	air	BEC
10^{38}cm^{-3}	10^{30}cm^{-3}	10^{23}cm^{-3}	10^{22}cm^{-3}	10^{19}cm^{-3}	$10^{13} - 10^{15}\text{cm}^{-3}$

Table 1.2: Typical number densities of some materials in comparison to those at the centre of a BEC.

As an example, a cloud of 10^6 ^{87}Rb atoms held in a harmonic potential of frequency $\omega/2\pi = 100\text{Hz}$ at $T = 100\mu\text{K}$ has a phase-space density of $\rho \sim 10^{-7}$ and a thermal radius of $R_T \approx 50\mu\text{m}$. The same cloud at $T = 1\mu\text{K}$ has $\rho \approx 0.1$ and $R_T \approx 15\mu\text{m}$. The BEC transition temperature for the above cloud occurs around $T_c \approx 450\text{nK}$. Typical trapped samples contain between 10^3 and 10^7 atoms and have an experimental trap lifetime in the range 1-100s. Section 2.7 discusses the BEC transition in more detail.

1.3 Why ^{39}K ?

A relative newcomer to the condensate family, ^{39}K was condensed for the first time in 2007 [36] in the LENS¹ group in Florence following several years of pioneering studies by this and other groups into the collisional properties of this isotope and its suitability for BEC experiments [47, 48, 49, 50, 51, 52, 53, 54, 55, 56, 57, 58, 59, 60]. The fermionic isotope ^{40}K was first cooled to degeneracy in 1999 by the JILA

¹ European Laboratory for Non-Linear Spectroscopy

group [26], while the other bosonic potassium isotope, ^{41}K , was first condensed at LENS in 2001 [32]. Amongst other findings, it was demonstrated that ^{87}Rb was well suited to act as a refrigerant for sympathetic cooling of ^{39}K and ^{41}K [32, 59]. The existence and properties of multiple Feshbach scattering resonances in ^{39}K were predicted and observed [60] and several interspecies ^{39}K - ^{87}Rb and ^{41}K - ^{87}Rb Feshbach resonances have also been found [61, 58, 36, 62].

^{39}K is an attractive species to work with¹. The existence of other bosonic and fermionic isotopes, both of which have also been cooled to degeneracy, allow experiments to be performed on ultracold Bose-Bose and Bose-Fermi mixtures in which the two species possess almost identical masses² [65]. ^{39}K 's several broad Feshbach resonances, located at moderate magnetic fields, allow fine tuning of the s-wave scattering length over a large range, from strongly attractive to strongly repulsive. The ability to cancel out interactions altogether enables precision atom-interferometry experiments to be performed as well as studies on phenomena such as Anderson localization [66, 67]. ^{39}K 's negative background scattering length, which constitutes a significant hurdle on the route to BEC, can be utilized in experiments on the effects of attractive interactions [25, 68, 69, 70, 71]. From a technical point of view, its well-understood level structure, high natural abundance (93.26%) and the availability of commercial laser systems at the relevant wavelengths also add to its appeal.

Working with this isotope poses several difficulties, however. Chief amongst these are (1) the inefficiency of conventional laser cooling mechanisms due to ^{39}K 's unresolved excited-state hyperfine structure, (2) the relative inefficiency of evaporative cooling due to the small background scattering length and (3) the instability of ^{39}K BEC resulting from the attractive nature of this background interaction strength. The first of these is overcome by careful choice of laser frequencies, the second by performing sympathetic cooling with ^{87}Rb and the third by harnessing a Feshbach resonance to change the interaction strength from attractive to repulsive. These problems and the measures for overcoming them are described in detail in chapters 2 and 3.

¹ No pun intended.

² The only other species-pairs for which this has been achieved are ^7Li - ^6Li [63] and ^{84}Sr - ^{87}Sr [64].

1.4 Thesis outline

The remainder of this thesis is structured as follows:

- Chapter 2 provides some theoretical background to the various techniques and phenomena utilized in the production and manipulation of ultracold atomic gases.
- Chapter 3 describes the design, assembly and performance of our apparatus for producing ultracold dual-species ^{87}Rb - ^{39}K clouds.
- Chapter 4 discusses experiments in which a condensed ^{39}K gas with tuneable interaction strength was used to investigate the role of excited-state saturation as the driving mechanism behind the Bose-Einstein condensation transition in a non-interacting gas.
- Chapter 5 describes our measurements of the interaction-shift in the BEC critical point. We observe the hitherto unseen beyond-mean-field effects on the shift in the critical temperature in addition to non-equilibrium effects in the regimes of very-weak and very-strong interaction strengths.
- In chapter 6 we summarize our results and mention possible directions for future work.

Appendices

The appendices at the end of this thesis include additional information that did not find a place in the main text but that may prove useful to others working on similar experiments. This includes

1. A summary of the relevant optical and physical properties of both ^{87}Rb and ^{39}K (appendix A).
2. A description of a compact system for rapid production of ^{87}Rb BECs assembled to provide a convenient platform for proof-of-principle experiments and testing of components (appendix B).
3. Experimentation with the use of a Spatial Light Modulator (SLM) for generation of Laguerre-Gauss beams, arbitrary optical potentials and dynamic control of trapping potentials (appendix C).
4. Information on the dimensions and anti-reflection (AR) coatings of the MOT chamber and the science cell (appendix D).

-
5. The formulae used for calculation of the magnetic fields generated by our various magnet coils (appendix E).
 6. Preliminary results for the design and testing of a setup for producing tightly-confining optical potentials for future studies of two-dimensional Bose gases with tuneable interactions (appendix F).

Publications arising from this work

- The results described in chapter 3 are summarized in:
 1. *Efficient Production of Large ^{39}K Bose-Einstein Condensates.*
R. L. D. Campbell, R. P. Smith, N. Tammuz, S. Beattie, S. Moulder, and Z. Hadzibabic, *Phys. Rev. A* **82**, 063611 (2010)
- The results of chapter 4 on the role of saturation in BEC were published in:
 2. *Can a Bose gas be saturated?*
N. Tammuz, R. P. Smith, R. L. D. Campbell, S. Beattie, S. Moulder, J. Dalibard and Z. Hadzibabic, *Phys. Rev. Lett.* **106**, 230401 (2011)
- Our measurements of the interaction shift in the BEC critical point, as described in chapter 5, appear in:
 3. *Effects of Interactions on the Critical Temperature of a Trapped Bose Gas.*
R. P. Smith, R. L. D. Campbell, N. Tammuz, and Z. Hadzibabic, *Phys. Rev. Lett.* **106**, 250403 (2011)
- Analysis of beyond-mean-field contributions to the condensed fraction were published in:
 4. *Condensed Fraction of an Atomic Bose Gas Induced by Critical Correlations.*
R. P. Smith, N. Tammuz, R. L. D. Campbell, M. Holzmann, and Z. Hadzibabic, *Phys. Rev. Lett.* **107**, 190403 (2011)

2

Theoretical background

“Why should things be easy to understand?”

Thomas Pynchon, *quoted in Playboy (March 1977)*

Abstract

This chapter summarizes some of the theory underlying the various stages in the production and manipulation of our ultracold ^{39}K and ^{87}Rb gases. In the interests of conceptual clarity and convenient browsing, the chapter is structured so as to roughly correspond to the progression of the experimental procedure used to create the degenerate and quasi-degenerate clouds which constitute the starting point for our investigations. We discuss the principles behind (i) laser cooling and trapping, (ii) magnetic trapping, (iii) evaporative cooling, (iv) optical trapping, (v) Feshbach scattering resonances, (vi) the properties of thermal and condensed atomic clouds and (v) absorption imaging.

2.1 Laser cooling and trapping

Laser cooling and magneto-optical trapping have established themselves as the starting point of virtually every single ultracold atom experiment conducted today. The use of laser light for cooling and trapping atoms enjoys a rich and distinguished history, including the award of the 1997 Nobel prize in Physics [72, 73, 74] for development of the related experimental methods and theoretical understanding. However, the mechanical effects of radiation on matter particles had been hypothesized and investigated long before the first proposals and experiments harnessing these effects to cool atoms were carried out in the mid 1970's. Table 2.1 presents a chronology of milestones related to these theoretical and experimental studies.

Year	Name	Contribution
1619	Keppler	In 1619 treatise, “De Cometis”, hypothesises that the deflection of comet tails away from the sun is a consequence of pressure exerted by solar rays.
1873	Maxwell	In “Treatise on Electricity and Magnetism” [75], showed that radiation pressure is equal to energy density of electromagnetic wave.
1876	Bartoli	Derived, from arguments based on 2 nd law of thermodynamics, radiation pressure equal to that calculated by Maxwell [76, 77].
1901	Lebedev	First measurement of light pressure on a solid body using container of water and torsional balance [78].
1901-3	Nichols & Hull	Use the torsional <i>Nichols radiometer</i> to measure radiation pressure [79, 80].
1909	Einstein	In [81], showed that Planck’s black-body formula implied that light quanta also carried quantized momentum $p = h/\lambda$.
1933	Frisch	Observed defection of a beam of sodium atoms by light resonant with a sodium energy level transition [82].
1975	Hänsch & Schawlow	Proposed using laser for cooling of neutral atoms [83].
1975	Wineland & Dehmelt	Proposed <i>laser</i> cooling of trapped ions [84].

1978	Ashkin	Proposed “a method of stably trapping, cooling, and manipulating atoms on a continuous-wave basis...using resonance radiation pressure forces” [85].
1978	Neuhauser <i>et al.</i>	Laser cooling of trapped ions to a few millikelvin [86].
1981-2	Andreyev / Phillips & Metcalf	Cooling of Na beams with laser light [87, 88]
1997	Chu, Phillips & C.-Tannoudji	Nobel prize “for development of methods to cool and trap atoms with laser light.” [74, 72, 73]

Table 2.1: Milestones in the understanding of the mechanical effects of light on matter.

The fields of atomic spectroscopy and atom clocks have also benefited hugely from the reduced Doppler shifts and increased interaction times afforded by magneto-optical traps (MOTs), in which many different atomic species can be cooled with relative ease to temperatures on the order of $100\mu\text{K}$. The physics governing laser cooling and the operation of MOTs has been presented and scrutinized in many excellent books [89, 90, 91], review articles [72, 73, 74, 92], research papers and theses. Here we provide a brief review of the main operating principles responsible for the laser cooling and trapping of atoms from a background vapour in our double-species ^{39}K - ^{87}Rb MOT. The basic theory is discussed in the context of a two-level system and in subsection 2.1.4 we discuss how well this approximation is realised in practice for our atomic species.

2.1.1 Atom-light interactions

The total force acting on atoms as a result of their interaction with an electromagnetic field is the result of three distinct processes taking place during the interaction. These are the absorption, spontaneous emission and stimulated emission of photons from the radiation field. The contribution of the first two of these is usually called the *scattering* or *radiation* force and the dispersive force arising from the third process is called the *dipole force*. These two components are often treated separately and in ultracold atom experiments typically play very distinct roles in the cooling and manipulation of trapped clouds. Laser cooling

and trapping constitute the first stage of the experimental sequence and rely on the scattering force, as described in 2.1.2 and 2.1.3. Optical trapping using the dipole force is utilized during the final part of the experiment, where its tight confinement and state-independent nature make it convenient for use in conjunction with evaporative cooling and Feshbach resonances, respectively. Here we outline a derivation, along the lines presented in [89], of the force resulting from the interaction between a two-level system and a plane-wave electric field along one spatial dimension, z . For an atom, this force arises from the interaction between the field and the dipole moment, $-e\mathbf{r}$, it induces in the atom. The Hamiltonian for the energy of a dipole in an electric field is

$$\mathcal{H} = -e\mathbf{E}(\mathbf{r}, t) \cdot \mathbf{r} \quad (2.1)$$

where $\mathbf{E}(\mathbf{r}, t)$ is the electric field operator and $e\mathbf{r}$ is the dipole moment operator. The force along the z -direction can be found using the Ehrenfest theorem as

$$F_z = -\left\langle \frac{\partial \mathcal{H}}{\partial z} \right\rangle = e \left\langle \frac{\partial}{\partial z} (\mathbf{E}(\mathbf{r}, t) \cdot \mathbf{r}) \right\rangle \quad (2.2)$$

Using the *dipole approximation*, which assumes a constant value of the electric field across the dipole (i.e. $\lambda \gg |\mathbf{r}|$), we can exchange the order of the derivative and the expectation value such that

$$F_z = e \frac{\partial}{\partial z} (\langle \mathbf{E}(\mathbf{r}, t) \cdot \mathbf{r} \rangle) \quad (2.3)$$

Since the atom has no dipole moment when in an energy eigenstate (i.e. $\langle g|\mathbf{r}|g\rangle = \langle e|\mathbf{r}|e\rangle = 0$), the dipole operator can be written as $\mathbf{r} = \mathbf{r}_{eg}|e\rangle\langle g| + \mathbf{r}_{eg}^*|g\rangle\langle e| = \mathbf{r}_{eg}\rho_{eg} + \mathbf{r}_{eg}^*\rho_{eg}^*$, where ρ_{eg} is the off-diagonal element of the density matrix $\rho = |\Psi\rangle\langle\Psi|$. The electric field operator is given by $\mathbf{E}(\mathbf{r}, t) = \mathbf{E}_0 \cos(\omega t - \mathbf{k} \cdot \mathbf{r})$ and the definition of the Rabi frequency is

$$\Omega \equiv \frac{-eE_0}{\hbar} \underbrace{\langle e|\mathbf{r}|g\rangle}_{\equiv X_{12}} \quad (2.4)$$

where we have defined $X_{12} \equiv \langle e|\mathbf{r}|g\rangle$. The force of equation 2.3 can then be written as

$$F_z = \hbar \left(\frac{\partial \Omega}{\partial z} \rho_{eg}^* + \frac{\partial \Omega^*}{\partial z} \rho_{eg} \right) \quad (2.5)$$

where in obtaining equation 2.5, the *rotating-wave approximation* (RWA), which assumes a near resonant field such that $\delta \equiv \omega_L - \omega_0 \ll \omega_L + \omega_0$, has been used. Splitting the derivative of the Rabi frequency into its real and imaginary parts according to

$$\frac{\partial \Omega}{\partial z} = (q_r + iq_i)\Omega \quad (2.6)$$

reduces equation 2.5 to

$$\begin{aligned} F_z &= \hbar q_r (\Omega \rho_{eg}^* + \Omega^* \rho_{eg}) + i \hbar q_i (\Omega \rho_{12}^* - \Omega^* \rho_{12}) \\ &= \frac{\hbar s}{1+s} \left(-\delta q_r + \frac{1}{2} \Gamma q_i \right) \end{aligned} \quad (2.7)$$

where $\delta = \omega - \omega_0$ is the detuning of the field from the transition frequency and in going from the first to the second lines of 2.7 we have inserted the expression for ρ_{eg} obtained from the steady-state solutions of the optical Bloch equations (OBE):

$$\rho_{12} = \frac{i\Omega}{2(\Gamma/2 - i\delta)(1+s)} \quad (2.8)$$

in which the *saturation parameter*, s , is given by

$$s \equiv \frac{s_0}{1 + (2\delta/\Gamma)^2} \quad (2.9)$$

with

$$s_0 \equiv \frac{2\Omega^2}{\Gamma^2} = \frac{I}{I_S} \quad \text{and} \quad I_S \equiv \frac{\pi \hbar c}{3\lambda_0^3 \tau} \quad (2.10)$$

with c the speed of light, λ_0 the resonance wavelength and $\tau = \Gamma^{-1}$ the transition lifetime. The above expression for the *saturation intensity*, I_S , can be found using Einstein's A and B coefficients and the intensity, I is related to the peak field value E_0 via: $I = \epsilon_0 c E_0^2 / 2$. Within the RWA, the field can be written as $\mathbf{E}(\mathbf{r}, t) = \mathbf{E}_0 \exp(-i(\omega t - \mathbf{k} \cdot \mathbf{r}))$. Inserting this expression into equation 2.6 and using the definition 2.4, we obtain

$$\begin{aligned} \frac{\partial \Omega}{\partial z} &= \frac{e}{\hbar} X_{12} \frac{\partial E_0}{\partial z} e^{-i(\omega t - \mathbf{k} \cdot \mathbf{r})} + i \frac{e}{\hbar} k_z X_{12} e^{-i(\omega t - \mathbf{k} \cdot \mathbf{r})} \\ &= \underbrace{\frac{1}{2s_0} \frac{\partial s_0}{\partial z}}_{q_r} \Omega + i \underbrace{k}_{q_i} \Omega \end{aligned} \quad (2.11)$$

where we have also made use of equation 2.10. Inserting these values of q_r and q_i

into equation 2.7, yields the total force, which can be generalized to three spatial dimensions by replacing the partial derivative with a gradient. This results in the following expression for the total force

$$\mathbf{F} = \underbrace{-\frac{\hbar\delta}{2} \cdot \frac{\nabla(I/I_S)}{1 + I/I_S + (2\delta/\Gamma)^2}}_{\text{Dipole force: } \propto \nabla I} + \underbrace{\hbar\mathbf{k} \frac{\Gamma}{2} \cdot \frac{I/I_S}{1 + I/I_S + (2\delta/\Gamma)^2}}_{\text{Scattering Force: } \propto I} \quad (2.12)$$

Scattering rate: $R_{\text{scatt}} = \Gamma\rho_{22}$

The first term on the right-hand side of equation 2.12 is the *dipole force*. It is proportional to the gradient of the field intensity and is the result of the refraction of light by the atom. For large detunings, such that $|\delta| \gg \Gamma$, the dipole force reduces to the derivative of the light shift due to the a.c. Stark shift obtained using time-dependent perturbation theory

$$\mathbf{F}_{\text{dip}} = -\nabla U_{\text{dip}} \simeq -\nabla \left(\frac{\hbar\Omega^2}{4\delta} \right) \quad (2.13)$$

In a non-homogeneous field, the difference in intensity across the atom results in a net force, whose direction is dictated by the field's detuning from the atomic resonance, as can be seen in equation 2.12: a red-detuned field ($\delta < 0$) gives rise to an 'attractive' force in the direction of highest intensity, while a blue-detuned field ($\delta > 0$) 'repels' atoms towards the region of lowest intensity. The dipole force vanishes on resonance ($\delta = 0$).

The second term in equation 2.12 is the *scattering force*. It arises from absorption of photons from the incident field and its form can equally be derived by considering that the force is equal to the rate of change of momentum. The momentum imparted by a single photon of wavevector \mathbf{k} is $\mathbf{p} = \hbar\mathbf{k}$ and the rate at which such photons are absorbed is given by $R_{\text{scatt}} = \Gamma\rho_{22}$ where ρ_{22} is the excited-state population, given by $\rho_{22} = (1 - w)/2$, with w the third component of the Bloch vector whose steady state value for a two-level system is¹

$$\begin{pmatrix} u \\ v \\ w \end{pmatrix} = \frac{1}{\delta^2 + \Omega^2/2 + \Gamma^2/4} \begin{pmatrix} \Omega\delta \\ \Omega\Gamma/2 \\ \delta^2 + \Gamma^2/4 \end{pmatrix} \quad (2.14)$$

¹ this result assumes the RWA.

The force is simply equal to the momentum transfer times the scattering rate: $\mathbf{F}_{\text{scatt}} = \hbar \mathbf{k} R_{\text{scatt}}$, which reproduces the second term in equation 2.12.

The following two subsections discuss the use of the scattering force for laser cooling and trapping of atoms. Broadly speaking, trapping in position-space requires a spatially-dependent restoring force and trapping in momentum-space requires a velocity-dependent restoring force. In a MOT, these are generated by engineering the space- and velocity-dependence of quasi-resonant photon scattering from an incident laser beam. Below we first discuss the case of a purely velocity-dependent force (‘Doppler cooling’), followed by the case of combined velocity- and spatially-dependent force (‘magneto-optical trapping’).

2.1.2 Doppler cooling

As discussed above, laser cooling relies on the momentum imparted to the atom during repeated stimulated-absorption/spontaneous emission cycles. Each absorption event results in the transfer of the photon’s linear momentum, $\hbar \mathbf{k}$, energy $\hbar \omega$ and angular momentum \hbar , to the atom, together with its promotion to a higher-lying energy state. The recoil from the subsequent spontaneous photon emission occurs isotropically and hence averages to zero over many absorption-emission cycles. As a result, a net force acts on the atom in the direction of the light propagation and with a magnitude given by the single-photon momentum recoil, $\hbar k$, multiplied by the photon scattering rate, R_{scatt} , as given by equation 2.12. The dipole force is negligible compared to the scattering force in this case since relatively small detunings are used, $\delta \sim \Gamma$ and the characteristic distance over which the beam intensity varies is large compared with the wavelength (i.e. $k\Gamma l \gg \delta \nabla l$). The velocity-dependence of this force arises from the Doppler effect which causes an atom in motion with velocity \mathbf{v} to experience a laser detuning given by $\mathbf{k} \cdot \mathbf{v}$. The effect, which has also given its name to this cooling method, therefore results in a combined detuning of

$$\delta_{\text{Dopp}}^{\pm} = \delta \mp kv \tag{2.15}$$

when the atoms are moving towards or away from the incident laser beam with velocity v , respectively. In order to see how the scattering force of equation 2.12 can be used to cool atoms, consider now two counter-propagating laser beams of intensity I and frequency ω . Each of these beams exerts a force on an atom moving with velocity v according to equation 2.12 using the detunings of equation

2.15, resulting in a total force given by

$$F_{\text{TOT}}(v) = F_+ + F_-$$

$$= \hbar k \frac{\Gamma}{2} \frac{I}{I_S} \left[\frac{1}{1 + I/I_S + (2\delta_{\text{Dopp}}^+/\Gamma)^2} - \frac{1}{1 + I/I_S + (2\delta_{\text{Dopp}}^-/\Gamma)^2} \right] \quad (2.16)$$

where the relative minus sign comes from the counterpropagating wavevectors. To see the velocity dependence more clearly, we consider the small-velocity limit $v \ll \delta/k$ and expand equation 2.16 to first order in v :

$$F_{\text{TOT}}(v) \approx \frac{4\hbar k^2 (I/I_S) (2\delta/\Gamma)}{[1 + I/I_S + (2\delta/\Gamma)^2]^2} v \equiv -\beta v \quad (2.17)$$

When the laser is red-detuned ($\delta < 0$), this has the form of a viscous damping force, acting to oppose the atom's motion and hence slowing it down, with the analogy of movement through a viscous medium leading to the adoption of the name *optical molasses* for this beam configuration. Figure 2.1 shows the form of

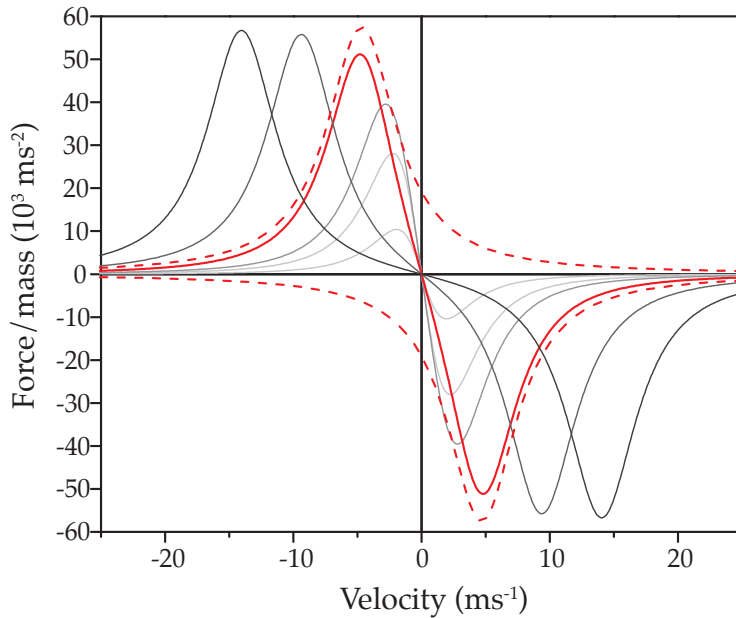


Figure 2.1: Acceleration due to scattering force in a 1D MOT plotted against atomic velocity. Curves are plotted for ^{87}Rb with $I/I_S = 1$ and for different laser detunings. From the innermost to the outermost curves, the detunings are: $-0.1\Gamma, -0.3\Gamma, -0.5\Gamma, -\Gamma, -2\Gamma, -3\Gamma$. The red dashed lines show the separate components of the force arising from each of the two counter-propagating beams for the case of $\delta = -\Gamma$.

this force as a function of atom velocity for various values of the (zero-velocity) beam detuning, δ . The molasses laser configuration can be extended in order to provide a viscous force along all three spatial directions by adding two more counter-propagating beam pairs, orthogonal to each other and to the first pair (i.e. six beams in total).

The Doppler limit

The *Doppler limit* represents the point at which Doppler cooling is balanced by the heating resulting from the discrete recoil events associated with the absorption and spontaneous emission from the laser beams. The light field of a single beam transfers an energy of $2\hbar\omega_r$ to an atom with each scattering event, where $\hbar\omega_r = \hbar^2 k^2 / 2m$ is the recoil energy, and does so at a rate of $2R_{\text{scatt}}$, with the factor of two accounting for the two counter-propagating beams and assuming no saturation of the transition (i.e. $I/I_S \ll 1$). The heating rate is therefore $4\hbar\omega_r R_{\text{scatt}}$. Equating this to the cooling rate $\mathbf{F}_{\text{TOT}} \cdot \mathbf{v}_x$, with \mathbf{F}_{TOT} given by equation 2.16, gives the steady-state kinetic energy

$$\frac{1}{2} m \overline{v_x^2} = -\frac{\hbar\Gamma}{8} \left(\frac{2\delta}{\Gamma} + \frac{\Gamma}{2\delta} \right) \quad (2.18)$$

Equating this to $\frac{1}{2} k_B T$ and minimizing with respect to the detuning, δ , yields the Doppler temperature

$$T_D = \frac{\hbar\Gamma}{2k_B} \quad (2.19)$$

obtained when $\delta = -\Gamma/2$. The Doppler temperatures for the transitions used in the cooling of ^{87}Rb and ^{39}K (see subsection 2.1.4) are $146\mu\text{K}$ and $145\mu\text{K}$, respectively, corresponding to velocities, $v_D = \sqrt{k_B T_D / m}$, of 12cm/s and 18cm/s .

Sub-Doppler cooling and the recoil limit

Temperatures below the Doppler limit can be obtained in optical molasses [93], most notably via the mechanism known as *Sisyphus cooling* [94, 95, 96, 97]. Sub-Doppler cooling relies on the existence of magnetic sublevels in the atomic ground state¹, which were omitted from the discussion above. Figure 2.2 illustrates this mechanism in a simplified system consisting of a $J = 1/2$ ground state and a $J' = 3/2$ excited state.

¹ For example the m_F sublevels of the hyperfine states - see subsection 2.1.4.

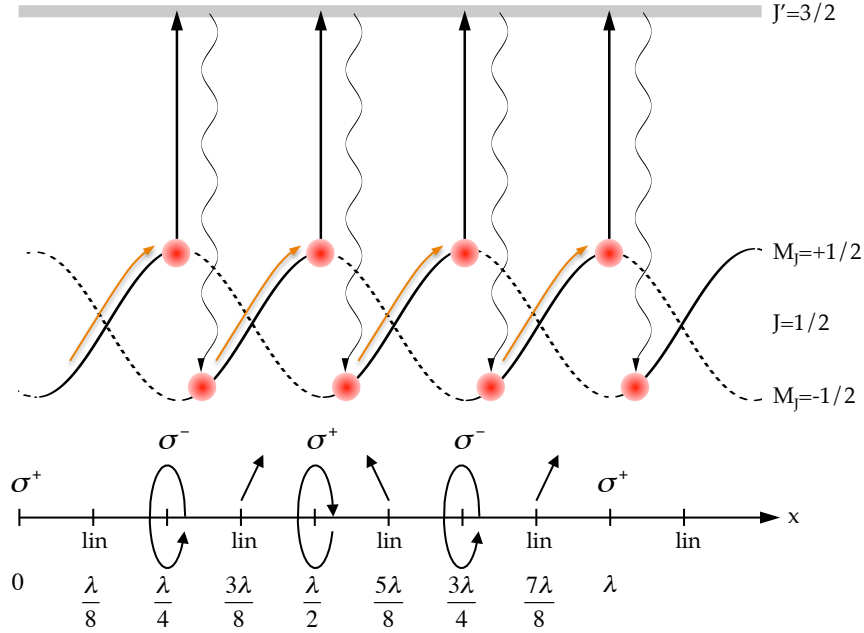


Figure 2.2: Illustration of the polarization-gradient (*Sisyphus*) cooling mechanism in the $\text{lin} \perp \text{lin}$ configuration. An atom in the $M_J = +1/2$ state at $x = 0$ moves along its potential curve until it reaches $x = \lambda/4$, at which the polarization is σ_- circularly polarized. The atom is excited to the $|J' = 3/2, M_J = -1/2\rangle$ state and decays preferentially down to the $|J = 1/2, M_J = -1/2\rangle$ state via spontaneous emission before the atom has moved a significant distance. The atom in the $M_J = -1/2$ state finds itself in a potential minimum and loses energy as it scales the potential landscape until it gets pumped back into $M_J = 1/2$ at $x = \lambda/2$, where the polarization is σ_+ -polarized.

In brief, the periodic polarization gradients that arise from the interference of counter-propagating MOT beams of different polarizations¹ cause a spatially-periodic modulation of the energies of the magnetic sublevels. This periodic potential is out of phase for different sublevels, with the maxima of one level coinciding with the minima of another. There follows a process of continuous back-and-forth optical pumping between the sublevels, with atoms at a potential peak absorbing a circularly-polarized photon and spontaneously emitting a higher-energy photon in order to decay to a lower-lying sublevel. The atom in this lower sublevel then continues moving until it reaches the next maximum in its potential and gets transferred back to the original state, which is now the lower-lying of the two. The name given to this mechanism refers to the fact that the atom continually finds itself ascending the potential landscape, only to be

¹ Most examples consider two beams linearly-polarized along orthogonal directions (the $\text{lin} \perp \text{lin}$ configuration) but the effect is also present for two circularly-polarized beams of opposing handedness (the $\sigma_+ - \sigma_-$ configuration).

quasi-instantaneously transferred to a neighbouring potential minimum in order to repeat the process.

The limit of this mechanism is reached when the atom's energy loss in being transferred to the potential minimum, proportional to $I/|\delta|^1$, is balanced by the recoil energy it acquires during spontaneous emission. The lowest temperature achievable in Sisyphus cooling is thus reached when this potential depth, which is proportional to the light intensity ($U_0 \propto I/|\delta|$), becomes equal to the kinetic energy imparted to an atom by the spontaneous emission of a photon, the so-called *recoil energy*, giving

$$T_{\text{rec}} = \frac{(\hbar k)^2}{2mk_{\text{B}}} \quad (2.20)$$

The recoil temperatures for ^{87}Rb and ^{39}K are 180nK and 415nK, respectively. The corresponding recoil velocities are simply found from $k_{\text{B}}T_{\text{rec}} = \frac{1}{2}mv_{\text{rec}}^2$ and are equal to 5.88mm/s and 1.34cm/s, respectively, although in practice the light intensity cannot be reduced indefinitely and attainable temperatures are limited to several tens of recoil temperatures [98].

Since the velocity capture range of the sub-Doppler cooling mechanisms is significantly narrower than that of Doppler cooling, laser cooling sequences are usually divided into two distinct stages. A typical laser cooling sequence begins with a Doppler cooling stage, during which the detuning is on the order of the linewidth ($\delta \sim -\Gamma$) and the intensity is on the order of I_S . This provides a strong radiation force for initial cooling and brings the temperature into the capture range for sub-Doppler cooling. The detuning is then taken even further from resonance and the intensity is decreased in order to obtain a temperature below the Doppler limit. This strategy requires some modification in the case of a manifold of excited states to which transitions may occur during optical molasses, and furthermore is very sensitive to the proximity of these transitions to each other [99]. This is discussed in the context of ^{39}K in subsection 2.1.4 below while chapter 3 describes the sequence we employ in further detail.

2.1.3 Magneto-optical trapping

Although optical molasses can cool the atomic cloud, they cannot prevent the diffusion of atoms from the region in which the beams overlap and hence do not constitute a trap, for which a spatially-dependent restoring force is required. In

¹ See sections 2.1.1 and 2.5 for discussion of optical potentials.

a magneto-optical trap (MOT), this spatial dependence is established by making the laser detuning a function of the atom's position. This is accomplished by exploiting the Zeeman shifts of the atom's different magnetic sublevels in conjunction with the optical selection rules.

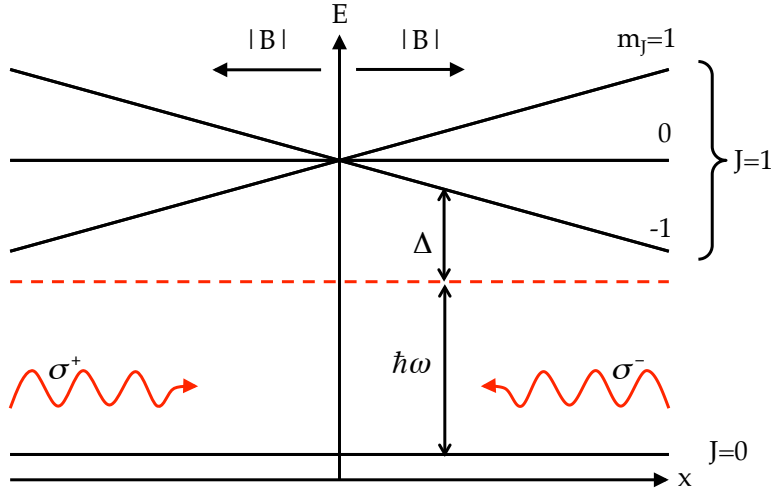


Figure 2.3: Illustration of the operating principle of a MOT in a $J = 0, 1$ system. A magnetic field gradient in conjunction with circularly polarized beams adds a spatial dependence to the scattering force used in the molasses configuration.

Figure 2.3 illustrates the MOT mechanism in a one-dimensional two-level system consisting of a $J = 0$ ground state and a $J = 1$ excited state, split into its three Zeeman sublevels, $m_J = -1, 0, +1$, by a linearly varying magnetic field. The two counterpropagating beams are circularly polarized in opposite senses and red-detuned from the atomic resonance frequency. The circular polarization of each beam is chosen such that the only transition it can induce ($\Delta m_J = \pm 1$ for σ^+/σ^- , respectively) is brought closer to resonance by the Zeeman shift whenever an atom moves away from the trap centre towards the beam. Helpfully, this Zeeman shift simultaneously ensures that the transition induced by the beam of opposite circular polarization is shifted further away from resonance and hence does not accelerate the atom along its direction of motion. Figure 2.4 shows the most common MOT configuration, consisting of the three orthogonal, counter-propagating optical molasses beam pairs, intersecting midway between a pair of anti-Helmholtz magnetic coils. The coils produce a magnetic field with a zero at the point midway along their mutual axis and increasing linearly with position in all directions such that its value is given by $\mathbf{B} = B'(x, y, -2z)$, where B' is the field gradient. See appendix E for a more detailed description of the field produced by this configuration. The total detuning of each beam from the relevant

transition is now given by

$$\delta_{\text{MOT}}^{\pm} = \delta \mp \mathbf{k} \cdot \mathbf{v} \pm (g_e m_e - g_g m_g) \frac{\mu_B B'}{\hbar} \mathbf{x} \equiv \delta \mp \mathbf{k} \cdot \mathbf{v} \pm \alpha \mathbf{x} \quad (2.21)$$

where the third term is the detuning due to the Zeeman shift, $U = -\mu \cdot \mathbf{B}$, between the two states (see section 2.3 below) and μ is the atom's magnetic moment (recall: $\mu_B \hbar \cong 1.4$ MHz/G). The subscripts 'g' and 'e' represent the lower and higher states in the transition, respectively.

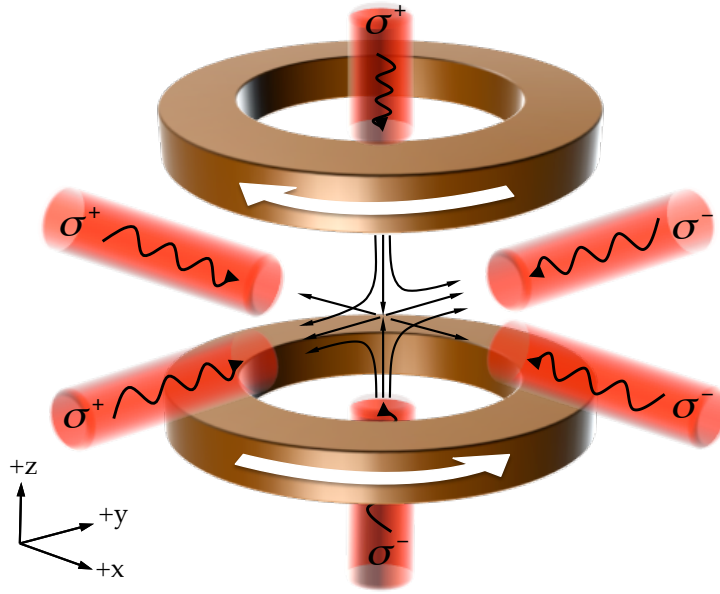


Figure 2.4: Relation between the currents generating the quadrupole field and the beam polarizations in a MOT. The black arrows indicate current direction and the notation on each beam indicates the type of transition it drives in the trapped atoms ($\sigma^{+/-}$). For this configuration, all the beams in the x and y directions are left-circularly polarized when viewed along their propagation direction (i.e. their polarization vector rotates anti-clockwise), whereas the beams in the z direction are right-circularly polarized.

The total scattering force now acquires a position-dependence in addition to the Doppler cooling velocity-dependence $F(v) \rightarrow F(x, v)$. Repeating the low-velocity expansion of equation 2.16 but using the detunings of equation 2.21, and also assuming a weak magnetic field, i.e., $v \ll \delta/k$ and $B \ll \hbar\delta/\mu_B$ yields

$$F(x, v) = \frac{4\hbar k (I/I_S) (2\delta/\Gamma)}{[1 + I/I_S + (2\delta/\Gamma)^2]^2} (kv + \alpha x) \equiv -\beta v - \kappa x \quad (2.22)$$

where the spring constant $\kappa = \alpha\beta/k$. The atom's equation of motion is therefore

$$\ddot{x} + \gamma_{\text{MOT}}\dot{x} + \omega_{\text{MOT}}^2 x = 0 \quad (2.23)$$

This is the equation of a damped harmonic oscillator in which $\gamma_{\text{MOT}} = \beta/m$ and $\omega_{\text{MOT}} = \sqrt{\kappa/m}$ are the damping coefficient and effective oscillation frequency, respectively, with m the atomic mass. For typical MOT parameters ($\delta = -\Gamma$, $I/I_S = 1$, $B' = 10\text{Gcm}^{-1}$), oscillation frequencies are on the order of a few kHz while damping rates are on the order of tens of kHz. The damping ratio $\zeta = \beta/(2\sqrt{m\kappa})$ is therefore much greater than one and the motion is overdamped. Any displacement of the atom within the MOT will (exponentially) decay towards the trap centre without oscillating [100, 101].

We note that in general, the presence of the MOT's magnetic field gradient greatly complicates the mechanisms normally responsible for sub-Doppler cooling due to the differential Zeeman shifts imparted to each of the magnetic sublevels. This can be qualitatively be viewed as resulting from the competition between the Larmor precession about the external field, and the optical pumping process which tends to align the atomic dipole with the orientation of the electromagnetic field [102].

2.1.4 Laser cooling of ^{39}K and ^{87}Rb

The basic theory of laser cooling is formulated for a two-level system, and while real atoms invariably possess a more complicated electronic level structure, the single valence electron of the alkali metals gives rise to a relatively simple level hierarchy which makes this family particularly convenient cooling targets. Indeed only recently have *non*-alkali atomic species such as Calcium [103], Magnesium [104], Strontium [103, 105], Argon [106], Krypton [106], Ytterbium [107], Dysprosium [108, 109] and others been used in laser cooling and degenerate-gas experiments.

Figure 2.5 shows part of the the hyperfine energy level structure for the bosonic species used in our experiments, ^{87}Rb and ^{39}K . More specifically, we focus on the D_2 transition between the $|L = 0, J = 1/2\rangle$ ground state and the $|L = 1, J = 3/2\rangle$ excited state manifolds. The natural linewidths of the D_2 lines in both ^{87}Rb and ^{39}K are approximately $\Gamma = 2\pi \times 6\text{MHz}$, i.e. an excited state lifetime of 26ns.

In both species, the ground state is split by the hyperfine interaction into $|F = 1\rangle$ and $|F = 2\rangle$ hyperfine states and the excited state ($5^2P_{3/2}$ for ^{87}Rb and $4^2P_{3/2}$ for

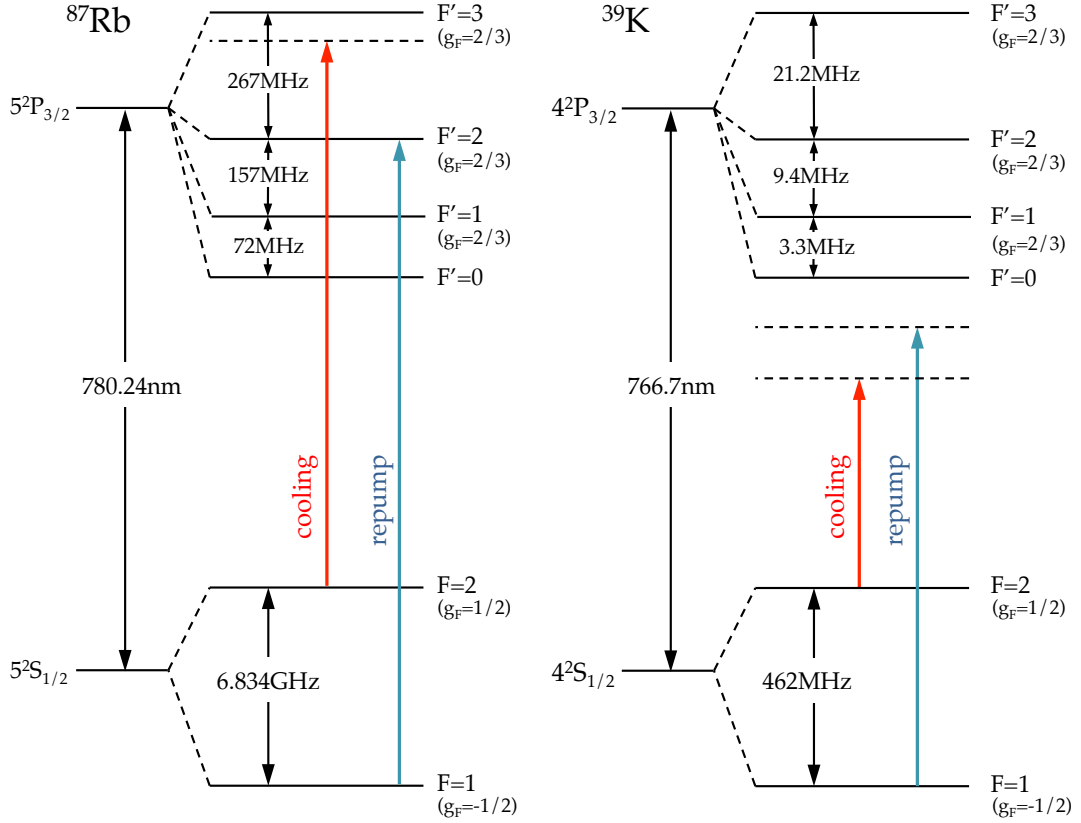


Figure 2.5: Hyperfine structure of the D_2 -line states in ^{87}Rb and ^{39}K . The total angular momentum of each state, $\mathbf{F} = \mathbf{I} + \mathbf{J}$, is shown together with its Landé g-factor, g_F . Red (blue) arrows indicate the cooling (repump) frequencies. The precise values of the detunings used in our experiments are given in table 3.2.

^{39}K) into $|F' = 1, 2, 3\rangle$ states. In our dual-species MOT, the role of the two-level system for both species is played by the $|F = 2\rangle$ and $|F' = 3\rangle$ hyperfine states, and it is the transition $|F = 2\rangle \rightarrow |F' = 3\rangle$ that constitutes the *cycling* or *cooling transition* used during laser cooling. The saturation intensities for the D_2 transitions in ^{87}Rb and ^{39}K are 1.67 mW cm^{-2} [110] and 1.75 mW cm^{-2} [111], respectively. Chapter 3 contains a detailed description of our experimental parameters, while appendix A contains a more detailed energy-level diagram for the two species.

The selection rule $\Delta F = 0, \pm 1$ implies that decay from $|F' = 3\rangle$ can only occur to the $|F = 2\rangle$ state. However, the finite linewidth of all the hyperfine levels together with the required detuning of the cooling beam mean that occasional excitation of atoms occurs from the $|F = 2\rangle$ to the $|F' = 2\rangle$ state. Decay from $|F' = 2\rangle$ to $|F' = 1\rangle$ is then allowed and as all the atoms gradually accumulate in the $|F' = 1\rangle$ state they are removed from the cycling transition and are no longer cooled. This

pumping is countered by the so-called *repump* beam, which is resonantly tuned to the $|F = 1\rangle \rightarrow |F' = 2\rangle$ transition. Atoms ‘repumped’ to $|F' = 2\rangle$ then have another chance at decaying to $|F = 2\rangle$ and hence back onto the cooling cycle. The cooling and repump transition are indicated in figure 2.5 as red and blue arrows, respectively.

The situation in ^{39}K is modified by the narrow, 34MHz, overall splitting of the excited-state hyperfine manifold [49]. This unresolved level structure has two main consequences for the laser cooling process:

1. Firstly, the unresolved excited-state gives rise to much stronger pumping into the $|F = 1\rangle$ ground state since the probability of $|F = 2\rangle \rightarrow |F' = 1, 2\rangle$ transitions is greatly increased. This requires the use of repump light of similar intensity to the cooling light in order to prevent accumulation of the atoms in the $|F = 1\rangle$ state. This pumping is so frequent that the contribution of the repump beam to the cooling process becomes comparable to that of the cooling beam. The functional distinction between the two is effectively blurred and the use of their original names is simply a matter of convention. In addition, use of the same detunings as used for other species ($\delta \sim \Gamma$), results in heating due to the blue-detuning of the beams from the nearby hyperfine states. For this reason, it has been found [47, 112, 49, 48, 113, 59] that the largest capture velocity is obtained with both the cooling and repump beams red-detuned from the entire excited-state manifold, as shown in figure 2.5.
2. Although this large detuning of both beams yields a large capture velocity¹, it does not produce an effective sub-Doppler cooling force [49] and under normal operating conditions, the temperatures achieved during optical molasses are on the order of 1mK. In general, sub-Doppler cooling mechanisms are only efficient when the excited-state hyperfine splitting is much larger than the natural linewidth Γ , as in Rb, Na and Cs, or when it is smaller than Γ , as in Sr [114, 105]. When it is on the order of Γ , as is the case for ^{39}K and ^{41}K , sub-Doppler cooling is impeded by heating forces or resonant photon reabsorption [99]. It has, however, been shown both theoretically [49, 99] and experimentally [115, 116] that sub-Doppler cooling of these isotopes is made possible by a suitable modification of the usual cooling strategy. Both [115] and [116] employ an initial Doppler cooling stage with both beams detuned from the entire excited-state hyperfine manifold. This

¹ Found experimentally in [47, 112] to exceed 30m/s.

is followed by a molasses stage that in general involves a significant *reduction* in the cooling beam's detuning and intensity, together with an even larger reduction in the detuning and intensity of the repump beam. With their respective strategies, [115] and [116] report temperatures of $34\mu\text{K}$ and $25 \pm 3\mu\text{K}$, respectively, for their ^{39}K clouds.

2.2 Optical pumping

At the end of the MOT and molasses stages, the atoms are distributed between the various $|F = 2\rangle$ Zeeman sublevels - magnetically trappable and untrappable alike - and must be transferred into the $|2, 2\rangle$ state prior to application of the quadrupole field in order to trap the highest possible atom number. In order to accomplish this, a uniform magnetic guide field is initially applied in order to define a quantization axis. It is important to ensure that this quantization field is not strong enough to take the magnetic sublevels out of resonance with the lasers. We use a coil pair aligned along the propagation direction of the pumping beam in order to produce a field of several Gauss at the location of the atoms. The atoms are then illuminated with a beam resonant with the $|F = 2\rangle \rightarrow |F' = 2\rangle$ transition and σ^+ -circularly-polarized with respect to the quantization axis. The $|F = 1\rangle \rightarrow |F' = 2\rangle$ repump light also remains on during the first half of this process.

Optical pumping relies on the fact that transitions driven by σ^+ -polarized light must satisfy $\Delta m_F = +1$. i.e., in our case $|2, m_F\rangle \rightarrow |2, m_F + 1\rangle$. From this excited $F' = 2$ state the atom can spontaneously decay to one of the ground states while obeying $\Delta m_F = 0, \pm 1$, and with a probability determined by the appropriate Clebsch-Gordan coefficients. The presence of the repump light ensures that any atoms decaying to the $F = 1$ ground state are transferred back into $F' = 2$ and kept on the pumping cycle. After several absorption/emission cycles, the atoms accumulate in the $|2, 2\rangle$ state, labelled 'stretched' since m_F is at its maximal value and 'dark' since, for lack of an $|m_F + 1\rangle$ state, it can no longer interact with the pumping light.

Transfer of all the atoms into the $|2, 2\rangle$ state is not only important for maximizing the number of *initially* trapped atoms in the magnetic trap, but also for limiting subsequent trap-loss collisions which reduce numbers, and cause heating. These processes are even more critical in our case since we rely on interspecies ^{87}Rb - ^{39}K collisions for the sympathetic cooling of ^{39}K . If a significant fraction of

these collisions are inelastic, sympathetic cooling will not be efficient enough to sufficiently increase the ^{39}K phase-space density and could prevent condensation of the sample. Indeed, extra effort is made during evaporative cooling to actively remove any $|2, 1\rangle$ atoms, whether initially present or subsequently created, from the trap (see section 3.9).

The inelastic collisions most likely to cause losses from our trap are so called hyperfine-changing collisions (HCC) of the type $\text{Rb } |2, 1\rangle + \text{K } |2, 2\rangle \rightarrow \text{Rb } |1, 1\rangle + \text{K } |2, 2\rangle + \text{KE}$, in which the ^{87}Rb ground state hyperfine energy, 6.8GHz, is released and divided between the kinetic energies of the two emerging atoms. The $|1, 1\rangle$ atom is anti-trapped and the $|2, 2\rangle$ atom is also ejected if its final kinetic energy exceeds the trap depth. The same process with the species reversed can also occur but presents a lesser threat since (a) there are far fewer ^{39}K atoms present and (b) the ^{39}K ground state hyperfine splitting, 462MHz, is much smaller than that of ^{87}Rb (although still larger than the trap depth). The process $|2, 1\rangle + |2, 1\rangle \rightarrow |2, 2\rangle + |2, 0\rangle$ can also occur, leading to further losses. By contrast, atoms in stretched states do not experience such spin-exchange collisions since the total angular momentum projection Σm_F , must be conserved in these collisions.

In addition to maximizing the number of trapped atoms and suppressing trap losses and heating, atoms in the $|2, 2\rangle$ state experience the tightest magnetic confinement and hence minimal contact with the transfer tube walls as well as the highest elastic collision rate for efficient evaporative cooling.

2.3 Magnetic trapping

Magnetic traps are used in order to provide a conservative potential which does not rely on photon absorption and hence enables atoms to ultimately be cooled to temperatures below the recoil limit. Our atoms possess a non-zero magnetic dipole moment and hence experience a force in the presence of an external magnetic field gradient, which can therefore be used to generate a suitable trapping potential. We capture our atoms in a purely magnetic trap generated by our quadrupole coils prior to transporting them to the science cell.

2.3.1 Energy shift in an external magnetic field

The energy shift experienced by an atom due to a static external magnetic field, B , is given by

$$H_B = \frac{\mu_B}{\hbar} (g_S S_z + g_L L_z + g_I I_z) B_z \quad (2.24)$$

where B_z is the component of the field along the z (quantization) axis, (S_z, L_z, I_z) are the operators for the z -components of the spin, orbital and nuclear angular momenta, respectively, and (g_S, g_L, g_I) are the corresponding Landé g -factors. If this energy shift is small compared to the hyperfine splitting

$$H_{\text{hfs}} = A_{\text{hfs}} \mathbf{I} \cdot \mathbf{J} \quad \Rightarrow \quad E_{\text{hfs}} = \frac{1}{2} A_{\text{hfs}} [F(F+1) - I(I+1) - J(J+1)] \quad (2.25)$$

arising from the coupling between the electronic and nuclear angular momenta, then $\mathbf{F} = \mathbf{I} + \mathbf{J}$ and m_f are good quantum numbers. A_{hfs} is the hyperfine structure constant, equal to $A_{\text{hfs}} = h \cdot 3.417\text{GHz}$ and $h \cdot 230.86\text{MHz}$ for ^{87}Rb and ^{39}K , respectively. Equation 2.24 can then be written as

$$H_B = \mu_B g_F F_z B_z \quad (2.26)$$

where g_F is the relevant Landé g -factor. The resulting *Zeeman* energy shift is simply linear in the field strength

$$U(\mathbf{r})_{|F, m_F\rangle} = -\boldsymbol{\mu} \cdot \mathbf{B}(\mathbf{r}) = \mu_B g_F m_F B_z \quad (2.27)$$

The force on an atom in such a potential is then

$$\mathbf{F}(\mathbf{r}) = -\nabla U(\mathbf{r}) = -\mu_B g_F m_F \nabla B_z \quad (2.28)$$

From equation 2.27, it follows that any states for which $g_F m_F > 0$ can lower their potential energy by moving to regions of lower magnetic field. These states are magnetically trappable in a local field minimum and are hence known as *low-field seeking* states. The Landé factors of the ground states of both ^{87}Rb and ^{39}K are $g_{F=1} = -1/2$ and $g_{F=2} = 1/2$, and hence the trappable $|F, m_F\rangle$ states of both species are $|1, -1\rangle$, $|2, 1\rangle$ and $|2, 2\rangle$.

When the external-field and hyperfine shifts are comparable, however, the full Hamiltonian $H = H_{\text{hfs}} + H_B$ has to be diagonalized. An analytical result exists for the energy shift of the states belonging to the fine-structure ground state

manifold (i.e. $L = 0$, $J = 1/2$) in the form of the *Breit-Rabi* formula [117]

$$E_{|J=1/2, m_J, m_I\rangle} = -\frac{\Delta E_{\text{hfs}}}{2(2I+1)} + g_I \mu_B m B \pm \frac{\Delta E_{\text{hfs}}}{2} \left(1 + \frac{4m x}{2I+1} + x^2\right)^{1/2} \quad (2.29)$$

In this formula $\Delta E_{\text{hfs}} = A_{\text{hfs}} (I + 1/2)$ is the hyperfine splitting, $m = m_I \pm m_J = m_I \pm 1/2$, $B = |\mathbf{B}|$ is the magnitude of the magnetic field and x is given by

$$x = \frac{(g_J - g_I) \mu_B B}{\Delta E_{\text{hfs}}} \quad (2.30)$$

For both ^{87}Rb and ^{39}K , $I = 3/2$. The energy shifts for the *D*-line ground state of ^{39}K are shown in figure 2.6.

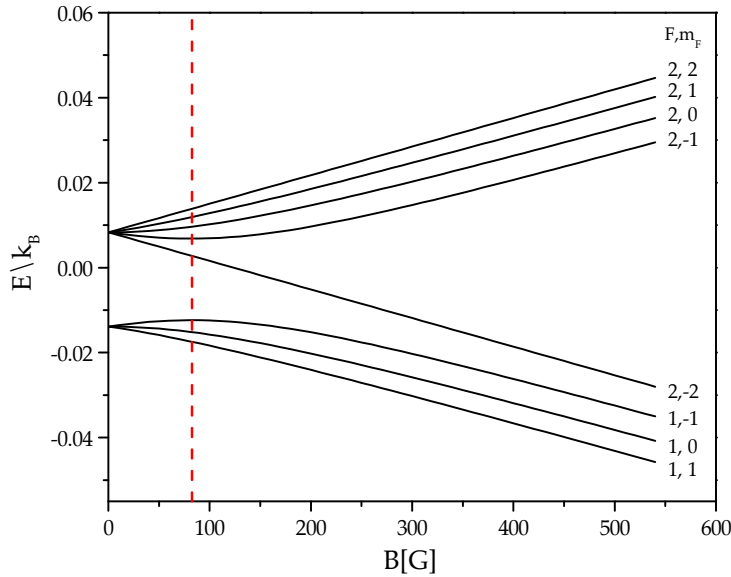


Figure 2.6: Hyperfine structure in the $4^2S_{1/2}$ ground state of ^{39}K in a magnetic field, calculated using the Breit-Rabi formula 2.29. States are labeled with their low-field quantum numbers $|F, m_F\rangle$. The dashed line shows the maximal field, 82.4G, at which the $|1, -1\rangle$ state can be magnetically trapped. The maximal trap depth for atoms in this state is roughly 1.48mK.

We make use of the Breit-Rabi formula, equation 2.29, in our experiments for the calibration of the magnetic field used to access the Feshbach resonance at 402.5G. This is done via RF spectroscopy on the transition between two magnetic sublevels in ^{87}Rb , the precise separation of which is obtained using the Breit-Rabi formula. Our procedure for doing this is described in subsection 3.11.3.

The depth of a magnetic trap is given by $U = \mu \Delta B$, where ΔB is the difference

between the field maximum and its minimal value. This depth can be expressed in units of temperature as $U = \mu_B g_F m_F \Delta B / k_B$. For example, neglecting gravitational effects, ^{87}Rb and ^{39}K atoms in the $|2, 2\rangle$ state experience a trap of depth $U = \mu_B \Delta B / k_B \cong (0.7\text{mK/G}) \times \Delta B$. Chapter 3 contains the details of the magnetic trap configurations used during the transport and sympathetic cooling stages of our experiments.

2.3.2 Non-adiabatic losses from magnetic traps

The atom's magnetic dipole moment precesses about the local external magnetic field at the Larmor frequency, $\omega_L = \mu B / \hbar$, and as long as the external field direction as experienced by the atom changes slowly with respect to ω_L the moment will adiabatically follow the field direction and hence remain in its trappable state relative to the instantaneous magnetic field. This criterion can be written as

$$\frac{1}{\omega_L} \frac{|\mathbf{v} \cdot \nabla \mathbf{B}|}{B} \ll 1 \quad (2.31)$$

i.e. that the change in field direction experienced by the atom during one precession about the field is much smaller than 2π . However from criterion 2.31, we notice an important problem: In regions of very low magnetic field, the adiabaticity criterion can be violated. Atoms of sufficient temperature will experience too rapidly changing a field and will transition to a different m_F state, most likely an untrapped one ($g_F m_F < 0$), and will hence be lost from the trap. These transitions are known as Majorana spin flips [118, 119] and especially plague traps with magnetic field zeros, at which atoms of arbitrarily low velocity are transferred to untrapped states and lost from the trap. Since the magnetic zero is also the place where the coldest atoms congregate, Majorana spin flips also cause acute heating of the atomic cloud and ultimately prevent the sample from reaching the temperatures required for entering the quantum degenerate regime [120, 121].

The quadrupole magnetic field produced by our MOT coils contains a magnetic zero at its origin and is therefore susceptible to such losses, rendering it unsuitable for sustained evaporative cooling. In order to address this problem, after transport of the atoms to the science cell in the quadrupole field the trap is modified so as to remove the zero-field region. This trap configuration consists of a harmonic potential whose minimum is offset from zero. More details about this QUIC (Quadrupole-Ioffe configuration) trap can be found in section 3.8.

2.4 Evaporative and sympathetic cooling

2.4.1 Evaporative cooling

Laser cooling as described in section 2.1 produces atom samples with temperatures below the Doppler limit but still significantly above the recoil limit. Typical MOT phase-space densities are on the order of $\rho \sim 10^{-6}$ and it was soon realised that a novel cooling technique was required in order to achieve the higher phase-space densities ($\rho \sim 1$) required for the onset of BEC. This led to the proposal of evaporative cooling [20] as a means of raising the phase-space density and was a key milestone on the route to the first experimental realizations of BEC. The first use of evaporative cooling was for cooling hydrogen atoms in 1988 [21].

Evaporative cooling relies on the selective removal from the trap of atoms with higher-than-average kinetic energy. Rethermalization of the gas via elastic two-body collisions, leaves the remaining atoms at a lower equilibrium temperature (see figure 2.7). The gradual removal of atoms with ever decreasing energies enables an arbitrary reduction of the temperature, limited in principle only by the initial number of trapped atoms. The current lowest reported temperature obtained via evaporative cooling is 450 ± 80 pK, achieved by the MIT group [122].

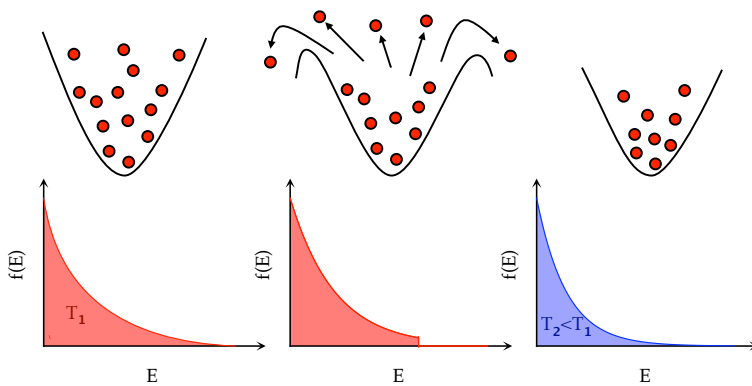


Figure 2.7: Principle of evaporative cooling. Lowering the trap depth removes atoms from the high-energy tail of the thermal distribution characterised by temperature T_1 (bottom left), after which the remaining gas re-equilibrates via elastic collisions at a lower temperature, $T_2 < T_1$ (bottom right).

2.4.2 RF and microwave evaporation

The most common technique for selective removal of high-energy trapped atoms relies on the spatially-varying Zeeman shift experienced by the atoms in the magnetic trap. Atoms with higher kinetic energies will be located further out in the magnetic potential according to $\frac{1}{2}mv^2 \approx g_F\mu_B m_F B$. High-energy atoms can therefore be selectively transferred to untrapped states by the application of resonant oscillating magnetic field. The most commonly used transitions used in evaporative cooling are the *RF transitions* between the magnetic sublevels of the hyperfine state in which the atoms are confined.

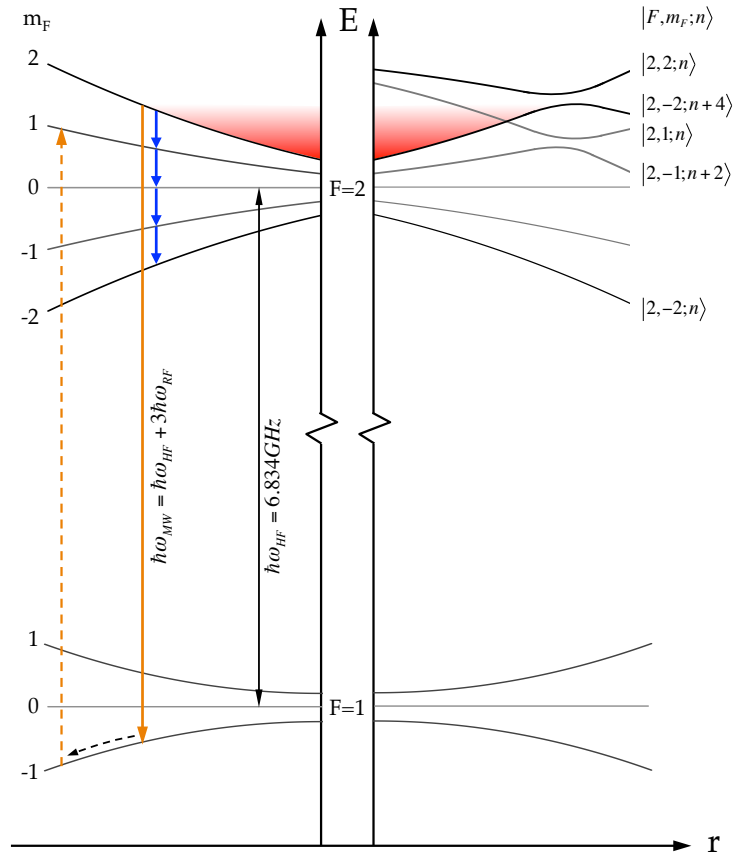


Figure 2.8: Evaporative cooling in a harmonic potential. Radio-frequency radiation tuned to the $\Delta m_F = 1$ resonance frequency induces a series of four single-photon transitions to the untrapped $|2, -2\rangle$ state. Within the dressed atom picture, The asymptotic state $|2, 2; n\rangle$ (where n is the number of photons) is adiabatically connected to the untrapped $|2, 2; n+4\rangle$ state by an effective four-photon transition. The hyperfine evaporation transition $|2, 2\rangle \rightarrow |1, 1\rangle$ is indicated by the orange arrow. The dashed orange arrow shows the route through which $|1, 1\rangle$ atoms can reach the $|2, 1\rangle$ state.

These $\Delta m_F = 1$ transitions occur on a surface of constant magnetic field defined by the condition

$$\hbar\omega_{\text{RF}} = \mu_B g_F B \quad (\text{RF evaporation}) \quad (2.32)$$

For ^{87}Rb and ^{39}K atoms in the $|2, 2\rangle$ state this radiation, also referred to as an *RF knife*, drives sequential single-photon transitions between the Zeeman sublevels, ultimately transferring the absorbing atoms into the untrapped $m_F = 0$ and the anti-trapped $m_F = -1, -2$ states which are removed from the trap. This process amounts to truncating the trap depth at the knife energy, which is normally expressed as a multiple, η , of the cloud's instantaneous temperature i.e.,

$$\hbar\omega_{\text{evap}} = \eta k_B T \quad (2.33)$$

where η is known as the *evaporation parameter*. The process is illustrated, within both the diabatic and dressed-state [95] pictures, in figure 2.8. For ^{87}Rb and ^{39}K atoms in the $|2, 2\rangle$ state for which $g_F = 1/2$, the resonance frequency for such a $\Delta m_F = 1$ transition corresponds to

$$\frac{\nu_{\text{RF}}}{B} = \frac{\mu_B g_F \Delta m_F}{h} = 1.4 \text{ MHz/G} \quad (2.34)$$

This method is problematic, however, for use in our sympathetic cooling stage since due to the almost identical potential experienced by the two species, as many ^{39}K as ^{87}Rb atoms would be removed from the trap. In order to circumvent this problem, we employ evaporative cooling on the ground-state hyperfine transition

of ^{87}Rb . The transition frequency of $\nu_{\text{evap}} \approx 6.834\text{GHz}$ gives this approach the name *microwave (MW) evaporation*. We induce transitions between the trapped $|2, 2\rangle$ state and the antitrapped $|1, 1\rangle$ state in ^{87}Rb by applying radiation at a frequency given by

$$\hbar\omega_{\text{MW}} = \hbar\omega_{\text{HF}} + 3\hbar\omega_{\text{RF}} \quad (\text{MW evaporation}) \quad (2.35)$$

In terms of temperature, the height of the evaporating knife in both cases is then

$$\begin{aligned} \frac{\nu_{\text{RF}}}{T} &= \frac{k_B}{2h} = 0.01 \text{ MHz}/\mu\text{K} \quad (\text{RF}) \\ \frac{\nu_{\text{MW}}}{T} &= \frac{3k_B}{2h} = 0.03 \text{ MHz}/\mu\text{K} \quad (\text{MW}) \end{aligned} \quad (2.36)$$

In experiments, an initial frequency is chosen for the knife which is subsequently

ramped down in order to ensure continual cooling of the sample. This procedure is known as *forced* evaporative cooling. During microwave evaporation, atoms transferred into the $|1, 1\rangle$ state can be transferred back up into the trapped $|2, 1\rangle$ state by the evaporation radiation on their way out of the trap (see figure 2.8). These $|2, 1\rangle$ atoms lead to heating and atom loss via spin-exchange collisions and hence need to be removed during evaporation. For this reason, during our hyperfine evaporation sequence we continuously sweep a second field in order to transfer any residual $|2, 1\rangle$ atoms to the untrapped $|1, 0\rangle$ state. See section 3.9 for more details.

Evaporation efficiency

Since this form of cooling relies on the removal of atoms, the overall efficiency of the process is best characterized by the gain in phase-space density, ρ , compared to the change in atom number, N . The most commonly used figure of merit for the evaporation efficiency is the logarithmic derivative, measuring the relative *fractional* changes in these quantities

$$\gamma = -\frac{d\rho/\rho}{dN/N} = -\frac{d\ln\rho}{d\ln N} \quad (2.37)$$

In the absence of any trap losses due to inelastic collisions the optimal rate for evaporative cooling, in the sense of yielding the largest atom number at the BEC transition temperature, is set by the initial temperature and by the elastic collision rate, $\Gamma_{\text{el}} = 1/\tau_{\text{el}}$, which is responsible for restoring the cloud to its equilibrium thermal distribution. However, in practice atoms are constantly lost from the trap due to background and three-body collisions at a rate $\Gamma_{\text{loss}} = 1/\tau_{\text{loss}}$ and this acts to oppose the rise in phase-space density caused by cooling. Therefore optimal evaporative cooling, in attempting to maximize the value of γ , relies on a trade-off between efficiency, as determined by the value of η , and cooling speed, as determined by the rate at which the knife is swept through the cloud.

As a limiting example, in the absence of inelastic losses η could be chosen to be arbitrarily large and the sweep rate arbitrarily slow, such that after an arbitrarily large time a *single* atom containing an arbitrarily large fraction of the cloud's kinetic energy would be evaporated from the trap, cooling the remaining atoms to a corresponding arbitrarily low temperature. It is therefore apparent that the number to be maximized for efficient evaporation is $R = \tau_{\text{loss}}/\tau_{\text{el}}$, the ratio of

‘good’ elastic collisions to ‘bad’ inelastic collisions (i.e. the number of elastic collisions per trapping time). This is simply stating that the atoms should re-equilibrate as fast as possible compared to the rate at which they are being lost from the trap.

In our experiments the initial value of η is usually chosen to be around 7-8, both for evaporation of ^{87}Rb in the QUIC trap (see section 3.8) as well as for the optical evaporation of ^{39}K in the CDT (see section 2.5). The evaporation speed is then empirically found by maximizing the phase-space density at the end of the evaporation sweep.

Runaway regime

A desirable regime to enter during evaporative cooling is that of so-called *runaway evaporation*, in which the elastic collision rate

$$\tau_{\text{el}} = \sigma n \bar{v} \quad (2.38)$$

increases as the temperature is decreased. Here σ is the scattering cross-section, n is the density and \bar{v} is the mean thermal velocity. This implies that the increase in density due to the reduction in temperature more than compensates for the concomitant reduction in thermal velocity *and* atom number. Within a simple model¹, the scaling of temperature with number can be expressed as $T \propto N^\beta$ with $\beta = (\eta - 3)/3$. Similarly, The volume scales as $V \propto N^\alpha$ with $\alpha = (\eta - 3)/2$. Hence the scattering rate above is found to scale as

$$\sigma n \bar{v} \propto N^{1-\beta} \quad (2.39)$$

which implies that runaway cooling requires $\beta > 1$ or $\eta > 6$. By contrast, in a uniform system the decrease in temperature leads to an overall decrease in the elastic scattering rate and hence to a drop in the evaporation efficiency. In general, the dependence of the density in a power-law trap with exponent ν is given by

$$n(r) = n_0 e^{\frac{-Ar^\nu}{k_B T}} \quad (2.40)$$

which leads to a temperature dependence of $n_0 \propto T^{-3/\nu}$. This implies that in a linear potential ($\nu = 1$) the runaway regime is entered for a lower value of the ratio R and evaporative cooling is hence more efficient. See [123, 22, 124] for

¹ Found by solving: $3k_B(N + dN)(T + dT) = 3Nk_B T + \eta k_B T dN$

a more detailed discussion. This benefit of the linear potential is harnessed in our experiments with an optically-plugged quadrupole trap, as described in appendix B. Another experimental constraint on the evaporative cooling procedure is the requirement that the finite frequency-width of the evaporation knife, due to power-broadening, magnetic field noise, etc., be smaller than the temperature of the remaining atoms. Careful field stabilization and choice of radiation power throughout the evaporation ramp can mitigate these effects [125, 126, 127, 128].

2.4.3 Sympathetic cooling

Introduction and principles

There are circumstances, however, in which attempting to perform direct evaporative cooling on an atomic species is undesirable. This is the case, for example, when the scattering length is very small or when one is working with a low-abundance species and wishes to avoid the heavy atom losses inherent to evaporative cooling¹. For fermionic species at low temperatures, s-wave collisions are forbidden by the Pauli exclusion principle and therefore these species also require the use of an indirect evaporation procedure [129, 26, 27, 130, 131].

The aim of sympathetic cooling is the cooling of a ‘target’ gas, in thermal contact with a ‘buffer’ gas, by forced evaporative cooling of the buffer gas. The temperature of the target atoms is reduced through their thermalization with the cold buffer-gas reservoir. Since the cooling of both species depends on the removal of only one species from the trap, for a given initial buffer gas number there is a natural tradeoff between the final size of the cooled load and the lowest achievable temperature. The background triplet scattering length of ³⁹K is small and negative, with a value of $a_{\text{bg}} = -33a_0$ [132, 60], where a_0 is the Bohr radius, $a_0 \approx 0.53\text{\AA}$. Furthermore, the Ramsauer-Townsend minimum in the s-wave scattering cross-section in ³⁹K occurs at a temperature of $T \sim 320\mu\text{K}$, where contributions from higher partial waves are still small ($\sigma_l \propto T^{2l}$, [133]). These facts, together with the modest MOT numbers compared to the temperatures achieved by laser cooling, make sympathetic cooling of ³⁹K the most promising approach for cooling this species². The effectiveness of ⁸⁷Rb as a buffer gas for ³⁹K has

¹ An exception to this is the recent direct evaporative cooling of the low-abundance species ⁸⁴Sr and ⁸⁶Sr [38, 39, 40], made possible by the existence of a metastable state in which a large number of atoms could be accumulated during laser cooling.

² Despite these difficulties, the Florence group has recently reported on the condensation of ³⁹K without a sympathetic cooling stage.

already been demonstrated in a series of experiments [59, 36]. Furthermore, the use of an 8.5G-wide inter-species Feshbach resonance located at 317.9G in the $|1, 1\rangle$ states of ^{87}Rb and ^{39}K enables the enhancement of the ^{39}K - ^{87}Rb scattering cross section from its background value of $a_{\text{KRb}} = 36a_0$ to values on the order of $a_{\text{KRb}} \approx 150a_0$ and hence increase the efficiency of sympathetic cooling, as is carried out in [36].

A model of sympathetic cooling

A simple and analytically soluble model for sympathetic cooling has been proposed and used by the Aspect group in 2001 [134] in order to better understand the results of their experiments on simultaneous production of BECs in samples of ^{87}Rb containing atoms in the $|2, 2\rangle$ and $|1, -1\rangle$ states. In these experiments, the $|1, -1\rangle$ state (the buffer gas) was evaporated directly, since due to its smaller magnetic moment its spatial extent in the magnetic trap was larger, while the $|2, 2\rangle$ component (the target gas) was cooled to degeneracy sympathetically via elastic collisions with the $|1, -1\rangle$ atoms. A similar experiment with the same components had already been performed in the Wieman group in 1997 [129]. Below we review this model and in chapter 3 we apply it to the results of our ^{87}Rb - ^{39}K sympathetic cooling measurements.

In addition to the discretization of what is actually the continuous process of atom removal and thermal re-equilibration, this model makes some further assumptions.

1. Both species are assumed to always be thermalized with themselves and with each other i.e., the thermalization rate is much higher than the cooling rate.
2. The gas is described by classical statistics (i.e., the classical equipartition theorem, allocating $\frac{1}{2}k_B T$ to each degree of freedom, is valid)
3. The number of target atoms, N_2 is taken to be constant.
4. Atoms escaping from the trap neither collide nor exchange energy with the remaining atoms.

Initially, the total energy of N_1 buffer and N_2 target atoms in a harmonic trap is

$$E = 3(N_1 + N_2) k_B T \quad (2.41)$$

Assuming a number, dN_1 , of atoms is evaporatively removed from the trap with an energy cutoff of $\eta k_B T$, the corresponding (negative) energy change is

$$dE = dN_1 (\eta + \kappa) k_B T \quad (2.42)$$

where $\kappa \in [0, 1]$ is a function of η and of the effective dimension of the surface on which evaporation takes place [22]. After rethermalization at a new temperature, $T + dT$, the total energy is

$$E + dE = 3(N_1 + dN_1 + N_2) k_B (T + dT) \quad (2.43)$$

Substituting in Eqns. 2.41 and 2.42, and keeping only first-order terms yields

$$\frac{dT}{T} = \alpha \frac{dN_1}{N_1 + N_2} \quad (2.44)$$

with $\alpha = (\eta + \kappa) / 3 - 1$. Assuming evaporation at constant η , we get

$$T = T_{min} \left(\frac{N_1}{N_2} + 1 \right)^\alpha \quad \text{with} \quad T_{min} = T_{init} \left(\frac{N_2}{N_1^{init}} \right)^\alpha \quad (2.45)$$

where T_{init} and N_1^{init} are the initial values of the respective quantities and N_2 has been neglected with respect to N_1^{init} in the expression for T_{min} . This last approximation is valid since in order to reduce the temperature by several orders of magnitude, the initial fraction of target atoms in the gas has to be small. In our experiments its value is no larger than 1/10.

2.5 Optical trapping

In this section we briefly discuss the optical dipole force, introduced in section 2.1, which provides the dominant contribution to the total optical force when the light field is *far-detuned* from resonance and the scattering force is weak. A non-magnetic trapping potential is required for experiments utilizing Feshbach resonances, especially in our case since the $|1, 1\rangle$ state in which our resonance exists is high-field seeking and therefore magnetically untrapped. Feshbach resonances involve the application of a uniform magnetic field, as discussed in the following section, and are therefore incompatible with non-uniform magnetic trapping potentials. In addition, the tight confinement provided by optical traps enables more efficient evaporative cooling, which we employ following the sympathetic cooling stage of our ^{39}K production sequence, as described in chapter 3.

As mentioned previously, the dipole force arises from the interaction of the atom's induced dipole with the intensity gradient of the light field. This is a conservative force and hence can be related to a potential which can be used for trapping and manipulation of atoms. This can be seen more clearly by integrating the expression for the dipole force in equation 2.12, which we repeat here for clarity:

$$U_{\text{dip}}(\mathbf{r}) = - \int \mathbf{F}_{\text{dip}} \cdot d\mathbf{r} \quad \text{with} \quad \mathbf{F}_{\text{dip}} = -\frac{\hbar\delta}{2} \cdot \frac{\nabla(I/I_S)}{1 + I/I_S + (2\delta/\Gamma)^2} \quad (2.46)$$

$$\begin{aligned} U_{\text{dip}}(\mathbf{r}) &= \frac{\hbar\delta}{2} \ln(1 + I/I_S + (2\delta/\Gamma)^2) + \mathcal{C}_1 \\ &= \frac{\hbar\delta}{2} \ln(1 + (I/I_S + 1)/(2\delta/\Gamma)^2) + \mathcal{C}_2 \\ &\approx \frac{\hbar\delta}{2} \frac{\Gamma^2}{(2\delta)^2} \frac{I}{I_S} \quad ((\delta/\Gamma)^2 \gg I/I_S) \\ &= \frac{3\pi c^2 \Gamma}{2\omega_0^3 \delta} I(\mathbf{r}) \end{aligned} \quad (2.47)$$

where ω_0 is the transition frequency. In the above, we have assumed a large detuning and low intensity, $(\delta/\Gamma)^2 \gg I/I_S$, have neglected any constant factors along the way and have used the relation $I_S = \pi\hbar c/3\lambda^3\tau$ of equation 2.10. Within the same large-detuning approximation, the scattering rate from equation 2.12 is given by

$$R_{\text{scatt}}(\mathbf{r}) = \frac{3\pi c^2}{2\hbar\omega_0^3} \left(\frac{\Gamma}{\delta}\right)^2 I(\mathbf{r}) \quad (2.48)$$

A semi-classical model can also be used to derive the optical dipole potential, as is done for example in [135], which also contains a more exhaustive review of optical trapping of neutral atoms. By using the expression for the complex atomic polarizability, derived using the classical Lorentz oscillator model [136], the resulting expressions are

$$\begin{aligned} U_{\text{dip}}(\mathbf{r}) &= -\frac{3\pi c^2}{2\omega_0^3} \left(\frac{\Gamma}{\omega_0 - \omega} + \frac{\Gamma}{\omega_0 + \omega} \right) I(\mathbf{r}) \\ R_{\text{scatt}}(\mathbf{r}) &= \frac{3\pi c^2}{2\hbar\omega_0^3} \left(\frac{\omega}{\omega_0} \right)^3 \left(\frac{\Gamma}{\omega_0 - \omega} + \frac{\Gamma}{\omega_0 + \omega} \right)^2 I(\mathbf{r}) \end{aligned} \quad (2.49)$$

which reduce to equations 2.47 and 2.48 when the field is tuned closer to resonance

such that $|\delta| \ll \omega_0$ and the second terms in the above equations can be neglected.

Hence red-detuned light ($\delta < 0$) gives rise to negative potentials, attracting atoms to intensity maxima, while blue-detuned light ($\delta > 0$) attracts atoms to intensity minima. Atoms can therefore be trapped in a suitably configured intensity distribution. Since the potential depth scales as I/δ while the scattering rate scales as I/δ^2 , dipole traps typically use high intensities and large detunings to keep scattering as low as possible while providing a sufficiently deep potential. A common way to create such a confining potential is in the intersection region of two non-parallel red-detuned beams, as is done in our experiments, or using a single red-detuned beam and relying on the finite Rayleigh range to provide the axial confinement [137, 138]. Periodic optical lattices can also be generated by the standing-wave interference pattern of pairs of counter-propagating red- or blue-detuned beams [139, 135].

2.6 Feshbach resonances

As discussed in chapter 1, one of the main motivations for our use of ^{39}K is the precise tuning of the interparticle interaction strength over a broad range afforded by the existence of a wide and conveniently-located Feshbach scattering resonance in the atoms' absolute ground state. This resonance gives us access to a large range of interaction strengths, from strongly repulsive to strongly attractive and including the special case of an ideal, non-interacting, gas. This external control over the scattering length requires only the application of a suitable homogeneous magnetic field to the atoms, as discussed below.

The following provides a description of the rudiments of scattering theory and Feshbach resonances, and is intended only to introduce the relevant quantities and parameters which will be referred to throughout the rest of this thesis, as well as providing references for further reading.

2.6.1 Scattering theory

When an incident particle with momentum k , in the form of a plane wave $\psi_{\text{inc}} = e^{i\mathbf{k}\cdot\mathbf{r}}$, scatters from a spherically symmetric potential, $V(r)$, the asymptotic form of the overall wavefunction, $\psi_k(\mathbf{r})$ at a large distance compared to the effective

range of the potential, is given by [140]

$$\psi_k(\mathbf{r}) \sim e^{i\mathbf{k}\cdot\mathbf{z}} + f(k, \theta) \frac{e^{ikr}}{r} \quad (2.50)$$

where θ is the angle between the momentum of the incoming plane wave and that of the scattered wave. $f(k, \theta)$ is the amplitude of the outgoing spherical wave and is called the *scattering amplitude*. At low energies, only partial waves with zero angular momentum ($l = 0$) contribute to the outgoing wavefunction. This can be understood qualitatively as higher partial waves of angular momentum quantum number l not possessing sufficient energy to cross the centrifugal energy barrier, $\hbar^2 l(l+1)/(2m_r r^2)$, where r is the interparticle distance, and simply being reflected from the scattering potential without sampling the short-range potential $V(r)$. In this limit the scattering amplitude sheds its angular dependence and approaches a constant, $-a$, called the *scattering length*. Hence in the $k \rightarrow 0$ limit of vanishingly-low-energy collisions, the wavefunction reduces to

$$\psi(\mathbf{r}) = 1 - \frac{a}{r} \quad (2.51)$$

and the scattering length can therefore be associated with the intercept of the asymptotic wavefunction ψ along the radial axis. Comparing equation 2.51 with the solution of the radial Schrödinger equation allows us to relate the scattering length, a , to the phase shift δ_0 accumulated, in the same low-energy limit, by the asymptotic scattered wavefunction during the time it spends inside the effective range of the scattering potential and gives

$$a = -\lim_{k \rightarrow 0} \frac{\tan \delta_0}{k} \quad (2.52)$$

The scattering cross-section, σ , can be obtained from the scattering amplitude using

$$\frac{d\sigma}{d\Omega} = |f(\theta)|^2 \quad \Rightarrow \quad \sigma = 2\pi \int_{-1}^1 |f(\theta)|^2 d(\cos \theta) \quad (2.53)$$

which in our low-energy limit with $f(\theta) = -a$ gives

$$\sigma = 8\pi a^2 \quad (2.54)$$

where a factor of 2 has been added to the result of the integration due to the requisite symmetrization of the bosonic wavefunction [140].

2.6.2 Feshbach resonances

In scattering theory, *open channels* and *closed channels* refer to the collection of quantum states in which particles are allowed or forbidden, respectively, to emerge from a scattering event by energy conservation. If E_{tot} is the total energy of the incoming particles, defined by $E_{\text{tot}} = E_{\psi_1} + E_{\psi_2} + E_{\text{kin}}^{1-2}$, where E_{ψ_1/ψ_2} are the internal energies of the particles in states ψ_1/ψ_2 and E_{kin}^{1-2} is their relative kinetic energy, then any channel with energy $E \leq E_{\text{tot}}$ is called an open channel and any channel with $E > E_{\text{tot}}$ is called a closed channel. A closed channel can involve, for example, two particles that are in different internal states to those of the incoming particles, and the difference in energy between the two molecular scattering potentials is then determined by the difference in the internal energies of the two states.

A Feshbach resonance (see [42], and references therein) occurs when the energy of an incoming open elastic channel¹ is magnetically tuned so as to coincide with that of a bound (molecular) state of an energetically closed channel. This tuning can be accomplished when the two channels possess different total magnetic moments and therefore experience a differential Zeeman shift in the presence of an external magnetic field. The difference between the energy of the incoming state and that of the closest bound state is then

$$E - E_0 = \Delta\mu(B - B_0) \quad (2.55)$$

where $\Delta\mu$ is the difference between the magnetic moments of the two channels and E_0 and B_0 are the energy and magnetic field positions of the resonance. This scenario is illustrated in figure 2.9.

In the vicinity of a Feshbach resonance, the dependence of the s-wave scattering length on the external magnetic field is conventionally described by

$$a(B) = a_{\text{bg}} \left(1 - \frac{\Delta}{B - B_0} \right) \quad (2.56)$$

where a_{bg} is the background scattering length far from the resonance and the parameter Δ is the resonance width, defined as the distance between the resonance centre and the field, B_{zc} , at which the scattering length vanishes - the so called

¹ i.e. one in which the initial and final relative kinetic energies are equal.

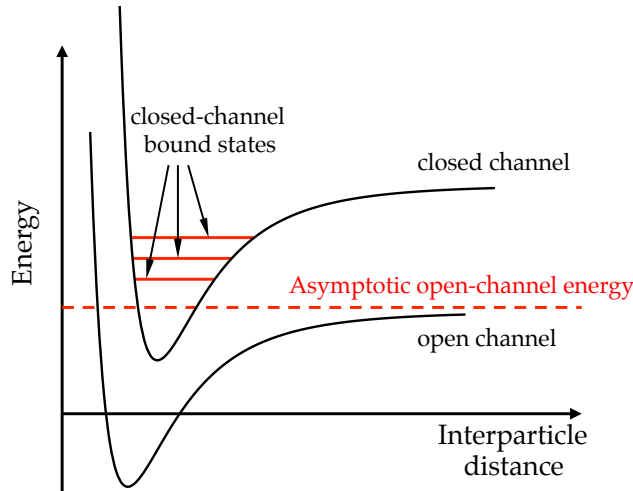


Figure 2.9: A Feshbach scattering resonance occurs when the energy of two particles in an open collisional channel coincides with that of a bound state in a closed molecular channel. The distance between the two molecular potentials can be tuned by an external magnetic field.

*zero-crossing*¹

$$\Delta \equiv B_{zc} - B_0 \propto \frac{1}{a_{bg} \Delta\mu} \quad (2.57)$$

Equation 2.56 can be intuitively understood as the result of second order perturbation theory, with the second order process describing incoming particles coupling to an intermediate closed channel which then decays into two particles exiting in an open channel. This intuitive understanding, together with equations 2.55, 2.56 and 2.57 can also be used to see that the positive scattering length which arises when the energy of the incoming channel is higher than that of the closed-channel bound state, leads to a *repulsion* between the states (similarly to the optical potential of section 2.5) and that a negative scattering length correspondingly leads to an interparticle *attraction* when the incoming energy is lower than that of the bound state.

The variation of the scattering length with magnetic field described by equation 2.56 is shown in figure 2.10 for the position and width of the resonance used in our experiments - 402.5G and 52G, respectively.

It is worth noting that in the vicinity of the zero-crossing i.e. $B \approx B_{zc}$, the

¹ i.e. the width characterizes the field range over which the resonance dominates the contributions of other states to the scattering length.

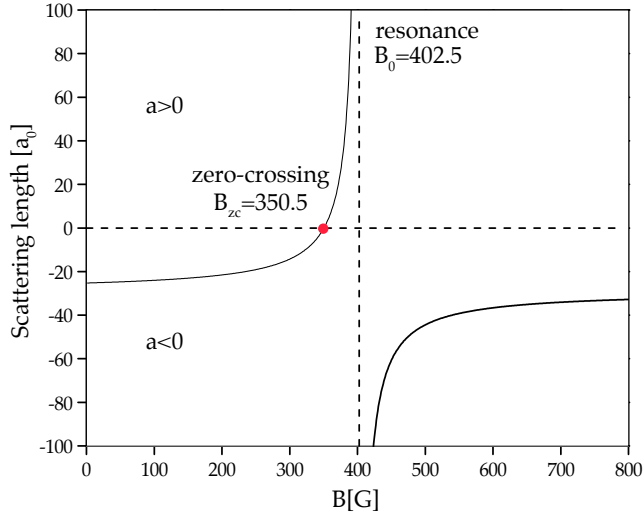


Figure 2.10: Variation of the scattering length with magnetic field in the vicinity of the 52G-wide Feshbach resonance at 402.5G used in our experiments.

scattering length is given approximately by

$$a(B) \approx \frac{a_{bg}}{\Delta} (B - B_{zc}) \quad (2.58)$$

Therefore when precise control of the scattering length near the zero-crossing is desired for experiments on extremely weakly-interacting gases, a resonance with a small background scattering length and a large resonance width is advantageous. This is precisely the case in ^{39}K whose $-33a_0$ background scattering length and 52G-wide resonance make it a natural candidate for experiments such as those investigating Anderson localization [67, 141, 142] and interferometric experiments wishing to minimize the effects of interactions [143].

The Feshbach resonances present in the $|F = 1\rangle$ ground state of ^{39}K , as well as several inter-species ^{87}Rb - ^{39}K resonances, have been discovered and investigated in a series of experiments by the group at LENS [59, 60, 36, 58, 62, 61]. The techniques described in the preceding sections can be used in order to lower the trapped cloud's temperature into the regime of quantum degeneracy, in which the effects of quantum statistics must be accounted for in describing the system's thermodynamic behaviour. The following section outlines perhaps the most well known manifestation of these effects in the field of ultracold atoms - the Bose-Einstein condensation transition.

2.7 Bose-Einstein Condensation

The theory of Bose-Einstein condensation in ideal and interacting gases has been expounded, discussed and dissected in the pages of a huge collection of literature, including books [123, 144], review articles [45, 145], research papers and theses. Below we very briefly review some of the main results, most of which will be discussed in further detail in chapters 4 and 5 in the context of our experiments on the thermodynamics of ^{39}K Bose gases and are given here in order to introduce the main quantities of interest and their origins.

2.7.1 Non-interacting gas

The mean occupancy, $f(\epsilon_{\mathbf{p}})$, of a single-particle state of energy $\epsilon_{\mathbf{p}}$ in an ideal Bose gas in thermodynamic equilibrium at temperature T is given by the Bose-Einstein distribution function

$$f(\epsilon_{\mathbf{p}}) = \frac{1}{e^{(\epsilon_{\mathbf{p}} - \mu)/k_B T} - 1} \quad (2.59)$$

where k_B is the Boltzmann constant and μ is the chemical potential, enforcing the conservation of particle number. The total atom number is therefore given by the normalization condition

$$N_{\text{tot}} = \sum_{\mathbf{p}} f(\epsilon_{\mathbf{p}}) \quad (2.60)$$

Replacement of the summation by an integration does not correctly account for the occupancy of the ground state and therefore the total atom number is divided into a ground-state contribution in addition to the excited state number

$$N_{\text{tot}} = N_0 + N_{\text{ex}} = N_0 + \int_0^{\infty} f(\epsilon)g(\epsilon)d\epsilon \quad (2.61)$$

where $g(\epsilon) = \frac{\mathcal{V}}{4\pi^2} \left(\frac{2m}{\hbar^2}\right)^{3/2} \sqrt{\epsilon}$ is the 3D density of states¹ with \mathcal{V} the system volume and N_0 is the ground-state occupancy. Within the semi-classical approximation and in the presence of an external potential, $V(\mathbf{r})$, the single-particle energies are given by $\epsilon_{\mathbf{p}}(\mathbf{r}) = p^2/2m + V(\mathbf{r})$. With the substitution $x = p^2/2mk_B T$, the integral in equation 2.61 for the number of atoms in excited states can be written

¹ We assume all particles are in a single spin state.

as

$$n_{\text{ex}}(\mathbf{r}) = \frac{N_{\text{ex}}}{\mathcal{V}} = \frac{2}{\sqrt{\pi}\lambda_{\text{dB}}^3} \int_0^\infty \frac{x^{1/2}}{z^{-1}e^x - 1} dx \quad (2.62)$$

where $n_{\text{ex}}(\mathbf{r}) = N_{\text{ex}}/\mathcal{V}$ is the excited-state ('thermal') density distribution, the parameter $z(\mathbf{r})$ is defined as $z(\mathbf{r}) = e^{[\mu - V(\mathbf{r})]/k_B T}$ and λ_{dB} is the thermal de Broglie wavelength, given by

$$\lambda_{\text{dB}} = \sqrt{\frac{2\pi\hbar^2}{mk_B T}} \quad (2.63)$$

The result of the integral in equation 2.62 is

$$n_{\text{ex}}(\mathbf{r}) = \frac{g_{3/2}(z(\mathbf{r}))}{\lambda_{\text{dB}}^3} \quad (2.64)$$

where the polylogarithm $g_{3/2}$ is given by

$$g_\gamma(z) = \sum_{n=1}^{\infty} \frac{z^n}{n^\gamma} \quad (2.65)$$

Therefore, armed with the functional form of the external potential, the total atom number and the temperature, equation 2.62 can be solved for the excited-state spatial density distribution.

Uniform system

In an infinite uniform system, $V = 0$, and since for an ideal gas $\mu \leq 0$, the value of $z(\mathbf{r})$ cannot exceed unity and hence the value of $g_{3/2}(z(\mathbf{r}))$ cannot exceed $g_{3/2}(1) = \zeta(3/2) = 2.612$. This bound on the excited-state atom density signals the onset of condensation, with any additional particles present in the system constrained to occupy the ground state. The temperature at which this occurs can be found by inserting $z(\mathbf{r}) = 1$ into equation 2.64 and solving for T .

$$T_c = \frac{2\pi\hbar^2}{mk_B} \left(\frac{n}{g_{3/2}(1)} \right)^{2/3} \approx 3.31 \frac{\hbar^2 n^{2/3}}{mk_B} \quad (\text{uniform, ideal gas}) \quad (2.66)$$

This is the temperature at which the number of atoms in excited states is equal to the total atom number, and using equations 2.66 and 2.61, the condensate

fraction at temperatures below T_c may be obtained as

$$\frac{N_0}{N_{\text{tot}}} = 1 - \left(\frac{T}{T_c}\right)^{3/2} \quad (\text{uniform, ideal gas}) \quad (2.67)$$

In summary, for a uniform system, the onset of BEC occurs when the *density* reaches the critical value $n_{\text{crit}} = 2.612/\lambda_{dB}^3$ i.e. the phase-space density $\rho \equiv n_{\text{crit}}\lambda_{dB}^3 = 2.612$.

Harmonic potential

For a three-dimensional harmonic potential of the form

$$V(\mathbf{r}) = \frac{1}{2}m(\omega_x^2x^2 + \omega_y^2y^2 + \omega_z^2z^2) \quad (2.68)$$

the density of states is given by $g(\epsilon) = \frac{1}{2(\hbar\bar{\omega})^3}\epsilon^2$, with $\bar{\omega} = (\omega_x\omega_y\omega_z)^{1/3}$ the geometric mean of the trapping frequencies. Performing the integral of equation 2.64 over \mathbf{r} and setting $\mu = 0^1$, yields the equivalent expression to 2.66 for the critical temperature for saturation of the excited state atom *number*.

$$T_c = \frac{\hbar\bar{\omega}}{k_B} \left(\frac{N}{\zeta(3)}\right)^{1/3} = 0.94\frac{\hbar\bar{\omega}}{k_B}N^{1/3} \quad (\text{harmonic potential}) \quad (2.69)$$

where $\zeta(\alpha) = \sum_{n=1}^{\infty} n^{-\alpha}$ is the Riemann zeta function. This can equally be expressed as a critical number for a given temperature

$$N_c = \zeta(3) \left(\frac{k_B T}{\hbar\bar{\omega}}\right)^3 = 1.202 \left(\frac{k_B T}{\hbar\bar{\omega}}\right)^3 \quad (\text{harmonic potential}) \quad (2.70)$$

Using equation 2.69 the expression for the condensed fraction in an ideal harmonically confined gas is given by

$$\frac{N_0}{N_{\text{tot}}} = 1 - \left(\frac{T}{T_c}\right)^3 \quad (\text{harmonic potential}) \quad (2.71)$$

Below T_c , one has $\mu = 0^2$ and equation 2.64 for the density distribution of the

¹ Condensation occurs in general when the chemical potential reaches its maximal value, namely the lowest value of the potential energy $\min(V(\mathbf{r}))$. For the 3D harmonic potential considered here, this corresponds to the zero-point energy $\frac{1}{2}\hbar\sum_{i=1}^3\omega_i$ which can be neglected at temperatures when $k_B T \gg \hbar\bar{\omega}$

² Neglecting the zero-point energy - see previous footnote

excited-state atoms reduces to

$$n_{ex}(\mathbf{r}) = \frac{g_{3/2}(e^{-V(\mathbf{r})/k_B T})}{\lambda_{dB}^3} = \frac{g_{3/2}(e^{-m\omega^2 r^2/2k_B T})}{\lambda_{dB}^3} \quad (\text{harmonic potential}) \quad (2.72)$$

The density profile of the *condensate* wavefunction in the harmonic potential is

$$n_0(\mathbf{r}) = |\phi_0(\mathbf{r})|^2 = \left(\frac{m\bar{\omega}}{\pi\hbar}\right)^{3/2} \exp\left[-\left(\frac{x}{a_x}\right)^2 - \left(\frac{y}{a_y}\right)^2 - \left(\frac{z}{a_z}\right)^2\right] \quad (2.73)$$

where $\phi_0(\mathbf{r})$ is the single-particle ground state wavefunction, whose widths are given by the corresponding oscillator lengths $a_i = \sqrt{\frac{\hbar}{m\omega_i}}$.

2.7.2 Weakly-interacting gas

Interactions between the atoms modify the above results and will be discussed in more detail in chapters 4 and 5. Here we only discuss some of the properties of the condensate.

The Gross-Pitaevskii equation

At the low energies where s-wave scattering dominates and collisions can be described as contact interactions, the effective interaction strength is given by

$$g = \frac{4\pi\hbar^2 a}{m} \quad (2.74)$$

where a is the scattering length described in section 2.6, N is the atom number and m is the mass. The equilibrium state of the condensate is governed by the time-independent Gross-Pitaevskii (GP) equation

$$\left\{-\frac{\hbar^2}{2m}\nabla^2 + V(\mathbf{r}) + g|\psi|^2\right\}\psi = \mu\psi \quad (2.75)$$

where $\psi = \psi(\mathbf{r})$ is the many-body wavefunction and the non-linear third term on the left-hand side accounts for the mean-field interaction energy produced by atom ensemble. The density and atom number are then

$$n(\mathbf{r}) = |\psi(\mathbf{r})|^2 \quad \Rightarrow \quad N = \int |\psi(\mathbf{r})|^2 d\mathbf{r} \quad (2.76)$$

A corresponding mean-field description of the non-condensed component will be presented in chapter 4.

The Thomas-Fermi approximation

The Gross-Pitaevskii equation, 2.75, has a simple solution which is valid for sufficiently large clouds, such that the kinetic energy term is much smaller than the interaction energy term and can be neglected in the GP equation. In this approximation, the atom density can therefore be found as

$$\{V(\mathbf{r}) + g|\psi|^2\}\psi = \mu\psi \quad \Rightarrow \quad n(\mathbf{r}) = |\psi(\mathbf{r})|^2 = \frac{\mu - V(r)}{g} \quad (2.77)$$

Hence the boundary of the cloud is given by $V(r) = \mu$, which for the harmonic potential of equation 2.68 gives a so-called Thomas-Fermi radius of

$$R_i^2 = \frac{2\mu}{m\omega_i^2}, \quad i = x, y, z \quad (2.78)$$

The chemical potential, μ is found from the normalization condition of equation 2.76 to be

$$\mu = \frac{\hbar\bar{\omega}}{2} \left(\frac{15Na}{\bar{a}_{ho}} \right)^{2/5} \quad (2.79)$$

where $\bar{a}_{ho} = \sqrt{\frac{\hbar}{m\bar{\omega}}}$ is the harmonic oscillator length associated with the mean trapping frequency, $\bar{\omega}$. The condensate density therefore has the form of an inverted parabola

$$n(\mathbf{r}) = |\psi|^2 = n_0 \left(1 - \frac{x^2}{R_x^2} - \frac{y^2}{R_y^2} - \frac{z^2}{R_z^2} \right) \quad (2.80)$$

See section 3.15 for a description of how these functions are used to extract physical parameters from images of the atomic cloud.

2.8 Absorption imaging

In most ultracold atom experiments, information about the system is extracted from images of the atomic density distribution, with the vast majority of experiments utilizing optical techniques in order to measure this spatially-dependent quantity. Several optical imaging schemes exist, each with its own advantages and drawbacks, lending themselves to imaging under different experimental con-

ditions. In general, different techniques rely on either the absorptive or dispersive components of the atom-light interaction, which predominantly either attenuate or introduce a phase shift of the incident light field. The relative contribution of each of these components is determined by the density of the cloud and the detuning of the probe light. Below is a brief description of the most commonly-used imaging technique - absorption imaging.

Absorption imaging relies on the attenuation of an incident beam as a result of being partially absorbed by the atomic sample, with the shadow cast by the cloud in the plane of the atoms being imaged onto a charge-coupled device (CCD) by an imaging system¹. According to the Beer-Lambert law, described below, the spatially varying intensity profile recorded on the CCD is a function of the cloud's spatially varying optical density, which is itself directly proportional to the density distribution of the cloud, integrated along the propagation axis of the imaging beam. Physical quantities are then inferred from the form of this density profile (see section 3.15 for a description of our analysis procedure). The dynamic range of this technique is limited to imaging optical densities no higher than roughly 4, since achieving detectable transmission at these densities requires a large detuning, which would also lead to a significant dispersive contribution to the interaction, causing spreading of the refracted light beyond the collection range of the optics and leading to a false absorption signal [145]. In order to avoid this problem, dense clouds are allowed to expand during time-of-flight (TOF) such that their optical densities are sufficiently reduced to obtain a strong enough signal-to-noise ratio. This is especially important for condensed clouds, whose in-situ optical densities are typically on the order of a few hundred.

2.8.1 Theory of absorption imaging

For a monochromatic beam of intensity $I(x, y)$, propagating through a cloud of density n , the change in beam intensity, ΔI upon passing a distance dz is given by the product of the photon energy, the scattering rate and the number of particles per unit area, ndz

$$\frac{dI}{dz} = -\hbar\omega R_{scatt}n = -\sigma nI \quad (2.81)$$

¹ c.f. Plato's Allegory of the Cave.

where in the second equality the scattering rate, σ is given by

$$\sigma = \frac{\overbrace{3\lambda^2}^{\equiv \sigma_0}}{2\pi} \frac{1}{1 + I/I_S + (2\delta/\Gamma)^2} \quad (2.82)$$

obtained from the scattering rate in equation 2.12 and the saturation intensity, I_{sat} of equation 2.10. Integrating equation 2.81, gives an exponential decay of the intensity as the beam propagates through the cloud

$$I(x, y) = I_0(x, y) \exp \left[-\sigma \int n(x, y, z) dz \right] \equiv I_0(x, y) e^{-OD} \quad (2.83)$$

where the optical density, OD , is defined by

$$OD(x, y) = \sigma \underbrace{\int n(x, y, z) dz}_{\text{column density, } \bar{n}(x, y)} = -\ln \left(\frac{I(x, y)}{I_0(x, y)} \right) \quad (2.84)$$

Hence imaging the intensity distribution gives us direct access to the singly-integrated number density, also known as the column density, $\bar{n}(x, y)$, of the cloud, from which physical properties such as atom number and temperature can be extracted (see section 3.15). The total atom number can be found using equation 2.84

$$N = \int n(\mathbf{r}) d^3\mathbf{r} = \frac{1}{\sigma} \int \int OD(x, y) dx dy \quad (2.85)$$

In practice, stray light impinging on the CCD even in the absence of the imaging beam can bias the measured optical density, and so a background ‘dark’ image is also recorded and subtracted from each of the intensity profiles on the right-hand side of equation 2.84 prior to division. Equation 2.84 therefore becomes

$$OD(x, y) = -\ln \left(\frac{I(x, y) - I_{dark}(x, y)}{I_0(x, y) - I_{dark}(x, y)} \right) \quad (2.86)$$

To summarise, an image with the atoms present is captured (yielding $I(x, y)$) followed by an image in the absence of the atoms but in the presence of the imaging beam (yielding $I_0(x, y)$). Finally, either one or two background images are taken in the absence of both atoms and imaging light (yielding $I_{dark}(x, y)$). Section 3.14 describes our absorption imaging setup and procedure, while section

3.15 discusses the methods by which we extract the temperature of the cloud, as well as the number of atoms in the condensate and in the thermal component, from these absorption images.

3

Design, assembly and performance of our ^{39}K - ^{87}Rb apparatus

“Keep cool but care.”

Thomas Pynchon, *V*.

Abstract

This chapter describes the design and construction of our apparatus for producing ultracold ^{39}K and ^{87}Rb clouds, as well as the experimental procedure we utilize in order to cool the samples to quantum degeneracy and the results of the various stages within this process. It is intended to serve as a manual or field-guide of sorts for any student tasked with the assembly of a similar experimental setup, or indeed maintenance and expansion of the one described here. Care has been taken to try and motivate the choice of various aspects of the experimental apparatus and sequence, not only in order to reflect the large portion of my and my colleagues' work that has gone into the system's design and construction, but also in the hope that others will benefit from this information as I have benefited from reading about others' experiences and insights.

3.1 Sequence overview

Mirroring the structure of chapter 2, the sections of this chapter trace the progression of a typical experimental sequence culminating in a condensed cloud of over 4×10^5 ^{39}K (or 8×10^5 ^{87}Rb) atoms confined in a purely optical trap. The general outline of such a sequence is as follows:

The experiment takes place within an ultra-high vacuum (UHV) chamber (Section 3.2). Potassium and Rubidium atoms are released from heated dispensers and the desired isotopes, ^{39}K and ^{87}Rb , are jointly cooled and confined in a magneto-optical trap (MOT) formed by three pairs of dual-frequency, counter-propagating frequency-locked laser beams (Section 3.3) and a quadrupole magnetic field (Section 3.4). Both species are then optically pumped into magnetically-trappable states and transferred into a purely magnetic quadrupole trap (Section 3.6) for transport (Section 3.7) to the ‘science cell’ located in the higher-vacuum region of the vacuum chamber in preparation for the subsequent evaporative cooling stage. Figure 3.1 shows a diagram of the vacuum chamber, translation stage and quadrupole coil mount.

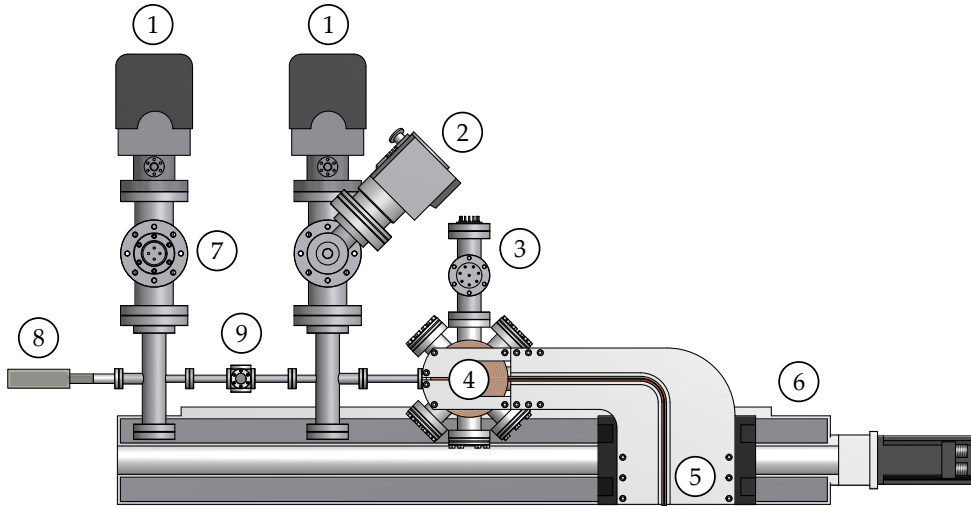


Figure 3.1: Diagram of the vacuum chamber, translation stage and quadrupole coil support. Visible are (1) the ion pumps, (2) turbo pump, (3) atom source module, (4) MOT cell and quadrupole coils, (5) quadrupole coil mounting arm, (6) translation stage, (7) Ti-Sub pump, (8) science cell and (9) six-way cube.

In the science cell, the linear magnetic potential generated by the quadrupole coils is converted into a harmonic potential with a non-zero field minimum (Section 3.8) in order to avoid the spin-flip losses which occur in zero-field regions. There

follows a stage of sympathetic evaporative cooling, in which ^{87}Rb atoms with above-average kinetic energy are forcibly ejected from the magnetic trap, leaving behind colder atoms whose return to thermal equilibrium leads both to cooling of the ^{87}Rb atoms and to efficient cooling of the ^{39}K atoms with which they are in contact (Section 3.9). In preparation for the application of a magnetic Feshbach field, both species are transferred into a crossed optical dipole trap (CDT) formed by a far-red-detuned IR laser (Section 3.10). The ^{87}Rb is then removed from the CDT by a resonant light pulse and the ^{39}K transferred into its $|F = 1, m_F = 1\rangle$ ground state, in collisions of which a broad, conveniently-located Feshbach resonance exists. The homogenous Feshbach field is then applied in order to bring the inter-particle scattering length to a large, positive value (Section 3.11). This is followed by an optical evaporation stage during which the CDT power is gradually lowered. The ^{39}K is thus evaporatively cooled to the desired temperature and its phase-space density increased, if desired, through the condensation critical point. In order to extract information about the sample, all magnetic and optical fields are extinguished and the cloud is illuminated with a resonant light pulse, in the presence of a magnetic guide field, after several milliseconds of free expansion. An absorption image of the illuminated cloud is recorded on a CCD camera (Section 3.14) and physical information extracted from it by means of a least-squares fit to a theoretical absorption profile (Section 3.15). We begin, therefore, with a description of our vacuum system.

3.2 Vacuum system

3.2.1 Background

The vacuum chamber to which the atoms are confined - and inside which all our experiments take place - is one of the key components of any cold-atom apparatus. Collisions with room-temperature background atoms cause heating of the species under study and invariably transfer sufficient energy to cause the ejection of atoms from the trapping potential. The rate of these ‘one-body’ background collisions depends on the ambient pressure and is minimized by ensuring as high a vacuum as possible in the trap region.

Cloud lifetimes on the order of several minutes are desirable in order to provide sufficient time for efficient evaporative cooling and to ensure that experiments can be performed in thermodynamic equilibrium. Such lifetimes typically require an ultra-high vacuum (UHV) in the region of 10^{-11}mbar . In addition, since we

wish our dual-species MOT to be fully loaded from a background vapour of ^{87}Rb and ^{39}K in a few seconds, we require a higher pressure in the MOT region. A pressure on the order of 10^{-9}mbar is high enough to provide rapid MOT loading, while being low enough to ensure that a sufficient number of atoms survive the transport to the lower-pressure region without being lost to background collisions on the way. This pressure difference between the two stages of the experiment lends itself to the idea of spatially separating the regions in which the MOT and evaporation steps take place in order to guarantee optimal conditions for each process [146].

The design of the vacuum chamber also dictates the amount of access available to the science cell. Access is required for the various trapping and imaging beams with their associated optics, as well as for the placement of the numerous magnetic coils used in the generation of the magnetic trapping potentials, the Feshbach field, compensation fields and required field gradients. In this context too, separation of the MOT and science cell regions is advantageous, as it allows us to greatly increase access to the atomic sample. This section will describe the design, implementation and performance of our vacuum system, which utilises a double-differential configuration to achieve a pressure ratio on the order of 10^3 between the MOT and science cell regions of the system. We initially outline some guiding principles and define some useful quantities to be used in the design of vacuum chambers with specific desired characteristics.

3.2.2 Pressure regime

In designing our vacuum system, it is important to remember that at the pressures of interest, the gas inside the chamber is well within the molecular flow regime, in which the mean free path of a molecule is much longer than the characteristic dimension of the apparatus [147]. This is quantified by the so-called Knudsen number $\text{Kn} = \lambda/D$, where λ is the mean free path and D is the characteristic dimension, which for a tube would be its diameter. As an example, from simple kinetic theory, for pressures on the order of $P = 10^{-10}\text{mbar}$ and at room temperature, the number density $n = p/k_B T$ is around $2 \cdot 10^{12}\text{m}^{-3}$, implying a mean free path $\lambda = (n\sigma)^{-1}$ of over 4km for nitrogen molecules (whose diameter is around 3.7\AA). The ratio of molecule-chamber to molecule-molecule collisions is typically given by a few times the Knudsen number and so at these pressures and temperatures, molecule collisions occur almost exclusively with the chamber walls and not with each other. In the molecular flow regime ($\text{Kn} \gg 1$), the

conductance of a tube whose length is not much longer than its diameter, to an accuracy of a few percent, is given by [147]:

$$C_{\text{tube}} = \frac{12.4D^3/L}{1 + 4D/3L} \text{ls}^{-1} \quad (3.1)$$

where D and L are the tube diameter and length in cm, respectively. This expression is obtained by combining the conductance of a tube whose length *is* much larger than its diameter, with that of an aperture appropriate to the entrance area of the tube.

3.2.3 Differential pumping

In order to achieve a pressure ratio of two or three orders of magnitude, we make use of a two-stage differential pumping setup. The basic principle of differential pumping is illustrated in figure 3.2a. Two regions of the vacuum chamber, one of which is connected to a pump of speed S , are separated by a low-conduction section of conductance C_1 ¹.

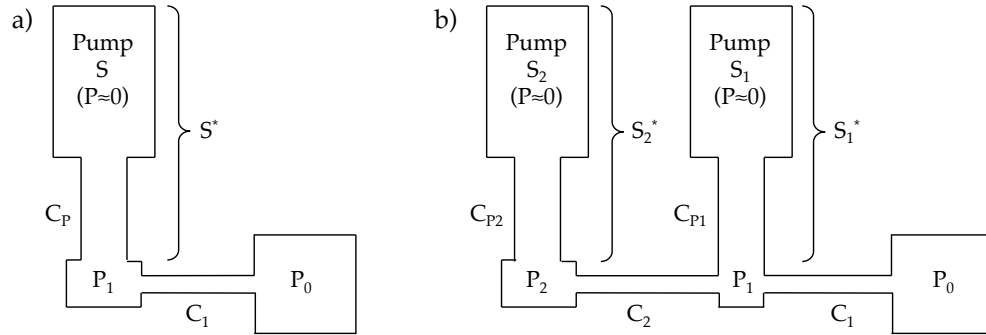


Figure 3.2: Differential vacuum schematic. a) Single differential pumping stage. A chamber connected to a vacuum pump of speed S is connected to another, higher-pressure, chamber via a low-conductance section, C_1 . The conductance of the section connecting the pump to the first chamber is denoted by C_P and the pressures in the low- and high-pressure chambers are denoted by P_1 and P_0 , respectively. b) Two-stage differential pumping simply adds a second differential stage to the setup described in (a).

We can estimate the pressure in different regions of the chamber using the useful analogy between the chamber parameters and those of electrical circuits obeying

¹ Note: The units of both conductance, C , and pumping speed, S , are ls^{-1} .

Ohm's law, $V = I \cdot R$. The throughput, Q , related to the particle flow rate by $dN/dt = Q/k_B T$, is analogous to the electrical current, I . The pressure, P , is analogous to the voltage, V , and the tube conductance, C , is analogous to the electrical conductance, $G = 1/R$. Pumps are modelled as regions of zero pressure and pumping speed S . It is important to remember to combine the pump's speed with the conductance, C_P , of the tube leading to the pump in order to obtain the effective pumping speed, S^* according to $1/S^* = 1/S + 1/C_P$.

The vacuum 'circuit' shown in figure 3.2a can then easily be seen to consist of a 'pressure divider', and the ratio of pressures in the first and second chambers is given by:

$$\frac{P_1}{P_0} = \frac{1/S^*}{1/S^* + 1/C_1} = \frac{C_1}{C_1 + S^*} \approx \frac{C_1}{S^*} \quad \text{where} \quad C_1 \ll S^* \quad (3.2)$$

The generalization to a second differential stage, as shown schematically in figure 3.2b is given by:

$$\frac{P_2}{P_0} = \frac{1}{P_0} \cdot \left(P_1 \cdot \frac{C_2}{C_2 + S_2^*} \right) = \frac{C_1}{C_1 + S_1^* + (C_2 S_2^*) / (S_2^* + C_2)} \cdot \frac{C_2}{C_2 + S_2^*} \approx \frac{C_1 C_2}{S_1^* S_2^*} \quad (3.3)$$

where the last approximation is valid when $C_1, C_2 \ll S_1^*, S_2^*$. In addition to these considerations, other important principles to follow are the minimization of internal surface area to reduce outgassing, the use of high-conductance tubes near pump intakes and the use of low-outgassing materials such as stainless steel and titanium.

3.2.4 Our chamber

The schematic layout of our vacuum system is shown in figure 3.3. The MOT and science cells are connected by a *transfer* tube 65cm in length, with an inner diameter (ID) of 10mm. Two ion pumps are located 19cm and 49cm along this tube, providing the double-differential described above. The tubes connecting the ion pumps to the transfer tube are 38mm in diameter near the transfer tube and 63mm in diameter at the pump entrance. They are both 30cm long, with the one nearest the science cell incorporating a vertically-mounted titanium-sublimation (Ti-Sub) pump. Located on the transfer tube, halfway between the two ion pumps, is a small six-way cube incorporated in order to allow viewing

of the cloud during transport for diagnostic purposes and/or to allow for a preliminary evaporative cooling step. The conductances of the components labelled in figure 3.3 are listed in Table 3.1. In the absence of any pressure source in the science cell region we expect $P_2 = P_3$, and using equation 3.3 we obtain an estimate for the pressure differential of $P_0/P_2 \approx 1600$. In practice, we observe a pressure difference of around 300 estimated from the ratio of MOT and magnetic trap lifetimes. We attribute this discrepancy to outgassing from the vacuum components and helium diffusion through the science cell walls.

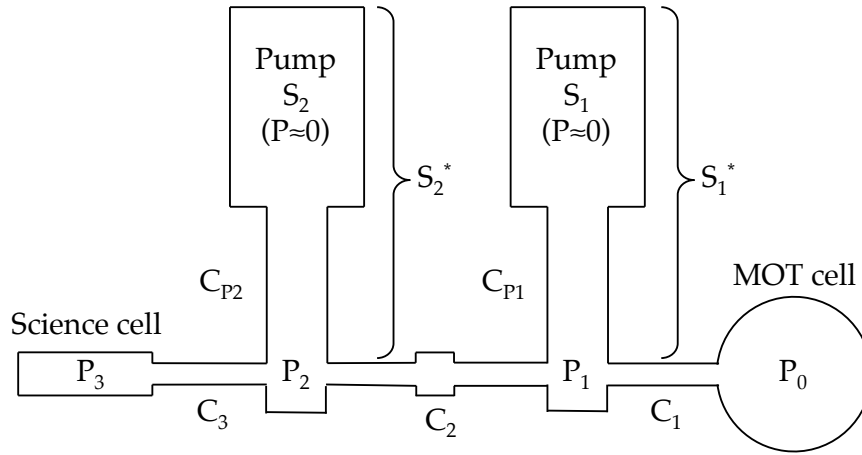


Figure 3.3: Schematic of our double-differential vacuum chamber, showing the MOT cell, science cell, transfer tube and pumps. The labels P_{0-3} indicate the pressure at different positions and $C_{1-3,P1,P2}$ indicate conductances.

Part	Length [mm]	Diameter [mm]	Conductance [ls ⁻¹]
C_1	126	10	0.72
	60	16	
C_2	300	10	0.4
C_3	160	16	2.51
C_{P1}, C_{P2}	210	63	33.16
	90	38	
S_1, S_2	0	63	60
S_1^*, S_2^*	300	—	21.36

Table 3.1: Dimensions and conductances of the main segments in our vacuum chamber. Refer for figure 3.3 for the location of each part.

3.2.5 Pumps and gauges

There is no one type of vacuum pump capable of establishing the required 10^{-14} drop between atmospheric pressure and our ultra-high vacuum and hence a sequence of pumps is used during the chamber's evacuation to reach the desired pressure range.

Roughing and turbo pumps

After initial assembly of the vacuum chamber, an all-metal right-angle valve located near the MOT cell is used to connect a turbo-molecular pump¹, with its exhaust venting into the intake of an oil-free scroll pump². In addition to serving as a backing pump for the turbo pump, which cannot vent to atmospheric pressure, this scroll pump is the *first* to get turned on and brings the chamber down to a pressure of around 5×10^{-2} mbar in a matter of seconds. The oil-free design of the scroll pump ensures that no liquid finds its way out via the turbo pump into the chamber. The turbo pump is then activated and left to pump on the chamber for the duration of the system's bakeout (see section 3.2.9).

Ion pumps

During the cooling phase after the bakeout, when the pressure has dropped below $\sim 10^{-6}$ mbar, two ion pumps³ are turned on. These pumps act as getters for any atoms that enter the region between their cathode and anode and hence act as pumps on the chamber. The ion pumps, after bakeout, bring the pressure in the chamber down to below 10^{-11} mbar and are operated continuously throughout the several-year lifetime of the apparatus in order to continuously remove from the system any excess atoms released from our atom sources, outgassed impurity atoms from the metal components of the chamber and any helium migrating through the walls of the quartz science cell.

Since these pumps rely on large magnetic fields, it is in general desirable to distance them from the main experimental region in order to minimize the effects of stray fields, which in turn implies a reduction of their effective pumping speed. Additional magnetic shielding⁴ made from nickel-coated low-carbon steel has also been fitted to both ion pumps to reduce the stray

¹ oerlikon Leybold TURBOVAC TW 70 H

² Leybold SC5D

³ Gamma Vacuum, TiTan 75S

⁴ Gamma Vacuum, 75S-6S

magnetic field near the science cell. According to the manufacturer's specifications, at the location of the atoms in the science cell this results in a reduction of the stray field from a value of 0.282G to 0.1G. The pumps used in our experiment have an effective pumping speed of between 60-70 ls^{-1} at pressures between 10^{-10} - 10^{-6} mbar, respectively, They are located no closer than 30cm from the science cell, have a quoted lifetime of 50,000 hours at a pressure of 10^{-6} mbar and a maximal bakeout temperature of 250°C.

Titanium sublimation pump

In addition, a titanium sublimation (Ti-Sub) pump¹ is mounted near the science cell and is occasionally activated in order to enhance the vacuum. Titanium sublimation pumps are getter pumps often used in addition to ion pumps to remove molecules such as H₂, N₂, O₂, CO₂ and H₂O. A current on the order of 50A is used to sublimate a thin layer of titanium onto an inner surface of the chamber, which then reacts with active gas molecules to form low vapour-pressure compounds that are bound to the film. The pump is mounted so as to provide as large an area as possible on which to deposit the titanium film. which is replenished once it has saturated. In our case, the pump is only activated for 1.5 minutes at 47A roughly once every six months. Since this pump produces no magnetic fields it can be placed in close proximity to the experimental region and hence maximize its pumping speed.

Bayard-Alpert gauge

Although the ultimate benchmark for our vacuum is the lifetime of our trapped cloud, we are able to obtain estimates of the pressure from a Bayard-Alpert ionisation gauge² mounted in close proximity to the science cell (see figure 3.6). In addition, the ion current readout from the ion pumps can be used to estimate the pressure according to the approximate formula: Pressure = $10^{-3} \times$ Current, with pressure and current in millibars and amperes, respectively.

3.2.6 MOT cell

The region of the vacuum chamber inside which the MOT will be formed has to fulfil several criteria. Firstly, it must be able to accommodate the three orthogonal

¹ Varian, TiSub Cartridge

² VACOM, BAIS sensor

pairs of counter-propagating cooling/trapping laser beams (see section 3.4). The diameter of these beams defines the capture volume of the MOT and so in order to collect large atom numbers, large beams and windows are necessary. Secondly, there are several considerations when choosing the separation between the coil pair used to generate the quadrupole magnetic field, required for operation of the MOT as well as for trapping of the atoms during transport to the science cell. These considerations are related to the size of the coils used, which in turn determines the spatial extension of the quadrupole field and hence the trapping volume. In addition to a large trapping volume, the ability to produce large field gradients at the atoms' location is important for ensuring that as many atoms as possible are safely transported to the science cell and are not lost *en route* in the narrow tube connecting the two regions. Large field gradients are also required in order to maximize the efficiency of evaporative cooling (see section 2.4). We would hence like the smallest coils that provide sufficient MOT trapping volume, and that can still be spaced such as to maximize the field gradient they produce at a given current. The maximal field gradient at the centre of a single coil pair is obtained when the coil separation is equal to the coil radius, as described in appendix E. The MOT cell must also provide a path to the atomic sources as well as a means of collecting the MOT fluorescence which serves as a probe of the number of trapped atoms.

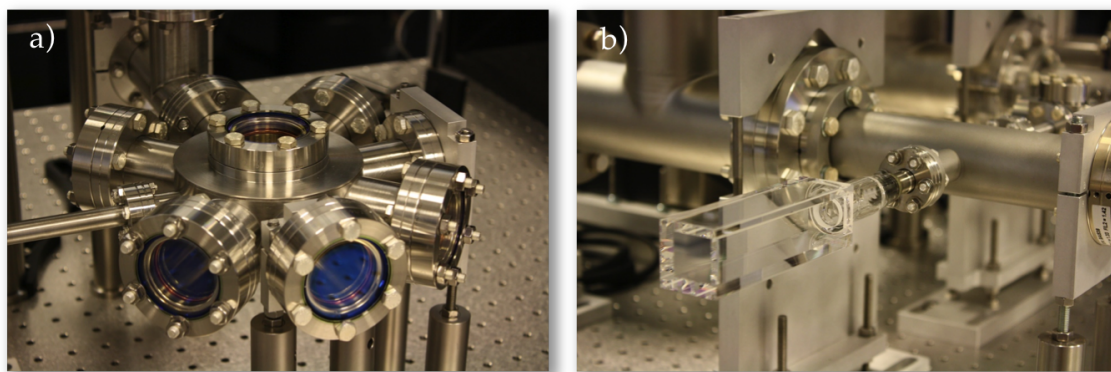


Figure 3.4: a) Image of the MOT chamber showing the viewports, transfer tube (left) and atom source module (background). b) Science cell mounted on vacuum chamber prior to the addition of the various surrounding beams and magnet coils.

With these considerations in mind, a custom non-magnetic, stainless steel (316LN) MOT cell was designed and manufactured¹. The cell consists of a cylindrical chamber of 110mm diameter and 44mm height, incorporating eight $2\frac{3}{4}$ "

¹ Fabricated by Kurt J. Lesker Company

(DN35CF) viewports, a further 2³/₄" (DN35CF) flange for mounting of the atom source module, and a smaller 1¹/₃" (DN16CF) flange for connecting the differential vacuum tube. The viewports are made from Kodial glass, mounted in 316LN flanges, and are AR coated on both sides with a coating optimized for 767nm and 780nm. The viewports are distanced from the central part of the chamber in order to allow vertical compensation coils to be mounted around the vertical flanges as well as to allow the quadrupole coil support, mounted on the translation stage, to hold the coils as close as possible to the cell itself while having sufficient clearance to translate them to the other end of the chamber. Figure 3.4a shows the assembled MOT cell prior to chamber bakeout.

3.2.7 Science cell

In the interests of maximizing optical access and versatility, and minimizing any unwanted magnetic fields caused by eddy currents, we have chosen to use a science cell consisting of a rectangular quartz cell¹. This is manufactured from highly polished, optical quality Spectrosil[®] Quartz in a fusing process utilizing no intermediate bonding materials, and is annealed after assembly to remove any residual strain. Spectrosil[®] Quartz (also known as Far UV Quartz) has good transmission properties in the range 190 - 2700nm. Prior to assembly, a broadband anti-reflection (AR) coating is applied to the external walls of the cell to ensure high transmission at the wavelengths which are to be used for imaging of both species (767 and 780nm) as well as trapping and manipulation of the ultracold cloud (532nm and 800-1100nm). The cell's outer dimensions are 30×30×110mm and the cell wall thickness is 5mm. This thickness was chosen so as to avoid permeation of helium into the cell, while allowing a sufficient inner volume for trapping and imaging purposes, as well as avoiding any optical birefringence that might be caused by mechanical stress to the cell wall during evacuation of the chamber. The outer dimensions were chosen so as to allow placing of trapping and Feshbach coils in close proximity to the atoms in order to allow sufficiently large fields and steep gradients to be applied. Figure 3.4b shows the mounted science cell during chamber assembly and appendix D contains a more detailed diagram of the cell in addition to reflectance spectra for the AR coating at both normal and 45° incidence.

The quartz cell is connected to the rest of the vacuum chamber by means of a

¹ Manufactured by Starna Scientific Ltd.

graded glass-to-metal seal which is required in order to overcome the difference in coefficients of thermal expansion between the steel and quartz components of the chamber during bakeout as well as during normal operation. The DN16CF flange attached to the glass-to-metal seal is made from non-magnetic 316LN stainless steel in order to minimize eddy currents near the trap centre.

3.2.8 Atom sources

The vapours of ^{87}Rb and ^{39}K from which our MOT is loaded are released into the MOT cell from a set of commercial vapour sources¹. In total, eight sources are currently installed in our vacuum chamber, four sources on each of two 8-pin electrical feedthroughs². The feedthroughs are connected to two perpendicular arms of a T-shaped tube, the third arm of which is attached directly to the MOT cell. After installation inside the vacuum chamber, the sources are thermally activated during the bakeout process (which also expedites the removal of the Indium used to seal the sources) and subsequent release of atoms is affected by running a current of between 4-8A through the desired source. In order to accommodate experiments involving any of the commonly used Rb or K isotopes, we have installed sources of four different compositions: The bosonic ^{85}Rb and ^{87}Rb isotopes can be released either from one of two natural-abundance Rb sources (72% ^{85}Rb , 28% ^{87}Rb , 50mg total per source³) or from one of two ^{87}Rb -enriched sources (98% ^{87}Rb , 50mg total per source⁴). We also have two types of K sources installed in the system: two natural-abundance sources containing 93% of the bosonic ^{39}K , 0.012% of the fermionic ^{40}K and 6.7% of the bosonic ^{41}K (60mg total per source⁵), and two ^{40}K -enriched (10%) sources (25mg total per source⁶). Figure 3.5 shows a schematic of the source module and an image of one of the two feedthroughs on which our sources are mounted.

We have learnt two valuable lessons regarding the use and mounting of this type of vapour source. The first is that mounting of these tube-shaped containers with the tube opening facing down is highly undesirable since the alkali metal can partially or fully detach from the walls of the tube. In the best case this only

¹ Alvatec, Alvasources[®]

² Kurt J. Lesker, EFT0084033

³ AS-3-Rb-50-V

⁴ AS-3-Rb87(98%)-50-V

⁵ AS-3-K-60-V

⁶ AS-3-K40 (10%)-25-V - The ^{40}K -enriched sources were produced by Alvatec, using material processed by Technical Glass Inc. (since renamed Precision Glassblowing).

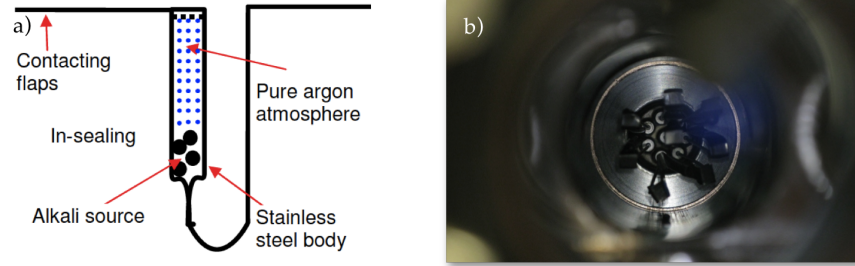


Figure 3.5: a) Schematic of the commercial atom sources used in our system. The source is connected to an electrical feedthrough via the contacting flaps. Prior to bakeout the source material is kept in a pure Argon atmosphere, which is released when the source's indium seal is melted. b) Image of the sources mounted on the electrical feedthrough in the system.

reduces the sublimation rate of the material due to the decreased contact with the heated walls, and in the worst case can lead to the material falling out of the source. Since the material in the sources is actually an alloy of the specific alkali metal (K or Rb) with Bismuth (Bi) and has a very low vapour pressure, this does not change the pressure in the chamber although it does, naturally, render the source useless. Secondly, we have found that during the activation of any source a significant amount of material is deposited on the surfaces of other nearby sources, even though their openings face the same direction. This results in small but noticeable amounts of Rb being released from K sources and vice versa. To preclude this it is recommended to mount all sources of each element, rather than a combination, on a single feedthrough.

For the experiments described in this thesis, an enriched ^{87}Rb source was typically fired for 1.5mins at 5A at the start of every day and for $\sim 30\text{s}$ during each experimental cycle in the course of measurements, with a ^{39}K source being fired once, typically for 1.5mins at 6A, every several weeks.

3.2.9 Assembly and bakeout

Assembly

In order to achieve pressures in the range $< 10^{-11}\text{mbar}$, it is crucial to remove as many of the impurity atoms adsorbed onto the interior surfaces of the chamber as well as those trapped inside the bulk of the metal vacuum components during their production. Even very small amounts of contamination from skin oils, grease,

lint and water vapour can prevent or hugely delay the achievement of a sufficient vacuum and so all contact with the vacuum components during chamber assembly must be carried out using clean latex gloves to prevent any fingerprints being left on inner surfaces. Prior to assembly, every component is thoroughly cleaned using acetone and rinsed with methanol, with any suitably small components also being cleaned beforehand in an ultrasonic bath¹. It is important to work quickly in order to minimize exposure of interior surfaces to air in order to limit the amount of water vapour condensing on them. All vacuum connections are made using ConFlat flanges, non-reusable copper gaskets and silver-plated vacuum bolts. Figure 3.6 shows the assembled vacuum system prior to baking.

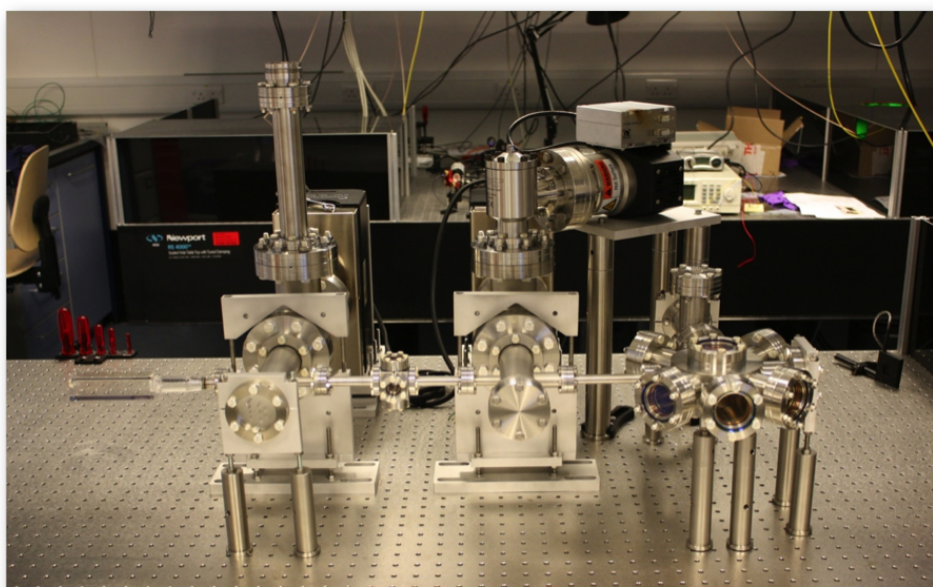


Figure 3.6: Assembled vacuum system with turbo pump connected prior to bake-out. The (vertical) Ti-Sub pump and the pressure gauge feedthrough pins are visible on the left, near the science cell.

Bakeout

Following assembly, the entire chamber undergoes a baking stage during which its temperature is gradually elevated to around 200°C . It is held at this temperature for two weeks while continuously being pumped by the turbo and ion pumps. The elevated temperature (exponentially) accelerates the outgassing of impurity atoms trapped inside the metal components during their production as well the traces

¹ Langford Electronics, Sonomatic 375

of water and other organic hydrocarbons adsorbed onto the chamber surfaces during assembly. These released atoms are then removed from the system by the pumps. It is important to bake the entire system as any unbaked areas will act as condensing surfaces for desorbed atoms which will then be redistributed after cool-down.

In preparation for the bakeout, the entire system is wrapped in resistive heating tapes¹ which are connected to mains-voltage variacs² in order to control their temperature. Thermocouples are then placed against the chamber walls in several strategically-chosen locations in order to provide local probes of the temperature. This is important in order to ensure the relatively slow (not exceeding 2-3°C/minute) and uniform heating required in order to avoid large temperature gradients which could damage the vacuum due to differential expansion of the materials making up the chamber. The chamber is then wrapped in several layers of aluminium foil for insulation and the voltage across the heating tapes gradually increased. The temperature of the thermocouples is measured using a 16-channel thermocouple monitor³ and is monitored and logged using a LabView VI communicating with the thermocouple monitor over GPIB. The variac voltages are adjusted in order to ensure smooth, uniform and gradual heating of the system to its final temperature. Figure 3.7 shows the system during preparation for baking and during the baking itself.

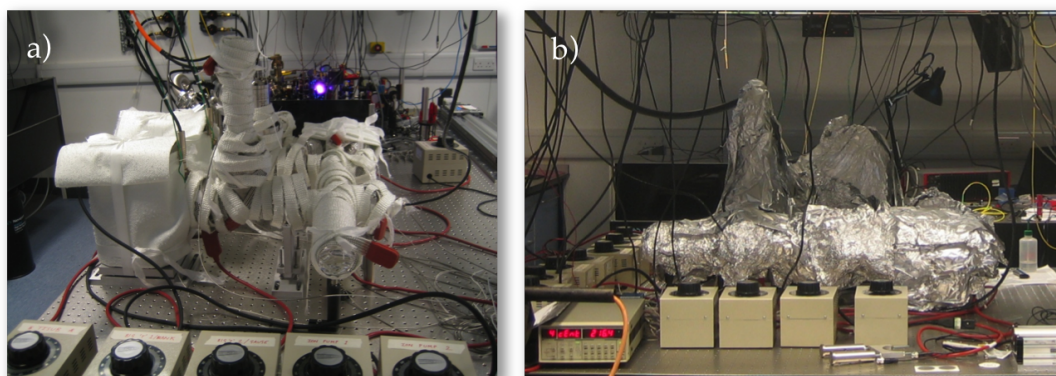


Figure 3.7: The vacuum chamber before (a) and during (b) bakeout.

The most sensitive parts of the system during baking are the ion pumps, science cell and viewports. Above 250°C the ion pumps' permanent magnets start losing magnetisation. The maximal bakeout temperature of the quartz science cell is

¹ Tyco Thermal Controls, isopad TeMS2, 40W/m, max. 260°C.

² Clairtronic, 10551

³ Stanford Research Systems (SRS), SR630

280-300°C, while that of the Kodial viewports is 350°C. The glass-to-metal seal on the science cell is especially sensitive to temperature gradients. The ionisation gauge is also activated during the bakeout - once the pressure drops into its operation range ($P < 5 \times 10^{-2}$) - in order to efficiently remove impurities released during its initial degassing. It can be baked to 250°C while still activated (400°C while disconnected).

The process is reversed to bring the system back to room temperature at a pressure in the region $< 10^{-11}$ mbar, with the turbo and roughing pumps being valved off when the pressure is between 10^{-8} – 10^{-9} mbar, leaving only the ion pumps active. The measurement limit of our ionization gauge is $\sim 3 \times 10^{-11}$ mbar¹. To illustrate the exponential dependence of the pressure on the chamber temperature, figure 3.8 shows a plot of the logarithm of the pressure, as measured by the pressure gauge, against the inverse temperature, measured by a thermocouple close to the gauge, during system cool-down. The (approximate) linearity of this plot is consistent with the Clausius-Clapeyron relation, $dP/dT = L/(T\Delta V)$, where P is the pressure, T the temperature, L the latent heat and ΔV the volume change.

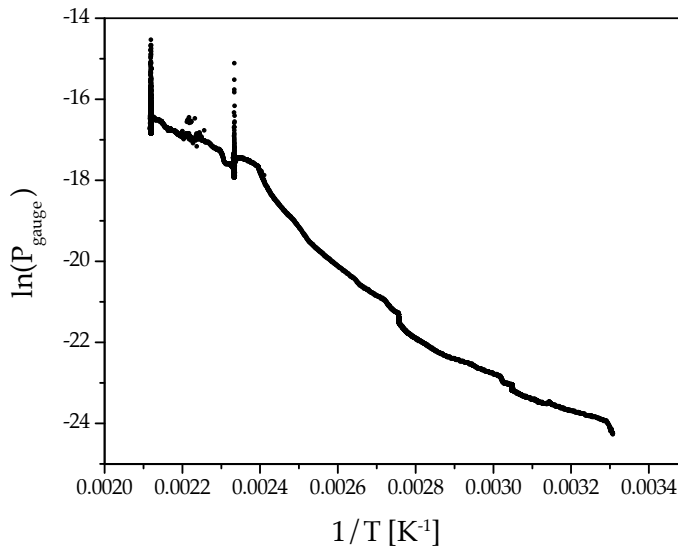


Figure 3.8: Natural logarithm of the pressure, $\ln(P_{gauge})$, during chamber bakeout, plotted against the inverse temperature, $1/T$. The pressure spikes around $T \approx 150^\circ\text{C}$ and 200°C are due to activation of the Ti-Sub pump during the bakeout.

¹ This limit is set by the pump's so-called 'x-ray limit' at which the pressure-dependent ion current becomes smaller than the pressure-independent electron current caused by the photoelectric effect

Note regarding vacuum leaks:

As an additional note, it is worth mentioning that at some point during the system's day-to-day operation, a small leak was introduced by a collision between the translating quadrupole coil mount and one of the horizontally-mounted flanges on the MOT cell. The leak was opened at the joint between the MOT cell and the transfer tube and was detected by spraying the region with helium and observing the sharp rise in system pressure. Rather than re-bake the chamber, we opted to try and seal the leak using a purpose-made silicon resin sealant¹. The sealant is applied directly to the leak and requires several days to fully cure at room temperature. This successfully restored UHV pressure and has not presented any problems in the several years since its application, with typical 1/e lifetimes of 300s being achieved for thermal clouds in the science cell.

3.3 Laser System

The light used for laser cooling, optical pumping (see section 3.6) and imaging (see section 3.14) of the atom cloud is required to address specific atomic transitions and hence must possess a narrow linewidth compared with both the Doppler width and the splitting between the hyperfine states involved. Laser linewidths are typically stabilized to below the linewidth of the relevant atomic transition, which for the cooling transitions of ⁸⁷Rb and ³⁹K are ($2\pi\times$) 6.07MHz and 6.04MHz, respectively. Linewidths on the order of 1MHz and below are easily achieved by commercially available stabilized diode lasers. Our laser system consists of a combination of external-cavity-stabilized diode lasers (ECDL) and tapered amplifier (TA) modules. The ECDLs emit light with a linewidth below 1MHz, a mode-hop-free tuning range typically between 20-50GHz and powers in the range 80-150mW, while the TA chips are designed to amplify the power of the diode lasers to around 1W while preserving their spectral characteristics. An overview of the laser system is shown in figure 3.11 in addition to the more detailed description below. We also make use of far-off-resonant light to generate the optical dipole potential used in our optical trap (section 3.10), as well as for our experiments with optically-plugged magnetic traps (appendix B) and two-dimensional confinement (appendix F).

¹ Kurt J. Lesker, KL-5-5B

3.3.1 Saturated absorption and locking scheme

Despite their narrow linewidths and relative stability, ECDL lasers are not immune from unacceptable long-term frequency drifts. In order to preclude these drifts and to ensure that the lasers are tuned precisely to the desired frequency, all our diode lasers are actively locked to atomic transitions in a vapour cell containing a sample of the desired atomic species (Rb or K). The locking scheme employs the well-known technique of saturated-absorption spectroscopy [90, 148] in order to obtain Doppler-free absorption spectra from which an appropriate error signal can be derived and fed back to the laser in order to stabilize its frequency. Figures 3.9 and 3.10 show the saturated absorption spectra obtained for ^{87}Rb and ^{39}K , respectively, using the beam configurations illustrated in figure 3.11 and described in the following two subsections.

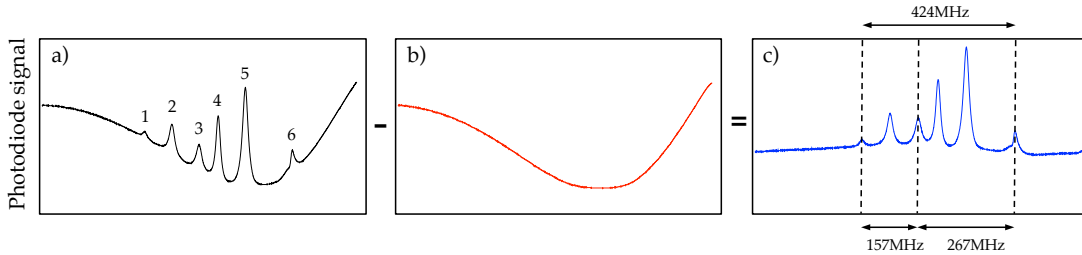


Figure 3.9: Saturated-absorption spectroscopy on the $|F = 2\rangle \rightarrow |F'\rangle$ transition on the D_2 line of ^{87}Rb . (a) Absorption spectrum showing saturated-absorption peaks superposed on the background Doppler spectrum. The peaks labelled 1, 3 and 6 are the $|F = 2\rangle \rightarrow |F' = 1, 2, 3\rangle$ transitions, respectively, and the peaks labelled 2, 4 and 5 are the $|F = 2\rangle \rightarrow |F' = 1/2\rangle$, $|F = 2\rangle \rightarrow |F' = 1/3\rangle$ and $|F = 2\rangle \rightarrow |F' = 2/3\rangle$ crossover peaks, respectively. Figure (b) shows the Doppler spectrum in the absence of saturated absorption and (c) the signal resulting from subtraction of the latter from the former. The relative positions of the peaks can be deduced from the spacings indicated in figure (c), with crossover peaks located halfway between the participating transitions.

3.3.2 Rb lasers

The ^{87}Rb cooling light is derived from an integrated master-oscillator-power-amplifier (MOPA) unit¹, providing $\approx 800\text{mW}$ of 780nm light at its main output. The unit's rear auxiliary output provides several mW in total, part of which is

¹ Toptica, TA100

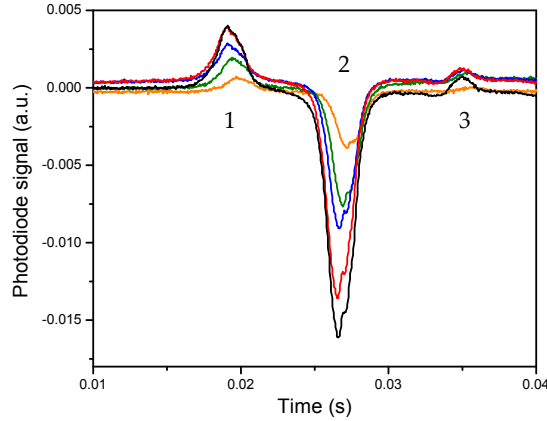


Figure 3.10: Saturated Absorption spectroscopy on the D_2 transition of ^{39}K . The figure shows the large $|F = 1\rangle \rightarrow |F'\rangle / |F = 2\rangle \rightarrow |F'\rangle$ crossover dip to which we lock our ^{39}K master laser. Shown are the saturated absorption curves at vapour cell temperatures of 19.8°C (orange), 35°C (green), 40°C (blue), 45°C (red) and 50°C (black).

sent to a saturated-absorption locking setup and part of which is used for imaging light. The saturated-absorption setup contains a double-pass AOM driven at approximately 98MHz and is used to offset-lock the laser frequency to $2 \times 98 = 196\text{MHz}$ *above*¹ the $|F = 2\rangle \rightarrow |F' = 2, 3\rangle$ crossover peak which is located approximately 133MHz *below* the $|F = 2\rangle \rightarrow |F' = 3\rangle$ cooling transition i.e. 63MHz blue detuned. All subsequent frequency tuning of the cooling, imaging and pumping beams is carried out with this double-pass AOM in order to preserve the beam alignment. The imaging beam is then brought into resonance by another single-pass AOM operating at around 67MHz, while the cooling beam is brought to a detuning of approximately -3Γ by another single-pass AOM operating near 83MHz. The light used for optical pumping (see section 2.3) is split off after this AOM and is passed through another single-pass AOM at 200MHz in order to be able to bring it into resonance with the $|F = 2\rangle \rightarrow |F' = 2\rangle$ transition during optical pumping.

The ^{87}Rb repump light is generated by a separate ECDL², locked via a separate saturated-absorption setup to the $|F = 1\rangle \rightarrow |F' = 1, 2\rangle$ crossover peak, 78.5MHz below the $|F = 1\rangle \rightarrow |F' = 2\rangle$ repump transition and brought into resonance by a single-pass AOM operating at approximately 78MHz.

¹ i.e. at a higher frequency

² Toptica, DL100

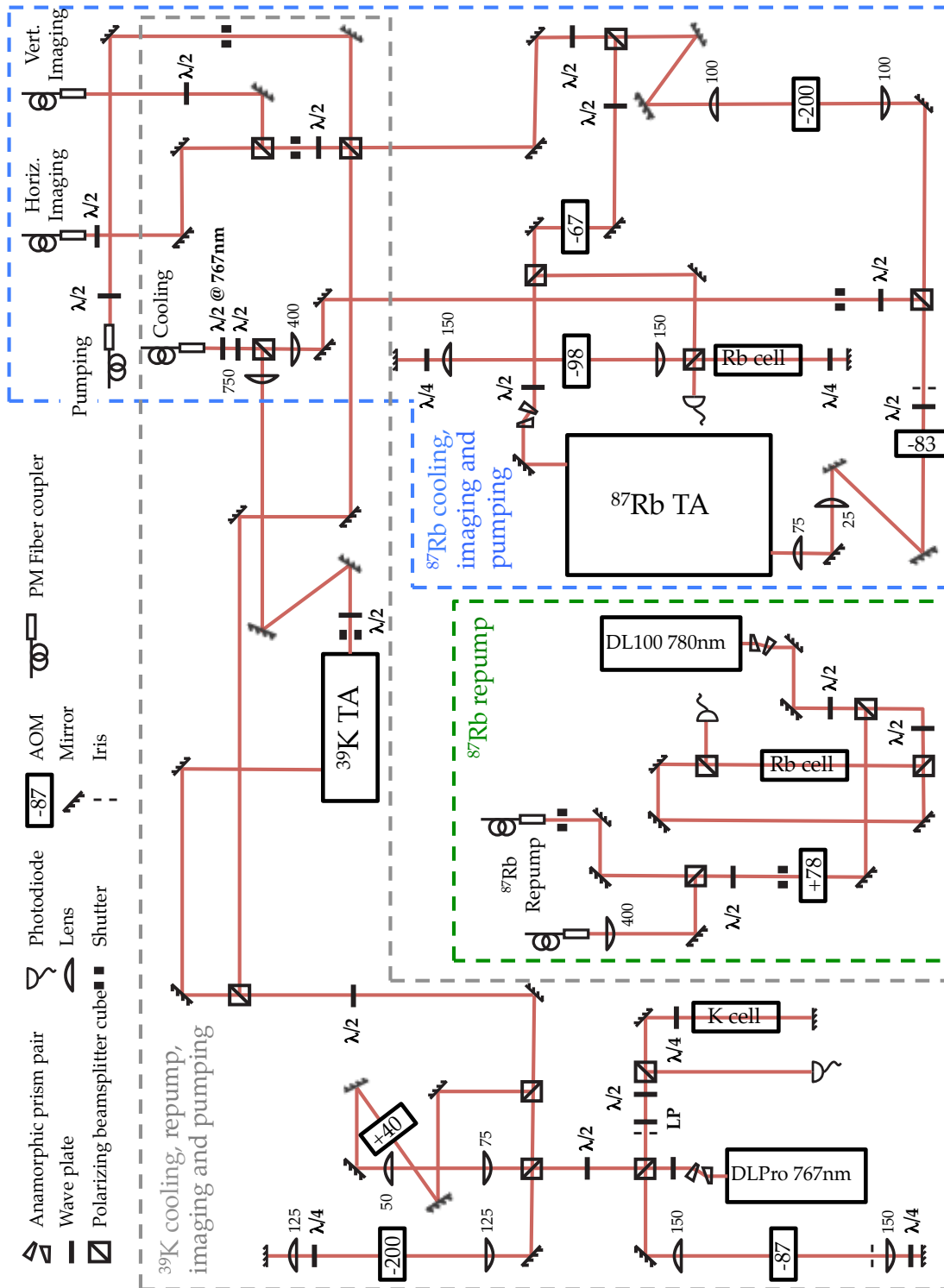


Figure 3.11: Overview of the laser system used to generate the cooling, repump, imaging and pumping beams used in the experiment. See text for a detailed description.

3.3.3 K lasers

All the ^{39}K beams are derived from a single ECDL¹, providing roughly 80mW of 767nm light, with the cooling and repump beams seeding a TA unit² with a maximal output power of approximately 1.5W. Light is split off from the ECDL output and a double-pass AOM operating at 87MHz is used to offset-lock the laser $2 \times 87 = 174\text{MHz}$ below³ the $|F = 1, 2\rangle \rightarrow |F'\rangle$ crossover dip, which is itself 231MHz red (blue) detuned from the $|F = 2\rangle$ ($|F = 1\rangle$) states i.e. the laser gets locked approximately 57MHz red of the $|F = 1\rangle \rightarrow |F'\rangle$ transition. The light not used for locking is again split into two beams, with one traversing a double-pass 200MHz AOM to generate the cooling/imaging/pumping beam and the other encountering a single-pass 40MHz AOM to bring this repump beam closer to its final frequency. The cooling and repump beams are then overlapped on a polarizing beamsplitter cube (PBS) and the overlapped, orthogonally polarized beams are then rotated with a halfwave plate in order to tune the balance between the cooling and repump power seeding the TA. In order to ensure perfect spatial overlap of the MOT beams for both ^{39}K and ^{87}Rb , we overlap the combined ^{39}K cooling/repump beam with the ^{87}Rb cooling beam. The two beams are spatially overlapped using a PBS cube and their polarizations are aligned prior to fibre coupling using a dichroic waveplate⁴, designed to act as a half-wave plate at 767nm and a full-wave plate for 780nm. All coupling is done into polarization-maintaining (PM) single-mode fibres. The ^{39}K imaging and pumping beams are likewise overlapped with their ^{87}Rb counterparts before being coupled and sent to the vacuum system, while the fibres containing the repump and cooling light are sent to the fiberport cluster located near the vacuum chamber.

3.3.4 Shutters

Complete extinction of laser beams requires the use of opaque mechanical shutters since AOMs always exhibit small amounts of leakage light into the diffracted beams. We use Thorlabs⁵ and Sunex⁶ shutters, whose characteristic opening and shutting times are on the order of 1-2ms. The vibrations caused by the Thorlabs

¹ Toptica, DLPro

² Sacher Lasertechnik, TEC-400

³ i.e. at a *higher* frequency than the $|F = 2\rangle \rightarrow |F'\rangle$ transition.

⁴ LENS-Optics GmbH, W2M25-767&780

⁵ Thorlabs, SH05

⁶ Sunex Inc., SHT934

shutters can temporarily perturb the locking of nearby lasers and are reduced by mounting them on sorbothane shock-absorbing posts. In addition we have also made use of home-made shutters, produced from voice-coil actuators found in generic hard disk drives. The design follows that of the Melbourne group¹ [149, 150].

3.3.5 AOMs and drivers

Fine adjustment of laser frequencies, on the order of $\lesssim 1\text{MHz}$, is accomplished using acousto-optic modulators (AOM). These devices rely on Bragg-like scattering of an incident laser beam from a travelling refractive-index grating, generated by an RF signal in the range $f \sim 20\text{-}400\text{MHz}$, to shift both the frequency and the direction of the outgoing beam and hence can be used to control the beam's detuning as well as acting as high-speed switches, respectively. Most AOMs allow frequency shifts over a range of $\pm 20\%$ of their centre frequencies with the deflection speed of the models used in our experiments² depending on the beam width roughly as $15\text{ns}/100\mu\text{m}$.

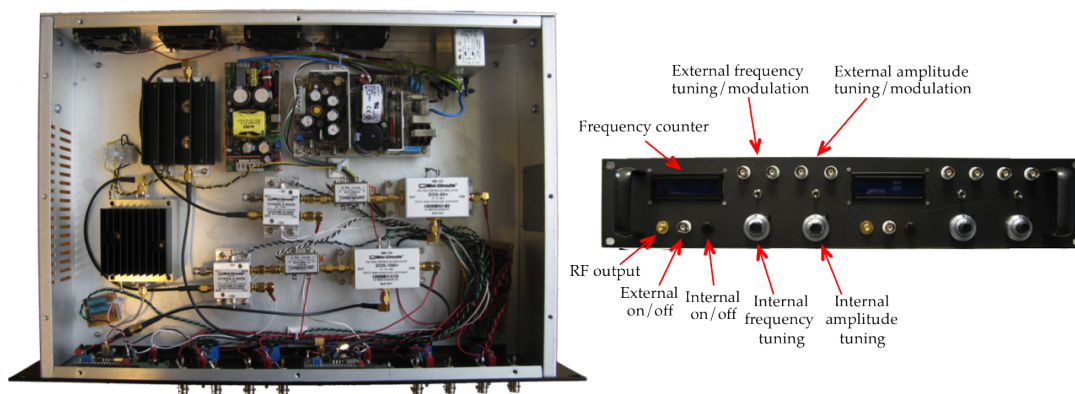


Figure 3.12: (a) Dual-channel AOM driver interior. Visible for each channel from right to left are the VCOs³, attenuators⁴, switches⁵ and amplifiers⁶. Also visible are the power supplies and fans (top) and frequency counters (bottom). Two amplifiers of different gains are used in this driver in order to drive AOMs requiring differing amounts of drive power without risking damage due to excess power. (b) Driver front panel.

¹ <http://optics.ph.unimelb.edu.au/atomopt/shutter/shutter.html>

² Crystal Technology Inc., 3080-125, 3110-110, 3200-115 and AA Opto-Electronic

³ Mini-Circuits, ZOS-50, ZOS-100, ZOS-200, ZOS-300

⁴ Mini-Circuits, ZX73-2500-S+

⁵ Mini-Circuits, ZYSWA-2-50DR

⁶ Delta RF Technology, LA2-1-525-30 and Mini-Circuits, ZHL-3A, ZHL-32A

The electronics required to drive an AOM consist of a voltage-controlled oscillator (VCO), a voltage-controlled attenuator and an amplifier which is required in order to generate the $\sim 1\text{W}$ of RF power required to drive most commercial AOMs at their maximal diffraction efficiency of 80-90%¹. Figure 3.12 shows the internal layout of one of the drivers constructed for use in our experiment.

3.3.6 Fiberport cluster

In order to divide the cooling and repump light into the six separate beams required for operation of our MOT, we have made use of a commercial *fiberport cluster*². This is a compact, modular assembly of fibre couplers, half-wave plates and polarizing beam splitters (PBS) designed to accept two beams at different input ports and to allow their relative intensities to be adjusted at each of six output ports by adjusting the alignment of the six half-wave plates. All inputs and outputs are coupled into polarization-maintaining single-mode optical fibres and the light intensity at both inputs can be monitored from built-in photodiodes to which $\sim 1\%$ of each input beam is diverted. When calculating the powers at each of the six outputs, it is important to take account of the imperfections in the PBS cubes, which typically reflect $\sim 5\%$ of the p-polarized light together with $\sim 100\%$ of the s-polarized component.

The triple-wavelength beam containing the ^{39}K cooling/repump frequencies and the ^{87}Rb cooling light is sent into the first fiberport-cluster input while the ^{87}Rb repump light is sent into the second input. Due to the PBS cube imperfections, perfect balancing of all the power from one input, i.e. $\sim 17\%$ at each output, results in the second input being distributed between the outputs with values between 7-25% of the total power at this input. Since the precise balancing of the (relatively weak) ^{87}Rb repump light is not crucial to the operation of the MOT, we take care to balance the triple-wavelength ‘cooling’ beam outputs, and allow the Rb repump to remain unbalanced.

3.4 Magneto-optical trap (MOT)

The preceding sections described our vacuum system and laser setup, both of which play a role in multiple stages of the experiment. We now turn to describing

¹ As opposed to switching speed, maximal diffraction efficiency grows with beam diameter.

² Shäfter + Kirchhoff GmbH, Fiber Port Cluster 2-to-6

in more detail the individual stages of the experimental sequence, from collection and cooling in the dual-species MOT via sympathetic cooling in the science cell and ending with evaporative cooling in the optical dipole trap and time-of-flight imaging.

3.4.1 MOT laser parameters

As mentioned in section 2.1.4, the unresolved excited-state hyperfine manifold in ^{39}K leads to strong pumping of atoms into the $|F = 1\rangle$ state (requiring comparable ‘cooling’ and ‘repump’ intensities) and potentially to strong heating due the blue-detuning from nearby states (requiring detuning of both cooling and repump beams from the entire excited-state manifold).

For ^{39}K during the MOT phase, we use detunings of -7.6Γ and -4.6Γ from the ^{39}K $|F = 2\rangle \rightarrow |F' = 3\rangle$ and $|F = 1\rangle \rightarrow |F' = 2\rangle$ transitions, respectively. However, in order to achieve lower ^{39}K temperatures prior to magnetic trapping, during the last 40 ms of the MOT stage, the two detunings are reduced to -1.5Γ and -4.1Γ , respectively, while the repumping intensity is also slightly reduced. This results in lower temperatures of several hundred μK without an appreciable drop in atom number [49]. For ^{87}Rb during typical MOT operation, the cooling light is detuned by -3.1Γ from the cycling transition, while the repump light is close to resonance with the $|F = 1\rangle \rightarrow |F' = 2\rangle$ transition. Under these conditions, the atom numbers in our single-species ^{87}Rb and ^{39}K MOTs saturate at roughly 5×10^9 and 1×10^9 , respectively, after $\sim 10\text{s}$ of loading. Simultaneous trapping of ^{87}Rb and ^{39}K results in a roughly 15% reduction in ^{87}Rb number and a factor of ~ 3 reduction in the ^{39}K number due to light-assisted interspecies collisions.

3.4.2 MOT field gradient

In optimizing the size of the ^{87}Rb and ^{39}K MOTs individually, we have found field gradients of $9.6\text{G}/\text{cm}$ and $8\text{G}/\text{cm}^1$, respectively, to yield the largest MOTs for our laser parameters. However, when both species are trapped together, their relative abundances also influence the optimal conditions and we have empirically found a weaker gradient of $6.4\text{G}/\text{cm}$ to provide the best results in terms of final ^{39}K condensate size.

¹ Along the ‘strong’ axis, connecting the coil centres.

The MOT stage is followed by 6ms of optical molasses. During this step the ^{87}Rb cooling light is taken further away from resonance to -4.9Γ , the ^{39}K cooling beam detuning is left at -1.5Γ and the ^{39}K repump detuning is increased to -4.1Γ . Table 3.2 summarizes the laser and magnetic field parameters during the MOT and molasses stages.

Laser parameters		
Beam	Detuning [Γ]	Total power (at atoms) [mW]
MOT (duration: $\sim 20\text{s}$)		
^{87}Rb Cooling	-3.1	130
^{87}Rb Repump	0	10
^{39}K Cooling	-7.6 (-1.5 during final 40ms)	155
^{39}K Repump	-4.6 (-4.1 during final 40ms)	155
Molasses (duration: 6ms)		
^{87}Rb Cooling	-4.9	60
^{87}Rb Repump	0	10
^{39}K Cooling	-1.5	110
^{39}K Repump	-4.1	10
Beam diameter ($1/e^2$) [cm]		
~ 3		
Field gradient (strong) [G/cm]		
6.4 (9.6 during final 40ms)		
Atom number (approx.)		
5×10^9 (^{87}Rb -only)	1×10^9 (^{39}K -only)	$4 \times 10^9 / 3 \times 10^8$ (^{87}Rb - ^{39}K)

Table 3.2: Summary of MOT and molasses parameters. Detunings for the ^{87}Rb beams refer to the $|F = 2\rangle \rightarrow |F' = 3\rangle$ and $|F = 1\rangle \rightarrow |F' = 2\rangle$ transitions for the cooling and repump beams, respectively. Detunings for the ^{39}K beams refer to the entire excited-state hyperfine manifold, $|F = 2\rangle \rightarrow |F' = 3\rangle$ and $|F = 1\rangle \rightarrow |F' = 2\rangle$, respectively.

3.5 Quadrupole and compensation coils

Here we describe the electromagnetic coils used to establish the quadrupole field for our MOT as well as the compensation coils used for nulling stray fields in the MOT region.

3.5.1 Quadrupole coils

In addition to providing the magnetic field for our MOT, our main quadrupole coils are also responsible for confining the atoms during transport to the science cell and during the initial evaporative cooling stage, as well as generating the quadrupole component of our quadrupole-Ioffe configuration (QUIC) magnetic trap, in which sympathetic cooling of ^{39}K by ^{87}Rb takes place.

The coils are wound from insulated, hollow, circular copper tubing (OD: 4mm, ID: 2.8mm) and consist of 40 turns (4×10) with an inner diameter of 51mm and an outer diameter of 135mm. They are mounted 100mm apart (at their closest point), as close as possible to anti-Helmholtz configuration in order to maximize their gradient (see appendix E), and provide a field gradient of 160G/cm along the vertical (strong) axis when run at a current of 200A. The wound coils are coated in protective epoxy and mounted in a heavy-duty aluminium support designed to firmly hold the coils, enable their mounting onto the translation stage, eliminate mechanical vibrations due to water flow and magnetic forces, and ensure sufficient optical access both at the MOT and science cell ends of the apparatus (see figure 3.13). A narrow slit is machined into the brackets supporting the coils themselves in order to avoid eddy currents being formed near the location of the atoms when the coils are turned off.

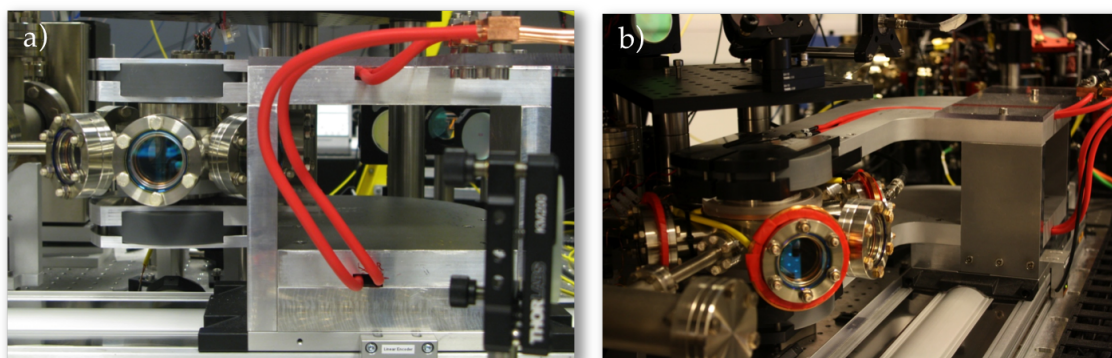


Figure 3.13: (a) Quadrupole coil pair mounted on the translation stage and (b) MOT compensation coils mounted on the MOT cell flanges. The red pipes carry current and cooling water to the quadrupole coils.

The two coils are connected in series and their current is provided by a 6kW (30V, 200A) DC power supply¹ down 35mm²-gauge cables, connected to the coils

¹ Delta Elektronika, SM 30-200

via copper adapters designed to also allow easy connection of water-cooling hoses to each coil. The current is controlled remotely by an analog signal to the power supply and is switched digitally using a high-voltage IGBT¹.

3.5.2 Coil safety

The IGBT driver circuit is also responsible for switching off the current in the event of the coils overheating or a drop in the cooling water flow. A thermistor² with a threshold temperature of 60°C is mounted on each quadrupole coil and a third thermistor is mounted to the large copper heatsink to which the IGBT is bolted. A varistor is connected in parallel with the IGBT in order to shunt away any current from transient voltage spikes that would otherwise damage the IGBT. In addition, a flow switch³ near the coils is used to ensure the flow does not drop below 0.5lmin⁻¹. These four signals must all be normal in order for current to be allowed to pass through the coils.

3.5.3 Compensation coils

The various sub-Doppler cooling mechanisms at work - and hence the lowest temperatures attainable - during optical molasses are sensitive to both the direction and magnitude of any magnetic fields present [90, 151]. Transfer of the maximal number of atoms, with the highest possible phase-space density, into the purely magnetic trap further requires the MOT to have a regular shape, its centre to overlap with that of the magnetic trap and its free-space expansion to be isotropic and determined only by the cloud temperature. Furthermore, a well-defined quantization axis is required during the optical pumping stage prior to magnetic trapping (see section 2.3).

Meeting these criteria requires the cancellation of any stray magnetic fields at the location of the atoms, arising from the earth's magnetic field or nearby instrumentation⁴. Field compensation is accomplished by three orthogonal coil pairs mounted directly onto the flanges of the MOT cell through which the cooling and repump beams are directed (see figure 3.13b). The pair providing the vertical compensation field is mounted around the top and bottom flanges of the MOT

¹ SEMIKRON, SEMiX 402GB066HDs

² EPCOS, B59901D0060A040

³ Gentech International, FS-10

⁴ Ion pumps in particular produce significant static magnetic fields

cell. They consist of 9 turns (3×3) of 1mm-diameter enamelled copper and have an inner diameter of 90mm. The other two pairs consist of 40 turns (5×8) of 1mm-diameter enamelled copper wire with an inner diameter of 72mm. Each horizontal pair produces a field of roughly 0.6G/A at its centre and the vertical pair generates roughly 1.7G/A. The currents to these coils are provided by a 3-output, low-ripple power supply¹.

Despite not being mounted precisely in Helmholtz configuration due to space constraints, the coil separation was chosen so as to achieve as uniform a field in the trap centre as possible, with the non-uniformity estimated numerically to be around $-0.012\text{GA}^{-1}\text{cm}^{-2}$ for the horizontal pairs and $-0.002\text{GA}^{-1}\text{cm}^{-2}$ for the vertical pair. The independently-controlled currents in each coil pair were adjusted in order to optimize the number and temperature of atoms transferred into the quadrupole magnetic trap.

Note

For a description of the Feshbach, compensation and guide-field coils mounted about the science cell, see section 3.11.

3.6 Optical pumping and magnetic capture

Our optical pumping and magnetic capture stages proceed as follows:

- At the end of the 6ms molasses stage, all cooling beams are extinguished and both repump beams are left on for a further 1ms in order to transfer all atoms into their respective $|F = 2\rangle$ manifolds. The guide field is then given $800\mu\text{s}$ to ramp up before both pumping beams are switched on for $200\mu\text{s}$. The repump beams are only on for the first $100\mu\text{s}$.
- Immediately after the optical pumping stage described above, all lights are extinguished and the quadrupole coils are abruptly switched on at 40 G/cm (strong axis) in order to capture the atoms, and then linearly ramped up to 160 G/cm in 50ms. The capture efficiency is typically $\sim 80\%$ for ^{87}Rb and $\sim 65\%$ for ^{39}K .

¹ Hameg Instruments, HM7042-5

3.7 Transport

3.7.1 Background - moving vs. stationary coils

Once the atoms have been optically pumped and magnetically trapped, they must be transported over a distance of roughly 75cm to their final position within the science cell. There exist several experimental approaches to the problem of transporting laser-cooled atoms from one region of an experimental apparatus to the other. This transport should transfer the maximal number of atoms while remaining as adiabatic as possible. Some of the schemes that have been developed and previously demonstrated include:

- Use of moving red-detuned optical tweezers [152, 153]
- Use of resonant ‘push beams’ in conjunction with a 2D ‘atomic funnel’ MOT to create a slow atom beam [154, 155, 156, 157, 57, 158, 159]
- Use of a chain of static magnetic coils in which coordinated control of the currents allows the creation of a moving magnetic trap [146, 160]
- Use of a single magnetic coil pair, translated by means of a mechanical stage and confining the atoms magnetically for the duration of the transport [161, 162, 163, 164].

Given the vibrational stability issues encountered in translation of the lenses used in moving optical tweezers [152, 165], the need for multiple additional laser beams and magnetic coils associated with the ‘push beam’ method, and the many coils and sensitive current optimization required for the static coil scheme, we opted to implement a moving coil system in our experiment.

Advantages This scheme has the advantages of conceptual simplicity, ease of setup and optimization and the use of only a single coil pair, significantly reducing the construction, mounting, alignment and water-cooling burdens compared to the static coil method.

Disadvantages The main disadvantages of the moving coil method are the need for care to minimize vibrations due to the coil translation and the extra volume swept out by the translation stage and any coil mounts, which would normally be available for mounting components.

Both of these disadvantages can be ameliorated through prudent design of the vacuum chamber geometry, the coil mount and the transport sequence. The

high-precision translation stages and control/feedback electronics commercially available today allow for great accuracy and repeatability, and we have found this method to perform very well in our experiments.

3.7.2 Track details

The translation stage selected for our transport system¹ is capable of 900mm of travel, is fitted with an optical linear encoder with $0.5\mu\text{m}$ resolution², a 6000rpm brushless servo motor³ and is controlled via a servo drive/controller⁴ communicating with our control PC.

An important selection criterion is the use of a ball-screw-based stage instead of a linear-motor-based stage to ensure that any magnetic field generated by the track is localized as far as possible from the science cell. The magnets in a linear-motor translation stage are located along the whole length of the track as well as on the moving stage itself, whereas a ball-screw stage relies on a motor located at its far end to rotate a precision screw which translates the stage along the track. We position the motor at the MOT-cell end of the chamber, as far as possible from the science cell. We have also found it *crucial* to ‘de-energize’ the track (i.e., shut down the motor) immediately after the transport stage to eliminate electronic RF noise emitted by the motor which was observed to severely reduce the number of trapped atoms.

The quadrupole coils are mounted to the translation stage via an aluminium supporting ‘arm’ (see figure 3.13b), which also provides a channel for the electrical and water connections to the coil tubing. These are held within a flexible, articulated cable housing⁵ one end of which is anchored to the optical table and the other end of which is free to follow the track motion, keeping the water hoses and electrical cables out of any beam paths while providing strain relief and sufficient bend radius.

¹ Parker 406XR series. Full part number: 406.900XRSD5.H14L13.C10.M29.E3.B1.R1.P1, from which the various features and specifications can be extracted.

² Renishaw, RGH24Z30F00A

³ Part number: SMH82.6003.8.14.21D65.2

⁴ Compax3, C3 S063 V2 F10.I12.T11

⁵ igus, E-Chain System[®], 2500.09.125.0

3.7.3 Transport parameters and efficiency

The 741.21mm transfer takes approximately 1.7s and the parameters used are given in Table 3.3.

Travel distance	jerk	acceleration	velocity
741.21 mm	50,000 mm/s ³	5,000 mm/s ²	500 mm/s

Table 3.3: Transport parameters. Jerk is the time-derivative of the acceleration, and the acceleration and velocity given represent peak values.

We typically transfer well over 50% of the atoms from the MOT to the science cell, with the transfer efficiency for ³⁹K lower than for ⁸⁷Rb since its higher temperature leads to removal from the trap via contact with the transfer tube walls. The temperature of these ‘evaporated’ atoms can be estimated by equating the spatial extent of the cloud, $r_{cloud} \approx k_B T / \mu_B B'$, with the transfer tube radius, $r_{tube} = 0.5\text{cm}$. For our gradient of $B' \approx 80\text{G/cm}$ along the weak trap direction, this gives a temperature of $T_{evap} \approx 2.7\text{mK}$.

3.8 QUIC trap

Our ³⁹K cloud must ultimately be transferred into a purely optical trap prior to condensation in order to access the desired Feshbach resonance in the magnetically anti-trapped $|1, 1\rangle$ state. However, the ³⁹K sample must be cooled prior to this transfer in order to ensure the maximal initial atom number in the optical trap. This is accomplished via sympathetic cooling with ⁸⁷Rb and our precise cooling targets are described in section 3.9. With ⁸⁷Rb alone it is possible to evaporate directly in the quadrupole trap in the presence of an optical ‘dimple’ potential [166] offset from the trap centre, and in this way produce optically-trapped condensates of 5×10^5 ⁸⁷Rb atoms with less than 10s of evaporation. However, ³⁹K cannot be effectively cooled sympathetically in similarly short evaporation sweeps due to the relatively small K-Rb interspecies background scattering length $a_{K-Rb} \simeq 36a_0$ [58], where a_0 is the Bohr radius $a_0 \approx 0.53\text{\AA}$, compared to $a_{Rb} \simeq 99a_0$ [167] for ⁸⁷Rb.

As mentioned in section 2.3, the region of very low magnetic field at the centre of the quadrupole trap restores the degeneracy of the Zeeman states and allows adiabatic transitions to untrapped states which are rapidly lost from the trapping potential. Long evaporation sweeps in the quadrupole trap are

therefore prohibited due to loss of ^{39}K atoms via such Majorana flips as well as via inelastic collisions with $|2, 1\rangle$ ^{87}Rb atoms likewise created by Majorana transitions. Here too, several schemes have been proposed and demonstrated in order to address the presence of these Majorana spin flips by ensuring that the atoms do not experience a region of zero magnetic field. In our system, we have chosen to implement a so-called Quadrupole-Ioffe configuration (QUIC) trap, a Ioffe-Pritchard-type trap first realised by Esslinger *et. al.* in 1998 [168] and subsequently used by many other groups. This configuration offsets the trap minimum to a positive value while converting the linear quadrupole trap to a harmonic trapping potential.

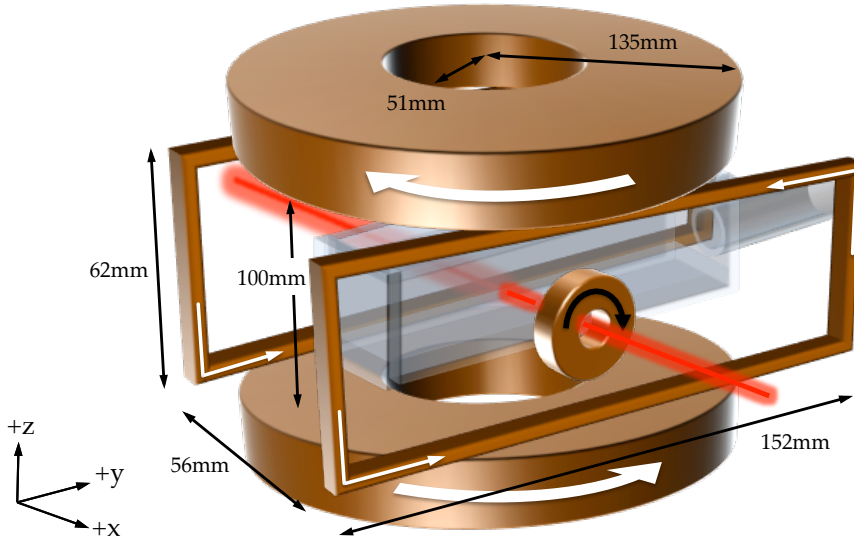


Figure 3.14: Schematic of the QUIC trap coil configuration in our system. The quadrupole coil pair in conjunction with the Ioffe coil generate the offset harmonic potential, with the rectangular *anti-bias* coil pair opposing the field along the axis of the Ioffe coil. See table 3.4 for a summary of the coil parameters.

3.8.1 Trap configuration

The QUIC configuration consists of a pair of coils producing a quadrupole field together with a third coil whose axis is oriented perpendicular to that of the quadrupole coils as shown in figure 3.14. This third coil is known as the *Ioffe* coil and is responsible for producing the offset harmonic confinement when its field is superposed with the quadrupole field.

In addition to the Ioffe coil, we make use of an additional ‘anti-bias’ Helmholtz coil pair, also shown in figure 3.14, to provide a uniform field in the opposite direction to that created by the Ioffe coil along its axis. This anti-bias field is used in order to provide better control over the trapping potential during loading of the QUIC trap and the subsequent transfer into the optical trap.

3.8.2 Pros and cons

The quadrupole field used in our QUIC trap is generated by the same quadrupole coil pair used in our MOT and transport stages. Since the atoms are already confined in this quadrupole field upon arrival in the science cell, conversion into the QUIC trap is relatively straightforward and efficient, consisting of simply ramping up the Ioffe and anti-bias coils so as to retain the largest number of atoms possible in the resulting harmonic potential. Other advantages of the QUIC configuration include its simplicity, the relatively large optical access afforded by the reduced number of coils compared to other configurations and the good mode-matching that can be achieved between this type of trap and the gaussian intensity profile of the optical dipole trap due to the harmonic nature of the confinement (as opposed, for example, to the optically plugged trap discussed in appendix B).

Disadvantages of this configuration are the weaker confinement compared to the quadrupole trap, which makes evaporative cooling less efficient as mentioned in section 2.4, as well as the fact that during its operation the centre of the QUIC trapping potential is displaced from the quadrupole trap centre in the direction of the Ioffe coil, potentially reducing optical access to the cloud. We overcome this problem by evaporating in the displaced QUIC before ramping up the appropriate currents in order to temporarily restore the cloud to the centre of the cell prior to loading of the optical trap.

3.8.3 Trapping potential

The QUIC trap fields are similar to those produced by a standard Ioffe-Pritchard configuration near the trap minimum [169], consisting of a harmonic potential with a non-zero offset. To obtain an estimate for the trapping frequencies, we can use the near-origin approximation for the field produced by a single coil¹ to

¹ See equation E.3 in appendix E

write the field produced by the Ioffe coil as

$$\begin{aligned} B_{\text{ax}}^{\text{Ioffe}} &= B_0 + B'_{\text{ax}}x + B''_{\text{ax}}(x^2 + (y^2 + z^2)/2) \\ B_{\text{rad}}^{\text{Ioffe}} &= \frac{1}{2}B'_{\text{ax}}\sqrt{y^2 + z^2} - B''_{\text{ax}}x\sqrt{y^2 + z^2} \end{aligned} \quad (3.4)$$

where we have written the radial coordinate as $\rho = \sqrt{y^2 + z^2}$. B'_{ax} is the axial field gradient, B''_{ax} is the axial field curvature and we have used the coordinate system of figure 3.14. This field is superposed with that of the quadrupole trap $B_{\text{quad}} = B'(x, y, -2z)$ and the axial gradient B'_{ax} is chosen to cancel the quadrupole gradient B' along the Ioffe coil axis at the quadrupole centre (i.e. $B'_{\text{ax}} = -B'$). Combining the two fields and keeping only terms to second order in position yields the following for the total field

$$\begin{aligned} |B_{\text{tot}}| &= \sqrt{\mathbf{B}_{\text{Ioffe}}^2 + \mathbf{B}_{\text{quad}}^2} \\ &\approx B_0 + B''_{\text{ax}}x^2 + \frac{1}{2} \left(\frac{(\frac{3}{2}B')^2}{B_0} - B''_{\text{ax}} \right) \rho^2 \end{aligned} \quad (3.5)$$

where we have reinserted the radial coordinate, ρ . The trapping potential hence has the form

$$U = g_F m_F \mu_B B \approx U_0 + (1/2)m\omega_{\text{ax}}^2 x^2 + (1/2)m\omega_{\text{rad}}^2 \rho^2 \quad (3.6)$$

with the trapping frequencies given by

$$\omega_{\text{ax}} = \sqrt{\frac{2g_F m_F \mu_B B''_{\text{ax}}}{m}} \quad \omega_{\text{rad}} = \sqrt{\frac{g_F m_F \mu_B}{m}} \left(\frac{(\frac{3}{2}B')^2}{B_0} - B''_{\text{ax}} \right)^{1/2} \quad (3.7)$$

For typical values of the bias field, quadrupole gradient and axial curvature used in our sequence ($B_0 = 5.3\text{G}$, $B' = 64\text{Gcm}^{-1}$ and $B''_{\text{ax}} = 120\text{Gcm}^{-2}$, respectively), this predicts trapping frequencies of $\omega_{\text{ax}} = 2\pi \times 21(14)\text{Hz}$ and $\omega_{\perp} = 2\pi \times 76(51)\text{Hz}$, respectively. Since the radial frequency is usually significantly higher than the axial frequency, atoms in the QUIC trap occupy an elongated, cigar-shaped potential. Figure 3.15a shows the magnetic field profile along the axial direction as the current in the Ioffe coil is increased in 5A increments with the quadrupole gradient held at 80G/cm. In addition to the primary minimum moving towards the Ioffe coil, a second field minimum appears outside the science cell and the two minima approach each other until eventually joining to form an offset harmonic

potential. There is therefore a risk during the Ioffe coil ramp-up, that atoms will collide with the cell wall on their way to the secondary minimum. The intuitive role of the anti-bias field is to ensure that the primary minimum is deep enough during the Ioffe-coil ramp-up such that when atoms do start spilling into the secondary minimum it is already within the science cell and the atoms are not lost via collisions with the cell wall, as illustrated for our experimental parameters in figure 3.15b.

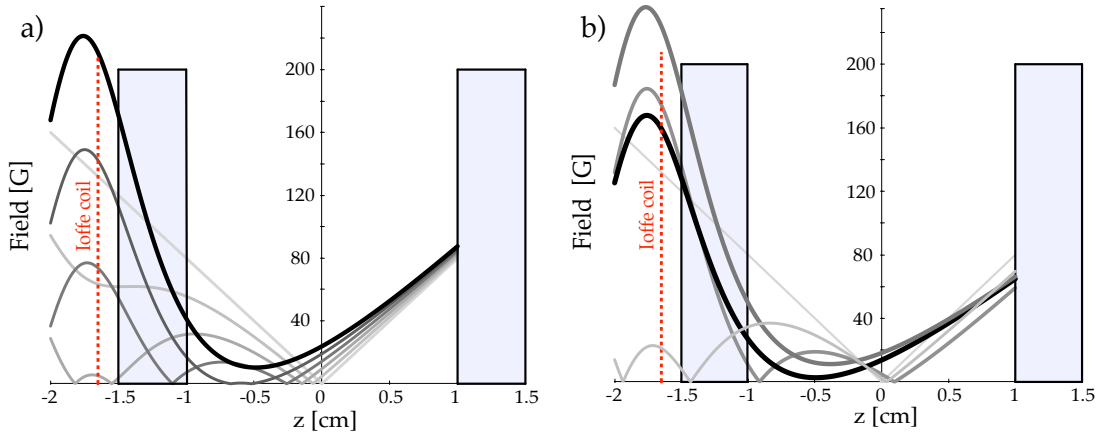


Figure 3.15: Field profile along the Ioffe coil axial direction (a) without and (b) with the anti-bias field contribution. The red dashed line shows the position of the Ioffe coil and the shaded regions show the locations of the science cell walls. In (a), the Ioffe current is increased (light to dark, 0-25A) in 5A increments with the quadrupole gradient held at 80G/cm. Atoms spilling into the secondary minimum collide with the cell wall. Figure (b) shows the profile at various points (light to dark) through our actual experimental sequence, with the anti-bias field, directed along $-z$, ensuring that atoms entering the secondary minimum do not collide with the cell wall.

Figure 3.16 shows images of the cloud in the QUIC trap taken perpendicular to the Ioffe coil axis (i.e. vertically in the lab frame) and showing a sequence with progressively increasing anti-bias field. As the anti-bias field is increased, with the Ioffe field remaining unchanged, the initially-tight axial confinement gradually relaxes until the dual minima can clearly be seen.

3.8.4 Ioffe coil and trap loading

Our Ioffe coil is located between the two quadrupole coils, at a distance of 2mm from the outer wall of the science cell along its long edge (see figure 3.14). The coil consists of 18 turns (3×6 , axial \times radial) of 1mm-diameter enamelled copper

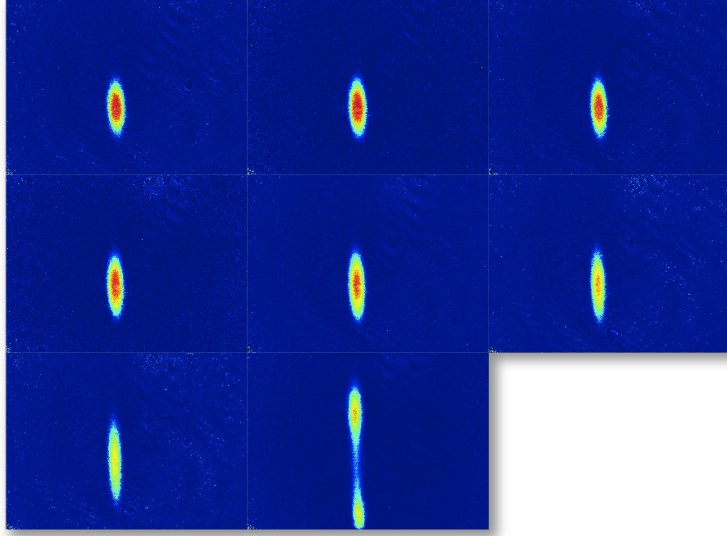


Figure 3.16: Finding the anti-bias voltage in the compressed QUIC trap to provide maximal compression without creating a magnetic field zero. The trapped cloud is imaged perpendicular to the trap axis and the Ioffe coil is located at the bottom of the image. From top left to bottom right: 22.77G, 23.16G, 23.82G, 24.49G, 25.15G, 25.81G, 26.47G and 27.14G

wire, and has a clear inner diameter of 10mm. It is mounted on a water-cooled copper block with a clearance hole through which both the axial imaging and the 2D confinement beams can access the cell.

Conversion of the quadrupole trap to a QUIC configuration as efficiently as possible requires coordination between the currents in the quadrupole, Ioffe and anti-bias coils. The transfer sequence lasts 5s in total and is shown in figure 3.17, with the axial field value at various points during the transfer shown in figure 3.15.

With the quadrupole coils at 200A (80G/cm, weak axis), the Ioffe coil is ramped up over 500ms to a current of 24A while the anti-bias coil pair is simultaneously ramped up to 19.3A (28G) in order to counter the movement of the trap minimum towards the cell wall caused by the Ioffe coil field. The current in the quadrupole coils is then reduced to 160A (64G/cm, weak axis) over 250ms, after which the anti-bias current is ramped down to 3.4A (5G) over 500ms and finally, 250ms later, the Ioffe coil current is gradually ramped down to its final value of 19.7A over 3.5s, during which the trap centre moves gently towards the cell wall, causing some removal of the hottest atoms from the trap.

With this procedure 4×10^8 ^{87}Rb and up to 4×10^7 ^{39}K atoms are loaded into

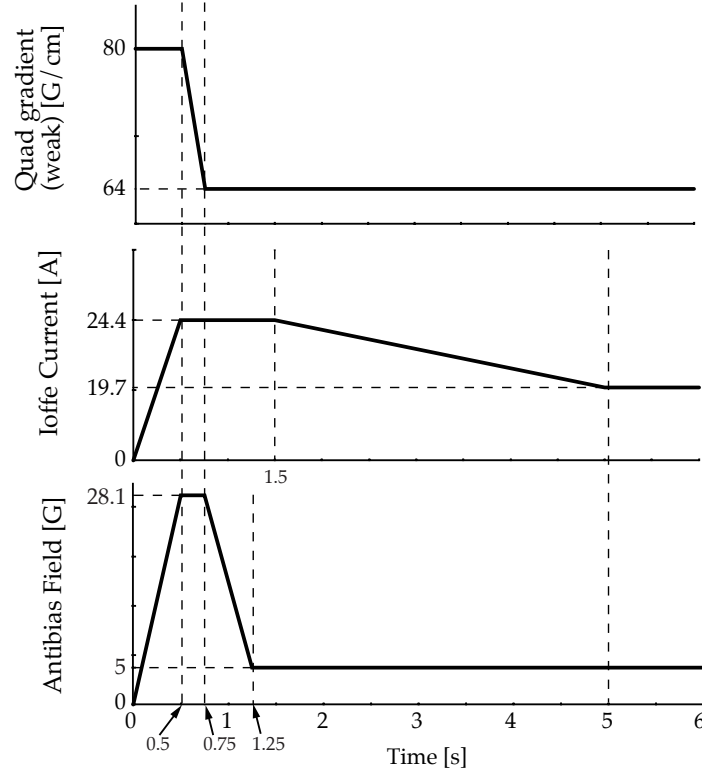


Figure 3.17: QUIC transfer sequence. Currents and field values of the quadrupole, Ioffe and anti-bias coils during conversion of the quadrupole field into the QUIC configuration.

the QUIC trap and these final currents result in trapping frequencies of $\omega_z/2\pi = 14$ (21) Hz axially and $\omega_r/2\pi = 43$ (64) Hz radially with respect to the Ioffe coil axis for ^{87}Rb (^{39}K) in the $|2, 2\rangle$ ground state, in the presence of the 5G bias field. In addition to numerical simulation, trapping frequencies in the QUIC trap were determined by measuring the differential gravitational sag, $\Delta z \equiv z_{\text{Rb}} - z_{\text{K}}$, between the trapped ^{87}Rb and ^{39}K clouds, from which the frequencies can be obtained using $\Delta z = \left(1 - \frac{m_{\text{K}}}{m_{\text{Rb}}}\right) \frac{g}{\omega_{\text{Rb}}^2}$.

3.9 Sympathetic cooling

Our sympathetic cooling target is to bring as large a number of ^{39}K atoms as possible to a temperature of approximately $5\mu\text{K}$. This goal is motivated by two factors:

1. As discussed in section 3.10, this temperature coincides with the optimal temperature found for loading the largest possible ^{39}K samples into our

optical trap.

- In our QUIC trap, the difference between the gravitational sags, g/ω_r^2 , for ^{87}Rb and ^{39}K is $73\mu\text{m}$. This corresponds to the (vertical) thermal radii for the two species, $R_T^{\text{Rb}} \approx R_T^{\text{K}}$, at a temperature of roughly $4\mu\text{K}$, where $R_T = \sqrt{k_B T / (m\omega_r^2)}$. Below this temperature, the reduced spatial overlap between the species renders sympathetic cooling inefficient.

The forced evaporation of the ^{87}Rb buffer gas is carried out by inducing the $|F=2, m_F=2\rangle \rightarrow |1, 1\rangle$ transition between the $|2, 2\rangle$ state of our trapped atoms, and the anti-trapped $|1, 1\rangle$ state residing in the lower hyperfine ($F=1$) ground state (see figure 3.18). These two states are separated by the ground state hyperfine splitting of 6.835 GHz, in addition to their relative Zeeman shifts due to the presence of the magnetic trap, which in this case gives a total splitting of: $f_{MW} = f_{HF} + 3\mu_B B$. We evaporate on this ‘microwave’ transition rather than the more closely-spaced Zeeman transitions in order to avoid cutting directly into the ^{39}K cloud. The ^{39}K atoms are cooled via their elastic collisions with the cold ^{87}Rb reservoir.

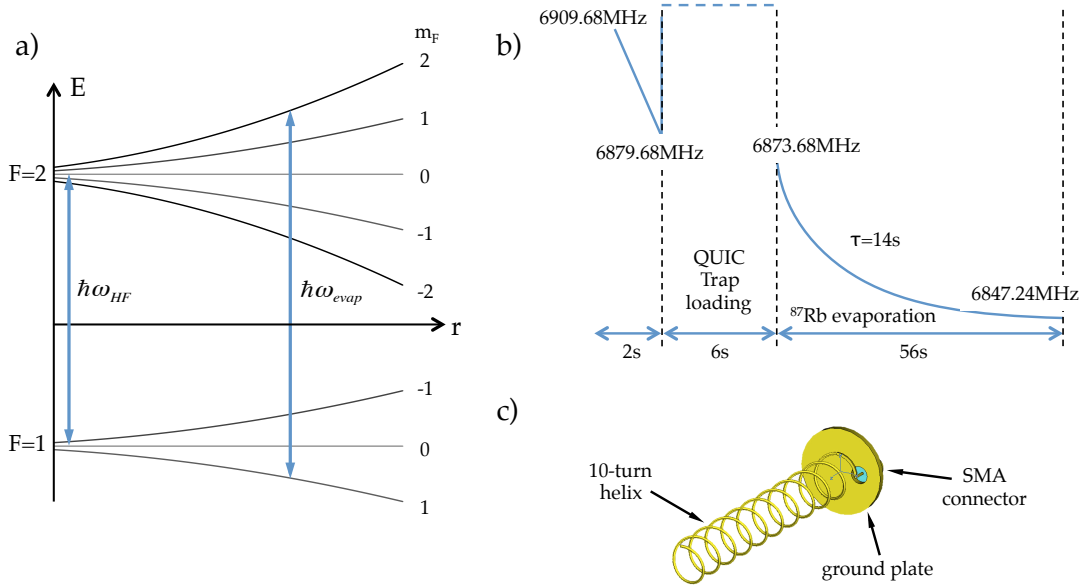


Figure 3.18: Hyperfine evaporation of ^{87}Rb . (a) ^{87}Rb atoms in the $|2, 2\rangle$ state are transferred to $|1, 1\rangle$ using a microwave-frequency sweep. The 5G field offset at the QUIC trap centre allows us to also selectively remove residual $|2, 1\rangle$ atoms using a second, simultaneous sweep as described in the text. (b) The sweep sequence used for hyperfine evaporation includes a 2s preliminary evaporation in the quadrupole trap, a 6s interval during ramp-up of the QUIC trap and a 56s evaporation sweep with a time constant of 14s. (c) The helix antenna used for the evaporation (modified from [170]).

The sympathetic cooling sequence proceeds as follows: In order to transfer as many ^{39}K atoms into the QUIC trap as possible, we perform a short sympathetic cooling stage while still in the pure quadrupole trap, ramping the microwave frequency from 6909.68MHz to 6879.68MHz linearly in 2s. The knife is then lifted to a high frequency during the 6s loading of the QUIC trap. Once our ^{87}Rb - ^{39}K mixture has been loaded into the QUIC trap, we employ a 56s exponential sweep of the frequency from 6873.68 to 6847.24MHz with a 14s time constant. To obtain the starting frequency, we first find the ‘bottom of the trap’ i.e., the frequency at which all atoms are just evaporated. Equation 2.36 then allows us to pick an initial temperature from which to commence evaporation. The long sweep is required in order to allow for thermalization between ^{39}K and ^{87}Rb atoms due to the small value of $a_{\text{K-Rb}}$, whereas in ^{87}Rb -only experiments we observe an almost identical efficiency with a shorter evaporation time of 32s. In addition, during the evaporation time, we continually sweep a separate microwave source between 6838 and 6844MHz. The 5G field offset at the minimum of our QUIC trap allows this sweep to remove any $|2, 1\rangle$ ^{87}Rb atoms without affecting the atoms in the $|2, 2\rangle$ state.

Hardware

The microwave radiation is delivered to the atoms from an antenna driven by a function generator¹ via an amplifier². In order to achieve efficient evaporation, it is desirable for as much of the power delivered to the antenna to be radiated in order to maximize the magnetic field strength at the location of the atoms. Our antenna consists of a ten-turn helix with an overall length of 10cm, wound from 1mm copper wire around a teflon tube of wall thickness 0.4mm and inner diameter 14mm. The helix is connected to a 30mm-diameter copper ground plate fitted with an SMA connector and is impedance matched to the voltage source by deforming the first 1/4 turn closest to the ground plate. The output power of our 25dB-gain amplifier is limited to 38dBm ($\sim 6.3\text{W}$), with the added directivity³ of the antenna, $D_{\text{peak}} \approx 4.5$ ($D_{\text{dBi}} = 10 \log[D] \approx 6.5$), providing sufficient power at the atoms to perform efficient state transfer. Figure 3.18b shows the helix antenna and figure 3.18c shows the antenna’s directivity measured for both linear polarization components. See Igor Gotlibovych’s project report for more details

¹ Agilent, N5183A MXG

² Microwave Amplifiers Ltd., AM53-6.7-7-25-38

³ Antenna directivity is defined as the ratio of the power density radiated in the direction of strongest emission to that of an ideal isotropic radiator radiating the same total power.

on the setup and characterization of the microwave system [170]. The radiation used for removal of $|2, 1\rangle$ ^{87}Rb atoms during the evaporation sweep is derived from a sweep generator¹ and is added to the main evaporation frequency on a power combiner² before being sent to the amplifier and helix antenna.

3.9.1 Sympathetic cooling results

Figure 3.19 shows absorption images³ of both ^{39}K and ^{87}Rb taken at various points during the sympathetic cooling sequence.

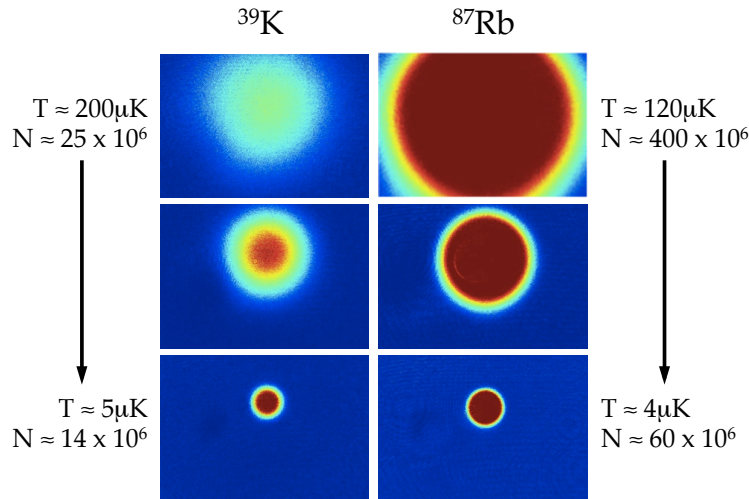


Figure 3.19: Sequence of images taken at the start, middle and end of a typical sympathetic cooling sequence. While ^{87}Rb cools from 120 to $4\mu\text{K}$, losing roughly a factor of seven in atom number, ^{39}K is cooled from 200 to $5\mu\text{K}$ with less than a factor of two drop in number.

Figure 3.20 shows the evolution of the phase-space density of both the ^{87}Rb and the ^{39}K components against their respective numbers during the sympathetic cooling stage in the QUIC trap.

We can characterize the efficiency of our sympathetic cooling using the evaporation parameter, γ , defined in the discussion of evaporative cooling in section 2.4. For ^{87}Rb alone, we observe very efficient cooling with $\gamma = 3.6$. For ^{39}K we observe an extremely steep rise in phase-space density with only small atom loss, indicating the effectiveness of our sympathetic cooling. The temperature of the ^{39}K cloud is reduced from 200 to $5\mu\text{K}$ while the atom number is reduced by less

¹ Agilent/HP, 83622A synthesized sweeper

² Mini-Circuits, ZX10-2-71-S+

³ See section 3.14.

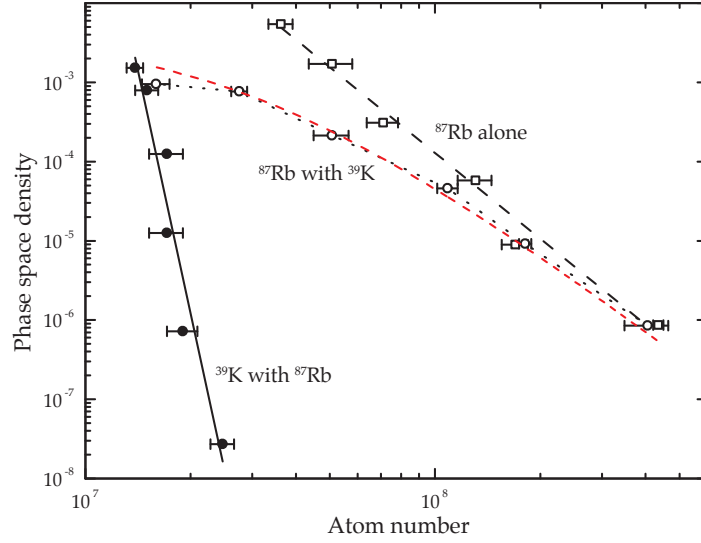


Figure 3.20: Evolution of phase-space density with atom number during sympathetic cooling. The solid black line shows ^{39}K cooling with less than a factor of two drop in number. The dotted black line shows the data for ^{87}Rb in the presence of ^{39}K and the dashed black line shows ^{87}Rb alone. The dashed red line shows the result of a fit to the sympathetic cooling model of [134], described in section 2.4.

than a factor of two, from $\sim 25 \times 10^6$ to $\sim 14 \times 10^6$. The trap lifetime would account for a roughly 20% reduction in N_{K} over the evaporation period, so the observed loss shows evidence for some inelastic processes. By analogy with conventional evaporative cooling we can express the efficiency of this process with an effective $\gamma_{\text{symp}} \approx 20$.

Using the expression for the peak phase-space density of a non-degenerate cloud of N atoms, at temperature T , in a 3D harmonic potential of mean frequency $\bar{\omega}$

$$\rho_0 = n_0 \lambda_{\text{dB}}^3 = N \left(\frac{\hbar \omega}{k_B T} \right)^3 \quad (3.8)$$

in conjunction with equation 2.45¹ allows us to model the evolution of the ^{87}Rb phase-space density with (decreasing) atom number and compare it to our experimental results. A fit to the data is shown in figure 3.20. This fit has assumed a constant ^{39}K number, taken to be the mean of the initial and final values, and yields the result $\alpha = 1.47 \pm 0.03$ for the evaporation parameter $\alpha = (\eta + \kappa) / 3 - 1$ defined in this model. Assuming a constant value of $\eta = 7$ throughout the evaporation, results in the prediction $\kappa = 0.41$. Despite its simplicity, the model of

¹ Reminder: $T_{\text{Rb}} = T_{\text{min}}(N_{\text{Rb}}/N_{\text{K}} + 1)^\alpha$ with $T_{\text{min}} = T_{\text{Rb}}^{\text{init}}(N_{\text{K}}/N_{\text{Rb}}^{\text{init}})^\alpha$

[134] is seen to provide a good fit to the data. Figure 3.21 shows the temperature of the ^{39}K cloud as a function of the number of ^{39}K atoms remaining at the end of the evaporative cooling stage. The temperature can be seen to approach the final temperature reached by ^{87}Rb in the absence of ^{39}K .

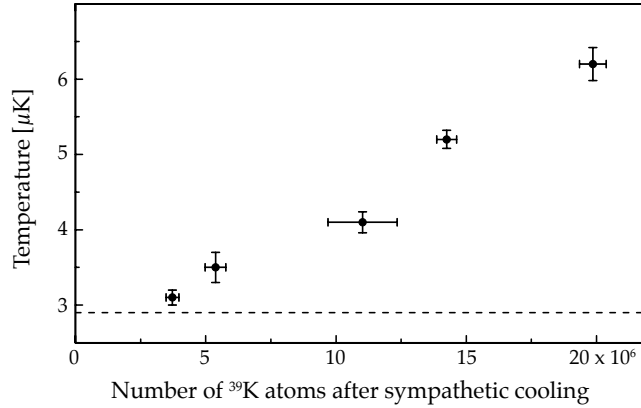


Figure 3.21: ^{39}K temperature as a function of the number of ^{39}K atoms remaining at the end of the sympathetic cooling.

3.10 Crossed dipole trap (CDT)

The final cooling stage is performed in a crossed optical dipole trap (CDT) after transfer of the atoms from the QUIC trap. The light for our crossed optical dipole trap is generated by a 10W, single-mode, linearly polarized, CW, Ytterbium fibre laser¹, with a wavelength of $\lambda = 1070\text{nm}$ and a linewidth specified at $\delta\lambda \approx 1.5\text{nm}$. The laser is fitted with a collimator to produce a beam with a $1/e^2$ diameter of 5mm and a $1/e^2$ divergence of 0.3mrad. The red-detuning of the beam from the D_2 transition for both species produces an attractive potential, with atoms drawn to the intensity maximum at the beam centre.

Our trap is formed by a single beam arranged in a ‘bow-tie’ configuration as shown in figure 3.22.

This configuration, as opposed to two independently-controlled beams, was chosen in order to maximise the amount of trapping power available. The beam is initially telescoped down to a 1mm diameter by a lens pair in order to enable it to pass through a 110MHz AOM², selected primarily for its large active aperture. The beam then has its polarization cleaned up by a polarizing beamsplitter

¹ IPG Photonics, YLM-10-LP-SC

² Crystal Technology Inc., 3110-197

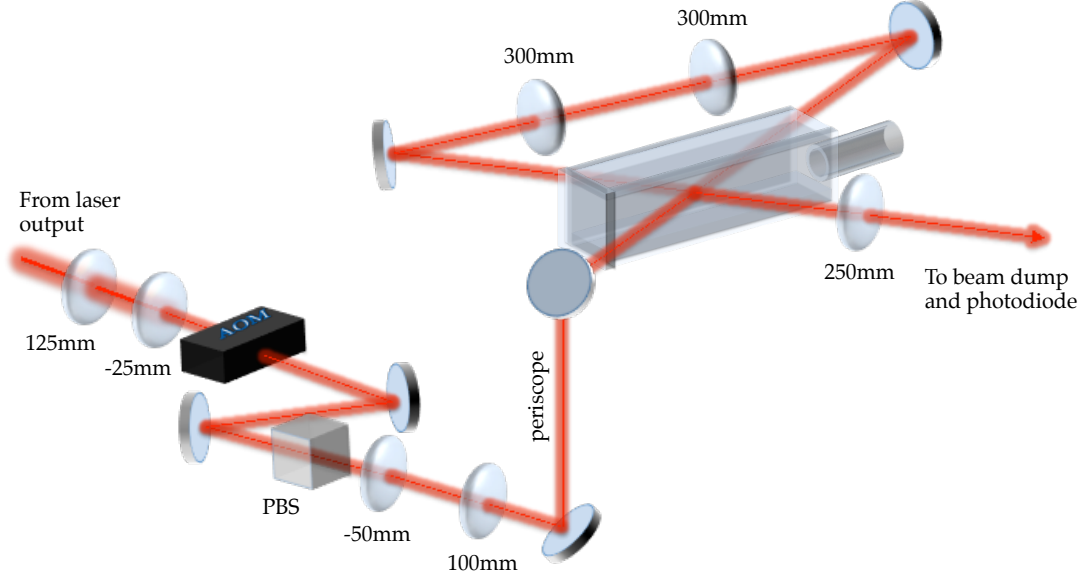


Figure 3.22: CDT optics layout. The beam diameter is initially reduced by a 1:5 telescope before passing through an AOM and PBS cube. It is then expanded and focussed at the atoms by another lens pair. After passing through the cell, the beam is collimated, refocussed and sent back to cross itself orthogonally, before being sent to a beam dump and monitor photodiode. Distances are not to scale.

cube, before being expanded and refocused at the centre of the science cell by a concave-convex lens pair ($f = -50/+100\text{mm}$) mounted in a rigid cage system. This lens configuration allows simple adjustment of the beam waist between 100 and $160\mu\text{m}$. After passing horizontally through the science cell, the beam is collimated, reflected and focused back to cross itself orthogonally with the same waist. A maximum power of 7.5W per beam reaches the atoms, although we normally limit this to 7W to ensure power stability.

The beam has a Gaussian intensity profile and so the combined potential taking into account both beams as well as gravity, and neglecting the Rayleigh range, which for our $140\mu\text{m}$ waist is $z_R = \frac{\pi\omega_0^2}{\lambda} \approx 6\text{cm}$, can be written as

$$\begin{aligned}
 U_{\text{tot}}(x, y, z) &= \overbrace{-U_0 e^{-2\left(\frac{x^2+z^2}{w_0^2}\right)}}^{\text{Beam along 'y'}} \overbrace{-U_0 e^{-2\left(\frac{y^2+z^2}{w_0^2}\right)}}^{\text{Beam along 'x'}} + \overbrace{mgz}^{\text{gravity}} \\
 &\approx -U_0 \left(1 - 2\left(\frac{x^2+z^2}{w_0^2}\right)\right) - U_0 \left(1 - 2\left(\frac{y^2+z^2}{w_0^2}\right)\right) + mgz \\
 &= -2U_0 \left(1 - (x^2 + y^2 + 2z^2)/w_0^2\right)
 \end{aligned} \tag{3.9}$$

where U_0 is the peak potential created by a *single* beam and w_0 is the beam waist. The potential can thus be approximated, for small displacements ($x, y \ll \omega_0$), as harmonic, with the trapping frequency along the z -direction larger by a factor of $\sqrt{2}$ than those along the x and y directions. Further discussion of the trap characteristics, including trap-depth, frequency, gravitational sag and anharmonicity simulations, can be found in the doctoral thesis of Robert Campbell.

Intensity stabilization

The optical trapping potential can be stabilized, and its depth varied over two orders of magnitude, by means of a servo loop consisting of the AOM through which the beam is initially passed, a photodiode¹ and a proportional-integral-derivative (PID) controller, whose output is fed back to the AOM in order to stabilize the beam intensity in proportion to a reference voltage provided by our computer-controlled analog voltage sources (see section 3.16). The photodiode is illuminated by a small (but constant) fraction of the total CDT power, picked off the main beam by a glass microscope slide after both its traversals of the science cell.

3.10.1 Transfer into the CDT

In preparation for transfer of the atoms into the CDT, the QUIC trap is translated to the centre of the science cell as follows: The quadrupole gradient is reduced linearly from 128G/cm to 80G/cm over 1s, while the current in the Ioffe coil is simultaneously ramped up from 19.7A to 28A. During the second half of this ramp, the anti-bias field is linearly increased from 5G up to 22.8G.

In order to load the CDT from the QUIC trap, the power in the CDT beam is linearly ramped up to 6.8W in 1s, followed by a 0.5s settling time. Over the following second, the quadrupole gradient is reduced to 48G/cm, the anti-bias field to 3.72G and the Ioffe coil current to 15.6A. The quadrupole and Ioffe coils are then abruptly switched off, leaving the atoms confined solely by the CDT, whose depth at this point is $\sim 30\mu\text{K}$ for ^{39}K and $\sim 35\mu\text{K}$ for ^{87}Rb . The anti-bias field remains on in preparation for the removal of the ^{87}Rb from the trap (see below).

¹ Thorlabs, DET36A/M

Figure 3.23 shows the number of ^{39}K atoms transferred into the CDT as a function of their final number in the QUIC trap, together with the temperatures before and after the transfer. For samples with temperatures of up to $6\mu\text{K}$ in the QUIC trap, equivalent to an evaporation parameter of $\eta \sim 5$, we observe a constant transfer efficiency of $\sim 60\%$. This constant factor is due to the imperfect spatial overlap between the two trapping potentials and is limited by the geometries of the two traps, despite the large ($140\mu\text{m}$) CDT waist being beneficial. For the QUIC trap frequencies specified above for ^{39}K , the radial and axial *diameters* of the cloud at $5\mu\text{K}$ are $2R_T \approx 160$ and $500\mu\text{m}$, respectively, using $R_T = \sqrt{k_B T / m \omega^2}$.

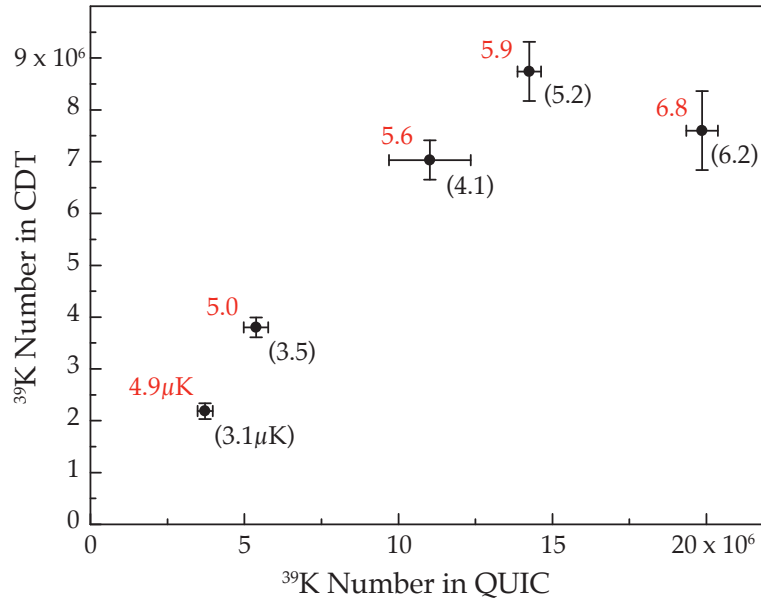


Figure 3.23: Transfer efficiency from QUIC to CDT. Plot shows number of ^{39}K atoms initially in the CDT as a function of the final number in the QUIC trap, together with the temperatures before (in brackets) and after the transfer.

For comparison, the loading efficiency was measured for a $100\text{-}\mu\text{m}$ beam waist and was found to be limited to $\sim 20\%$, saturating at around a third of the available CDT power. We cannot currently increase our beam waist without decreasing the trap depth since we are operating at our maximum available laser power. We typically load 8×10^6 ^{39}K atoms into the CDT at a temperature of $6\mu\text{K}$, from the 13×10^6 atoms remaining in the QUIC trap.

3.10.2 Optical evaporation strategy

With our atoms in the CDT, we are faced with the decision of how to proceed with cooling of the ^{39}K atoms. Since the potential is now state-independent, reduction of the trap depth is accomplished by reducing the CDT beam intensity. In order for sympathetic cooling to be effective in the CDT, the total trap depth for ^{87}Rb has to be lower than that for ^{39}K so that the former can be removed without loss of the latter. The relative trap depths for ^{87}Rb and ^{39}K depend on the competition between two factors: (1) the strength of the electric dipole potential for the two species and (2) the deformation of the potential by gravity. Both effects are larger for ^{87}Rb , the former due to the smaller detuning of the CDT beam from the ^{87}Rb D line and the latter because of its higher mass. As a result, at our initial laser intensities the effect of gravity is negligible and atoms are preferentially lost along the CDT beams such that the trap depth is higher for Rb. Only at sufficiently low intensities does gravity distort the trapping potential enough for the Rb trap depth to fall below that of K, making sympathetic cooling viable. See the corresponding chapter of Robert Campbell's thesis for a more detailed discussion of the optical trap depth. We therefore choose to switch to direct evaporation of ^{39}K and immediately after transfer of both species into the CDT we remove any remaining ^{87}Rb atoms from the trap with a 2ms pulse of imaging light in order to prevent any spin-exchange collisions during the subsequent state transfer of ^{39}K into the $|1, 1\rangle$ state, as described below.

3.10.3 State transfer

In order to prevent collapse of the ^{39}K cloud at low temperatures due to its attractive interactions [68, 69, 171], as well as to increase the evaporative cooling efficiency, we tune the scattering length to a positive and large value by means of a magnetic Feshbach resonance¹. The Feshbach resonance on which our experiments rely occurs in $|1, 1\rangle + |1, 1\rangle$ collisions of ^{39}K and so in preparation for the application of the uniform Feshbach magnetic field, we transfer the entire population from the $|2, 2\rangle$ to the $|1, 1\rangle$ state. The transfer is accomplished by a 35ms Landau-Zener sweep of the magnetic bias field from 3.72G to 3.14G in the presence of 469.3MHz radiation, after all ^{87}Rb has been removed from the trap.

The 469MHz signal is generated by the same function generator used to pro-

¹ See section 2.6

duce our 6.8GHz ^{87}Rb -evaporation radiation; its 5dBm output is controlled by a voltage-controlled RF switch¹ and amplified by a broadband RF amplifier² to a power of approximately 4W (36dBm) before being sent to a single-loop antenna of 36mm diameter, mounted horizontally less than 20mm from the location of the atoms. The amount of radiated power, measured by means of a small pick-up coil was found to be hugely increased by the insertion of a tuneable 1-3pF capacitor³ in series with the antenna, whose primary role is the cancellation of the dominant inductive reactance of the antenna, $X_{\text{loop}} = \omega L_{\text{loop}}$, with the inductance, L_{loop} , given by [172, 173]

$$L_{\text{loop}} = \mu_0 a \left[\ln \left(\frac{8a}{b} \right) - 2 \right] \quad (3.10)$$

where $a = 18\text{mm}$ and $b = 0.5\text{mm}$ are the loop and wire radii, respectively⁴. The use of such ‘tuning capacitors’ for impedance matching of loop antennas is well known [172, 173]. The resonating capacitance is found by equating the two reactances: $(\omega C)^{-1} = \omega L_{\text{loop}}$, which for our parameters gives $C = 1.4\text{pF}$ and does not account for any ohmic losses due mainly to the skin effect in the wire. The circumference of our antenna is $C \approx 11.3\text{cm}$, i.e. $C \approx \lambda/6$ at 469MHz, classifying it as a small-to-intermediate size loop.

Direct optical evaporation of ^{39}K proceeds, after the state transfer and ramp-up of the Feshbach field, via an exponential sweep of the beam intensity over 6s from its initial value of 6.7W per beam down to the desired final depth, which depends on the desired final temperature or condensed fraction.

3.10.4 Trap frequencies

In order to measure the CDT trapping frequencies, we excite an oscillation of the trapped cloud and extract its centre-of-mass position as a function of time. We prepare a small, fully condensed cloud by performing an optical evaporation sweep to an almost negligible trap depth (a few nK) and then abruptly ramping up the trapping beam power to a final depth of $2.6\mu\text{K}$ in a two-piece linear ramp of total duration 110ms, as shown in figure 3.24a.

The centre-of-mass vertical coordinate of each image was found from a fit to a

¹ Mini-Circuits, ZY5WA-2-50DR

² Delta RF Technology, LA2-1-525-30

³ Vishay BCF280905215, 1-3.5pF, 300VDC voltage rating, can withstand 600V for 1 minute

⁴ Expression 3.10 for the inductance is valid for $b \ll a$ i.e. when the wire radius is much smaller than the loop radius.

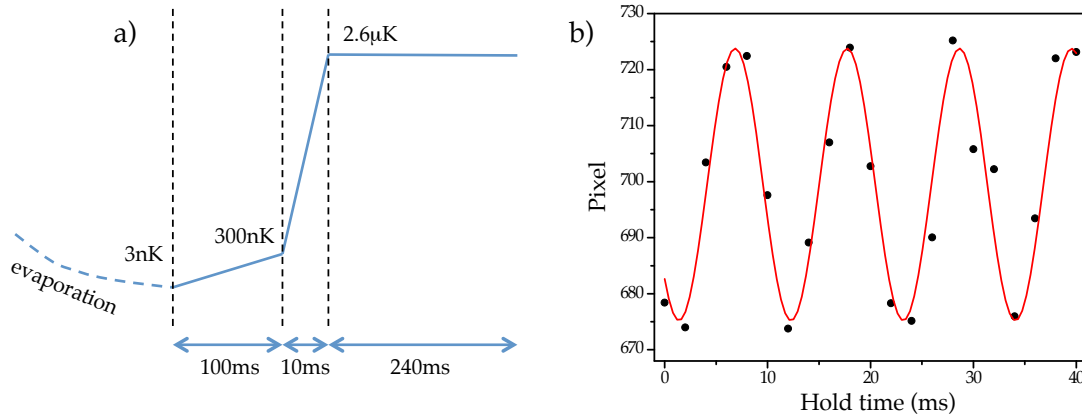


Figure 3.24: Measuring the CDT trapping frequency. (a) following optical evaporation, the CDT intensity profile is ramped up over 110ms and (b) the centre-of-mass position of the cloud is measured after a variable oscillation time and fit to a sine function to extract the trap frequency.

pure Thomas-Fermi profile. Figure 3.24b shows the oscillation in the vertical direction, together with a best-fit sinusoid which yields a frequency along the z -axis (vertical in lab frame) of $91.8 \pm 1.0\text{Hz}$. A numerical simulation of the CDT trapping potential, including the effects of gravity, yields a predicted frequency of $\omega_z = 93.9\text{Hz}$ for this trap depth assuming no misalignment between the CDT beams, in good agreement with the data.

3.11 Feshbach field and Feshbach resonance

With the ^{39}K atoms transferred to the $|1, 1\rangle$ state, we can now access the Feshbach resonance at 402.5G in order to tune the s-wave scattering length to the desired value. As discussed in chapter 2, this is accomplished by application of a homogeneous magnetic field and this section describes the coils used, their mounting about the science cell, their field calibration and our measurements used for locating the position of the resonance and the zero-crossing.

3.11.1 Feshbach coils

The Feshbach field is generated by a Helmholtz coil pair, with each coil consisting of 14 turns (2×7 , axial \times radial) wound from 4mm outer-diameter (OD) copper tubing (ID: 2.8mm), coated in extra-thin heat-shrink material and having an inner diameter of 70mm. The coils are mounted 37mm apart at their closest point and produce a field of approximately 540G at the point midway between

them when operated at their maximal current of 200A. These parameters were chosen in order to provide access to the 402.5G-resonance while keeping the size of the coils sufficiently small so as to be able to place them in close proximity to atoms, within the space between the science cell and the quadrupole coils. The field curvature at the location of the atoms is numerically estimated to be $7 \times 10^{-4} \text{GA}^{-1} \text{cm}^{-2}$.

3.11.2 Science cell coil mount

The Feshbach coil pair, as well as 5 auxiliary Helmholtz coil pairs (two axial, two transverse and one vertical, with respect to the science cell's long axis¹, the RF-evaporation antenna and the 462MHz hyperfine state-transfer antenna are mounted in their respective positions around the science cell by a single mounting structure, designed to hold all the above components within the restricted space between the science cell and the moving quadrupole coils.

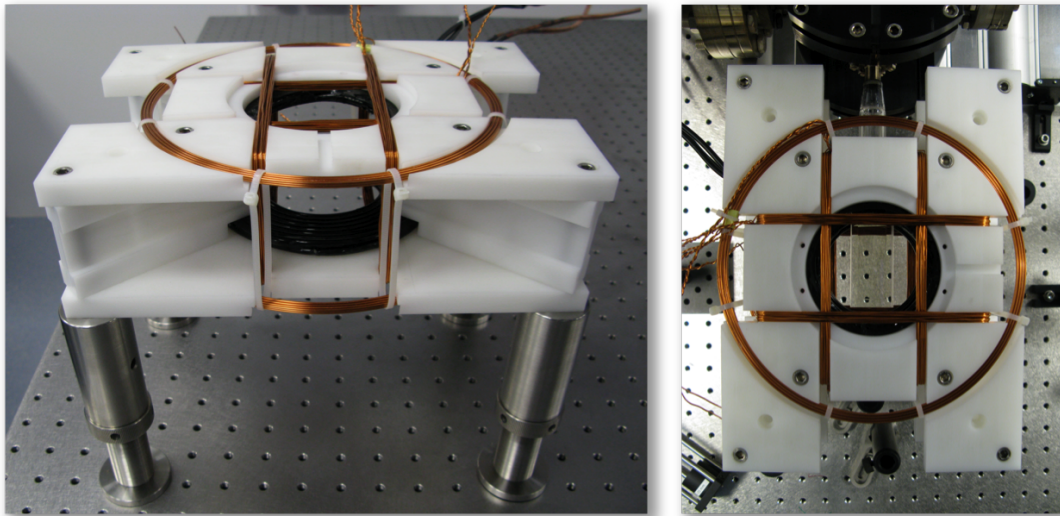


Figure 3.25: The mount constructed for supporting the Feshbach, compensation, anti-bias and TOP trap coils. An additional mount (not shown) is attached so as to fit within the upper coil's inner diameter and supports the meniscus constituting the first component of the multi-element objective used for vertical imaging (see section 3.14) at a distance of approximately 15mm from the science cell's outer wall.

The auxiliary coils are used for providing the uniform compensation and bias fields required during different stages of the experimental sequence such as QUIC

¹ See figure 3.6.

trap loading, state transfer and imaging. The mount is constructed from Polyoxymethylene¹, a thermoplastic material possessing high stiffness, dimensional stability and machinability, often used as a replacement for metals in mechanical parts. This was used in order to avoid any eddy currents arising from the rapid switching of the Feshbach, anti-bias and Ioffe coils during the experimental sequence. Figure 3.25 shows the coil mount before and after its insertion into the apparatus, and the specifications of all the coils mounted in the vicinity of the cell are summarized in table 3.4.

Name	ID [mm]	Turns	Wire \varnothing [mm]	Spacing [mm]	Field [G/A]	Role
Feshbach	70	2 \times 7	4/2.8	37	2.6	Feshbach resonance
Compensation (transverse field)	62 \times 152	8	0.71	56	1.14	Horizontal imaging guide
Compensation (axial field)	74 \times 149	8	0.71	56	1.14	—
Compensation (vertical field)	190	3 \times 7	1	70	2.28	Vertical imaging guide
TOP (transverse field)	62 \times 152	10	1	56	1.46	QUIC anti-bias/ double-shuttering
TOP (axial field)	74 \times 149	10	1	56	1.43	—
Ioffe	10	3 \times 6	1	NA	-	QUIC trap
RF antenna	36	1	1	NA	-	Evaporative cooling
462MHz antenna	36	1	1	NA	-	^{39}K state transfer
Microwave antenna	15	10 (helix)	1	NA	-	^{87}Rb evaporation

Table 3.4: Summary of the various coils mounted in the vicinity of the science cell and their properties.

¹ Also known as acetal, or by one of its trade names, Delrin.

3.11.3 Feshbach field calibration

We perform RF spectroscopy on the $|2, 2\rangle \rightarrow |2, 1\rangle$ transition of ^{87}Rb in order to calibrate the field produced by the Feshbach coils. This is carried out by applying RF radiation to a cold, $|2, 2\rangle$ ^{87}Rb cloud with a fixed frequency corresponding to the splitting between the $|2, 2\rangle$ and $|2, 1\rangle$ states in the presence of a 402.5G field. The splitting is found from the Breit-Rabi formula of equation 2.29 to be $\nu_{402.5G} = 249.444\text{MHz}$, and this radiation is applied using the same function generator and loop antenna used for ^{39}K state transfer (section 3.10.3). The voltage controlling the current in the Feshbach coils is then swept linearly in 200ms over sequential overlapping intervals with a width of 0.004V and centred at increments of 0.002V, until we observe transfer of the entire cloud to the $|2, 1\rangle$ state (see figure 3.26).

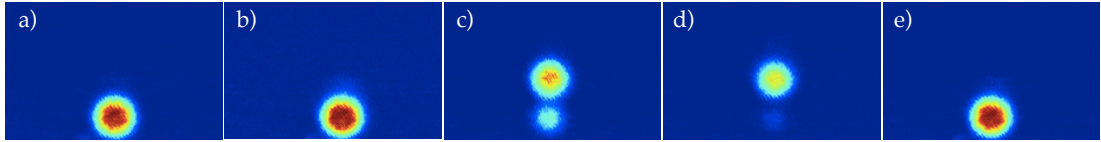


Figure 3.26: A typical sequence of images used for calibration of the Feshbach field. The atoms are irradiated with a frequency corresponding to the energy splitting at 402.5G and the *control* voltage is swept over a series of overlapping intervals: (a) 3.800V \rightarrow 3.804V, (b) 3.802V \rightarrow 3.806V, (c) 3.804V \rightarrow 3.808V, (d) 3.806V \rightarrow 3.810V, (e) 3.808V \rightarrow 3.812V. Transfer of atoms from the $|2, 2\rangle$ state (lower cloud) to the $|2, 1\rangle$ state (upper cloud) is monitored. In this case, transfer occurs somewhere in the overlap between intervals (c) and (d) i.e. at a voltage of 3.807V, which therefore corresponds to a field of 402.5G.

In order to distinguish between the two states during imaging, a Stern-Gerlach field is applied in order to spatially split the two components during time of flight. The Stern-Gerlach field is applied by jumping the quadrupole coil current to 46A over 1-2ms in order to generate a gradient of $\approx 20\text{G}$ during the 14ms time of flight, and results in a larger deflection for the $|2, 2\rangle$ component. Both components are simultaneously imaged by our σ^+ -polarized $|F = 2\rangle \rightarrow |F' = 3\rangle$ light, with the Feshbach field being switched off 5ms prior to the imaging pulse. In the current setup, we have found a control voltage value of 3.807V to correspond to a field of 402.5G, and we use this procedure to periodically ensure that this calibration has not drifted. Below we describe the experiments carried out in order to characterize the resonance, namely location of the resonance centre and the zero-crossing field.

3.11.4 Detecting the resonance

The presence of Feshbach resonances is most commonly detected by monitoring atom losses in the cloud as the scattering length is tuned across the resonance. In the vicinity of a Feshbach resonance, the scattering length rises sharply, as described by equation 2.56, leading to an increase in the rate of inelastic three-body collisions. The three-body coefficient, K_3 , for these collisions, defined by $\dot{n} = -K_3 n^3$, is expected to rise sharply with the s-wave scattering length and for low-energy collisions at large scattering length, has been predicted to scale with its fourth power, $K_3 \propto \hbar a^4/m$ [174]. Experimental results consistent with this prediction have been reported [175]. The divergence of a on resonance therefore causes a correspondingly sharp rise in the inelastic collision rate. These three-body collisions result in the formation of a diatomic molecule, with the binding energy released in the process being removed by the third colliding atom. Since the final energy of this atom usually exceeds the trap depth, this process results in atom loss from the trap. Furthermore, since this three-body recombination takes place preferentially in the denser, cooler region of the cloud, the ejected atom removes an energy below the mean thermal energy and hence causes heating of the sample. To see this more quantitatively, we can consider the mean potential energy associated with a thermal atom at temperature, T , trapped in a harmonic potential and participating in such a three-body process

$$\langle U \rangle = \frac{\int U n^3 dV}{\int n^3 dV} = \frac{1}{2} k_B T \quad (3.11)$$

with $U = m\omega^2 r^2/2$ and $n = n_0 \exp[-m\omega^2 r^2/2k_B T]$. This is less than the $\frac{3}{2}k_B T$ mean potential energy in the gas and hence each atom lost due to three-body recombination releases an energy of $k_B T$ into the system.

Observation of these sharp loss and heating features is therefore a useful signature of the resonance and can be used to locate its centre. We perform this Feshbach spectroscopy on our trapped ^{39}K atoms using the following procedure:

1. The atoms are held in the $|1, 1\rangle$ state in the optical trap at a temperature of around $1.2\mu\text{K}$.
2. The Feshbach field is taken to a value of approximately 403.9G and held at this value for 10ms. This is done in order to try and eliminate the common asymmetry in the loss profile that results from the field having to pass

through the resonance centre on its way to values that lie beyond it, and hence suffering excess losses compared to field values on the same side of the resonance as the initial field value. We therefore choose an initial field value as close as possible to the resonance centre.

3. The field is then swept to a final value in 20ms and held at this value for 100ms. This hold time is chosen so as to allow for a significant maximal drop in atom number at the resonance, while not losing enough atoms so as to blur the resonance peak as a result of reducing the density enough for the losses to ‘saturate’.
4. The cloud is released from the trap and absorption imaged after an 8ms time-of-flight. Upon release, the field value is taken close to the zero-crossing at 350G in order to prevent any additional losses during TOF.
5. The atom number and temperature of the cloud are extracted and averaged over 5 repetitions of the above sequence.

The results of this sequence are shown in figure 3.27. The atom number is seen to drop sharply by a factor of two while the temperature concurrently rises by approximately 25% at a field value very near 402.5G. The agreement of this value with the results reported by other groups [60, 176] give us confidence in our field calibration and experimental procedure. Note that in figure 3.27 we also observe additional losses and heating on the attractive (high-field) side of the resonance centre, compared to those on the repulsive side. This is likely due to the asymmetry in the three-body loss coefficient K_3 on either side of the resonance [176, 177], with the $a < 0$ value of K_3 being around 100 times larger than its $a > 0$ counterpart just 0.3G from the resonance centre¹.

3.11.5 Detecting the zero-crossing

Two procedures have been used by various groups in attempting to detect the location of the zero-crossing for a given resonance.

1. The vanishing of the scattering cross-section causes a drop in the efficiency of evaporative cooling due to the divergence of the rethermalization time (see section 2.4). This can be detected as a peak in the final temperature achieved during the evaporative cooling stage and, in the case of free,

¹ see figure 1c of [176]

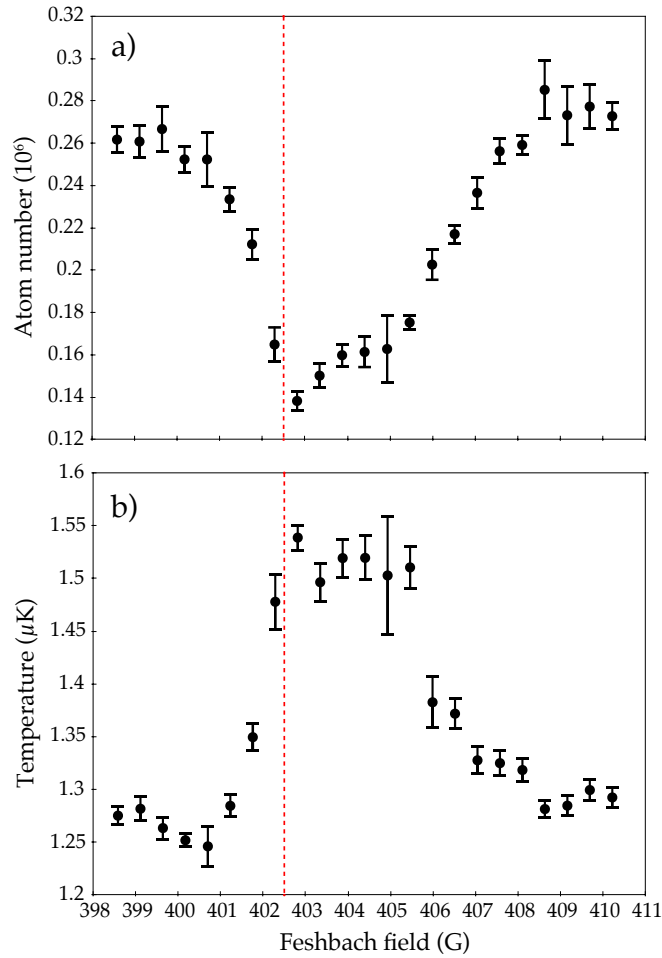


Figure 3.27: Detection of the resonance centre. The location of the resonance manifests itself as a sharp drop in the atom number and a corresponding rise in the temperature due to the sharp rise in the rate of inelastic three-body collisions. The resonance centre was found at 402.5G, in excellent agreement with previous results [60, 176].

unforced evaporation, as a peak in the number of atoms remaining in the trap [178, 179]. Similarly, in heteronuclear systems the zero-crossing of inter-species resonances is found by monitoring the efficiency of sympathetic cooling as reflected in the final temperature and atom number of the target gas, which both take on their peak values at the zero-crossing [61, 180, 181].

2. Alternatively, the zero-crossing can be located by observation of the onset of collapse of the condensate. This manifests itself in an abrupt drop in atom number when the condensate becomes unstable. This instability occurs at a negative value of the scattering length when the atom number increases

sufficiently such that the self-attractive forces due to the negative scattering length outweigh the repulsive force due to the zero-point energy of the atoms in the harmonic trap [68, 69, 182, 171].

We have searched for the zero-crossing using the latter method. A ^{39}K condensate is held in the CDT for three seconds, during the last 100ms of which the Feshbach field is ramped from an initial value of around 390G to a value in the predicted vicinity of the zero-crossing at 350G in 50ms and held at this value for a further 50ms. The cloud is then imaged after a 15ms TOF. Figure 3.28 shows a sequence of images taken as the Feshbach field approaches and then passes the zero-crossing from above. After an initial, coarser, search the range of final values was narrowed and the onset for the fragmentation of the condensate was found to appear at a field of between 350.2G and 349.7G. We therefore place the zero-crossing at a field of $350.0 \pm 0.2\text{G}$, giving a resonance width of $\Delta = 52.5\text{G}$, in very good agreement with theoretical predictions and other experimental results [60, 36].

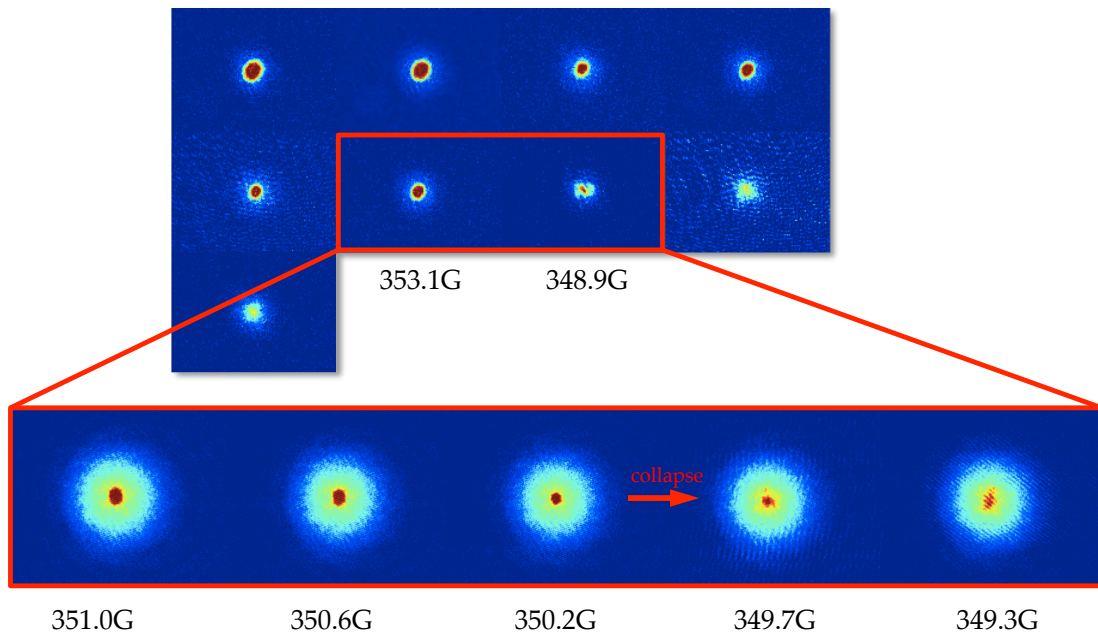


Figure 3.28: BECs during coarse- and fine-tuning of the field near the zero-crossing

A more accurate estimate could perhaps be obtained by utilizing the first of the two techniques mentioned above and measuring the final temperature of the ^{39}K cloud after the direct evaporative cooling stage in the CDT.

3.12 Onset of BEC in ^{39}K

Evaporative cooling in the CDT is used to take the ^{39}K sample across the BEC critical point. Figure 3.29 shows a sequence of images taken at various points during evaporative cooling in the CDT, along with their density profile fits as described in section 3.15 below.

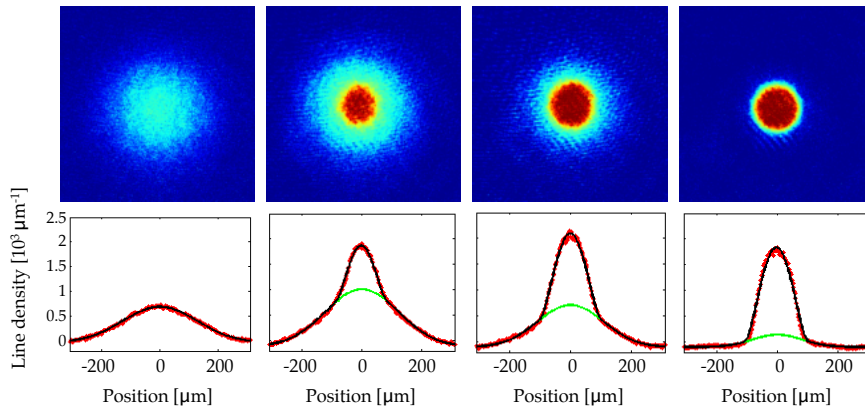


Figure 3.29: Optical evaporation of ^{39}K across T_c . The leftmost image is taken above T_c and in the following images the condensed fractions are 0, $\approx 20\%$, $\approx 40\%$ and $\approx 80\%$, respectively, with the condensate number growing from approximately 1.5×10^5 to 4.2×10^5 as the temperature decreases from 170nK to 50nK. The bottom row shows the theoretical fits to the data as described in section 3.15.

3.13 Sequence summary

Figure 3.30 shows an overview of a typical experimental sequence for producing condensed clouds of ^{39}K in the CDT, including a plot of the evolution of both the ^{87}Rb and ^{39}Rb peak number densities as a function of their temperature throughout the sequence.

3.14 Imaging setup and procedure

This section describes the optical setups we use in order to capture absorption images, both horizontally and vertically in the lab frame, following release of the cloud from the magnetic or optical trapping potential. We also describe our *double-shuttering* imaging procedure and the fitting procedure used to extract physical information from the resulting absorption images.

#	Stage	duration	N_K / N_{Rb}	T
1.	MOT	15s	$2 \times 10^8 / 4 \times 10^9$	1.5mK / 300 μ K
2.	Optical Molasses	6ms	-----	600 μ K / 50 μ K
3.	Optical pumping	200 μ s	-----	-----
4.	Magnetic capture	50ms	$1.3 \times 10^8 / 3.2 \times 10^9$	-----
5.	Transport	2.7s	-----	-----
6.	Transfer to QUIC	6s	$2.5 \times 10^7 / 4 \times 10^8$	200 μ K / 100 μ K
7.	Sympathetic cooling by ^{87}Rb	56s	$1.4 \times 10^7 / 6 \times 10^7$	5 μ K / 4 μ K
8.	Transfer to CDT	2s	$8 \times 10^6 / 3 \times 10^7$	6 μ K / 5 μ K
9.	Removal of ^{87}Rb	2ms	-----	-----
10.	^{39}K state transfer	35ms	-----	-----
11.	Feshbach field ramp-up	5ms	-----	-----
12.	Optical evaporation of ^{39}K	6s	4×10^5 (^{39}K)	$\sim 400\text{nK}$
13.	TOF (+Imaging)	20ms (+180 μ s)	4×10^5 (^{39}K)	$\sim 400\text{nK}$

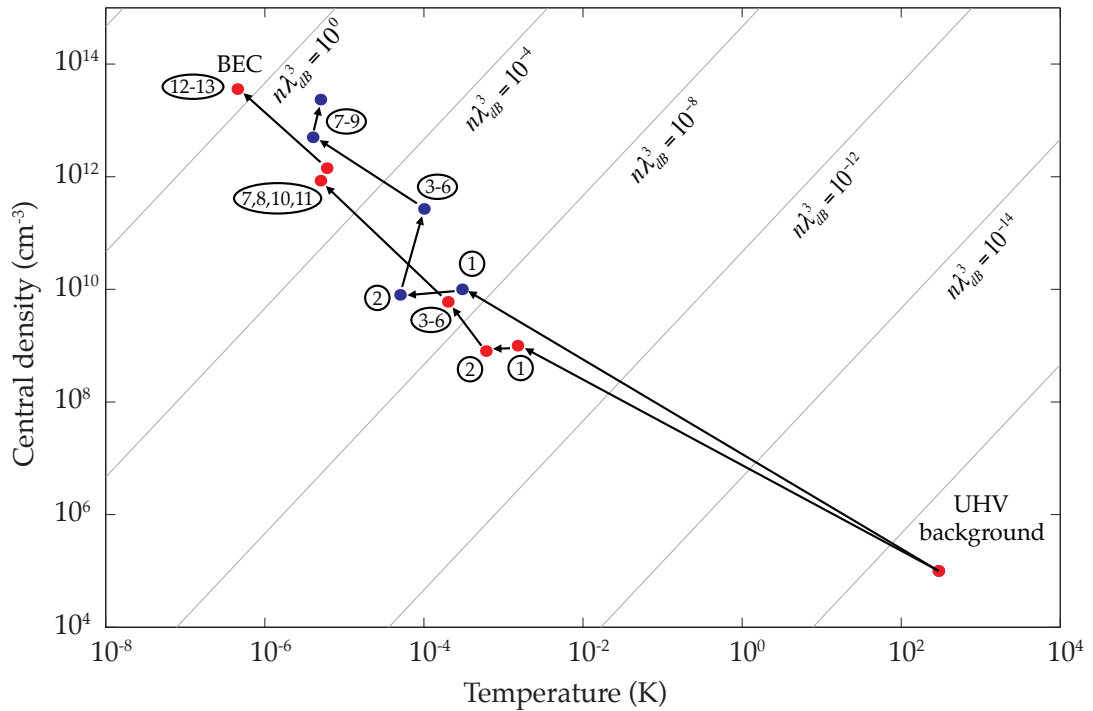


Figure 3.30: Summary of the experimental sequence for cooling ^{39}K to quantum degeneracy. The table shows the duration of each step together with the associated atom numbers and temperatures and the plot shows the evolution of both species' peak number densities against their temperatures. Labels on the plot correspond to rows in the table and lines of constant phase-space density are indicated.

3.14.1 Horizontal imaging system

Our horizontal imaging system is an adaptation of the compound-lens design proposed by Alt [183]. The motivation behind this design is to construct a high-numerical aperture objective using cheap, off-the-shelf optical components by using the aberrations present in each component to cancel each other, as well as the aberrations introduced by the science cell wall, and hence achieve diffraction-limited performance with a working distance large enough so as not to obstruct the paths of the CDT beams. The original constraints presented in [183] were similar to those of our system in the horizontal direction and the only change was the use of a standard meniscus as the first element instead of the custom meniscus used by Alt. The recalculation of the lens spacings and the assembly and testing of the objective were carried out by Alexandre Dureau using the OSLO optimization package, and the detailed results can be found in his project report [184].

In brief, the surface of the first meniscus in the objective is located $\approx 27\text{mm}$ from the science cell wall along the optical axis, and the CCD surface is located $\approx 111\text{mm}$ from the final surface of the focussing achromatic doublet. These spacings represent only initial guesses. The objective is mounted on a translation stage and the distances are optimized empirically so as to focus on the atomic cloud since it may not be situated precisely in the centre of the cell.

Horizontal-imaging magnification

The magnification of the horizontal imaging system is determined by measuring the centre-of-mass (CoM) position of a dropped cloud at various times after its release from the trapping potential, and fitting its trajectory to that expected for free fall under gravity, $h = \frac{1}{2}Mgt^2$. Our knowledge of the camera's pixel size and the fall time allows us to obtain the effective pixel size, i.e. the magnification. For the horizontal objective, we obtain a magnification of $M_{\text{horiz}} = 2.8$

3.14.2 Vertical Imaging system

The vertical imaging system was also designed by Alexandre Dureau and full details are available in his report. The main additional constraint on this system was the need to leave room for the translating quadrupole coils

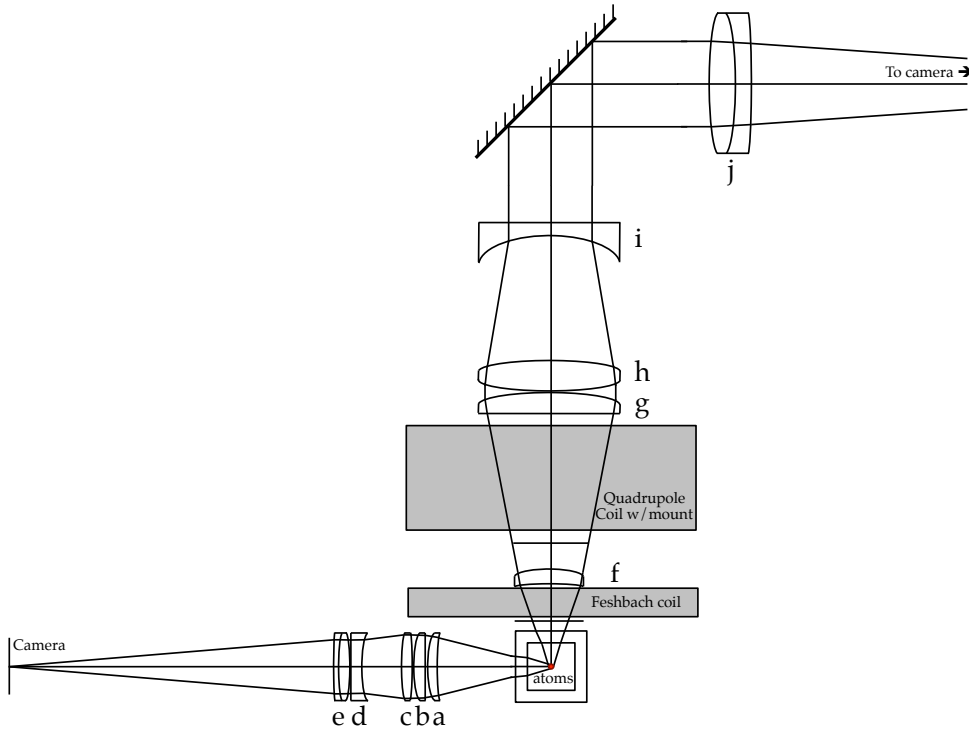


Figure 3.31: Overview of the horizontal and vertical imaging systems around the science cell.

Label	Description	Part number
Horizontal objective		
a	1" meniscus, $f=100\text{mm}$	LE1234-B
a \rightarrow b	2.53mm	
b	1" plano-convex lens, $f=75\text{mm}$	LA1608-B
b \rightarrow c	2.80mm	
c	1" bi-convex lens, $f=100\text{mm}$	LB1676-B
c \rightarrow d	12.64mm	
d	1" plano-concave lens, $f=-75\text{mm}$	LC1582-B
d \rightarrow e	arb.	
e	1" achromatic doublet, $f=100\text{mm}$	AC254-100-B
e \rightarrow CCD	$\approx 110\text{mm}$	

Table 3.5: Descriptions, separations and part numbers for the components of our horizontal imaging system. Labels correspond to those shown in figure 3.31 and unless otherwise stated, part numbers are from Thorlabs. See Alexandre Dareau's project report for further details.

as shown in figure 3.31, with the imaging beam passing through the coil centre. In order to cover as large a solid angle as possible, 2" optics were used for this system, and a custom meniscus was mounted in close proximity to the science cell in order to further increase the effective numerical aperture.

Label	Description	Part number
Vertical objective		
f	25mm Custom meniscus, $R_1 = 26.06\text{mm}$, $R_2 = -78.16\text{mm}$	Lens-Optics GmbH.
f \rightarrow g	$\approx 54\text{mm}$	
g	2" plano-convex lens, $f=150\text{mm}$	LA1417
g \rightarrow h	2.53mm	
h	2" bi-convex lens, $f=100\text{mm}$	LB1630
h \rightarrow i	2.80mm	
i	2" plano-concave lens, $f=-75\text{mm}$	LC1315
i \rightarrow j	$\approx 150\text{mm}$	
j	2" achromatic doublet, $f=200\text{mm}$	AC508-200-B
j \rightarrow CCD	$\approx 200\text{mm}$	

Table 3.6: Descriptions, separations and part numbers for the components of our vertical imaging system. Labels correspond to those shown in figure 3.31 and unless otherwise stated, part numbers are from Thorlabs. See Alexandre Dureau's project report for further details.

Vertical magnification

We obtain the magnification of the vertical imaging system by simultaneous vertical and horizontal imaging of a cloud released from the CDT after roughly 20ms time-of-flight. Since in this time, any anisotropy due to the trapping potential will have decayed away we can assume that the vertical and horizontal sizes of the cloud are equal. Our knowledge of the horizontal-imaging magnification (see above) and the pixel size therefore allow us to infer the vertical-imaging magnification. We obtain a magnification in this direction of $M_{\text{vert}} = 5.2$ when using a doublet of focal length 200mm as the final element.

3.14.3 Cameras and double shuttering

The camera model currently used in both the horizontal and vertical imaging systems¹ utilizes a so-called ‘interline’ CCD. The advantage of this type of sensor from our perspective is that it enables two separate images to be captured in very rapid succession, with inter-frame times as low as $5\mu\text{s}$. This *double-shuttering* feature, often used in particle image velocimetry (PIV) applications, allows us to effectively remove the effects of beam inhomogeneity from our final OD profile since any of the inevitable inhomogeneities in the imaging laser beam will not have time to fluctuate between the images taken with and without the atomic cloud - the I and I_0 of equation 2.86, respectively - and will hence be efficiently divided out when extracting the optical density. The primary disadvantage of this type of sensor is its relatively modest quantum efficiency at the imaging wavelengths, approximately 25%, compared to more sophisticated back-illuminated and electron-multiplying (EMCCD) cameras, in which efficiencies of $> 95\%$ are achievable. The camera is controlled via a custom graphical user interface (GUI) running within MATLAB, that automatically generates the final OD image(s) for each experimental run and also allows browsing and basic analysis of images in real time.

Double-shuttering procedure

Since double-shuttering relies on the use of a masked region of the CCD for temporary storage of the first exposure while the second exposure is recorded, the duration of the second exposure must be at least as long as the time required for the camera to read out the first exposure from behind the mask ($\approx 80\text{ms}$). Therefore, since a double-exposure pair with very different exposure times is used to capture I and I_0 , an identically exposed pair must be used to capture the dark background images for each of the two (see equation 2.86). Therefore two double-exposures are used to record four images, with the third serving as the dark image for the first and the fourth serving as the dark image for the second.

3.14.4 Imaging procedure

Our ^{39}K imaging sequence proceeds as follows:

¹ PCO imaging, pixelfly QE, double shutter, pixel size: $6.45\mu\text{m}$, sensor: Sony ICX285AL

1. The Feshbach field is switched off 5ms prior to the end of time-of-flight.
2. Since our ^{39}K atoms are held in the $|1, 1\rangle$ state, while we wish to image on the cycling $|F = 2\rangle \rightarrow |F' = 3\rangle$ transition, immediately prior to imaging all the atoms are pumped back into the $|2, 2\rangle$ state by a $100\mu\text{s}$ pulse of repump light.
3. The atoms are then illuminated with an $80\mu\text{s}$ pulse of circularly polarized, low-intensity light ($I/I_S \approx 0.2$), resonant with the $|F = 2\rangle \rightarrow |F' = 3\rangle$ transition, and an image of the intensity in the plane of the atoms is recorded by the camera¹. During the imaging pulse, a quantization axis is defined by applying a guide field of several Gauss along the propagation direction of the imaging beam using the transverse compensation coils (see table 3.4).
4. A second imaging pulse is applied $60\mu\text{s}$ after the end of the first in order to image the unattenuated beam profile, $I_0(x, y)$. During this $60\mu\text{s}$ interval, the vertical compensation field is rapidly pulsed to a few (~ 10) Gauss in order to detune the atoms from the imaging light and hence make them invisible to the imaging beam.
5. Approximately 600ms later, a pair of background dark images is captured, with the CDT being briefly pulsed beforehand at the correct moment in order to replicate more precisely the lighting conditions under which the first two images were taken.

3.14.5 Double-species imaging

We have also successfully used double-shuttering to obtain simultaneous images of the ^{87}Rb and ^{39}K clouds. Three double-exposures are taken, with the first, third and fifth images constituting I , I_0 and I_{dark} for the first species, respectively, and the second, fourth and sixth providing the same for the second species.

3.14.6 Cross section calibration

The inferred atom number depends on the value used for the absorption cross-section, σ , of equation 2.54. Assuming the ideal theoretical resonant cross-section for a two-level system with transition wavelength λ , $\sigma = \frac{3\lambda}{2\pi}$, typically underestimates the atom number. This is mainly due to imperfections in the polarization

¹ typical camera exposure time: $110\mu\text{s}$

of the imaging beam and is identified in our experiments by comparing the critical atom number, N_c , in a weakly-interacting gas with the theoretical prediction given by Hartree-Fock mean-field theory (see chapter 4). In calculating the theoretical prediction we also take into account the effects of the estimated trap anharmonicity and finite system size [46], which are less than 3% and 1%, respectively. For ^{87}Rb we observed a reduction in the cross-section by a factor of 1.5 ± 0.3 . For ^{39}K , the experimental value of N_c was initially extracted from a series taken at $135a_0$, giving a cross-section reduction factor of 1.9 ± 0.3 . More careful measurements on very weakly-interacting clouds as part of our investigation of the interaction-shift of the critical point yielded a factor of 1.5.

3.15 Image analysis

As discussed above, at the end of a typical experimental run four images are captured using two double-shutter exposures, and the optical density profile $\text{OD}(x, y)$ is generated using equation 2.86. In order to extract quantitative information from these optical density profiles, we fit them to theoretical predictions of the density profile after the appropriate time-of-flight, in which the temperature, the thermal atom number and the condensed atom number are directly related to the fitting parameters, as described below. For purely thermal, uncondensed clouds far from the critical point, the absorption image is fitted with a Gaussian profile of the form:

$$\text{OD}_{\text{therm}}(x, y) = \text{OD}_{\text{therm}}(0) e^{-\frac{(x-x_0)^2}{2\sigma_x^2} - \frac{(y-y_0)^2}{2\sigma_y^2}} \quad (T \gg T_c) \quad (3.12)$$

where x_0 and y_0 are the coordinates of the distribution peak, σ_x and σ_y are the widths and $\text{OD}(0)$ is the peak optical density. For thermal clouds near or below the critical temperature, the fitting function used is the singly-integrated version of equation 2.72 for the Bose-enhanced distribution:

$$\text{OD}_{\text{therm}}(x, y) = \frac{\text{OD}_{\text{therm}}(0)}{g_2(1)} g_2\left(e^{-\frac{(x-x_0)^2}{2\sigma_x^2} - \frac{(y-y_0)^2}{2\sigma_y^2}}\right) \quad (T \leq T_c) \quad (3.13)$$

At high temperatures, as well as far from the cloud centre, the dilogarithmic profile of equation 3.13 approaches the Gaussian distribution of equation 3.12. Fully-condensed clouds are likewise fitted with the singly-integrated version of

equation 2.80

$$\text{OD}_{\text{cond}}(x, y) = \text{OD}_{\text{cond}}(0) \max \left(1 - \frac{(x - x_0)^2}{R_x^2} - \frac{(y - y_0)^2}{R_y^2}, 0 \right)^{3/2} \quad (3.14)$$

For partially condensed clouds, a bimodal fit is used to differentiate between atoms belonging to the condensed and thermal components and the fitting function is simply the sum of equations 3.13 and 3.14. In addition, the fitting routine also allows for gradients in the x and y directions, as well as a global offset. The most general fitting function therefore has the form

$$\begin{aligned} \text{OD} = & \underbrace{A_1 \cdot g_2 \left(e^{-\frac{(x-A_4)^2}{2A_2^2} - \frac{(y-A_5)^2}{2A_3^2}} \right)}_{\text{thermal component}} + \underbrace{A_6 \cdot \max \left(1 - \frac{(x-A_9)^2}{A_7^2} - \frac{(y-A_{10})^2}{A_8^2}, 0 \right)^{3/2}}_{\text{BEC component}} \\ & + \underbrace{A_{11} \cdot x + A_{12} \cdot y}_{\text{gradients}} + \underbrace{A_{13}}_{\text{global offset}} \end{aligned} \quad (3.15)$$

3.15.1 Triple-pass fitting procedure

Fitting all thirteen of these parameters simultaneously is clearly computationally expensive and inevitably returns unreliable results. Therefore we make use of an automated three-pass fitting procedure, designed streamline the process of extracting all the required parameters while providing much more reliable and accurate values [185, 186]. Our ‘triple-pass’ fitting sequence is as follows:

1. **The first pass** performs a bimodal fit with a global offset but no gradients i.e. $A_1 - A_{10}$, A_{13} of equation 3.15. The (relatively crude) results of this fit will serve as initial guesses in subsequent fits.
2. **The second pass** performs a g_2 -only fit, including a global offset and gradients, in order to find the thermal component i.e. $A_1 \rightarrow A_5$, $A_{11} \rightarrow A_{13}$ of equation 3.15. In this fit, a region of radius $\alpha R_{x,y}^{TF(1)}$, where α is a user-chosen factor (typically 1.1) and $R_{x,y}^{TF(1)}$ is the BEC radius found in the first pass, centred on the BEC-centre found in the first pass, is excluded from the data prior to fitting. This is done in order to prevent the BEC peak from artificially reducing the width found by the thermal-only fit. The results of this fit are used to determine the thermal atom number.

3. **The third pass** performs a TF-only fit i.e. $A_1 - A_5$ of equation 3.15. This is done by performing a full bimodal fit, including gradients and global offset, but holding all the g_2 , gradient and offset parameters at the values obtained for them in the second pass and allowing only the five TF parameters to vary. The results of this fit are used to determine the condensate number.
4. Finally, a number of ‘excluded-region’ g_2 -only fits are performed, excluding from the data regions with user-selected radii, typically chosen to be multiples (e.g. 0.8, 0.9, 1, 1.1 and 1) of the thermal radius, centred on the BEC centre found in the third pass. The results of these fits are used to determine the temperature of the cloud and its error.

3.15.2 Number and temperature extraction

The **temperature** along the i -th direction ($i = x/y$) is extracted from the measured width of the cloud in pixels, σ_i , after t -ms time-of-flight, according to [145]

$$T_i = \frac{m(\sigma_i \cdot a_{\text{pix}})^2}{k_B} \cdot \frac{\omega_i^2}{10^6 + \omega_i^2 t^2} \approx \frac{m(\sigma_i \cdot a_{\text{pix}})^2}{k_B t^2} \quad (3.16)$$

where a_{pix} is the effective pixel size found from the imaging magnification, ω_i is the angular trapping frequency in the i direction, m is the atom mass, k_B is the Boltzmann constant and the temperature is given in μK . The factor of 10^6 in the denominator is introduced since t is taken in ms. The second approximation is valid for long times-of-flight, when t is much larger than the in-trap oscillation period.

The **thermal atom number**, in millions, is given by

$$N_{\text{therm}} = 1.202 \left(\frac{2\pi}{\sigma} \right) \cdot A_1 \cdot \sigma_x \cdot \sigma_y \cdot a_{\text{pix}}^2 \times 10^{-18} \quad (3.17)$$

where σ is the absorption cross-section and A_1 is the amplitude (i.e. A_1 of equation 3.15). The **condensed atom number**, also in millions, is obtained using

$$N_{\text{cond}} = \frac{2\pi}{5\sigma} \cdot A_6 \cdot R_x \cdot R_y \cdot a_{\text{pix}}^2 \times 10^{-18} \quad (3.18)$$

where A_6 is the amplitude (i.e. A_6 of equation 3.15) and $R_{x/y}$ are the Thomas-Fermi widths in pixels (i.e. $A_{7/8}$ of equation 3.15).

3.16 Timing control

3.16.1 Background

In order to control the power supplies, AOMs, shutters, function generators, translation stage and other components of our experiment, analog and digital control voltages as well as serial communications are required. Furthermore, experiments of the type reported in this thesis, with certain stages requiring high temporal resolution, on the order of tens of μs and with overall durations on the order of a minute, would not be feasible without the sophisticated electronic devices that have become commercially available in the last few decades. This section briefly reviews the hardware and software components of our experimental control system.

3.16.2 I/O devices

Digital and analog signals for our experiments are generated by a series of PXI-based input/output (I/O) devices. These cards are mounted in a PXI chassis¹ communicating in real time with a PC² running the control software. We currently have 64 digital channels³ and 16 analog channels⁴ available, with extra channels easily added by purchasing additional output cards. In addition to the digital and analog channels, communication with instruments via RS-232 and GPIB is enabled via a 4-channel RS-232 PCI card⁵ installed in the control PC and a USB-based GPIB controller⁶. RS-232 and GPIB communications are used, for example, in remotely configuring the outputs of the various function generators, configuring and controlling the translation stage and logging the measurements of the thermocouple monitor used during the chamber bakeout.

We note here that compared to the so-called *hardware timing* of the digital and analog cards, which use a timing signal independent to that generated by the PC operating system, GPIB and RS232 are *software timed* protocols whose output timing is determined by the operating system and hence is subject to a much larger jitter. There is additional uncertainty on these timings since the receiving

¹ National Instruments, PXIe-1062Q

² 2.40GHz, Intel Core™2 Duo processor, Windows XP, 4Gb RAM

³ National Instruments, PXI-6533, PXI-6534

⁴ National Instruments, 2 × PXI-6713

⁵ Brainboxes Intashield, IS-400

⁶ National Instruments, GPIB-USB-HS

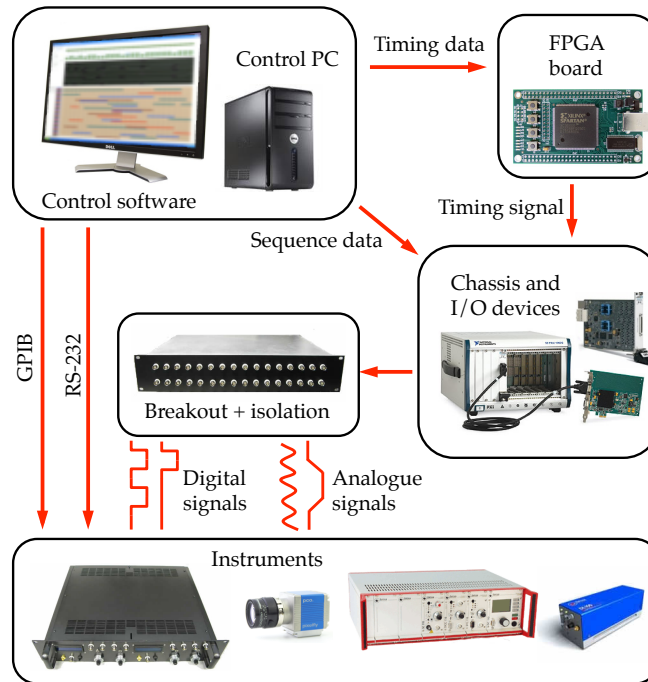


Figure 3.33: Schematic of the control hierarchy in the experiment. The Word Generator software communicates with the NI hardware to output digital and analog signals. These are interfaced to the rest of the experiment via optical and capacitive isolation circuits in order to avoid damage to the NI hardware from voltage spike in the apparatus.

devices also require a few ms in order to receive and output the command. We have found that the typical GPIB command strings used in our experiment, for example to change the frequency and time constant of an evaporation sweep, should not be instructed to be sent to the device less than roughly 100ms apart in order to ensure a reliable response.

3.16.3 Word Generator

In addition to allowing the user to easily explore different experimental procedures, well-designed control software enables swift debugging and optimization of experimental sequences and control over a wide range of devices. In our experiments we have made use of the Cicero Word Generator control package¹, authored by Aviv Keshet at the MIT Center for Ultracold Atoms² and generously made

¹ <http://web.mit.edu/~akeshet/www/Cicero/>

² <http://cuaweb.mit.edu/>

available under the terms of the GNU General Public License¹. This software² allows users to visually configure complex sequences and includes many time- and labour-saving features. In addition the software includes a *variable timebase* feature which allows for the creation of sequences of much greater duration at high temporal resolution by freeing the user from the constraint of a fixed timing resolution and instead calculating a custom timing signal that only updates output values when the experimental sequence requires their value to be changed. This feature can also be used in conjunction with an additional low-cost FPGA board³ to generate high-temporal-resolution sequences of effectively *infinite* duration, and we make use of this functionality in our sequence design. Figure 3.33 shows the path of the control signal from the control software, via the PC and PXI chassis to the breakout panels and finally the target instrument.

3.16.4 Digital and analog isolation

In order to protect the control hardware from voltage spikes that can occur within the various instruments, as well as attempting to reduce the presence of ground loops, all digital signals are isolated from the output cards by means of an optocoupler⁴ circuit prior to breakout of the signals to BNC connectors. Analog signals can also be isolated by means of an isolation amplifier⁵ circuit after their breakout into BNC connectors⁶. The two types of isolation boards are shown in figure 3.34, together with their respective single-channel circuit diagrams.

¹ <http://www.gnu.org/licenses/>

² Can be downloaded directly at: <http://sourceforge.net/projects/cicerowordgenerator/files/>

³ Opal Kelly Inc., XEM3001

⁴ Fairchild Semiconductor, 6N138

⁵ Burr-Brown, ISO124P

⁶ Breakout panel: National Instruments, BNC-2110

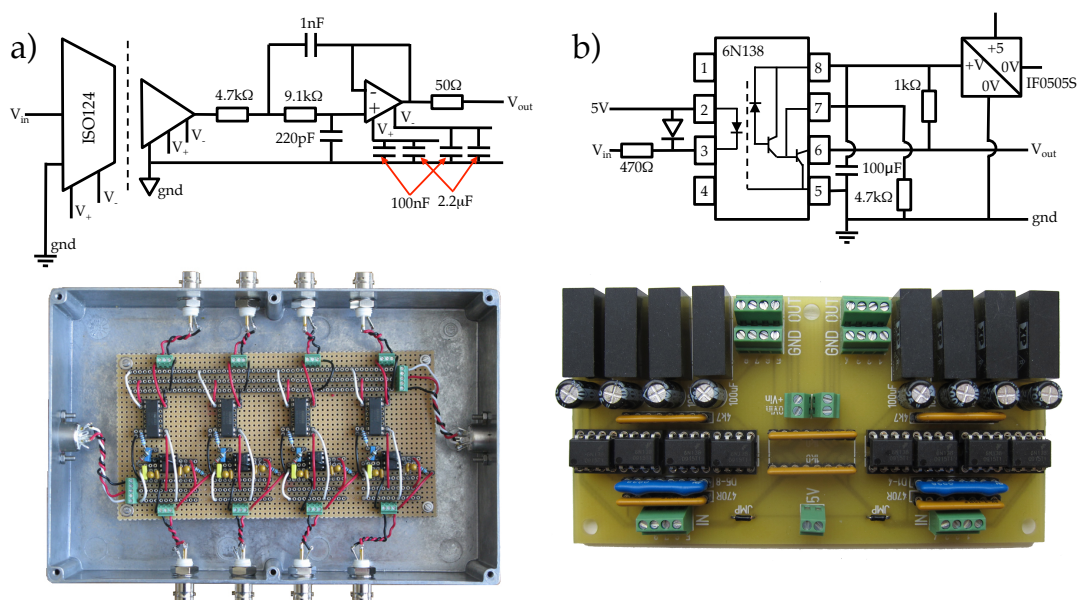


Figure 3.34: (a) Four-channel analog isolation module and (b) eight-channel optocoupler board for digital isolation (DC-DC converter). The optocoupler boards were constructed and tested by Alex Gaunt.

4

The role of saturation in Bose-Einstein condensation

“Proverbs for Paranoids:

1. You may never get to touch the Master, but you can tickle his creatures.”

Thomas Pynchon, *Gravity’s Rainbow*

Abstract

In this chapter, we describe the first experiments carried out following our condensation of ^{39}K . By harnessing our ability to tune the interaction strength, we have been able to test the validity of Einstein’s textbook picture of BEC as arising from saturation of the excited states of the system, as introduced in chapter 2. We observe strong deviation from the saturation picture. In the small-condensate limit, our results agree with a mean-field description of the interactions, while for larger condensates these theories fail to capture the observed behaviour. However, extrapolation of our measurements to the non-interacting limit allows us to recover Einstein’s picture in a non-interacting gas.

4.1 Introduction and motivation

Chapter 2 introduced the predictions for the onset of condensation in a non-interacting Bose gas, but also pointed out that interactions are expected to modify these predictions. This chapter presents the results of our investigations aimed at addressing the question of whether excited-state saturation is indeed the driving mechanism behind Bose-Einstein condensation, as originally envisaged by Einstein [187], and our attempts at elucidating the role of interactions in the BEC phase transition.

We recall that in the textbook theory of the non-interacting Bose gas, purely statistical arguments set an upper bound $N_c^{(\text{id})}$ on the number of atoms N_T occupying the excited states of the system (see chapter 2, [187], [188],[123] and [144]). In the case of the ideal, harmonically-confined Bose gas, the prediction for the critical value of N_T at which this saturation occurs is given by equation 2.70 [189].

$$N_T \leq N_c^{(\text{id})} = \zeta(3) \left(\frac{k_B T}{\hbar \bar{\omega}} \right)^3 \quad (4.1)$$

where T is the temperature, $\bar{\omega}$ is the geometric mean of the trapping frequencies and ζ is the Riemann function, with $\zeta(3) \approx 1.202$. The condensation observed in weakly-interacting harmonically-trapped atomic Bose gases [23, 24, 182] is generally believed to constitute a faithful representation of this statistical phase transition. Figure 4.1 illustrates the saturation prediction and shows a plot of the number of thermal (red line) and condensed (blue line) atoms as a function of the total atom number. We emphasize that the term ‘saturation’ in this context refers to the halt in the growth of the thermal component, predicted in the ideal-gas case to coincide with the onset of condensation.

The idea of systematically scrutinizing the role of this saturation mechanism in the BEC transition followed on from an observation made in the course of experiments on the critical point of a two-dimensional Bose gas in the ENS group (see footnote 31 of [190]). In these experiments, the linear slope of the curve dN_0/dN_{tot} above (the blue line of figure 4.1) above the critical point was found to take the value 0.7, clearly deviating from the unity slope expected for a saturated gas.

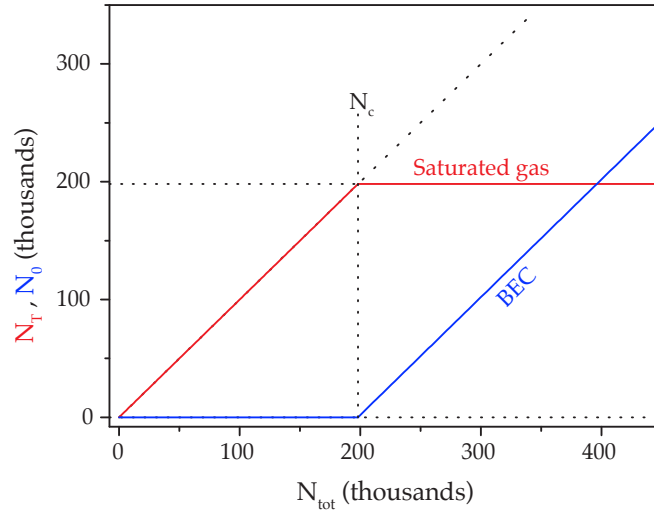


Figure 4.1: Saturated gas. The red and blue lines show the predicted thermal atom number, N_T , and condensed atom number N_0 , respectively, as a function of the total atom number $N_{\text{tot}} = N_0 + N_T$ for a saturated gas at fixed temperature. The critical point, N_c , is indicated by the vertical and horizontal dashed lines.

Chapter outline

This chapter proceeds as follows:

- We first describe the experimental procedure we employ in order to probe the saturation, or lack thereof, of our trapped gas (sections 4.2 and 4.3).
- We present the effects of varying both the interaction strength and the temperature on the degree of deviation from the behaviour of a saturated gas (section 4.4).
- In order to disentangle the roles of interaction strength and temperature in Bose-Einstein condensation, we present two mean-field theories - the Popov and self-consistent Hartree-Fock approximations - and compare our non-saturation measurements to their predictions (section 4.5).
- Our results demonstrate that above a certain condensate size, these mean-field theories can no longer reproduce the experimental observations and we adopt a more heuristic approach in order to quantify the lack of saturation in this regime (section 4.6).
- We use the results obtained using this approach to extrapolate to the limit of a non-interacting gas and show that in this limit the saturation picture

originally described by Einstein is recovered within our experimental errors (section 4.6.1).

- We then summarize and discuss our results in the context of previously-performed related experiments and the predictions of beyond-mean-field theories (section 4.7).

4.2 Experimental procedure for investigating saturation

In order to investigate the condensation process, we perform conceptually simple experiments in which the temperature of the gas is kept constant while the atom number is varied. We choose to vary the atom number by allowing the trapped sample to gradually decay as a result of three-body recombination, scattering of photons from the trapping laser beams and collisions with background atoms in the vacuum chamber. Temperature variations are kept to a minimum by stabilizing the power in the trapping lasers in order to fix the depth of the optical potential.

The experiment begins with a partially condensed gas of ^{39}K atoms in the $|F, m_F\rangle = |1, 1\rangle$ state, prepared as described in chapter 3, at a scattering length of $a = 135a_0$. Following preparation of the sample, the optical trap depth is raised slightly by ramping up the power in the trapping beams over 500ms in order to prevent further evaporation and maintain a steady temperature for the remainder of the experiment. The mean trapping frequencies for data taken at different temperatures varies between $\bar{\omega} = 60 - 80\text{Hz}$. Once the final CDT power is reached, the Feshbach field is ramped to its final value and the cloud is held for up to several tens of seconds while the atom number decays.

Figure 4.2 shows the relevant part of the experimental sequence. The orange and green lines show the value of the CDT power and Feshbach field, respectively, as a function of time. We perform measurements over a range of interaction strengths and at various temperatures. The temperature of a series is set by the final depth of the optical trap and the scattering length is set by the final value of the Feshbach field. We vary the scattering length over roughly an order of magnitude, $a = 40a_0 - 356a_0$, and the temperature over the range $T = 115 - 284\text{nK}$ for the different series. The dashed lines in figure 4.2 indicate the range of values taken on by the Feshbach field and CDT power for these measurements.

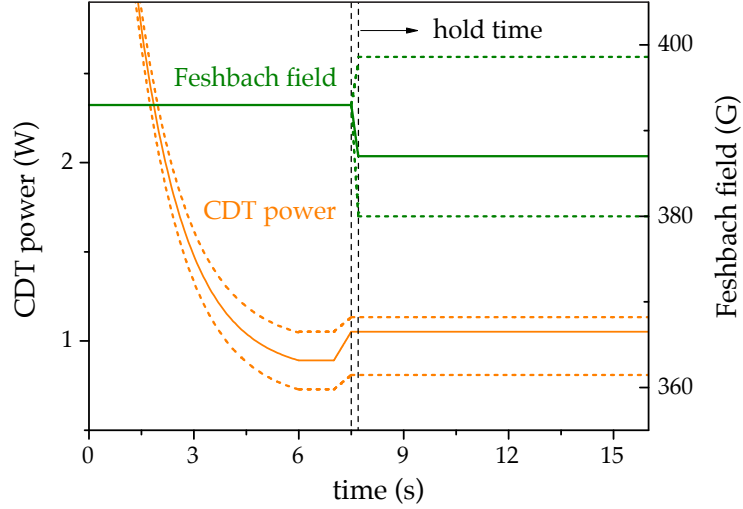


Figure 4.2: Experimental protocol. Orange and green lines show the value of the CDT power and the Feshbach field respectively, as a function of time. The atoms are cooled by an exponential ramp-down of the trap depth, with their final temperature being set by the final trap depth and the scattering length being held constant at $a = 135a_0$ during the ramp-down. The CDT power is then raised slightly in order to maintain a steady temperature during the ensuing hold time and once the final CDT power is reached the Feshbach field is ramped to its final value. Dashed lines delimit the ranges used for the two parameters in the different experimental series.

While the total atom number decays due to inelastic and background collisions, elastic collisions among the trapped atoms ensure equilibrium redistribution of particles between the condensate and the thermal gas. Since the density-dependent three-body recombination is expected to take place preferentially in the cooler, denser region of the trap, heating of the sample might be expected. Heating can also arise from light scattering in the optical trap. However any such heating is at least partially compensated by residual evaporation taking place in the finite-depth trap. For all the data presented in this chapter, the thermalization rate is much higher than the atom-loss rate and hence the details of the loss mechanism do not affect the quasi-static thermodynamic properties of the gas.

Ensuring thermal equilibrium

In general, a system with continuous dissipation can never be at true thermodynamic equilibrium. The proximity to equilibrium for atomic gases depends on the dimensionless parameter, $\gamma_{\text{el}}\tau$, measuring the relative rates of elastic and inelastic

processes. Here, γ_{el} is the elastic collision rate and τ is the timescale characterizing losses arising from inelastic processes, often taken to be the $1/e$ -lifetime of the cloud. Equilibration is usually taken to require 3 elastic collisions per particle [191] implying $\gamma_{\text{el}}\tau \gg 1$. Following [192], the mean elastic collision rate for each atom (γ_{el}) is given by

$$\gamma_{\text{el}} = n(0)v_{\text{th}}\frac{\sigma_0}{2} \quad (4.2)$$

with the central density, $n(0)$, the thermal velocity, v_{th} and the scattering cross-section, σ_0 , given by¹

$$n(0) = N\bar{\omega}^3 \left(\frac{m}{2\pi k_{\text{B}}T} \right)^{3/2} \quad v_{\text{th}} = \sqrt{\frac{8k_{\text{B}}T}{\pi m}} \quad \text{and} \quad \sigma_0 = 8\pi a^2 \quad (4.3)$$

For example, a cloud of 4×10^5 ^{39}K atoms at $T = 200\text{nK}$ and a scattering length of $a = 135a_0$ in an $\bar{\omega} = 80\text{Hz}$ trap has a mean elastic scattering time of $1/\gamma_{\text{el}} \approx 13\text{ms}$.

A basic condition for establishing global equilibrium in our system is that the characteristic inelastic-loss time, τ , should be larger than the period of the trapping potential, i.e. $\tau > 1/\bar{\omega}$. The period of our optical trap in these experiments varies between 2 – 2.7ms and we ensure that this global equilibrium criterion is fulfilled for all the data reported below. Occasionally, data series will fulfil the latter criterion without satisfying the former. For low scattering lengths this occurs due to the drop in the elastic collision rate and for high scattering lengths due to the drop in the inelastic-loss time. For this reason we excluded from our analysis series taken at scattering lengths and temperatures in which unreliable distortions of the data, such as large temperature variations, were ascribed to the onset of non-equilibrium effects. For example, for data series taken at $T \approx 180\text{nK}$, all series below roughly $a = 60a_0$ were excluded from the analysis. Chapter 5 contains a more detailed discussion of these equilibrium criteria in the context of our measurements of the critical point of our trapped gas, where the precision with which we want to measure the critical number N_c prescribes the value of $\gamma_{\text{el}}\tau$ for which our sample is effectively at equilibrium.

Extracting numbers and temperature

For each hold time, we extract the condensate number N_0 and the thermal number N_{T} from a triple-pass bimodal fit, as described in section 3.15, after 18ms of free

¹ Similar values of $n(0)$ (smaller than 10% difference) are obtained for our experimental parameters when using the ‘Bose-enhanced’ expression, $n(0) = \zeta(3/2)/\lambda_{\text{dB}}^3$.

time-of-flight expansion from the optical trap. Figure 4.3 shows the total number, N_{tot} , and temperature, T , versus hold time for an experimental series taken at a scattering length of $a = 135a_0$ and a temperature of 177nK. The temperature for $N_{\text{tot}} > N_c$ shows no drift and has a standard deviation of 3nK. We assign a nominal temperature, T^* , to the entire series. T^* is taken to be the experimentally measured temperature in the $N_0 \rightarrow 0$ limit, i.e. coinciding with the first non-zero condensate number.

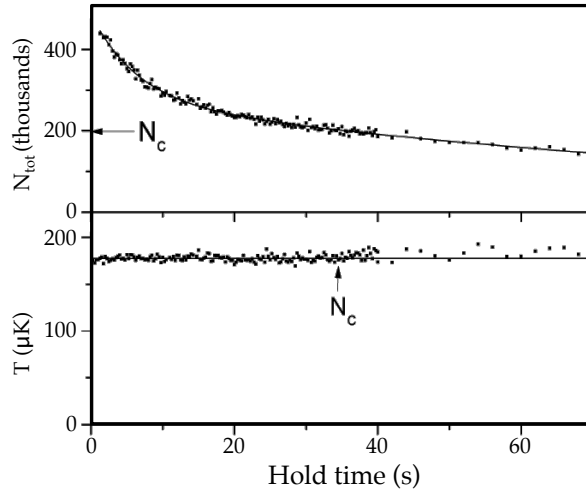


Figure 4.3: Total atom number and temperature against hold time for an experimental sequence taken with $a = 135a_0$ and $T = 177\text{nK}$. The temperature shows no drift for $N_{\text{tot}} > N_c$ and has a standard deviation of 3nK. The atom number is fitted with a double-exponential to guide the eye.

It is worth pointing out that harmonically trapped gases are well-suited for performing such experiments, which require reliable and high-precision distinction between the condensed and non-condensed components. This is due to the fact that, contrary to uniformly confined Bose-condensed systems such as liquid helium, condensation in harmonic traps manifests itself in coordinate space in addition to momentum space, causing the condensate to appear as a distinct peak in the atomic density distributions recorded after time-of-flight in experiments. This simplifies the extraction of occupation numbers from such distributions (see e.g. [46, 123]).

4.3 Observation of non-saturation

Figure 4.4 is a plot of the thermal and condensate numbers against the total atom number for the experimental series shown in figure 4.3. The total atom number

is obtained by a direct summation over the density distribution rather than being extracted from a fit to the data, and the relation $N_{\text{tot}} = N_0 + N_T$ is found to be satisfied for all data points to within 0.5%. The data has been overlain on the ideal-gas saturation predictions of figure 4.1.

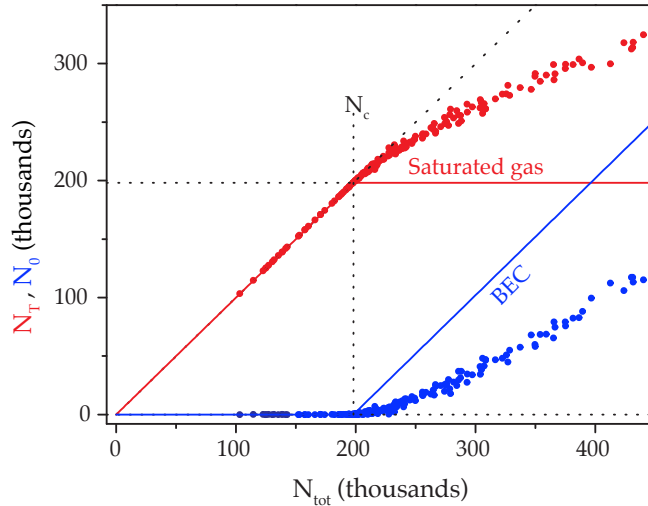


Figure 4.4: Non-saturation in a weakly-interacting Bose gas. The thermal (red) and condensed (blue) atom numbers are plotted against the total atom number for the data series of figure 4.3 ($a = 135a_0$, $T = 177\text{nK}$). Strong deviation from the ideal-gas saturation prediction is observed, with approximately half of the atoms added above the critical number being accommodated in the condensate.

The deviation of the experimental data from the ideal-gas prediction is striking. In this example, as the total number is increased from the observed critical value, $N_c \approx 200,000$, to 450,000, only half of the additional atoms accumulate in the condensate.

4.4 Varying interaction strength and temperature

As mentioned above, we repeat this procedure for a range of scattering lengths and temperatures, ensuring that for the chosen values rethermalization is rapid enough compared to the trap loss rate to maintain thermodynamic equilibrium. Figure 4.5 shows the results of 18 such experimental series, focussing on the region $N_{\text{tot}} > N_c$ in which the condensate is present, and plotting N_0 against $N_{\text{tot}} - N_c$. The solid line shows the prediction for a fully-saturated thermal component:

$N_0 = N_{\text{tot}} - N_c$. The deviation of the data from this prediction is clearly seen in all the series and grows with both a and T .

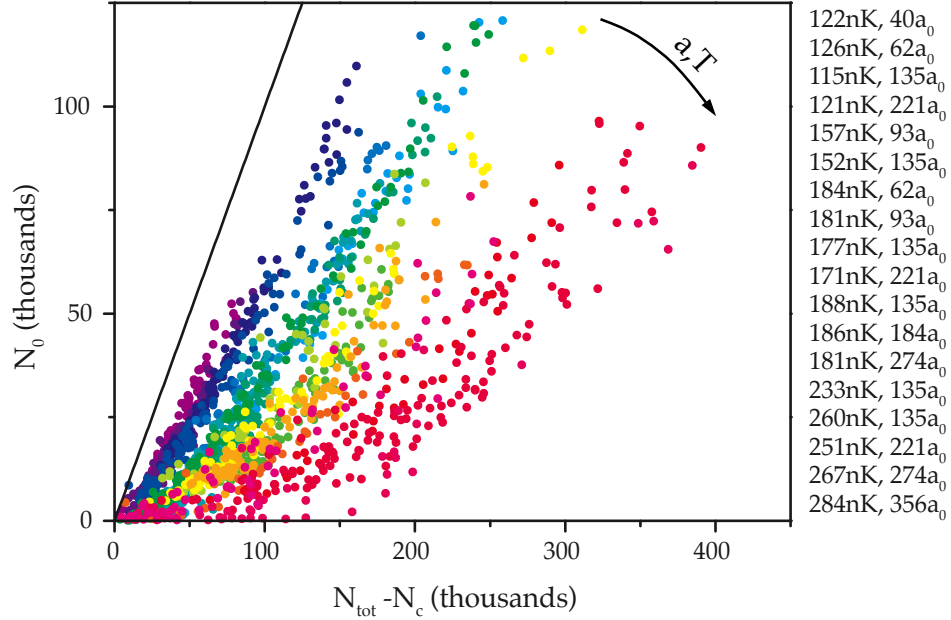


Figure 4.5: Deviation from the saturation prediction for a range of scattering lengths and temperatures. Shown is N_0 vs. $N_{\text{tot}} - N_c$ for 18 experimental series, with the values of the scattering length ($a = 40 - 356a_0$) and the temperature ($T = 115 - 284\text{nK}$) encoded in the colour of the data points (see legend). The solid black line is the saturated-gas prediction: $N_0 = N_{\text{tot}} - N_c$.

4.5 Mean-field theories of interacting gases

In this section, we briefly review the two schemes most commonly used for taking into account inter-atomic interactions - the Popov and self-consistent Hartree-Fock approximations. These are both mean-field theories which avoid the difficulty of solving the full many-body Schrödinger equation for an interacting system by reducing the many-body problem to a one-body problem via the introduction of an appropriate *mean field* potential generated by all the other particles. In general, the effects of interactions are only expected to become sizeable in the presence of a condensate, since only then does the peak density become sufficiently high for the interactions to significantly modify the system's properties.

We begin by tracing the derivation of the Hartree-Fock-Bogoliubov (HFB) mean field equations. The main approximation used in the derivation of these equations

(beyond the assumption of a contact interaction between the atoms and use of the Bogoliubov approximation further along) is the introduction of mean fields to replace what would otherwise be products of pairs of quantum field operators in the Hamiltonian. In this way, terms cubic and quartic in the field operators are reduced to linear and quadratic terms. In addition to simplifying the resulting equations for the condensate wavefunction and the excitation spectrum of the system, this scheme forms a starting point for the Popov and self-consistent Hartree-Fock approximations. The outlined derivation below roughly follows that described in several sources (for example [193], [194], [195], [196], [144] and [123]). Its main purpose is to introduce the mean-field description as well as to highlight the difference between the Popov and self-consistent Hartree-Fock approximations.

4.5.1 Hartree-Fock-Bogoliubov mean-field theory

Our starting point is the second-quantized many-body Hamiltonian for a Bose gas with contact interactions held in an external potential $V_{\text{ext}}(\mathbf{r})$ [123, 144]:

$$\hat{H} = \int \hat{\Psi}^\dagger(\mathbf{r}) \left(-\frac{\hbar^2 \nabla^2}{2m} + V_{\text{ext}}(\mathbf{r}) \right) \hat{\Psi}(\mathbf{r}) \, d\mathbf{r} + \frac{g}{2} \int \hat{\Psi}^\dagger(\mathbf{r}) \hat{\Psi}^\dagger(\mathbf{r}) \hat{\Psi}(\mathbf{r}) \hat{\Psi}(\mathbf{r}) \, d\mathbf{r}$$

where $\hat{\Psi}^\dagger(\mathbf{r})$ and $\hat{\Psi}(\mathbf{r})$ are the creation and annihilation field operators, respectively, and in accordance with the Born approximation the microscopic interaction potential has been replaced with an effective potential characterized by the coupling constant $g = 4\pi\hbar^2 a/m$ introduced in equation 2.74. The equation of motion for the field $\hat{\Psi}(\mathbf{r}, t)$ in the Heisenberg representation is obtained from this Hamiltonian as

$$i\hbar \frac{\partial \hat{\Psi}(\mathbf{r}, t)}{\partial t} = [\hat{\Psi}(\mathbf{r}, t), \hat{H}] = \left(-\frac{\hbar^2 \nabla^2}{2m} + V_{\text{ext}}(\mathbf{r}) \right) \hat{\Psi}(\mathbf{r}, t) + g \tilde{\Psi}^\dagger(\mathbf{r}, t) \tilde{\Psi}(\mathbf{r}, t) \tilde{\Psi}(\mathbf{r}, t) \quad (4.4)$$

where we have made use of the bosonic commutation relations

$$[\hat{\Psi}(\mathbf{r}), \hat{\Psi}^\dagger(\mathbf{r}')] = \delta(\mathbf{r}' - \mathbf{r}), \quad [\hat{\Psi}(\mathbf{r}), \hat{\Psi}(\mathbf{r}')] = [\hat{\Psi}^\dagger(\mathbf{r}), \hat{\Psi}^\dagger(\mathbf{r}')] = 0 \quad (4.5)$$

The non-condensed, time-varying component of the field can be separated from the stationary condensed component by writing the total field as the sum of a

condensate wavefunction and an operator describing the fluctuations of the field

$$\hat{\Psi}(\mathbf{r}, t) = \underbrace{\Phi(\mathbf{r}, t)}_{\text{condensate}} + \underbrace{\tilde{\psi}(\mathbf{r}, t)}_{\text{fluctuations}} \quad (4.6)$$

where the Bogoliubov approximation involves the assumption that since the ground state is macroscopically occupied, the number of non-condensed atoms is significantly smaller than the ground-state occupation number¹. This form for the total field is then inserted into the equation of motion 4.4. The self-consistent mean field approximation consists of the linearization of the interaction term cubic in the fluctuation field by reducing it to a set of interactions of a single field with the *mean field* produced by the other two fields according to

$$\tilde{\psi}^\dagger(\mathbf{r}, t)\tilde{\psi}(\mathbf{r}, t)\tilde{\psi}(\mathbf{r}, t) \simeq 2\langle\tilde{\psi}^\dagger(\mathbf{r})\tilde{\psi}(\mathbf{r})\rangle\tilde{\psi}(\mathbf{r}, t) + \langle\tilde{\psi}(\mathbf{r})\tilde{\psi}(\mathbf{r})\rangle\tilde{\psi}^\dagger(\mathbf{r}, t) \quad (4.7)$$

This yields an equation of motion whose stationary solution provides the equivalent of the Gross-Pitaevskii equation for the spatially-varying condensate wavefunction, $\Phi(\mathbf{r})$ ²

$$\left(-\frac{\hbar^2\nabla^2}{2m} + V_{\text{ext}}(\mathbf{r}) - \mu + g[n_0(\mathbf{r}) + 2n_{\text{T}}(\mathbf{r})]\right)\Phi(\mathbf{r}) + \underbrace{g\tilde{m}(\mathbf{r})\Phi^*(\mathbf{r})}_{\text{'anomalous' term}} = 0 \quad (4.8)$$

where the chemical potential, μ , has been introduced since the condensate wavefunction evolves in time according to $\Phi(\mathbf{r}, t) = \Phi(\mathbf{r})\exp(-i\mu t/\hbar)$ and we have introduced the condensate, thermal and ‘anomalous’ densities, $n_0(\mathbf{r})$, $n_{\text{T}}(\mathbf{r})$ and $\tilde{m}(\mathbf{r})$, respectively³

$$\begin{aligned} n_0(\mathbf{r}) &= |\Phi(\mathbf{r})|^2 \\ n_{\text{T}}(\mathbf{r}) &= \langle\tilde{\psi}^\dagger(\mathbf{r})\tilde{\psi}(\mathbf{r})\rangle \\ \tilde{m}(\mathbf{r}) &= \langle\tilde{\psi}(\mathbf{r})\tilde{\psi}(\mathbf{r})\rangle \end{aligned} \quad (4.9)$$

¹ The Bogoliubov approximation consists of replacing both the creation (\hat{a}_0^\dagger) and annihilation (\hat{a}_0) operators for the zero-momentum state by the real number $\sqrt{N_0}$, where N_0 is the condensate occupation number.

² The full expansion for the cubic field-operator term $\hat{\Psi}^\dagger(\mathbf{r}, t)\hat{\Psi}(\mathbf{r}, t)\hat{\Psi}(\mathbf{r}, t)$ within the mean-field approximation is given by: $\hat{\Psi}^\dagger(\mathbf{r}, t)\hat{\Psi}(\mathbf{r}, t)\hat{\Psi}(\mathbf{r}, t) \simeq |\Phi(\mathbf{r})|^2\Phi(\mathbf{r}) + 2[|\Phi(\mathbf{r})|^2 + \langle\tilde{\psi}^\dagger(\mathbf{r})\tilde{\psi}(\mathbf{r})\rangle]\tilde{\psi}(\mathbf{r}, t) + [\Phi^2(\mathbf{r}) + \langle\tilde{\psi}(\mathbf{r})\tilde{\psi}(\mathbf{r})\rangle]\tilde{\psi}^\dagger(\mathbf{r}, t) + 2\Phi(\mathbf{r})\tilde{\psi}^\dagger(\mathbf{r}, t)\tilde{\psi}(\mathbf{r}, t) + \Phi^*(\mathbf{r})\tilde{\psi}(\mathbf{r}, t)\tilde{\psi}(\mathbf{r}, t)$

³ This notation is roughly consistent with that of [194].

We also note that terms linear in $\tilde{\psi}(\mathbf{r}, t)$ have vanished from the original expansion when taking the time average since the fluctuations are assumed to obey $\langle \tilde{\psi}(\mathbf{r}, t) \rangle = \langle \tilde{\psi}(\mathbf{r}) \rangle = 0$. In the $T \rightarrow 0$ limit, when the thermal fraction can be neglected, equation 4.8 reduces to the Gross-Pitaevskii equation introduced in chapter 2 for the weakly-interacting gas.

We now turn our attention to obtaining the excitation spectrum in a similar manner. Substituting the field decomposition of equation 4.6 into the Hamiltonian of equation 4.4 and repeating the mean-field approximation for the resulting cubic and quartic terms in $\tilde{\psi}(\mathbf{r}, t)$ and $\tilde{\psi}^\dagger(\mathbf{r}, t)$ results in a Hamiltonian which can be diagonalized by the linear transformation

$$\begin{aligned}\tilde{\psi}(\mathbf{r}) &= \sum_i (u_i(\mathbf{r})\hat{\alpha}_i - v_i^*(\mathbf{r})\hat{\alpha}_i^\dagger) \\ \tilde{\psi}^\dagger(\mathbf{r}) &= \sum_i (u_i^*(\mathbf{r})\hat{\alpha}_i^\dagger - v_i(\mathbf{r})\hat{\alpha}_i)\end{aligned}\quad (4.10)$$

where $\hat{\alpha}_i^\dagger$ and $\hat{\alpha}_i$ are the creation and annihilation operators of the i -th elementary excitation, respectively. Collecting the coefficients of $\hat{\alpha}_i^\dagger$ and $\hat{\alpha}_i$ in the expanded Hamiltonian results in two coupled equations for the parameters $u_i(\mathbf{r})$ and $v_i(\mathbf{r})$ - the so-called **Hartree-Fock-Bogoliubov (HFB) equations**

$$\left(-\frac{\hbar^2\nabla^2}{2m} + V_{\text{ext}}(\mathbf{r}) - \mu + 2gn(\mathbf{r}) - \epsilon_i\right) u_i(\mathbf{r}) - gm(\mathbf{r})v_i(\mathbf{r}) = 0 \quad (4.11)$$

$$\left(-\frac{\hbar^2\nabla^2}{2m} + V_{\text{ext}}(\mathbf{r}) - \mu + 2gn(\mathbf{r}) + \epsilon_i\right) v_i(\mathbf{r}) - gm^*(\mathbf{r})u_i(\mathbf{r}) = 0 \quad (4.12)$$

with the total density, $n(\mathbf{r})$, and the anomalous term, $m(\mathbf{r})$, defined by

$$n(\mathbf{r}) = \langle \hat{\Psi}^\dagger(\mathbf{r})\hat{\Psi}(\mathbf{r}) \rangle = |\Phi(\mathbf{r})|^2 + \langle \tilde{\psi}^\dagger(\mathbf{r})\tilde{\psi}(\mathbf{r}) \rangle = n_c(\mathbf{r}) + n_T(\mathbf{r}) \quad (4.13)$$

$$m(\mathbf{r}) = \langle \hat{\Psi}(\mathbf{r})\hat{\Psi}(\mathbf{r}) \rangle = \Phi^2(\mathbf{r}) + \langle \tilde{\psi}(\mathbf{r})\tilde{\psi}(\mathbf{r}) \rangle = \Phi^2(\mathbf{r}) + \tilde{m}(\mathbf{r}) \quad (4.14)$$

4.5.2 Popov approximation

The Popov approximation [197, 194, 195, 198, 123, 144] consists of neglecting the anomalous density $\tilde{m}(\mathbf{r})$ in equations 4.8, 4.11 and 4.12. This eliminates the anomalous density term in equation 4.8 and replaces $m(\mathbf{r})$ and $m^*(\mathbf{r})$ in equations

4.11 and 4.12 by $n_0(\mathbf{r})$, where we have used the Bogoliubov approximation to replace $\Phi^2(\mathbf{r}) \simeq n_0$ (see equations 4.13 and 4.14).

The HFB equations therefore reduce to the **Popov equations**

$$\left(-\frac{\hbar^2 \nabla^2}{2m} + V_{\text{ext}}(\mathbf{r}) - \mu + 2gn(\mathbf{r}) - \epsilon_i \right) u_i(\mathbf{r}) - gn_0(\mathbf{r})v_i(\mathbf{r}) = 0 \quad (4.15)$$

$$\left(-\frac{\hbar^2 \nabla^2}{2m} + V_{\text{ext}}(\mathbf{r}) - \mu + 2gn(\mathbf{r}) + \epsilon_i \right) v_i(\mathbf{r}) - gn_0(\mathbf{r})u_i(\mathbf{r}) = 0 \quad (4.16)$$

In the semi-classical approximation, the kinetic energy operators, $-\hbar^2 \nabla^2 / 2m$, in equations 4.15 and 4.16 can be replaced by $p^2 / 2m$ and the excitation energies are obtained as

$$\epsilon(\mathbf{r}, \mathbf{p}) = \left[(p^2 / 2m + 2gn(\mathbf{r}) + V_{\text{ext}}(\mathbf{r}) - \mu)^2 - (gn_0(\mathbf{r}))^2 \right]^{1/2} \quad (4.17)$$

The density of non-condensed atoms in this approximation is then given by

$$n_{\text{T}}(\mathbf{r}) = \int \frac{d\mathbf{p}}{(2\pi\hbar)^3} \frac{p^2 / 2m + 2gn(\mathbf{r}) + V_{\text{ext}}(\mathbf{r}) - \mu}{\epsilon(\mathbf{r}, \mathbf{p})} \frac{1}{e^{\epsilon(\mathbf{r}, \mathbf{p}) / k_{\text{B}} T} - 1} \quad (4.18)$$

where $\epsilon(\mathbf{r}, \mathbf{p})$ is given by equation 4.17 and the factor multiplying the excitation distribution function is the ratio of the particle energy in the Hartree-Fock approximation (see below) to that in the Popov approximation. This corresponds to the number of non-condensed particles associated to a given excitation and ensures that we are effectively summing particles and not excitations when calculating the particle density, $n_{\text{T}}(\mathbf{r})$.

The condensate density, $n_0(\mathbf{r}) = |\Phi(\mathbf{r})|^2$ is found by solving equation 4.8 with the ‘anomalous’ term involving $\tilde{m}(\mathbf{r})$ omitted, namely

$$\left(-\frac{\hbar^2 \nabla^2}{2m} + V_{\text{ext}}(\mathbf{r}) - \mu + g[n_0(\mathbf{r}) + 2n_{\text{T}}(\mathbf{r})] \right) \Phi(\mathbf{r}) = 0 \quad (4.19)$$

within the Thomas-Fermi approximation, the first term of equation 4.19 can be neglected and the chemical potential is then given by

$$\mu = V_{\text{ext}}(\mathbf{r}) + g[n_0(\mathbf{r}) + 2n_{\text{T}}(\mathbf{r})] \quad (4.20)$$

The four equations, 4.17, 4.18, 4.19 and 4.20 must be solved self-consistently in

order to find the thermal and condensate densities.

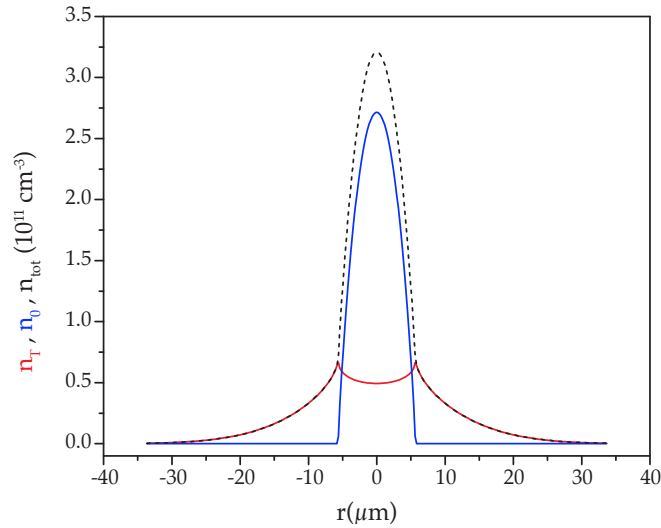


Figure 4.6: Popov density profiles. Cuts through the thermal (red) and condensate (blue) *in-situ* spatial density distributions for a cloud with $N_{\text{tot}} = 10^5$ atoms at $T = 150\text{nK}$. The dimple in the thermal cloud is a result of repulsion by the condensate. The black dashed line shows the total density distribution, $n_{\text{tot}} = n_{\text{T}} + n_0$.

We note that at very low temperatures, when the non-condensed fraction n_{T} can be neglected, the Popov spectrum of equation 4.17 reduces to the usual Bogoliubov quasi-particle excitation spectrum (see for example [199, 123]) and, as we have already mentioned, equation 4.19 for the condensate wavefunction reduces to the usual Gross-Pitaevskii equation introduced in chapter 2. At higher temperatures, when the condensed fraction $n_0(\mathbf{r})$ can be neglected, the Popov spectrum coincides with the Hartree-Fock spectrum (see below).

4.5.3 Self-consistent Hartree-Fock approximation

A further simplification of the full Hartree-Fock-Bogoliubov equations is the so-called self-consistent Hartree-Fock approximation, which is widely accepted as providing the simplest scheme for addressing the effects of atomic interactions in a Bose gas.

Mathematically, the approximation consists of again neglecting $\tilde{m}(\mathbf{r})$ in equations 4.8, 4.11 and 4.12 and in addition neglecting any of the collective effects arising in the HFB and Popov approximations. The latter approximation amounts to neglecting the parameter $v_i(\mathbf{r})$ in equations 4.10 and hence in equations 4.11 and

4.11, which therefore yield the simplified, single-particle, excitation spectrum

$$\epsilon_{\text{HF}}(\mathbf{r}, \mathbf{p}) = \frac{p^2}{2m} + V_{\text{ext}}(\mathbf{r}) + 2gn(\mathbf{r}) \quad (4.21)$$

with $n(\mathbf{r}) = n_c(\mathbf{r}) + n_T(\mathbf{r})$ as in equation 4.13. Within this approximation, the condensate density is still found from equation 4.19 and the thermal density $n_T(\mathbf{r})$ is now obtained using

$$n_T^{\text{HF}}(\mathbf{r}) = \int \frac{d\mathbf{p}}{(2\pi\hbar)^3} \frac{1}{e^{(\epsilon_{\text{HF}}(\mathbf{r}, \mathbf{p}) - \mu)/k_B T} - 1} \quad (4.22)$$

Physically, this approximation corresponds to treating the thermal component as a gas of ‘non-interacting’ atoms moving in a self-consistently determined mean-field potential given by

$$V_{\text{eff}}(\mathbf{r}) = V_{\text{ext}}(\mathbf{r}) + 2gn(\mathbf{r}) = V_{\text{ext}}(\mathbf{r}) + 2g[n_0(\mathbf{r}) + n_T(\mathbf{r})] \quad (4.23)$$

Two further simplifications can be made as a consequence of the relative diluteness of the thermal component compared to the condensate:

1. Firstly, one can neglect any influence of the thermal component on the spatial distribution of the condensate wave function¹. Setting $n_T(\mathbf{r}) = 0$ in equation 4.19 and applying the Thomas-Fermi (TF) approximation² gives the usual TF profile for the condensate

$$n_0(\mathbf{r}) = \max[(\mu_0 - V_{\text{ext}}(\mathbf{r}))/g, 0] \quad (4.24)$$

where the normalization condition $\int n_0(\mathbf{r})d\mathbf{r} = N_0$ on the condensate density yields the chemical potential

$$\mu_0 = \frac{\hbar\bar{\omega}}{2} \left(15N_0 \frac{a}{a_{\text{ho}}} \right)^{2/5} \quad (4.25)$$

Note that this expression is strictly equal to the actual chemical potential, μ , only in the zero-temperature limit. More generally, μ_0 provides the

¹ We note that in [186], a small deviation from this approximation was observed in the form of a $\sim 4\%$ compression of the condensate length from its predicted TF size.

² Use of the Thomas-Fermi approximation is valid as long as $N \gg a_{\text{ho}}/a$ (i.e. $N_0 \gg 100$ to 1000 for our parameters)

characteristic energy scale for the interactions¹ and its scaling with $N_0^{2/5}$ will inform the analysis of our experimental data (see section 4.6 below).

2. Secondly, we can neglect the mean-field energy, $2gn_{\text{T}}(\mathbf{r})$, due to the thermal component itself, so that the effective potential experienced by the thermal atoms is then given by

$$V_{\text{eff}}(\mathbf{r}) = V_{\text{ext}}(\mathbf{r}) + 2gn_0(\mathbf{r}) = |V_{\text{ext}}(\mathbf{r}) - \mu_0| + \mu_0 \quad (4.26)$$

Figure 4.7 shows an illustration of the potential, $V_{\text{eff}}(\mathbf{r})$, experienced by the thermal atoms in this approximation, which has the form of a 3D ‘Mexican hat’. We note that under these approximations, the Hartree-Fock theory reduces to the so-called ‘semi-ideal’ model, [200, 201, 202]. This model has been used in the analysis of several previous experiments, as discussed in section 4.7 at the end of this chapter.

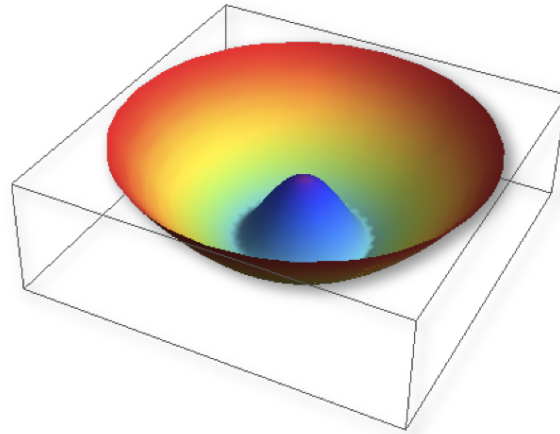


Figure 4.7: Illustration of the “Mexican hat” potential of equation 4.26 experienced by the thermal atoms as a result of their interaction with the condensate at the centre of the trap and the external harmonic potential.

In neglecting the contribution of the thermal atoms to the mean-field potential, the second approximation also amounts to neglecting the mean-field shift of the critical temperature due to interactions. This shift will be discussed in more detail in chapter 5 where our observation of the mean-field T_c shift, in addition to observation of beyond-mean-field effects on the critical temperature, are presented.

¹ In the zero-temperature Thomas-Fermi limit, for example, the chemical potential is related to the interaction energy per particle according to $E_{\text{int}}/N = (2/7)\mu_0$.

Using the above expression for $V_{\text{eff}}(\mathbf{r})$, the number of thermal atoms at a given temperature in the presence of a condensate of N_0 atoms can be estimated by integrating equation 4.22, i.e.

$$N_{\text{T}} = \frac{1}{(2\pi\hbar)^3} \int \left\{ \exp \left[\frac{1}{k_{\text{B}}T} \left(\frac{p^2}{2m} + V_{\text{eff}}(\mathbf{r}) - \mu \right) \right] - 1 \right\}^{-1} d^3p d^3r \quad (4.27)$$

Introducing the dimensionless variables

$$R = \frac{r}{R_{\text{T}}} \quad \alpha_0 = \frac{\mu}{k_{\text{B}}T} \quad (4.28)$$

with $R_{\text{T}} = \sqrt{k_{\text{B}}T/m\omega^2}$, we can express the thermal atom number after performing the momentum integral in equation 4.27 as

$$N_{\text{T}} = 4\pi \left(\frac{R_{\text{T}}}{\lambda_{\text{T}}} \right)^3 \int_{\sqrt{2\alpha_0}}^{\infty} R^2 g_{3/2}(e^{-R^2/2+\alpha_0}) dR \quad (4.29)$$

Making the substitution $X^2 = R^2 - 2\alpha_0$, the above integral becomes

$$\begin{aligned} N_{\text{T}} &= 4\pi \left(\frac{R_{\text{T}}}{\lambda_{\text{T}}} \right)^3 \int_0^{\infty} (X^2 + 2\alpha_0)^{1/2} g_{3/2}(e^{-X^2/2}) X dX \\ &\approx 4\pi \left(\frac{R_{\text{T}}}{\lambda_{\text{T}}} \right)^3 \int_0^{\infty} X^2 (1 + \alpha_0/X^2) g_{3/2}(e^{-X^2/2}) dX \quad (R_{\text{TF}} \ll R_{\text{T}}) \\ &= 4\pi \left(\frac{R_{\text{T}}}{\lambda_{\text{T}}} \right)^3 \underbrace{\int_0^{\infty} X^2 g_{3/2}(e^{-X^2/2}) dX}_{\zeta(3)\sqrt{\frac{\pi}{2}}} + 4\pi \left(\frac{R_{\text{T}}}{\lambda_{\text{T}}} \right)^3 \alpha_0 \underbrace{\int_0^{\infty} g_{3/2}(e^{-X^2/2}) dX}_{\zeta(2)\sqrt{\frac{\pi}{2}}} \\ &= \left(\frac{k_{\text{B}}T}{\hbar\omega} \right)^3 [\zeta(3) + \alpha_0\zeta(2)] \quad (4.30) \end{aligned}$$

In going from the first to the second row of equation 4.30 we have made the assumption that the condensate size is small compared to the thermal radius, $R_{\text{TF}} \ll R_{\text{T}}$, and hence that $\frac{\alpha_0}{X^2} \ll 1$. Using equation 4.1 for the ideal gas critical number, $N_{\text{c}}^{(\text{id})}$, we are left with

$$\frac{N_{\text{T}}}{N_{\text{c}}^0} = 1 + \frac{\zeta(2)}{\zeta(3)} \alpha_0 \approx 1 + 1.37\alpha_0 = 1 + 1.37 \frac{\mu}{k_{\text{B}}T} \quad (4.31)$$

It has in fact been shown [203, 196, 46] that the description of the thermodynamic behaviour of an interacting Bose gas in the thermodynamic limit for a given

atom number, trap geometry, scattering length, etc., is fixed by the values of two dimensionless parameters: the reduced temperature, $t = T/T_c^{(\text{id})}$, and the interaction parameter, η defined as

$$\eta \equiv \frac{\mu}{k_B T_c^{(\text{id})}} \simeq 1.57 \left(N^{1/6} \frac{a}{a_{\text{ho}}} \right)^{2/5} \quad (4.32)$$

where μ is the zero-temperature chemical potential in the Thomas-Fermi limit¹. In the experiments described in this chapter, η , which quantifies the relative importance of interactions, spans the range $\eta = 0.21 \rightarrow 0.61$. A related dimensionless interaction parameter is given by, a/λ_0 , the ratio of the scattering length to the thermal wavelength evaluated at the ideal-gas critical temperature. This parameter will be used in chapter 5 since most theories for the shift in T_c are formulated in terms of expansions in this quantity. η and a/λ_0 are related via $\eta \approx 2.3 \cdot (a/\lambda_0)^{2/5}$ and hence in the current experiments, we have probed the range $a/\lambda_0 = 2.7 \times 10^{-3} \rightarrow 3.6 \times 10^{-2}$. Physically, the origin of the non-saturation predicted in this Hartree-Fock scheme can therefore be understood as resulting directly from the geometry of the effective ‘Mexican hat’ potential allowing the thermal component to occupy a larger volume, which grows with increasing N_0 .

4.6 Comparing experiment and theory

We initially compare our measurements to the more analytically-tractable predictions of Hartree-Fock theory above. Guided by the scaling implied by equations 4.25 and 4.31, we plot the thermal atom number, N_T , as a function of $N_0^{2/5}$. Figure 4.8 shows this plot for the $a = 135a_0$, $T = 177\text{nK}$ series shown in figures 4.3 and 4.4. From equations 4.25 and 4.31 we define the ‘non-saturation slope’ S_{HF} :

$$S_{\text{HF}} = dN_T/d(N_0^{2/5}) = 1.37X \quad (4.33)$$

where X is an interaction parameter, defined by

$$X = \xi T^2 a^{2/5} \quad \text{where} \quad \xi = \frac{1}{2} \zeta(3) 15^{2/5} \left(\frac{k_B}{\hbar \bar{\omega}} \right)^2 a_{\text{ho}}^{-2/5} \quad (4.34)$$

The blue line in figure 4.8 corresponds to this prediction, with the y-axis intercept fixed by the measured value of N_c . As can be seen in figure 4.8, the Hartree-Fock non-saturation slope agrees well with the data in the regime of small condensates

¹ This has the same functional form as equation 4.25, with the replacement $N_0 \rightarrow N$.

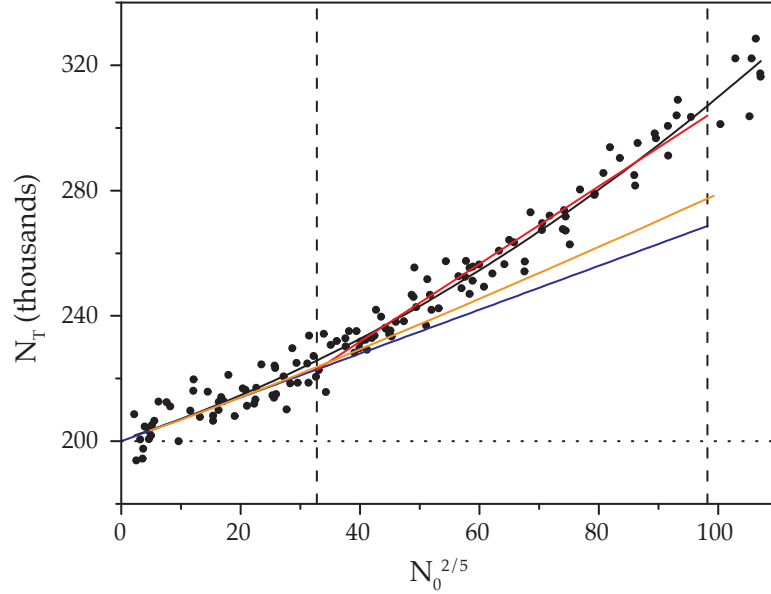


Figure 4.8: Quantifying the lack of saturation. The thermal number, N_T , is plotted against $N_0^{2/5}$ for the series shown in figures 4.3 and 4.4. The horizontal dotted line is the saturation prediction $N_T = N_c$. The blue line is the mean-field Hartree-Fock result of equation 4.31 for a harmonically trapped gas for the appropriate scattering length ($S_{\text{HF}} = 699$). The orange line is the prediction of the Popov approximation for the experimental parameters used. The solid red line is a linear fit to the data in the large-condensate regime, as discussed below, and the black line is a second-order polynomial fit to guide the eye.

with $N_0 \lesssim 10^4$, corresponding to $\mu_0/k_B T \lesssim 0.1$, whereas the data deviates from the HF prediction for larger values of N_0 . On figure 4.8 we have also plotted the prediction of the Popov theory for the relevant experimental parameters. In the small-condensate regime, the Popov result is almost indistinguishable from the Hartree-Fock prediction and its departure from the linear HF curve for larger condensates still fails to describe the observed growth of the thermal component.

In order to more quantitatively test the predictions of equation 4.31, we took several series at different scattering lengths ($a = 56 - 274a_0$) and temperatures ($T = 177 - 317\text{nK}$), focussing on the regime of very small N_0 . The method we use to reliably detect and measure small condensates involves turning off the interaction strength during time-of-flight and performing a direct summation of the optical density. It is described in more detail in chapter 5 in the context of our investigations into the interaction-shift of the transition temperature T_c . For each of these series, we fit the initial non-saturation slope $S_0 = dN_T/d(N_0^{2/5})$ for $N_0 \rightarrow 0$, and compare the result with the prediction $S_{\text{HF}} = 1.37X$. Figure 4.9

shows the results of this comparison, in which experiment and theory agree to within a few percent.

Since, as mentioned above, two *independent* parameters, t and η are required in order to fully capture the mean-field behaviour, we do not expect our simplified non-saturation slope S_0 to scale exactly with the interaction parameter, X . Despite this, the agreement with our single-parameter theory is good.

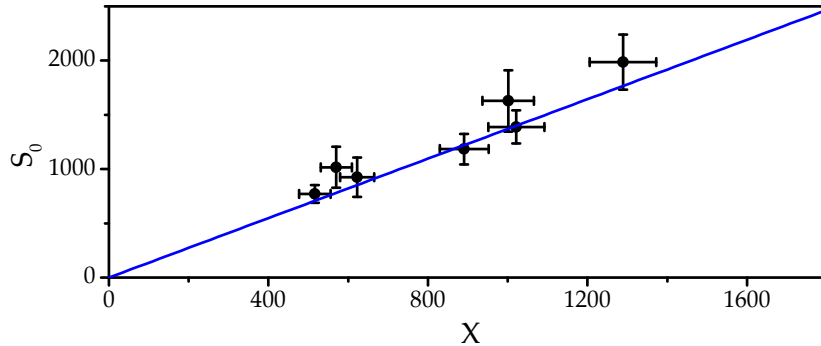


Figure 4.9: Agreement of the initial non-saturation slope, S_0 with the prediction of the ‘semi-ideal’ Hartree-Fock theory. The blue line shows the prediction of equation 4.31. The vertical error bars are statistical, with the $< 10\%$ systematic uncertainty on N_T and N_0 corresponding to a $< 6\%$ uncertainty in S_0 . Horizontal error bars include the 3Hz uncertainty in the trapping frequencies $\bar{\omega}/2\pi$ and (for ^{39}K) the 0.1G uncertainty in the position of the Feshbach resonance.

The agreement of figure 4.9 with HF theory is the first main quantitative result of this investigation. From it we can deduce that the initial non-saturation slope S_0 would indeed vanish in the non-interacting limit, in which $\mu_0 \rightarrow 0$ for any value of N_0 .

Figure 4.10a shows the predictions of the Popov approximation for the thermal and condensate numbers for different values of the scattering length, at a temperature of $T = 200\text{nK}$, while figure 4.10b shows the data of figures 4.3 and 4.4 compared to the Popov model for the same experimental parameters. It is apparent from this plot that the mean-field Popov model does not fully capture the extent of the non-saturation observed in our clouds.

In order to quantitatively study the non-saturation effects taking place at larger N_0 , where the data is no longer well described by the Hartree-Fock theory, we adopt a more heuristic approach. Although the observed increase of N_T with $N_0^{2/5}$ is not perfectly linear, over a broad experimentally relevant range it can be well quantified by a coarse-grained slope $S = \Delta[N_T]/\Delta[N_0^{2/5}]$, as indicated by the solid red line in figure 4.8. In order to treat data taken at different values of X ,

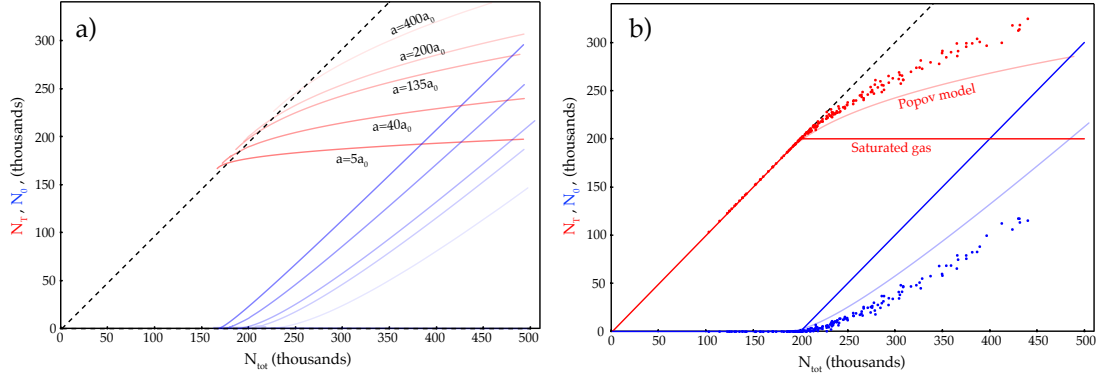


Figure 4.10: The Popov model. Figure (a) shows the predictions of the Popov approximation for different scattering lengths ($a = 5, 40, 135, 200, 400a_0$) at a temperature of $T = 200\text{nK}$. Figure (b) compares the experimental non-saturation data to the corresponding Popov prediction, which fails to fully capture the degree of non-saturation.

i.e. different values of a and T , equally, for each experimental series we consider the same range of values of $\mu_0/k_{\text{B}}T$, from 0.1 to 0.3. Note that this range spans more than an order of magnitude of N_0 values and encompasses the bulk of the data shown in figure 4.5.

It is worth pointing out that the data shown in figure 4.8 can equally be described by a second-order polynomial fit, instead of using the two slopes, S_0 and S . However, such a fit relies on precise measurements at very low N_0 , which are often not available. This is the reason we have chosen to use a single empirically defined parameter S for describing the experiments, valid over the typical range of N_0 values. Figure 4.11 shows the obtained slopes $S(a, T)$ for the 18 experimental series of figure 4.5. Within experimental error, all data points fall onto a straight line when plotted against the dimensionless variable, $X = \xi T^2 a^{2/5}$, supporting the assumption that $\mu_0/k_{\text{B}}T$ can still be used as the relevant interaction parameter.

In order to further demonstrate the universality of our results and the validity of our approach, figure 4.11 also shows data taken with a different atomic species, ^{87}Rb . This species was held in the $|F, m_{\text{F}}\rangle = |2, 2\rangle$ state and its scattering length of $a = 99a_0$ is not tuneable. Two series were taken with this species, at $T = 175\text{nK}$ and at $T = 203\text{nK}$. These two data points lie well within the spread of the ^{39}K data. The contributions of temperature drifts and finite-size effects to the data must also be considered. We compensate for the small temperature drifts as described below, while finite-size effects are shown to have no influence on the exhibited degree of non-saturation.

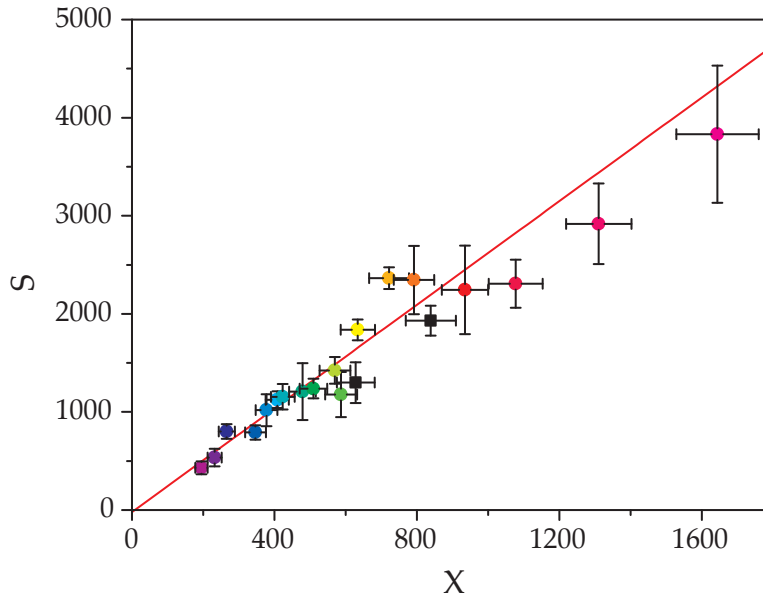


Figure 4.11: Saturation in the non-interacting limit. The large- N_0 slopes, S , for the 18 data series of figure 4.5 and two additional ^{87}Rb series (black points), plotted against the dimensionless interaction variable, X , of equation 4.34. An unconstrained linear fit to the data gives an intercept $S(0) = -20 \pm 100$, consistent with complete saturation in the ideal-gas limit. See the caption of figure 4.9 for an explanation of the error bars.

Correcting for temperature drifts

In our experimental series, we occasionally encounter temperature drifts of up to a few percent over the course of the series. We analytically correct for these drifts by scaling every (N_T, N_0) pair according to the scaling suggested by Hartree-Fock theory. We scale each experimental series by its nominal temperature, T^* . This corresponds to plotting $N_T(T^*/T')^3$ against $N_0^{2/5}(T^*/T')$ in figure 4.8, where T' is the temperature assigned to each data point. T' is found by first performing an exponential fit to a plot of measured temperature, T_m , against image index¹. The value of this fit gives each image a temperature, T_i . We then perform a linear fit to the plot of T_m/T_i against N_0 , yielding a factor, f_{N_0} , for each image². T' is then given by: $T' = T_i * f_{N_0}$. In plain words, this correction corresponds to scaling the thermal and condensate atom numbers of each data point to the relative values they would take on, according to the Hartree-Fock theory, were they at the nominal temperature of the series they belong to. This correction is

¹ This is to take account of temperature drifts resulting from changes in the lab environment over the course of the day

² This takes into account the drift of temperature with decreasing condensate number.

valid to first order, even though the HF theory is imperfect, since the temperature corrections involved are small.

Finite-size effects

The first correction to the ideal-gas prediction, $N_0/N_{\text{tot}} = 1 - (T/T_c^{(\text{id})})^3$, due to the effect of finite particle number has been found analytically by studying the large- N limit of the expression for the total number of particles at temperature T [204, 205, 206, 207]

$$N = \sum_{i=0}^{\infty} N(\epsilon_i) = \sum_{i=0}^{\infty} \frac{1}{e^{(\epsilon_i - \mu)/k_B T} - 1} \quad (4.35)$$

The result is given by

$$\frac{N_0}{N} = 1 - t^3 - \underbrace{\frac{3\omega_{\text{ho}}\zeta(2)}{2\bar{\omega}(\zeta(3))^{2/3}}}_{\text{finite-size correction}} t^2 N^{-1/3} \quad (4.36)$$

where ω_{ho} is the arithmetic mean of the trap frequencies and $t = T/T_c^{(\text{id})}$ is the reduced temperature introduced above. This expression has been shown to be indistinguishable from the exact value obtained using equation 4.35 already for $N = 1000$ [206]. As an example, for $t = 0.75$ and an atom number of 2×10^5 , with typical trapping frequencies, $\omega/2\pi = (65, 65, 84)\text{Hz}$, the condensed fraction is reduced by roughly 1.9% from its ideal gas value of 58%. However, inserting expression 2.69 for $T_c^{(\text{id})}$ shows that the shift in the absolute number N_0 does not depend on the total number N and is instead given by $\delta N_0 = -(k_B T/\hbar\bar{\omega})^2 (3/2)(\omega_{\text{ho}}/\bar{\omega})\zeta(2)$. At a given temperature, this is simply equivalent to a uniform shift in the critical number, which in figure 4.8, corresponds to a uniform vertical shift of the data. This does not affect the extracted non-saturation slopes and hence leaves the results of this chapter unchanged. Chapter 5 discusses finite-size effects on the shift of the critical temperature which must be taken into account when measuring the interaction-shift of $T_c^{(\text{id})}$.

4.6.1 Extrapolation to the non-interacting limit

The saturation prediction of equation 4.1 for an ideal gas ($a = 0$) corresponds to $S = 0$ at the origin of the graph in figure 4.11. It is important to distinguish

between the two ways in which the interaction variable, $X \propto T^2 a^{2/5}$, can approach zero. In the $T \rightarrow 0$ limit, N_T vanishes for any value of N_0 and so trivially $S = 0$. It is therefore important for us to demonstrate that the slope S depends only on the combination $T^2 a^{2/5}$, allowing us to obtain its value in the $a \rightarrow 0$ limit for any fixed, non-zero value of T . The solid red line in figure 4.11 shows the result of this extrapolation by means of an unconstrained linear fit to the data. The resulting value of the intercept, $S(0) = -20 \pm 100$, together with the demonstrated agreement with Hartree-Fock theory in the small- N_0 limit, confirm the concept of a saturated Bose gas over a broad range of experimentally relevant parameters.

4.7 Discussion and Conclusions

The experiments described in this chapter consisted of probing the dependence of the condensed fraction on the total atom number at a constant temperature. This contrasts with the numerous studies, dating from some of the earliest experimental investigations of BEC to the present day, which have focussed on measurement of the condensed fraction as a function of temperature and hence have never explicitly and systematically addressed the issue of non-saturation of the thermal component.

Nevertheless, these experiments drew attention to the need for a proper treatment of the effect of interactions on Bose-Einstein condensation by providing clear evidence of the inadequacy of ideal-gas theory. Below is a brief chronologically-ordered summary of those results most directly related to the experiments carried out in our group and described in this chapter and in chapter 5.

Already within the few years following the first experimental realization of BEC in dilute atomic gases, several experiments [208, 209, 210] compared the predictions of ideal-gas theory with their experimental findings. Figure 4.12 shows the chronological progression towards more precise condensed-fraction measurements, revealing ever more clearly the deviations from the ideal-gas picture.

The first experiment to clearly demonstrate non-ideal behaviour was [209] (see figure 4.12b), whose results also served as a helpful benchmark for subsequent development and testing of mean-field models for interacting clouds (see e.g. [201, 123]).

Later studies [211, 212] also observed deviation from ideal-gas theory and instead found agreement with the ‘semi-ideal’ theory [201, 200]. In [213], the authors explicitly investigated the mutual interactions between the condensed and thermal

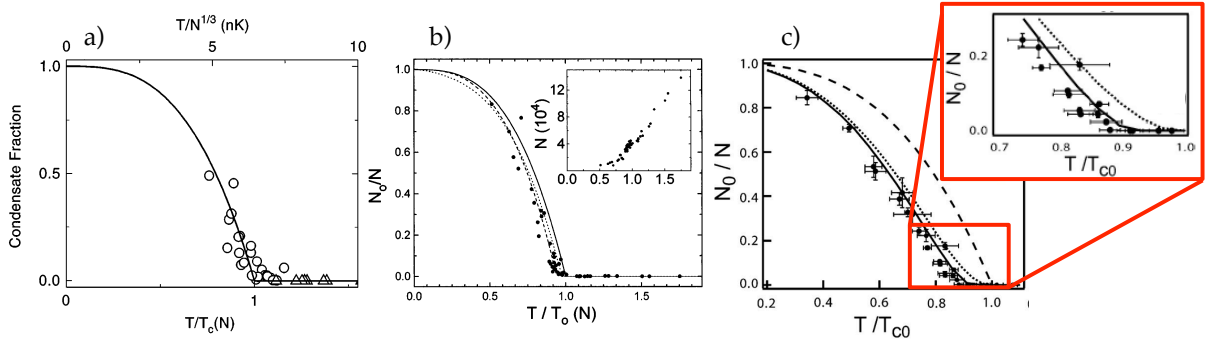


Figure 4.12: The results of [208] (figure (a)), [209] (figure (b)) and [186] (figure(c)) for the condensed fraction, N/N_0 , as a function of the reduced temperature, T/T_c^0 . The increasing precision of the measurements has enabled more detailed comparison with mean-field models.

components. This experiment focussed on the narrow region at the interface between the condensate and the thermal cloud, which was expected to be sensitive to these interactions. It was demonstrated that a dynamical model for the cloud's expansion based on the HFB theory presented in section 4.5 provided a good fit to the experimental data, which clearly displayed a repulsion of the thermal cloud by the condensate in images taken after time-of-flight (see Fig. 2 of [213]).

A more comprehensive study was performed in [186], which measured the condensed fraction, expansion energy and equilibrium shape of a partially-condensed ^{87}Rb cloud. The use of Bragg scattering enabled the detection of larger condensed fractions and accurate fitting of the thermal component at lower temperatures than any previous study. The resulting condensed-fraction curves showed clear deviation from the ideal-gas prediction (see figure 4.12c) and were compared to both the semi-ideal model [201, 200], including finite-size effects, and to the self-consistent Hartree-Fock theory described in section 4.5. The semi-ideal model failed to reproduce the results (as in our experiments) although the self-consistent Hartree-Fock theory yielded good agreement within experimental errors. The authors also investigated the effect of the thermal cloud on the condensate by studying its axial length as a function of temperature. The axial length is expected to grow very slowly due to the large aspect ratio of the trapping potential ($\omega_z/\omega_r \approx 0.02$) and hence to closely reflect its *in-situ* value. A compression of the condensate by the thermal cloud is observed. The semi-ideal model, which explicitly neglects such effects, unsurprisingly fails to fully account for this compression whereas the Hartree-Fock model provides good agreement with the data. This result again illustrates the over-simplicity of the semi-ideal model under typical

experimental parameters, as also shown by our results.

Furthermore, experiments described in [214] explicitly report the breakdown of Hartree-Fock mean-field theory in relatively small ($N_{\text{tot}} \approx 10^4$), nearly-1D clouds of ^{87}Rb . The authors observe the appearance of a quasi-condensate in the centre of the trap and show that Hartree-Fock theory fails to predict its existence, which is consequently attributed to interaction-induced correlations between the atoms as opposed to saturation of the excited states.

Two studies bearing conceptual similarities to the experiments reported in this chapter have been published in the last few years. In [215], condensation was studied in a spinor gas in which atoms were gradually transferred from two condensed spin components into an initially-unpopulated spin state. Non-saturation of the growing thermal cloud was not reported. However, since this component experiences a potential modified by interactions with the already existing condensates, it is probable that non-saturation effects were merely obscured by the complicated dynamics of the system. The second study reports on the realization of a BEC in a photon gas [216]. In this system, despite the absence of a direct interaction between the photons, their thermalization via collisions with the dye molecules within the microcavity to which they are confined leads to a second-order interaction between the light particles. The non-saturation arising from this effective interaction is visible in figure 2 of [216] as a clear increase of the area under the ‘thermal’ part of the spatial intensity distribution as the number of photons in the system is increased (at room temperature).

To this long line of investigations, the results of this chapter add the demonstration that under typical experimental circumstances, atomic Bose gases show strong deviation from the saturation picture. In addition, this deviation is not fully reproduced by the most commonly-used mean field theories. Our experimental control over the interparticle interaction strength, however, has enabled us to extrapolate our results to the non-interacting limit and to provide the first direct evidence for excited-state saturation as the driving mechanism behind Bose-Einstein condensation, confirming the purely statistical nature of the BEC phase-transition as originally described by Einstein. We expect these results to be generic to experiments on harmonically trapped 3D Bose gases with (relatively weak) short-range s-wave interactions.

There exist several possible avenues for future research :

1. We have so far measured only global properties (total numbers). In the

future it would be interesting to study saturation and other thermodynamic behaviour at the local level, by probing local thermal and condensate densities. This would enable us to infer the effective equation of state of the bulk system, as proposed in [217] and demonstrated, for example, in [218, 219, 220, 221].

2. The ability to probe local densities would also allow investigation of the effects of different interaction potentials, such as very strong or long-range interactions, which might influence saturation at the local level.
3. Trap geometry influences the behaviour of the thermal gas. The excluded-volume argument for non-saturation suggests that the effect grows with the dimensionality of the system and so it would be interesting to explore lower-dimensional as well as disordered geometries. In this context, Appendix F describes our progress towards the implementation of a tightly-confining optical potential for studies of two-dimensional systems.

5

Interaction-dependence of the BEC transition temperature

“...I tell you there is no such message, no such home – only the millions of last moments ... nothing more. Our history is an aggregate of last moments.”

Thomas Pynchon, *Gravity's Rainbow*

Abstract

*While chapter 4 was concerned with the effects of interparticle interactions on trapped gases **below** the critical temperature, in the presence of a finite condensed fraction, this chapter describes experiments on the effects of these interactions on the value of the transition temperature itself, i.e. in the limit of vanishing condensate fraction. We observe for the first time the beyond-mean-field (bMF) corrections to T_c in a harmonically-trapped gas and also observe non-equilibrium effects on the apparent critical temperature in the regime of both very weak and very strong interactions.*

5.1 Introduction and theory

As discussed in section 2.7, the critical temperature, T_c , is defined as the temperature at which the condensed fraction in the gas vanishes, $N_0 \rightarrow 0$ and is one of the most fundamental quantities in the study of the BEC phase transition. While clear predictions exist for the critical temperature of a non-interacting gas, the effects of (repulsive) interparticle interactions on the condensation temperature have been the subject of theoretical debate for over fifty years, since the pioneering work of Lee and Yang [222, 223] on a homogeneous gas of hard-core bosons.

Despite the success of mean-field theories in predicting a broad range of properties such as the spatial distribution of the dilute gas in a harmonic trap, its low-energy excitation spectrum and its small-amplitude oscillations, correlations between the atoms due to their interactions are also expected to play an important role in many phenomena. These include the properties of superfluid vortices, decoherence, quantum depletion, and others. Correlations also provide corrections to the predicted mean-field values of thermodynamic quantities such as the energy per particle and the transition temperature. Indeed, the former of these was recently measured in an experiment carried out in the ENS group in Paris using a gas of ^7Li [220], while observation of the latter is the subject of this chapter, which is structured as follows:

- Following a short summary of the theoretical predictions for the shift of T_c with interaction strength in both a uniform and harmonically-trapped gas, we briefly review previous experimental measurements of the transition temperature in trapped interacting clouds.
- We then describe our experimental sequence and analysis procedure for measuring the shift of the critical temperature over a wide range of interaction strengths, and present our results for those measurements believed to be at thermodynamic equilibrium.
- Finally we discuss the stringent requirements for performing equilibrium T_c measurements, which are violated in the regimes of either very weak or very strong interactions, and discuss their physical origins and significance.
- We conclude and discuss directions for future study.

5.1.1 T_c -shift in a uniform system

We recall that in an ideal, homogeneous bose gas, the transition temperature is given by

$$T_c^{(\text{id})} = \left(\frac{n}{\zeta(3/2)} \right)^{3/2} \frac{2\pi\hbar^2}{k_B m} \quad (5.1)$$

which corresponds to the condition that the phase-space density reach its critical value $n\lambda_0^3 = \zeta(3/2) \simeq 2.612$, as discussed in section 2.7. The fractional shift of this quantity by the inclusion of interactions is defined by

$$\frac{\Delta T_c}{T_c^{(\text{id})}} \equiv \frac{T_c}{T_c^{(\text{id})}} - 1 \quad (5.2)$$

and is usually calculated as a function of the *diluteness*- or *gas parameter*

$$\delta \equiv an^{1/3} \quad (5.3)$$

i.e. the effect of interactions can be increased by either raising the atomic density, n , or by increasing the scattering length, a , for example by accessing a Feshbach scattering resonance.

At the mean-field (MF) level, the shift of the uniform-system critical temperature vanishes identically. Within this approximation, the interaction energy is given by $U_{\text{int}} = 2gn$, where g is the interaction strength and n the density. A particle with momentum \mathbf{p} within this approximation therefore has an energy $\epsilon(\mathbf{p}) = p^2/2m + 2gn$. The result of this energy shift is a shift in the critical value of the chemical potential, μ_c , but not in that of the transition temperature. This is easily seen by looking at the modification of the equation of state from that of an ideal gas, arising from use of this expression for the energy (c.f. equation 2.64)

$$n\lambda_T^3 = g_{3/2}(e^{\beta\mu}) \xrightarrow{\epsilon(\mathbf{p}) \rightarrow \epsilon(\mathbf{p}) + 2gn} n\lambda_T^3 = g_{3/2}(e^{\beta(\mu - 2gn)}) \quad (5.4)$$

where $\beta = 1/k_B T$. At the transition, namely the point at which the argument of $g_{3/2}$ goes to 1, the criterion $n\lambda_T^3 = \zeta(3/2)$ remains unchanged. The chemical potential now has to reach a value higher by $2gn$ than its previous maximal value, but the value of T_c is unaffected. In general, any constant shift in the single-particle energies cannot change the critical temperature of the gas. A correct calculation of the T_c shift therefore requires taking into consideration the correlations which develop near the critical point and are not captured within

mean-field theory.

This is a challenging task and only in the first few years of this century has the community converged on a consensus for the functional dependence of the T_c shift on the gas parameter. For an overview of these developments, see *e.g.* [224, 225, 226, 227]. Table 5.1 summarizes the evolution of the theoretical predictions since the middle of the 20th century.

Year	Author(s)	Prediction
1953	Feynman [228]	$\Delta T_c < 0$
1958	Lee & Yang [223]	$\frac{\Delta T_c}{T_c^{(\text{id})}} \sim a\rho^{1/3}$
1960	Glassgold, Kaufman & Watson [229]	$\frac{\Delta T_c}{T_c^{(\text{id})}} \sim (a\rho^{1/3})^{1/2}$
1964	Huang [230]	$\frac{\Delta T_c}{T_c^{(\text{id})}} \sim (a\rho^{1/3})^{1/2}, (a > 0)$
1971	Fetter & Walecka [231]	$\frac{\Delta T_c}{T_c^{(\text{id})}} < 0$
1982	Toyoda [232]	$\frac{\Delta T_c}{T_c^{(\text{id})}} \approx -3.5(a\rho^{1/3})^{1/2}$
1992	Stoof [233]	$\frac{\Delta T_c}{T_c^{(\text{id})}} = c a\rho^{1/3} + O(a\rho^{1/3})$
1996	Bijlsma & Stoof [234]	$c=4.66$
1997	Grüter, Ceperley & Laloë [235]	$c=0.34$
1999	Holzmann, Grüter & Laloë [236]	$c=0.7$
1999	Holzmann & Krauth [237]	$c=2.3$
1999	Baym, Blaizot, Holzmann, Laloë & Vautherin [238]	$c=2.9$
1999	Huang [239]	$\frac{\Delta T_c}{T_c^{(\text{id})}} \approx 3.5(a\rho^{1/3})^{1/2}$
2000	Reppy <i>et. al.</i> [240]	$c=5.1^1$
2001	Arnold & Moore [224]	$c=1.32$
2001	Kashurnikov, Prokofev & Svistunov [241]	$c=1.29$
2003	Kleinert [242]	$c=1.14$
2004	Kastening [243]	$c=1.27$
2004	Nho & Landau [244]	$c=1.32$
2010	Betz & Ueltschi [245]	$c=-2.33$

Table 5.1: Summary of the various functional dependencies and numerical coefficients predicted (and measured: [240]) for the lowest-order shift in the critical temperature of the homogeneous dilute Bose gas.

¹ It was pointed out in [241] that the estimation of the interparticle scattering length in this study was not correct.

It is now generally accepted that in a dilute Bose gas the T_c shift is, to first order, linear in the gas parameter ([234, 238, 237, 240, 224, 241, 246, 225, 226, 227]), with repulsive interactions believed to *enhance* condensation, i.e. shift the transition temperature above its ideal-gas value¹, with the coefficient having a value of approximately $c \approx 1.3$ [224, 241]:

$$\frac{\Delta T_c}{T_c^{(\text{id})}} \approx 1.3an^{1/3} \approx 1.8\frac{a}{\lambda_0} \quad (5.5)$$

In the above expression, we have introduced the alternative interaction parameter a/λ_0 , with a the scattering length and λ_0 the thermal wavelength at the ideal-gas critical temperature. Conversion between the two parameters is done using the usual relationship $n\lambda_0^3 = \zeta(3/2)$.

5.1.2 T_c -shift in a non-uniform system

The problem of the interaction shift of T_c in experiments on ultracold atomic gases is made even more complex by the fact that these systems are produced in harmonic traps. For a harmonically trapped gas, the condensation temperature is defined for a given atom number N , rather than for a given density due to the inhomogeneity of the cloud.

As mentioned previously, the ideal gas prediction for the transition temperature in a trap of geometric-mean frequency $\bar{\omega}$ is

$$T_c^{(\text{id})} = \frac{\hbar\bar{\omega}}{k_B} \left(\frac{N}{\zeta(3)} \right)^{1/3} \quad (5.6)$$

where $\zeta(3) \approx 1.202$. This criterion corresponds to a phase-space density in the trap centre equal to the uniform-system critical value i.e. $n(0)\lambda_T^3 = \zeta(3/2)$. The interaction shift of the critical point can therefore be expressed either as a shift in the critical temperature for a given atom number, $\Delta T_c(N)$, for the purposes of comparison with theoretical literature, or as a shift in the critical number at a given temperature, $\Delta N_c(T)$, for easier visualization (as in figures 5.1 and 5.8, below) and more closely related to our experimental procedure for determining the critical point, described in section 5.3.

¹ Namely, condensation is predicted to occur at a phase space density below the ideal gas critical value of $\zeta(3/2) \approx 2.612$.

Two opposing effects compete in determining the overall shift of the critical point in a trapped gas: similarly to the homogeneous gas and in the spirit of the local density approximation (LDA), correlations near the critical point should act to reduce the critical density i.e. raise the critical temperature, as implied by equation 5.5. However in conjunction with this, the mean-field repulsion between the atoms broadens their spatial distribution and hence reduces their central density, causing a reduction in the critical temperature. For weak interactions, the latter effect dominates the former, giving rise to a positive value of ΔN_c , or equivalently a negative value of ΔT_c . Figure 5.1 illustrates these two competing effects.

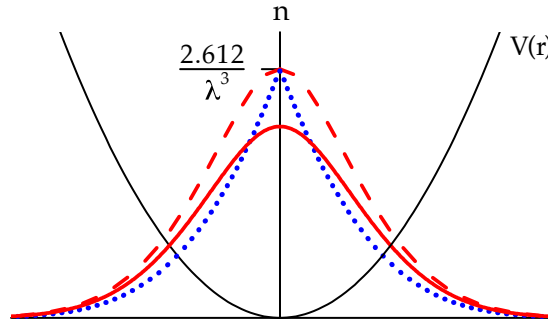


Figure 5.1: Opposing effects of interactions on the critical point of a Bose gas in a harmonic potential $V(r)$. Compared to an ideal gas (dotted blue line) with the same T_c , repulsive interactions reduce the critical density, but also broaden the density distribution (solid red line). Mean-field theory (dashed line) captures only the latter effect, and predicts an increase of the critical atom number N_c at fixed temperature T , equivalent to a decrease of T_c at fixed N .

The negative T_c shift due to the broadening of the spatial profile can be calculated within mean-field theory. This calculation was carried out in [198] and yields

$$\frac{\Delta T_c}{T_c^{(\text{id})}} \approx -1.33 \frac{a}{a_{\text{ho}}} N^{1/6} \approx -3.426 \frac{a}{\lambda_0} \quad (5.7)$$

where a_{ho} is the trap oscillator length $a_{\text{ho}} = \sqrt{\hbar/m\bar{\omega}}$. This prediction corresponds to the dashed-line spatial profile in figure 5.1 and we note that this result neglects finite-size effects as well as (by definition) the correlation effects mentioned above.

The dominance of the negative MF shift of T_c over the positive beyond-MF one goes beyond the difference in numerical pre-factors in equations 5.5 and 5.7. In contrast to the homogeneous case, at the condensation point in a non-uniform system only the central region of the cloud is close to criticality. The effect of critical correlations on T_c is therefore expected to be reduced by a factor $\sim (a/\lambda_0)^3$ compared to the uniform case, corresponding to the ratio of the volume of the

critical region to that of the thermal cloud. The MF result of equation 5.7 should therefore be exact at first order in a/λ_0 .

There have been several attempts to theoretically combine the effects of MF repulsion and beyond-MF correlations on T_c for a harmonically trapped gas [247, 248, 249, 250, 251], but no consensus has yet been reached beyond the expectation that the additional beyond-MF shift should be positive. Recent calculations, for example, predict a logarithmic term of the form $\ln\left(\frac{a}{\lambda_0}\right)\left(\frac{a}{\lambda_0}\right)^2$ in addition to the quadratic term, such that the full functional form (neglecting finite-size effects) is given by

$$\frac{\Delta T_c}{T_c^{(\text{id})}} \approx c_1 \frac{a}{\lambda_0} + \left(c'_2 + c''_2 \ln\left(\frac{a}{\lambda_0}\right) \right) \left(\frac{a}{\lambda_0}\right)^2 \quad (5.8)$$

with $c_1 = -3.426032$, $c'_2 = \frac{-32\pi\zeta(2)}{3\zeta(3)} = -45.856623$ and $c''_2 = -155$ [249].

Table 5.2 summarizes the T_c -shift predictions discussed in the preceding sections.

		Uniform	Harmonic
Ideal		$T_c^{(\text{id})} = \left(\frac{n}{\zeta(3/2)}\right)^{3/2} \frac{2\pi\hbar^2}{k_B m}$	$T_c^{(\text{id})} = \frac{\hbar\omega}{k_B} \left(\frac{N}{\zeta(3)}\right)^{1/3}$
Interacting	MF	$\frac{\Delta T_c}{T_c^{(\text{id})}} = 0$	$\frac{\Delta T_c}{T_c^{(\text{id})}} = -3.426 \frac{a}{\lambda_0}$
	bMF	$\frac{\Delta T_c}{T_c^{(\text{id})}} \approx 1.3an^{1/3}$ $\approx 1.8 \frac{a}{\lambda_0}$	$\frac{\Delta T_c}{T_c^{(\text{id})}} = c_1 \frac{a}{\lambda_0}$ $+ \left(c'_2 \ln \frac{a}{\lambda_0} + c''_2 \right) \left(\frac{a}{\lambda_0}\right)^2$ $+ O\left(\frac{a}{\lambda_0}\right)^3$

Table 5.2: Summary of the predicted critical temperatures and their interaction-induced shifts in uniform and harmonic trapping potentials.

5.2 Previous experimental studies

Previous measurements of the T_c shift have been performed for a/λ_0 ranging from 0.007 [252] to 0.024 [253]. The results of these measurements are consistent with the MF prediction of equation 5.7 within experimental errors and could not discern the effects of critical correlations. Below is a brief summary of a selection of these studies and their findings.

1. Ref. [209] reports the results of early experiments carried out using ^{87}Rb in a trap with $(\omega_x, \omega_y, \omega_z) = 2\pi \times (132, 132, 373)\text{Hz}$. The condensed fraction as a function of temperature is compared to the ideal-gas prediction $\frac{N_0}{N} = 1 - \left(\frac{T}{T_c^{(\text{id})}}\right)^3$, including finite-size effects, as shown in figure 5.2.

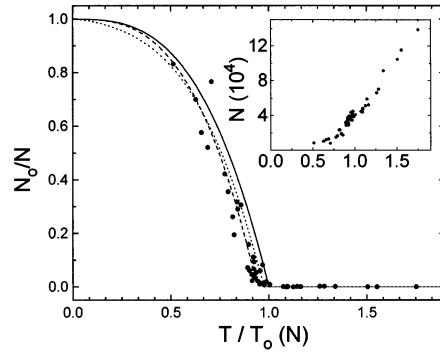


Figure 5.2: Condensed-fraction against reduced temperature, reproduced from [209]. Condensation occurs with 40,000 atoms at a temperature of 280nK.

A least-squares fit to the form $\frac{N_0}{N} = 1 - \left(\frac{T}{T_c}\right)^3$ yields a value of $T_c = 0.94(5)T_c^0$ for the critical temperature, with finite-size effects estimated to account for a shift of 3% from the ideal-gas value and interaction effects speculated to account for the remaining shift.

2. Ref. [210] reports on experiments using ^{87}Rb in a cigar-shaped trap with $(\omega_r, \omega_z) = 2\pi \times (11.7, 33.1)\text{Hz}$. Condensation occurs with $N \approx 1.5 \times 10^6$ and $T \approx 430\text{nK}$ and the results are compared to the ideal-gas prediction, as shown in figure 5.3.

Although a least-squares fit to the condensed fraction plot yielded $T_c = (0.96 \pm 0.15)T_c^0$ for the critical temperature, in these experiments the thermal and condensed atom numbers are determined from gaussian fits to both components and the overall accuracy in the atom number is estimated at 20%. The accuracy in the determination of the temperature is estimated at

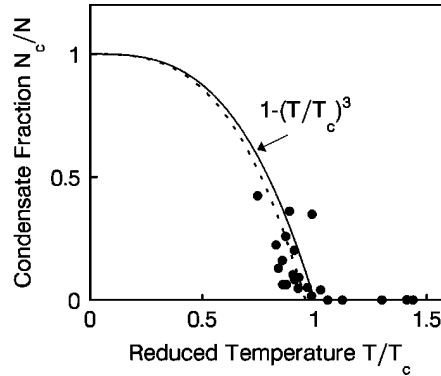


Figure 5.3: Condensed-fraction against reduced temperature, reproduced from [210].

15% and therefore no clear departure of the critical temperature from its ideal-gas value is observed within experimental error.

- Ref. [253] reports on a systematic study of the interaction shift in a ^{87}Rb gas. The interaction parameter is varied by changing the atom number loaded into the trap and the critical number is obtained by monitoring the appearance of a condensed component.

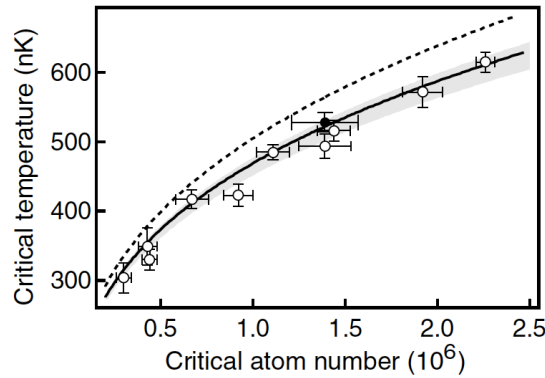


Figure 5.4: T_c -shift as a function of number, $T_c(N)$, as reported in [253].

Ideal-gas behaviour is excluded by over two standard deviations (see figure 5.4) and the data agree with the mean-field prediction of equation 5.7. Writing their results in the form $\Delta T_c/T_c^0 = \alpha N^{1/6}$, the authors obtain $\alpha = -0.009(1)_{-0.001}^{+0.002}$, compared to the prediction $\alpha \approx -0.007$ of equation 5.7. Within experimental sensitivity, no evidence is seen for the predicted condensate-enhancing effects of beyond-mean-field critical fluctuations.

The authors of [253] conclude that observation of beyond-mean-field effects should be made possible by: (1) improved thermometry, with an accuracy of 1% or better, (2) enhancement of the interaction shift, possibly through use

of a Feshbach resonance and (3) local measurement of the critical density near the trap centre, which should be most sensitive to critical fluctuations. The results reported in this chapter are precisely an implementation of the first two of these measures. Furthermore, a separate study performed in our group [254] has used measurements of the finite condensed fraction already present at the mean-field critical point to confirm the ‘condensate-boosting’ effect of critical fluctuations and the expected scaling behaviour of the condensed fraction with interaction strength. This study also provides a useful connection to the uniform-potential T_c -shift via the local density approximation (LDA). However, discussion of these results is beyond the scope of this thesis.

4. Ref. [252] reports on experiments performing *in-situ* phase-contrast imaging of trapped ^{23}Na clouds. Best agreement with the measured spatial profiles is provided by the Popov mean-field approximation (see section 4.5). The chemical potential extracted using this model is used to obtain an estimate of $\Delta T_c/T_c^0 = -0.027 \pm 0.001$ for the critical temperature, in good agreement with the prediction of equation 5.7, $\Delta T_c/T_c^0 \approx -0.025$.
5. The interaction shift in a **uniform** system was measured in a dilute sample of ^4He adsorbed in a porous glass (vycor) [240]. The gas parameter $an^{1/3}$ was varied over the range $0.03 \rightarrow 0.075$ (corresponding to $a/\lambda_0 = 0.021 \rightarrow 0.054$) by changing the density of adsorbed ^4He and T_c was measured via the onset of superfluidity in the sample (see figure 5.5).

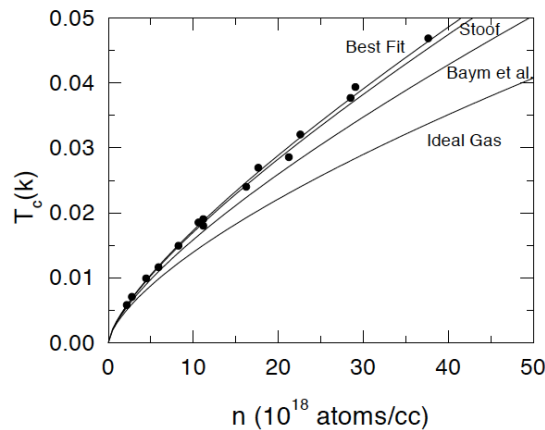


Figure 5.5: Critical temperature T_c as a function of density for the ^4H -vycor system. The onset of superfluidity is measured by observing the change in period of a torsional oscillator to which the sample is mounted. Figure from [240].

These measurements confirmed the positive sign of the shift, in qualitative

agreement with equation 5.5, but found a coefficient of 5.1 ± 0.9 for the linear coefficient, closer to the value calculated in [233, 234].

Figure 5.6 shows the mean-field prediction of equation 5.7, together with the experimental results reported in [209, 253] and [252].

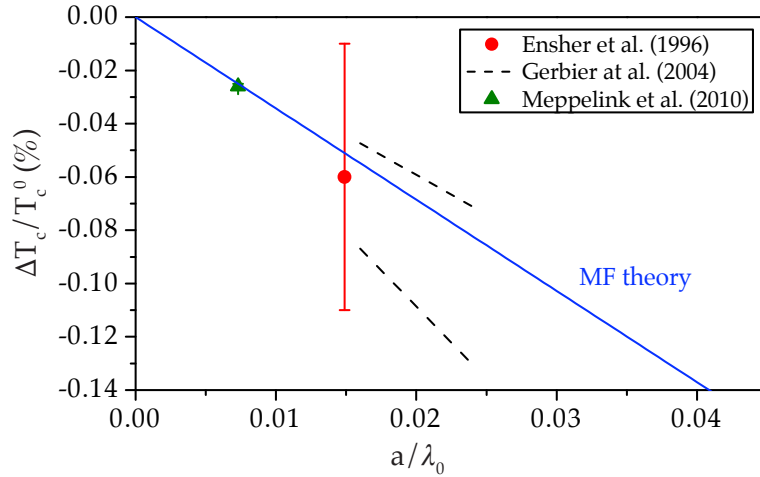


Figure 5.6: The mean-field prediction of equation 5.7 is shown (blue line), together with the measurements of [252] (green triangle), [209] (red point) and [253] (interval between dashed lines)

5.3 Experimental method

The experimental procedure we use to probe the critical point in our interacting gas is almost identical to that used in the non-saturation studies described in chapter 4. These measurements likewise begin with a partially-condensed ^{39}K gas, prepared in its $|F, m_F\rangle = |1, 1\rangle$ internal state in our crossed optical dipole trap. For the experiments described in this chapter, the geometric mean of the trap frequencies is in the range $\bar{\omega} = 2\pi \times (75 \rightarrow 85)\text{Hz}$ corresponding to measurements with atom numbers $N \approx (2 \rightarrow 8) \times 10^5$.

The critical point is measured by fixing the optical trap depth and allowing the total atom number to decay towards N_c via inelastic processes. Here too we rely on elastic collisions to redistribute atoms between the condensed and thermal components and on the fixed trap depth to maintain an essentially constant temperature (see figure 4.3).

We explore the range $0.001 < a/\lambda_0 < 0.06$ by exploiting the 402.5G Feshbach resonance in the $|1, 1\rangle$ state. The cloud is initially prepared at a scattering length of $a = 135a_0$, as described in chapter 3, which is then adjusted to the desired

value by ramping the Feshbach field to the appropriate strength over a few ms. The cloud is held for a variable hold time before being released from the trap and imaged after a 19ms time-of-flight. The total hold time required for the atom number to drop below N_c depends on the specific value of a being measured and the temperature, ranging between $5 \rightarrow 18$ s.

In addition to extending the a/λ_0 range over previous experiments, use of the Feshbach resonance allows us to eliminate several key sources of statistical and systematic errors, greatly improving both the precision and accuracy of our ΔT_c measurements. More specifically, turning off interactions during TOF allows us to detect smaller condensed fractions, and performing a low- a reference measurement for each interaction strength allows us to isolate the interaction shift and eliminate all a -independent systematic errors (see below).

1) Removal of interactions during time-of-flight

In order to home in on the critical point we use the Feshbach resonance to turn off the interactions during time-of-flight. To accomplish this we quickly (in $\lesssim 2$ ms) ramp the Feshbach field to the zero-crossing at 350G immediately after release of the gas from the trap. This minimizes the expansion of small condensates during TOF and allows us to reliably detect condensed fractions as small as $\sim 10^{-3}$ (see figure 5.7).

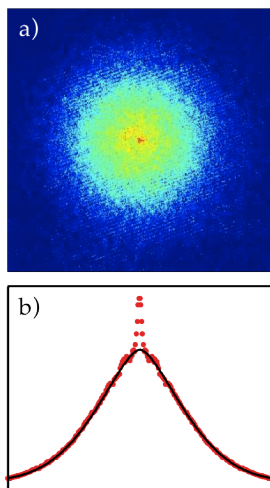


Figure 5.7: (a) An absorption image of a cloud with 450 000 atoms and a 0.14 % condensed fraction. We show an azimuthally averaged cut through the column density for illustrative purposes, while the full 2D distribution is used for fitting. The gas was prepared at a large scattering length, $a = 274 a_0$, but the interactions were turned off in TOF.

Once imaged, we determine small condensed numbers N_0 by performing a direct summation over the density distribution in the central part of the image, after

subtracting a fit to the smooth thermal background. For $N_0 > 2000$ this agrees with a standard Thomas-Fermi fit, but is more reliable for smaller condensates.

2) Reference measurements at low a

For each measurement series at a given a and λ_0 , we concurrently take a reference measurement with a different a , same $\bar{\omega}$ and very similar N , hence very similar λ_0 . This is done by alternating experimental runs at the two different scattering lengths. Specifically, for the reference point we choose a small a such that $a/\lambda_0 \approx 0.005$. Measurements at this value of the interaction parameter are still taken to be in thermal equilibrium, as discussed in section 5.5. With this procedure, we thus directly access the small T_c shift due only to the difference in a/λ_0 , and essentially eliminate all a -independent systematic errors that usually affect absolute measurements of $T_c(N, \bar{\omega}, a)$. These include uncertainties in the absolute calibration of N and $\bar{\omega}$, as well as the additional T_c shifts due to finite-size effects [46] and the small anharmonicity of the trapping potential [255]. Figures 5.8a and 5.8b show the relationship between the condensed (N_0) and thermal (N_T) atom number near the critical point and illustrate the differential measurement for one of our experimental series.

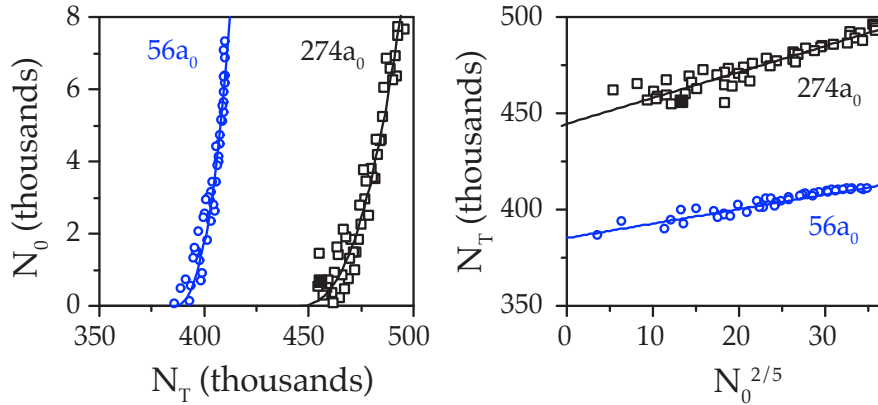


Figure 5.8: Determination of the critical point and differential interaction shift. (a) Condensed (N_0) versus thermal (N_T) atom number for two concurrently taken series with $a = 56a_0$ (blue circles) and $a = 274a_0$ (black squares). Note that all points correspond to condensed fractions below 2%. The data is scaled to the same temperature ($T = 240\text{nK}$) and shows the shift of the critical point in the form $\Delta N_c(T)$. The solid point corresponds to the image shown in figure 5.7. Solid lines show the extrapolation to $N_0 = 0$, necessary to accurately determine N_c . (b) N_T is plotted versus $N_0^{2/5}$ for the same data as in (a), showing more clearly the extrapolation procedure.

Systematic errors

In general, interactions increase the kinetic energy of atoms during TOF, resulting in an a -dependent error in the measured temperature which is not cancelled out by our differential measurements. To minimize this error we extract the temperature from a fit to only the wings of the thermal distribution, excluding the central thermal radius from the fit as described in section 3.15 (see also [186, 185]). The removal of interactions during TOF using the Feshbach resonance also serves to reduce this error, but the reduction of a is gradual over ≈ 2 ms. We have measured the difference between the (apparent) temperatures with and ‘without’ interactions during TOF to be approximately linear in a/λ_0 , and about 4% for $a = 400a_0$ and $\lambda_0 \approx 10^4 a_0$. By varying the time at which we turn off a , we estimate our residual error to be 1–2% at $a/\lambda_0 = 0.04$. This estimate is supported by numerical simulations which reproduce the experiments quite well.

Additionally, interactions modify the initial in-trap momentum distribution. This *reduces* the apparent T due to the positive chemical potential preferentially enhancing the population of low-energy states. We numerically estimate this effect to also be approximately linear in a/λ_0 , and about 1 – 2% at $a/\lambda_0 = 0.04$. Fortunately, the in-trap and in-TOF effects partially cancel, resulting in a net error in $\Delta T_c/T_c^{(\text{id})}$ of at most $\pm 1\%$ at $a/\lambda_0 = 0.04$.

5.4 Extracting the T_c shift

Extrapolating to find N_c

The critical temperature of an experimental series is found by measuring the temperature at the critical point, namely when $N_{\text{tot}} = N_c = N(N_0 \rightarrow 0)$. In order to precisely locate N_c , it is therefore essential to carefully extrapolate N_T to the $N_0 \rightarrow 0$ limit in order to accurately determine N_c . As can be seen in figure 5.8a, the rise of N_0 with N_T is not simply vertical due to the non-saturation of the thermal component in a partially condensed gas (c.f. chapter 4). Since our measurements take place at small N_0 , we perform the extrapolation using the Hartree-Fock non-saturation prediction described in section 4.6

$$N_T = N_c + S_{\text{HF}} N_0^{2/5} \quad (5.9)$$

with the non-saturation slope $S_{\text{HF}}(T, \bar{\omega}, a)$ calculated with no free parameters

using equations 4.33 and 4.34. This extrapolation is shown in figure 5.8b. The shot-to-shot temperature fluctuations near N_c are at the 1% level, while the T drift over the entire series is $< 10\%$. This drift is analytically compensated, as described in chapter 4, by applying the mean-field scaling, which amounts to plotting $N_T(T_c/T)^3$ against $N_0^{2/5}(T_c/T)$, as is done for the data presented in chapter 4.

Calculation of ΔT_c

The T_c *shift* for each series is obtained by comparing the measured value of T_c with that obtained from its corresponding low- a reference series. If the two series possessed identical N_c values, ΔT_c would simply be given by the difference in their respective transition temperatures. In order to correct for the small (few %) difference in N_c , we apply the ideal-gas scaling $T_c \propto N^{1/3}$ to the reference series temperature. i.e. $T_c^{\text{ref}*} = T_c^{\text{ref}}(N_c^{\text{m}}/N_c^{\text{ref}})^{1/3}$, where $(N_c^{\text{ref}}, T_c^{\text{ref}})$ and $(N_c^{\text{m}}, T_c^{\text{m}})$ are the critical number and temperature for the reference and ‘measured’ series, respectively. In plain words, $T_c^{\text{ref}*}$ is what the critical temperature of the reference series would be if it had the same value of N_c as the measured series. The final expression for the T_c shift is therefore given by

$$\frac{\Delta T_c}{T_c^{(\text{id})}} = \frac{T_c^{\text{m}} - T_c^{(\text{id})}}{T_c^{(\text{id})}(N_c^{\text{m}})} \quad (5.10)$$

where the value of $T_c^{(\text{id})}$ is obtained from $T_c^{\text{ref}*}$ using the mean-field shift, i.e. $T_c^{(\text{id})} = T_c^{\text{ref}*}/(1 - 3.426 \frac{a}{\lambda_0})$. We shift our results to ensure that our $a/\lambda_0 \approx 0.005$ reference point lies on the mean-field prediction, although assuming the ideal-gas value of $T_c^{(\text{id})}$ for $a/\lambda_0 = 0.005$ would not affect our results within error bars. Figure 5.9 summarizes our equilibrium measurements of the interaction shift $\Delta T_c/T_c^{(\text{id})}$. We took data with a range of atom numbers, $N \approx (2 \rightarrow 8) \times 10^5$ (corresponding to $T_c^{(\text{id})} \approx 180 - 330$ nK), in order to verify that our results depend only on the interaction parameter a/λ_0 .

The dashed blue line shows the MF result of equation 5.7, which agrees very well with the data for $a/\lambda_0 \lesssim 0.01$. For larger a/λ_0 we observe a clear deviation from this prediction. All data points are fitted well by a second-order polynomial (solid red line), $\Delta T_c/T_c^{(\text{id})} = b_1(a/\lambda_0) + b_2(a/\lambda_0)^2$, with $b_1 = -3.5 \pm 0.3$ and $b_2 = 46 \pm 5$. Calibration of the y-axis is done by ensuring that this fit extrapolates to $\Delta T_c/T_c^{(\text{id})} = 0$ for $a/\lambda_0 \rightarrow 0$. Within our error bars, the predicted

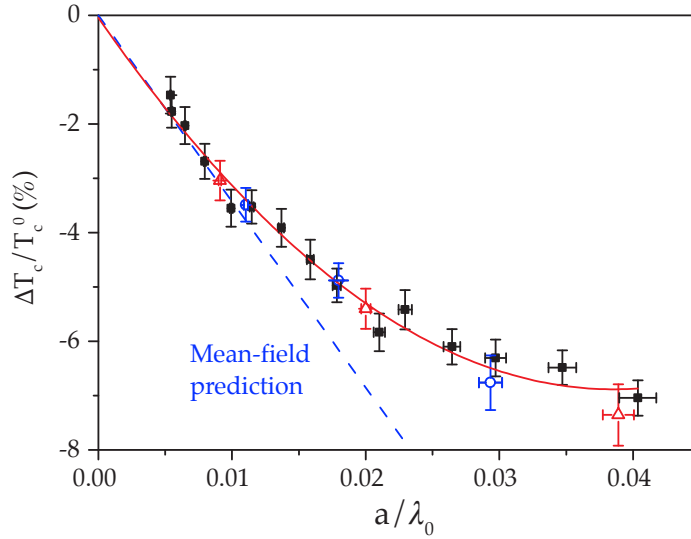


Figure 5.9: Interaction shift of the critical temperature. Data points were taken with $N \approx 2 \times 10^5$ (blue circles), 4×10^5 (black squares), and 8×10^5 (red triangles) atoms. The dashed line is the mean-field result $\Delta T_c/T_c^{(\text{id})} = -3.426 a/\lambda_0$. The solid line shows a second-order polynomial fit to the data (see text). Vertical error bars show standard statistical errors. Horizontal error bars reflect the 0.1 G uncertainty in the position of the Feshbach resonance.

small logarithmic corrections of equation 5.8 are not discernible. The value of b_1 is in excellent agreement with the MF prediction of -3.426 [198]. The value of b_2 strongly excludes zero, and its sign is consistent with the expected effect of beyond-MF critical correlations. These measurements provide the first clear observation of beyond-MF effects on the transition temperature of a harmonically trapped gas.

5.5 Non-equilibrium measurements

In this section we discuss the requirements on the relationship between the hold time in the CDT, t_{hold} , the elastic scattering rate, γ_{el} and the relevant atom-number decay time τ for the measurements of T_c to faithfully reflect the equilibrium properties of the gas. In general, a system with continuous dissipation can only be ‘close to’ thermodynamic equilibrium. For an atomic gas, the proximity to equilibrium depends on the dimensionless parameter $\gamma_{\text{el}}\tau$, which measures the relative rates of elastic and inelastic processes.

Following [192], we make use of the following expressions in calculating γ_{el} :

$$\begin{aligned}\gamma_{\text{el}} &= n(0)v_{\text{th}}\frac{\sigma_0}{2} \\ n(0) &= N\bar{\omega}^3\left(\frac{m}{2\pi k_{\text{B}}T}\right)^{3/2} \\ v_{\text{th}} &= \sqrt{\frac{8k_{\text{B}}T}{\pi m}}\end{aligned}\tag{5.11}$$

where $n(0)$ is the central density, v_{th} the mean thermal velocity and σ_0 the scattering cross-section. In practice the elastic scattering rate γ_{el} required for equilibrium measurements also depends on the precision with which measurements are made. In these experiments, we measure N_c to roughly 1%, and so we require that the gas continuously re-equilibrate on a timescale τ corresponding to only a 1% atom loss. This implies a value of γ_{el} roughly 100 times higher than would be naively assumed by taking the $1/e$ lifetime as the relevant timescale for decay of the cloud.

Equilibration is usually considered to take about 3 collisions per particle [191]. With this in mind, for all the measurements shown in figure 5.9 we made sure that the number of collisions occurring on the timescale τ fulfilled $\gamma_{\text{el}}\tau > 5$. All our data also satisfy the condition $t_{\text{hold}} > \tau > 1/\bar{\omega}$, necessary for global equilibrium to be established.

It is interesting to observe what happens if we violate these stringent equilibrium criteria. In figure 5.10a we show measurements with $N \approx 4 \times 10^5$ atoms ($\lambda_0 \approx 10^4 a_0$), extending beyond the equilibrium region shown in figure 5.9.

We still show only measurements satisfying $t_{\text{hold}} > \tau > 1/\bar{\omega}$ and $\gamma_{\text{el}}t_{\text{hold}} > 5$, so that there is nominally enough time for global equilibrium to be established. However if $\gamma_{\text{el}}\tau$ is not large enough, the elastic collisions cannot ‘keep up’ with the continuously present dissipation. The resulting non-equilibrium effects can thus not be eliminated by simply extending t_{hold} , but are an intrinsic property of the system. In figure 5.10b we plot $\gamma_{\text{el}}\tau$, based on γ_{el} calculated from equation 5.11 and τ measured near the critical point for each series. Individually, $\gamma_{\text{el}} \approx 0.7 - 1000 \text{ s}^{-1}$ and $\tau \approx 2 \text{ ms} - 1 \text{ s}$ vary vastly as a function of a (γ_{el} increasing and τ decreasing), but the breakdown of equilibrium appears to occur at very similar values of $\gamma_{\text{el}}\tau$ in the low- and high- a limit.

Since non-equilibrium phenomena necessarily depend on additional factors such

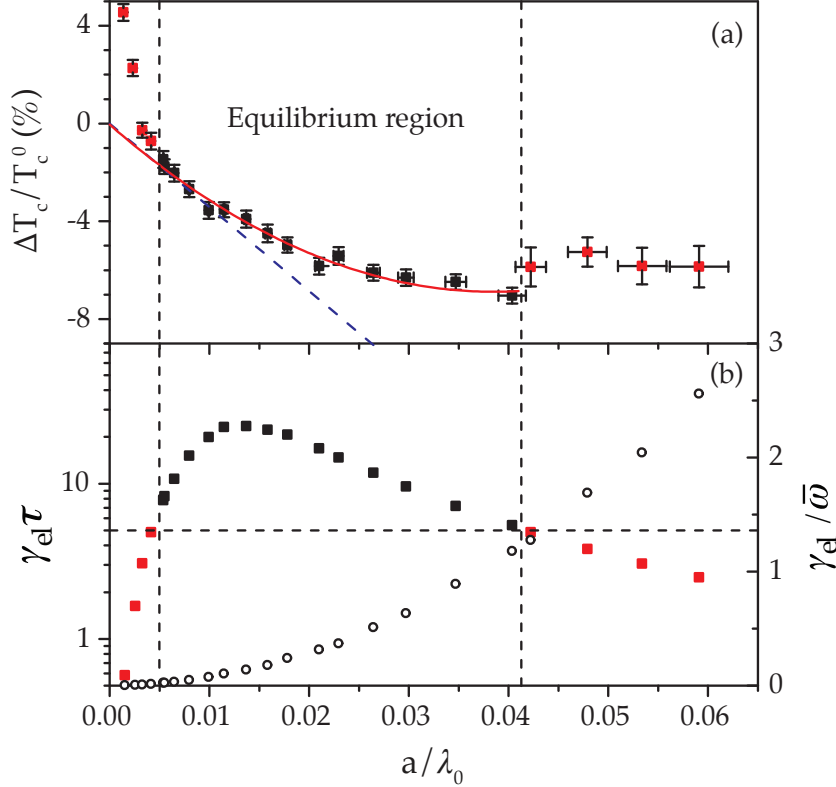


Figure 5.10: Non-equilibrium effects. (a) $\Delta T_c/T_c^{(id)}$ for $N \approx 4 \times 10^5$ atoms is determined following the procedure which assumes equilibrium (as in figure 5.8). At both very low and very high a the apparent T_c deviates from the equilibrium curve. (b) Equilibrium criteria: $\gamma_{el}\tau$ (solid squares) is the number of elastic collisions per particle during 1% atom-loss; $\gamma_{el}/\bar{\omega} = 1$ (open circles) marks the onset of the hydrodynamic regime.

as the initial conditions, we do not expect our quantitative results to be universal and instead discuss only the qualitative trends in our data. In the small- a limit we observe a smooth rapid rise of the apparent T_c above the equilibrium curve (and hence above $T_c^{(id)}$ for $a \rightarrow 0$). We can qualitatively understand this effect within a simple picture. In this regime, losses are most likely dominated by inelastic collisions with background particles ('one-body processes') which equally affect N_0 and N_T . The net effect of the equilibrating elastic collisions would therefore be to transfer atoms from the condensate to the thermal cloud. However the dissipation rate is too high compared to γ_{el} , and so N_0 remains non-zero even after the total atom number drops below the equilibrium critical value N_c (i.e. the measured T_c is above the equilibrium value). Although strictly speaking T is not defined out of equilibrium, the absolute value of the observed effect is sufficiently small that an equilibrium distribution function fits the data very well and provides a good measure of the energy content of the cloud.

Our measurements in the large- a limit suggest that the initial breakdown of equilibrium again results in condensates surviving above the equilibrium T_c . However the physics in this regime is much richer, with several potentially competing effects requiring further investigation. For example, three-body decay affects N_0 and N_T differently, the thermal component is far from saturation (chapter 4), and the gas also enters the hydrodynamic regime, $\gamma_{\text{el}}/\bar{\omega} > 1$ (see figure 5.10(b)).

5.6 Conclusions

In conclusion, we have performed high-precision studies of the effects of interactions on Bose-Einstein condensation of a trapped atomic gas. In the regime where equilibrium measurements are possible, our most important observation is the clear deviation from mean-field behaviour for sufficiently strong interactions. The additional positive shift of the critical temperature is a clear signature of the condensation-enhancing effect of critical fluctuations. These measurements should provide motivation and guidance for further theoretical studies of this difficult problem. We have also studied non-equilibrium condensation phenomena, for both very weak and very strong interactions. Further study of these effects should prove useful for understanding condensation in intrinsically out-of-equilibrium systems, such as polariton gases.

The interplay between trap geometry and interaction strength is also a promising direction for future research on both the shift in the critical point and the out-of-equilibrium behaviour of the system. Indeed, preparations are already underway in our group for generation of a two-dimensional trapping potential for exploring the effects of reduced-dimensionality on the thermodynamic behaviour of our gases. Preliminary designs and tests of the setup for generating these potentials optically are described in appendices C and F.

6

Summary and Outlook

“What goes around may come around, but it never ends up exactly the same place, you ever notice? Like a record on a turntable, all it takes is one groove’s difference and the universe can be on into a whole ‘nother song.”

Thomas Pynchon, *Inherent Vice*

It is my hope that this thesis has served two main purposes. The first was to provide relevant and useful information regarding the design and construction of an apparatus for reliable production of ultracold rubidium and potassium gases. During the design stage, we explicitly endeavoured to assemble an apparatus that was flexible, versatile and simple, while compromising as little on performance as possible. Plentiful optical access, the implementation of both magnetic and optical trapping potentials, the inclusion of fermionic ^{40}K sources, a reliable and straightforward transport mechanism and an abundance of coils for production of custom magnetic field configurations, should all contribute to the ability of this setup to serve as a platform for many successful experiments in the future. I hope that other students, both within our group and out, find this record of our experiences to be a helpful resource in their own studies.

We have used this system to produce condensed clouds of both ^{39}K and ^{87}Rb - the second group in the world to do so. A conveniently-located, broad Feshbach resonance in the ground state of ^{39}K makes this species one of the most attractive for systematic studies into the effects of interactions on the thermodynamic behaviour of cold gases. The second purpose of this thesis was the description of two experiments, carried out using condensed clouds of ^{39}K and fundamentally reliant on this precise control over the atoms' interaction strength. The first of these experiments scrutinized Einstein's original saturation picture as the driving mechanism behind BEC. The deviation from this idealized picture due to interatomic interactions was found to be very strong, and could only be captured quantitatively by a mean-field treatment in the regime of small condensate number. In the larger-condensate regime a more heuristic approach was used to quantify the lack of saturation and by extrapolation of our results to the non-interacting limit we were able to recover complete saturation in the ideal-gas limit. This provided the first direct experimental evidence for excited-state saturation as the basic mechanism behind BEC, confirming the purely statistical nature of this phase-transition as originally described by Einstein.

The second experiment described in this thesis made use of similar experimental techniques to those developed in the saturation study to perform high-precision measurements of the shift in the critical temperature induced by interparticle interactions. In addition to confirming the predictions of mean-field theory in the regime of weak interactions, we have provided the first observation of the effects of interparticle correlations, arising in the vicinity of the transition, on the critical temperature. These beyond-mean field corrections are in qualitative agreement with recent theoretical predictions and our measurements should serve as a useful guide for further theoretical efforts. As part of this study, we have also observed some intrinsic non-equilibrium behaviour of our trapped clouds in the regimes of both very weak and very strong interactions.

The technique shared by both of these experiments is their reliance on the gradual decay in atom number resulting from inelastic processes and background collisions. Trap-loss measurements have long been used to study collisional dynamics of trapped clouds in magneto-optical traps [256, 257, 258, 259, 260, 55] as well as of condensed clouds [261]. To these studies the current work adds the probing of thermodynamic quantities such as the condensed fraction and the critical temperature. There can be no doubt that many more insights are waiting to be extracted from such conceptually straightforward yet subtle experiments.

Many open questions remain, predominantly related to exploring the effects of interparticle interactions on the behaviour of these systems under different circumstances. These include, but are not limited to

- Confinement in potentials of reduced dimensionality.
- Confinement in periodic potentials.
- *In-situ* measurements of thermodynamic quantities.
- Novel interaction regimes, such as very strong interactions and long-range interaction potentials.
- Confinement in the presence of impurities and/or disorder.
- Trapping of Bose-Bose and Bose-Fermi mixtures in the presence of tuneable interspecies and intraspecies interactions.
- Manipulation using artificial optically-generated gauge potentials.

All in all, degenerate quantum gases promise to yield many physical insights and applications for years to come by providing an almost ideal test-bed in which to investigate many open questions in condensed matter physics, materials science, fundamental quantum mechanics and even cosmology [262, 263], as well as applications in fields ranging from metrology to quantum communication and quantum information processing.

Appendices

A

^{87}Rb and ^{39}K properties

General and optical properties of ^{87}Rb and ^{39}K . The ^{87}Rb data is taken from [110] and the ^{39}K data from [111], both of which contain references to the original data sources.

Property	^{87}Rb value	^{39}K value
Natural abundance	27.83(2) %	93.2581(44) %
Mass	86.909180520(15) amu	38.96370668(20) amu
Nuclear spin (I)	3/2	3/2
Atomic number (Z)	37	19
Melting point	39.31 °C	63.65 °C(336.8 K)
Boiling point	688 °C	774.0 °C(1047.15 K)
Vapor pressure at 293 K	4.0×10^{-7} mbar	1.3×10^{-8} mbar
Density at 293 K	1.53 g/cm ³	0.862 g/cm ³

Table A.1: General properties of ^{87}Rb and ^{39}K . Values taken from references [110] and [111], respectively.

Property	symbol	D_1 -line value	D_2 -line value
Frequency	ν	377.1074635(4) THz	384.2304844685(62) THz
Wavelength	λ	794.9788509(8) nm	780.241209686(13) nm
Wavenumber	$k/2\pi$	12578.950985(13) cm ⁻¹	12816.54938993(21) cm ⁻¹
Lifetime	τ	27.70(4) ns	26.24(4) ns
Natural linewidth	$\Gamma/2\pi$	5.746(8) MHz	6.065(9) MHz
Recoil velocity	v_{rec}	0.57754 cm/s	0.58845 cm/s
Recoil temperature	T_{rec}	348.66 nK	361.96 nK
Doppler temperature	T_D	137 μ K	146 μ K
Saturation intensity	I_s		1.669(2)mW/cm ²

Table A.2: D_1 - and D_2 -line optical properties of ⁸⁷Rb. Values taken from reference [110].

Property	symbol	D_1 -line value	D_2 -line value
Frequency	ν	389.286058716(62) THz	391.01617003(12) THz
Wavelength	λ	770.108385049(123) nm	766.700921822(24) nm
Wavenumber	$k/2\pi$	12985.1851928(21) cm ⁻¹	13042.8954964(4) cm ⁻¹
Lifetime	τ	26.37(5) ns	26.37(5) ns
Natural linewidth	$\Gamma/2\pi$	6.03(1) MHz	6.035(11) MHz
Recoil velocity	v_{rec}	1.329825973(7) cm/s	1.335736144(7) cm/s
Recoil temperature	T_{rec}	0.41436702 μ K	0.41805837 μ K
Doppler temperature	T_D	145 μ K	145 μ K
Saturation intensity	I_s		1.75mW/cm ²

Table A.3: D_1 - and D_2 -line optical properties of ³⁹K. Values taken from reference [111].

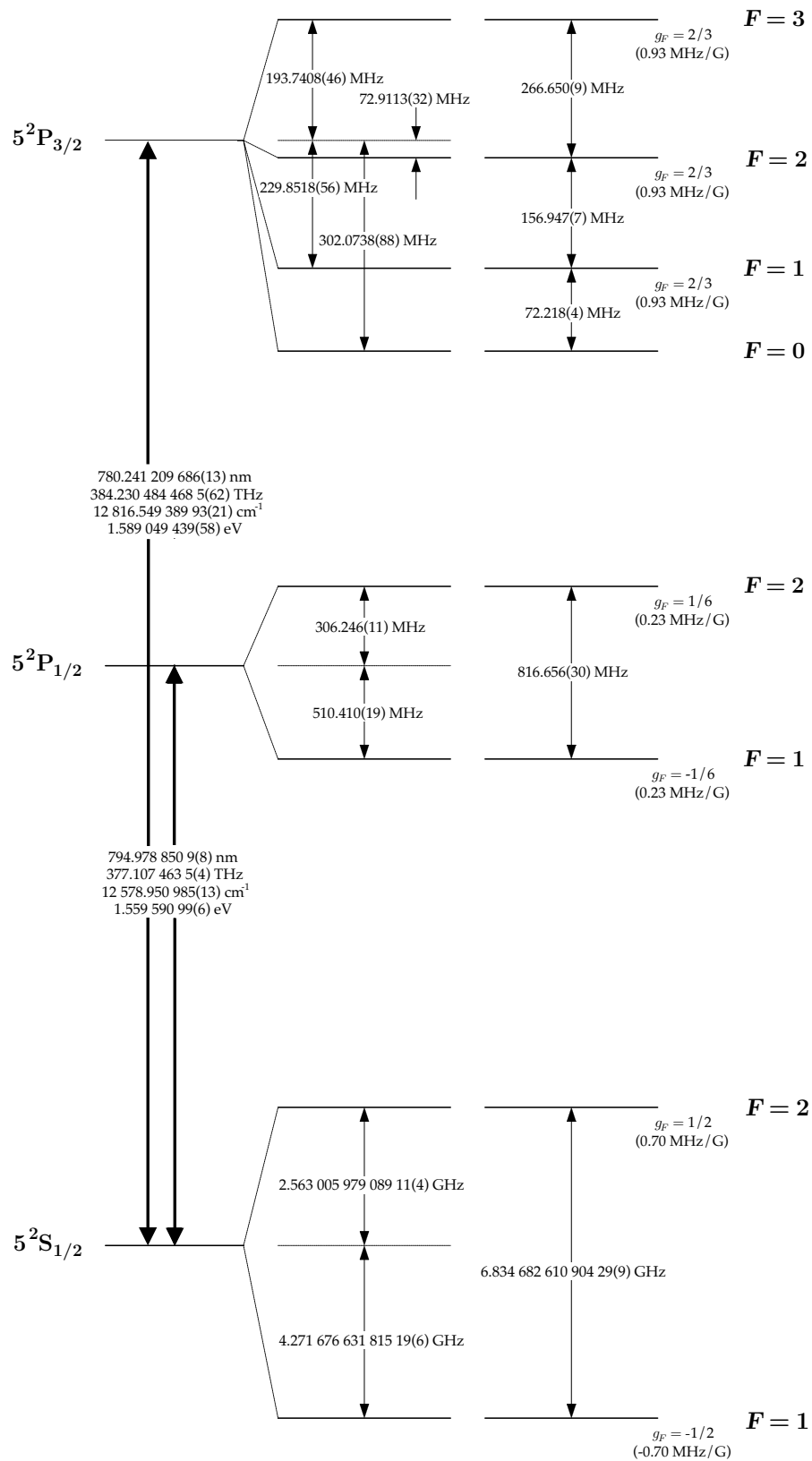


Figure A.1: ^{87}Rb D-line hyperfine structure. The Landé g_F -factors for each level are also given, with the corresponding Zeeman splittings between adjacent magnetic sublevels. Values taken from reference [110]

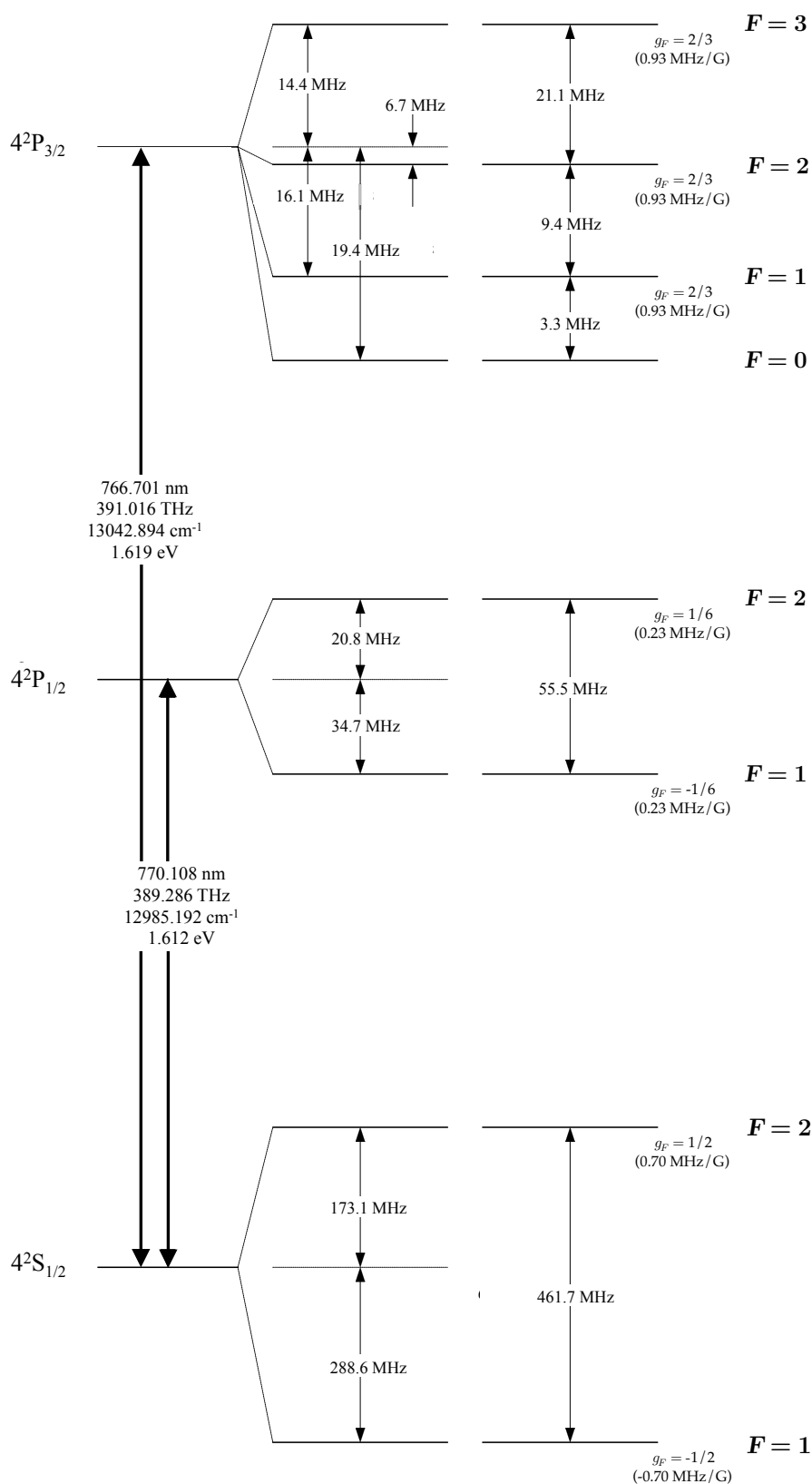


Figure A.2: ^{39}K D-line hyperfine structure. The Landé g_F -factors for each level are also given, with the corresponding Zeeman splittings between adjacent magnetic sublevels. Values taken from reference [111].

B

A compact system for the rapid production of ^{87}Rb BECs

During the first year of our work, in parallel with the design and assembly of the laser, imaging and control systems, we constructed a single-chamber apparatus intended to serve as a platform on which to test the performance of these various components . Initially intended to be used solely for the production of a MOT, it was realised soon after this goal was achieved that condensation of ^{87}Rb in this setup was a possibility. On the 24th Feb. 2009, we observed our first ^{87}Rb BEC in this system. Condensation was achieved by evaporative cooling in an optically-plugged quadrupole trap. This type of hybrid trap, utilizing both optical and magnetic forces, was used in the first observation of BEC in the MIT group in 1995 [24] and has since been used successfully in several other groups [264, 265, 266].

Several other compact machines for producing degenerate Bose gases have been demonstrated [267, 268, 269] and a commercial venture [270] has even been established to capitalize on the simplicity, reduced cost and versatility of such systems.

Below is a brief description of the setup and the sequence used in order to produce ultracold clouds in this relatively simple machine.

B.1 Vacuum chamber

The compact vacuum chamber consists of a circular quartz cell¹, fitted with seven 1" AR-coated quartz windows around its perimeter and two 2" AR-coated quartz windows on its top and bottom. This cell is connected to a stainless steel chamber via a 15cm long glass tube of 15mm diameter. The vacuum chamber is continuously pumped by a 45ls^{-1} ion pump² and can be connected to a turbo pump³ via an all-metal right-angle valve⁴ during bakeout. A Bayard-Alpert ionization gauge⁵ is fitted to the chamber for monitoring the pressure and a source module consisting of four atom sources⁶ mounted to an eight-pin electrical feedthrough⁷ is also fitted. Figure B.1 shows a top-view schematic of the chamber.

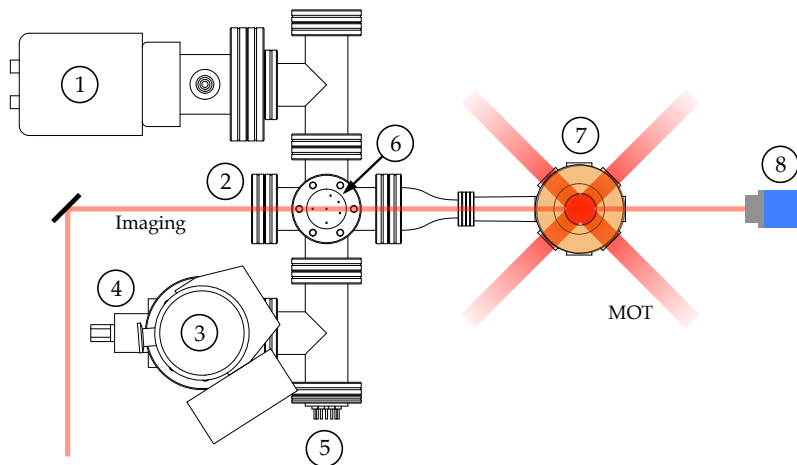


Figure B.1: Schematic of the small-system vacuum chamber. (1) Ion pump, (2) viewport for imaging/pumping/plug beams, (3) turbo pump, (4) right-angle valve, (5) atom source module, (6) ionization gauge and (7) glass MOT cell. Also shown are the MOT and imaging beams, the quadrupole coils and the CCD camera used for absorption imaging (8).

Figure B.2 shows images of the bare assembled system, the various magnetic coils

¹ Triad Technology, Inc.
² oerlikon Leybold IZ50
³ oerlikon Leybold TURBOVAC TW 70 H
⁴ VAT, Series 540 DN40
⁵ Varian, Inc., UHV-24p
⁶ Alvac, 2 × AS-3-K-30-V and 2 × AS-3-Rb-50-V
⁷ Kurt J. Lesker, EFT0084033

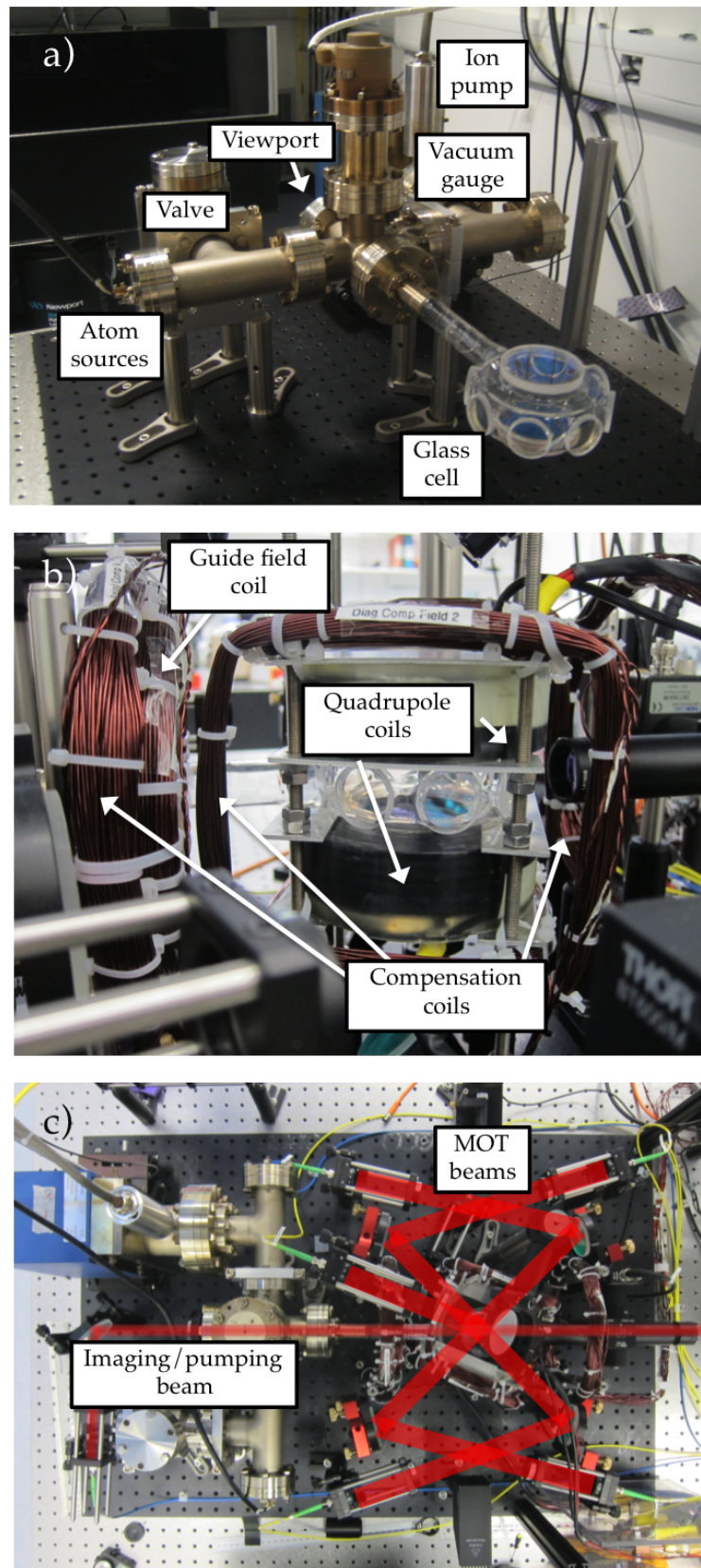


Figure B.2: (a) The bare system after assembly and bakeout, (b) the magnetic coils mounted around the cell and (c) a top view showing the directions of the MOT and imaging beams together with the optical components.

mounted about the glass cell and a top view of the apparatus indicating the beam paths of the MOT and imaging light.

B.1.1 Bakeout

Bakeout of the chamber proceeded in a similar manner to that of the main chamber, described in section 3.2.9, with the chamber being wrapped in heater tape and the applied heating current controlled using variacs. Temperatures at various locations were monitored using thermocouples and logged using a LabView VI. Figure B.3 shows an overview of the system pressure (black line), as well as the temperatures measured at various locations, during the first six days of the bakeout procedure. Clearly visible are the pressure spikes that accompany the raising of the temperature, followed by a gradual drop in the pressure - at constant temperature - as the released impurities are pumped from the system.

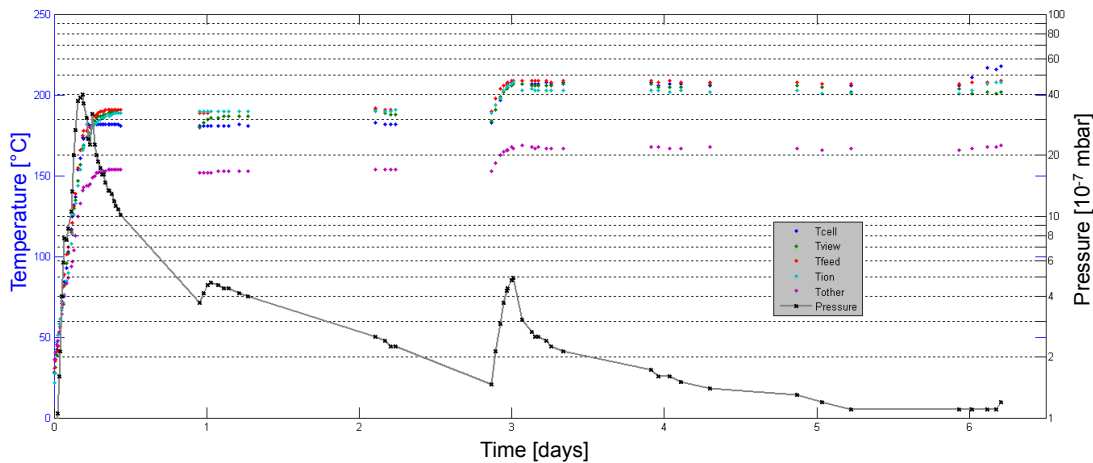


Figure B.3: Overview of the first six days of the bakeout process. The pressure as measured by the ionization gauge is shown in black and the temperatures at various locations along the chamber are shown by the coloured data points. Temperature rises are accompanied by pressure rises and subsequent decays as released impurities are removed by the pump.

B.2 Lasers and coils

The cooling, repump, pumping and imaging beams for cooling ^{87}Rb in this chamber are generated by the same laser system used for the main experiment and described in section 3.3. Similarly to the main experiment, once on the vacuum table, the cooling and repump beams are spatially overlapped before being split

into the six beams required for the 3D MOT. Figure B.4 shows the home-made fiberport cluster assembled for this purpose using a custom-machined baseplate together with commercially available miniature beamsplitter-cubes and mounts, half-wave plates, polarizers, fibre couplers, photodiodes and ‘tweaker’ plates for precision alignment¹. One input is used for the cooling beam and the second for the repumper. Initial alignment and testing of the fiberport cluster was carried out by a visiting student, Mehdi Lallouache.

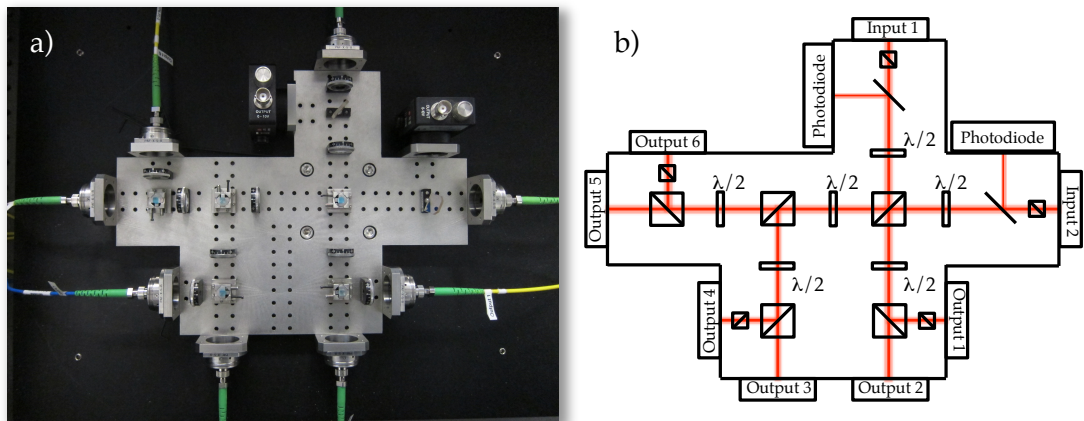


Figure B.4: (a) Image and (b) schematic of the home-made fiberport cluster for overlap and splitting of the ^{87}Rb cooling and repump beams.

Each beam is collimated to a diameter of approximately 1" and passed through a quarter-wave plate to produce the appropriate circular polarization. Two 2" mirrors are used to steer the beams through the cell. A total of 84mW of cooling light is divided equally between the six beams, with 10mW of repump light being divided less evenly due to imperfections in the fiberport cluster. In addition a diode-pumped solid-state (DPSS) 532nm laser², capable of outputting 18W of CW power, is used to provide a beam to be used for optical plugging of the quadrupole magnetic trap. The quadrupole magnetic field used both for operation of the MOT and for magnetic trapping is generated by a pair of coils mounted in anti-Helmholtz configuration above and below the cell. Each coil consists of 36 turns (6×6) of insulated copper tubing (OD: 4mm, ID: 2.8mm), encapsulated in an epoxy resin and wound with an inner diameter of 53mm, an outer diameter of 103mm and a height of 25mm. Cooling water is circulated within the copper tubing. The coils are mounted 30mm apart and are powered by a power supply³

¹ Thorlabs, Inc., Fiber Optomechanics range

² Coherent, Inc. Verdi V18

³ Delta Electronika SM15-200D

capable of providing up to 200A at 15.5V, corresponding to a field gradient of 400Gcm^{-1} along the strong (vertical) axis. Three smaller coil pairs mounted in approximately Helmholtz configuration, provide compensation fields and a single auxiliary coil is used to provide a guide field directed along the glass tube connecting the cell to the rest of the chamber.

B.3 Optical Plug

Optical plugging relies on the use of a repulsive (blue-detuned) laser beam to repel atoms from the central region of a quadrupole magnetic trap in which they are susceptible to Majorana spin flips. An advantage of this method is that the linearity of the quadrupole trap is preserved and hence evaporative cooling is more efficient than in a harmonic potential. This is crucial in our case, since the single-chamber design already limits the lifetime of our trapped clouds to several seconds. Our plug light is generated by a pumped Ti:Sapph laser¹, whose frequency is tuned in the range $\nu_{\text{plug}} = 740 \rightarrow 770\text{nm}$. The beam is sent to the vacuum chamber in a polarization maintaining fibre, and upon exiting from the fibre is focussed at the centre of the glass cell by a single, $f = 150\text{mm}$, 2" achromatic doublet². The beam path is shown in figure B.5.

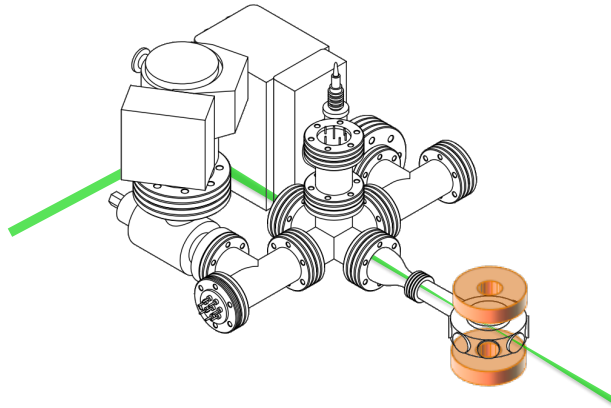


Figure B.5: Diagram of the system showing the propagation path of the plug beam.

As can be seen, the plug propagates along the weak quadrupole axis and hence breaks the rotational symmetry of the trap. The beam waist is chosen to be larger than the estimated hole region in order to avoid sensitivity to alignment

¹ Coherent, Inc., MBR-110

² Thorlabs, AC508-150-B-ML

instabilities, while still providing a high enough barrier to incident atoms to keep as many as possible away from the hole region. In our setup, we use a plug waist of $w_{\text{plug}} \approx 27\mu\text{m}$ and a peak barrier height of up to $750\mu\text{K}$. The addition of the optical plug potential to the magnetic quadrupole field creates an overall potential containing two minima on either side of the plug beam, as illustrated in figure B.6.

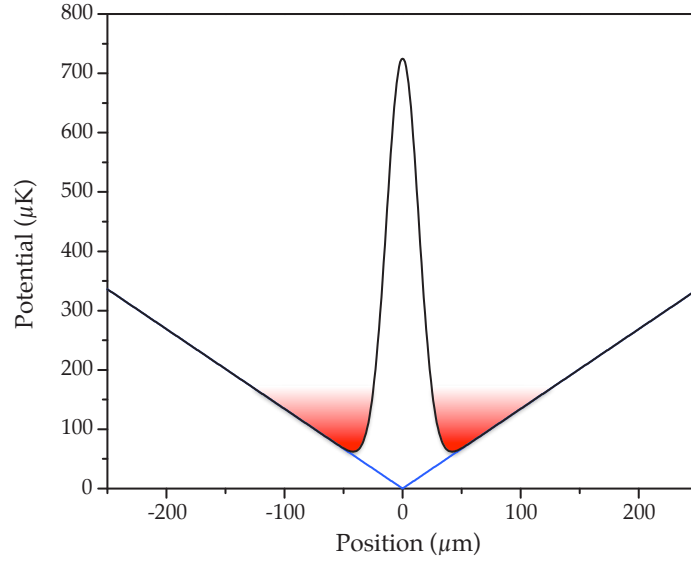


Figure B.6: Optically plugged quadrupole potential plotted against distance from the trap centre, for a strong-axis field gradient of 200Gcm^{-1} . The plug barrier shown is for a waist of $27\mu\text{m}$ and a peak height of $725\mu\text{K}$.

Assuming propagation along the y -direction and neglecting the Rayleigh range of $z_R = \pi w_0^2/\lambda \approx 4\text{mm}$ for our $27\mu\text{m}$ waist as well as gravity, the total potential is given by

$$\begin{aligned} U_{\text{TOT}} &= U_{\text{mag}} + U_{\text{plug}} \\ &= \mu_{\text{B}}g_{\text{F}}m_{\text{F}}B' \sqrt{x^2 + y^2 + 4z^2} + U_0 e^{-(x^2+z^2)/w_{\text{plug}}^2} \end{aligned} \quad (\text{B.1})$$

where B' is the magnetic field gradient and w_{plug} is the plug waist. Approximating the potential minimum as an anisotropic oscillator, the trapping frequencies are given by [24]

$$\omega_x = \omega_y \sqrt{\frac{4x_0^2}{w_{\text{plug}}^2} - 1}, \quad \omega_y = \sqrt{\frac{\mu_{\text{B}}g_{\text{F}}m_{\text{F}}B'}{2m x_0}}, \quad \omega_z = \sqrt{3}\omega_x \quad (\text{B.2})$$

where x_0 is the distance between the trap centre and the trap minimum. We have

found that displacing the plug slightly to one side of the trap centre yields larger condensate numbers due to the formation of a single trap minimum, similarly to the results reported in [265].

B.3.1 Light-Induced Atomic Desorption (LIAD)

Use of a single-chamber system conflicts with the opposing pressure requirements required for the MOT and evaporation stages, as discussed in section 3.2. To address this limitation, the technique of Light-Induced Atomic Desorption (LIAD) was pursued with the aim of obtaining a higher pressure of the target species during MOT loading and a sharp decrease in the pressure prior to the start of evaporation. Photon-stimulated desorption was first demonstrated by A. Gozzini et al. in 1993 [271] with the name *light-induced atomic desorption* being given to the phenomenon a year later [272]. LIAD makes use of incoherent short-wavelength (UV) light to desorb atoms from cell walls, analogously to the photoelectric effect for electrons. This increases the vapour pressure in the cell and can hence yield larger MOT numbers. Re-adsorption of atoms once the light is extinguished then lowers the pressure and hence increases the lifetime of the trapped atoms.

In recent years a number of groups have made use of this technique in cold-atom experiments in order to achieve larger, longer-lived and faster loading MOTs [273, 274, 275, 276, 277, 278, 279, 280, 281]. These experiments have explored the wavelength and intensity dependence of the desorption rate, as well as the effects of different adsorbing substrates, coatings and atomic species on the desorption dynamics. Figure B.7 shows our UV source and the layout of its control circuit.

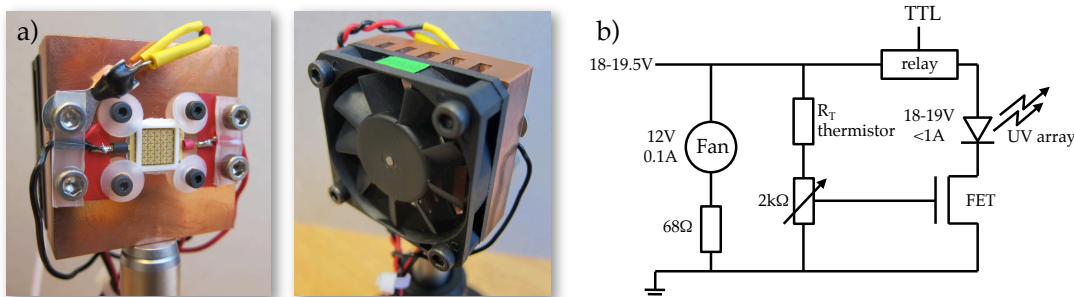


Figure B.7: (a) UV source mounted on a copper heatsink fitted with a fan and thermistor¹. (b) Control circuit for the UV source and fan. A relay² allows TTL switching of the light, while a FET³ is used to turn off the source in the event of overheating ($T > 70^\circ\text{C}$).

The source⁴ we use in our setup dissipates 18W of power and radiates 1250mW of power with a central wavelength of 374nm (FWHM: 12nm). It is clamped using thermally conducting paste to a 40x40x15mm finned copper heatsink fitted with a cooling fan⁵. A thermistor⁶ is mounted in close proximity to the UV source and is connected to a safety circuit in order to ensure the source is turned off in the event of overheating ($T > 70^{\circ}\text{C}$).

Somewhat disappointingly, we do not see the full benefits of LIAD in our system. This may be due to the material from which our cell is made or the nature of the AR coating on its viewports, although the exact reason remains unknown. We have found however, that extended illumination with the source (≥ 30 mins) allows us to double the final MOT size and therefore the source is now employed as an alternative mechanism to firing the conventional atom sources, which can impair the immediate functionality of the system.

Interestingly, when testing the effect of the UV source on our main ^{39}K - ^{87}Rb system MOT chamber, we noticed a reduction in the MOT size of approximately 50% over ~ 3 s when the UV was turned on. Turning the UV off caused the MOT to start growing immediately, reaching its former size after ~ 15 s. At the time this effect was attributed to the release of impurity atoms from the chamber walls. However, similar observations reported by a group at the National University of Singapore [282] were attributed to a different cause. Their MOT diminished in size only when the UV source was directed at the trapping region, and actually grew in size when the source was directed at a cell wall away from the MOT region. They therefore suspected that the depletion was due to the ionization of neutral ^{87}Rb from the excited $5P_{3/2}$ state to singly charged ^{87}Rb , a transition requiring radiation at 484nm or shorter.

B.4 Performance

The RF radiation required for evaporative cooling in the optically plugged trap is provided by a small 4-turn coil placed near the vertical cell window and driven

¹ EPCOS, B59901D0060A040
² Tyco Electronics, Axicom IM 23
³ Toshiba, 2SK3869
⁴ Enfis, UNO Tag (UVA)
⁵ BiSonic, SP401012M, 12V, 0.09A
⁶ EPCOS, B59901D0060A040

by a function generator¹ via an RF amplifier² outputting up to 2W. Figure B.8 shows sample images taken during alignment of the plug beam with respect to the ^{87}Rb cloud, following an evaporation sweep from roughly 15MHz to 1MHz.

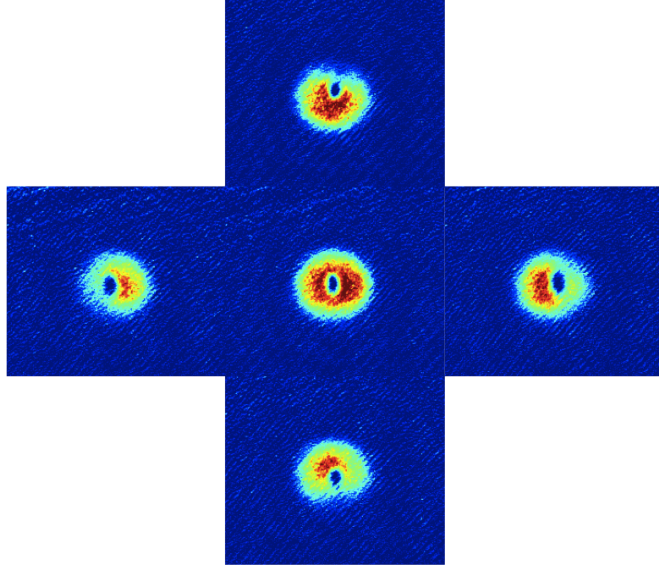


Figure B.8: Alignment of the optical plug. Images taken during the alignment process show the enhancement of atom number resulting from correct central alignment of the plug. In these images, the plug beam is left on during the short, 4ms, time-of-flight.

A typical experimental sequence proceeds as follows:

1. A several-second MOT stage is followed by 2.5ms of optical molasses and a $20\mu\text{s}$ optical pumping stage to transfer atoms into the $|2, 2\rangle$ state.
2. The polarized sample is then magnetically captured by abruptly turning on the quadrupole field with a gradient of 64Gcm^{-1} , which is then ramped up to 200Gcm^{-1} over the following 500ms.
3. At this point the plug beam is ramped up to expel atoms from the trap centre.
4. There follows a 300ms ‘settling’ hold in the quadrupole trap during which a 10MHz RF knife is applied. A first evaporation stage is then carried out, ramping the RF linearly from 10MHz to 2MHz over 3s in the 200Gcm^{-1} trap.

¹ Agilent 33250A

² Delta RF Inc., LA2-1-525-30

5. In order to reduce trap loss due to three-body collisions and scattering from the plug beam, we then decompress the quadrupole field to 80Gcm^{-1} in 200ms.
6. Following decompression the evaporation sweep is resumed, commencing from a lower frequency of 1.4MHz and sweeping logarithmically to the desired final frequency in 0.5s.

Using this protocol, we have been able to obtain condensates containing over 10^5 atoms. Figure B.9 shows a trapped cloud imaged at various stages during the evaporation sweep. The two distinct potential minima are clearly visible. Figure B.10 shows a bimodal fit to a partially condensed (28%) cloud, prepared as described above. Figure B.11 shows a sequence of images taken at 1ms intervals in the range 3-12ms after release from the trap.

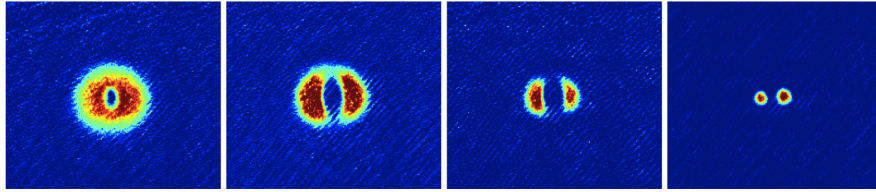


Figure B.9: Evaporation sequence in the plugged quadrupole trap. Two distinct minima are clearly visible and further evaporation will result in population of only one well due to slight asymmetries in the overall potential.

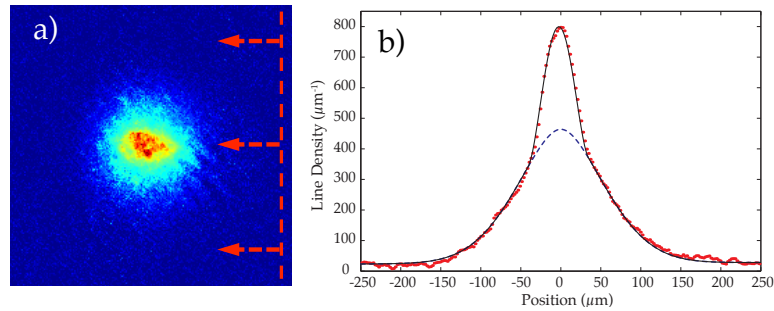


Figure B.10: Bimodal fit to a partially-condensed ^{87}Rb cloud. Fit carried out according to the triple-pass procedure described in section 3.15. This example possesses a condensed fraction of $N_0/N \approx 28\%$ and a temperature of $T \approx 500\text{nK}$, as obtained from a fit to the thermal wings.

Further details can be found in the first-year reports of Stuart Moulder, Robert Campbell, Igor Gotlibovych and Tobias Schmidutz.

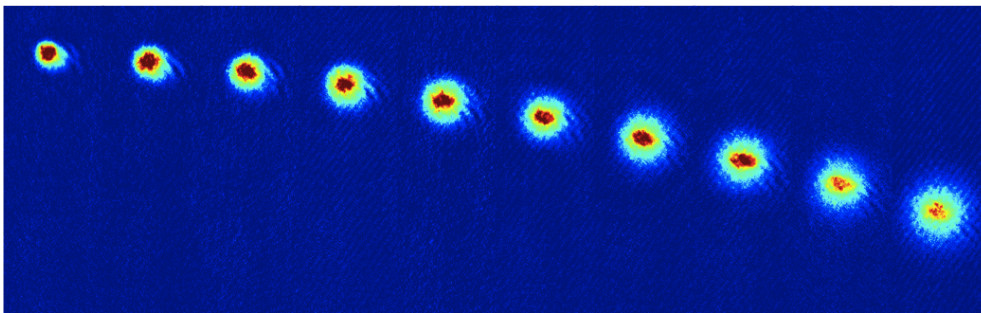


Figure B.11: Atoms in freefall. After evaporation to a trap depth of 145kHz a sequence of images was captured with the time-of-flight varied in 1ms intervals in the range 3-12ms.

C

Using Spatial Light Modulators for versatile creation of optical potentials

Manipulation of atoms for performing novel and high-precision experiments relies on our ability to generate the desired static or dynamic potential landscapes. As discussed in this thesis, optical trapping of neutral particles is a widely-used technique which has enabled confinement and manipulation of large numbers of particles as well as single atoms. The most common optical trap geometry is that produced by a Gaussian laser mode which provides an approximately harmonic trapping potential, as utilized in the experiments described in this thesis (see section 3.10). Periodic optical lattices with tuneable parameters can also be formed by interference of non-copropagating beams [135]. More recently, diffusive optical elements have been used to project optical speckle potentials onto trapped clouds for studies into the effects of disordered potentials [283, 67,

284, 285, 142]. In general, it is clear that the ability to produce a diverse range of optical potentials can provide access to many interesting experimental regimes.

C.1 Spatial Light Modulators

An emerging tool for creating highly-customisable optical potentials is the Spatial Light Modulator (SLM). The operating principle of an SLM is the ability to control (modulate) the phase and/or amplitude at different points within the wavefront of an incident beam. Knowing the subsequent propagation path of this modulated field enables production of a tailored field configuration at the location of the sample simply by a suitable choice of phase and amplitude modulation in the SLM plane. The modulation itself is accomplished by reflecting or transmitting the beam through an array of independently-controlled pixels. The most common SLM implementations are based on liquid crystal displays (LCD), although some purely intensity-modulating SLMs rely on a digital micromirror device (DMD) consisting of an array of deformable micromirrors to deflect light from the desired pixel and hence control the intensity attenuation. In an LCD-based SLM, phase control is provided by tuning the birefringence of each pixel, while intensity control is accomplished by rotating the beam polarization at each pixel in conjunction with polarizing filters, similarly to a conventional LCD projector. The SLM is controlled from a PC via a conventional video (DVI) interface. After the SLM, a lens is typically used to generate a far-field image of the beam at the location of the atomic cloud.

The nature of this device naturally makes it much more flexible than the use of static optical elements, such as phaseplates and masks, for the creation of arbitrary potentials and in addition opens up the possibility of dynamic manipulation of the atoms by real-time changes to the phase-pattern displayed on the SLM. The rate at which the pattern can be updated varies from device to device based on the method used to induce the phase-shift, but for the most common types (LCD) is on the order of 12Hz. SLMs based on ferroelectric liquid crystals can achieve frame rates on the order of 1kHz.

In order to explore the feasibility of using an SLM for generating optical potentials in future experiments, we conducted a trial using a commercial SLM¹ loaned from its manufacturer. Below, we briefly describe the experimental setup used for testing the SLM, as well as the three classes of optical potential whose

¹ Hamamatsu Photonics, LCOS-SLM X10468-04

production was trialled during these initial experiments with the SLM. These were the Laguerre-Gauss (LG) modes, the variably spaced sheets ('lids') and the arbitrarily-shaped potential.

C.2 Experimental setup

The setup used for testing of our SLM is shown in figure C.1. After emerging from a single-mode polarization-maintaining fibre¹, the 532nm beam is collimated to a $1/e^2$ -diameter of $\approx 6\text{mm}$ by an $f = 45\text{mm}$ lens² and reflected from two steering mirrors before being reflected from the SLM surface, passing through a 200mm lens³ and impinging on a CCD camera⁴. The final lens is located 200mm from both the SLM and the camera and all reflection angles are kept to a minimum.

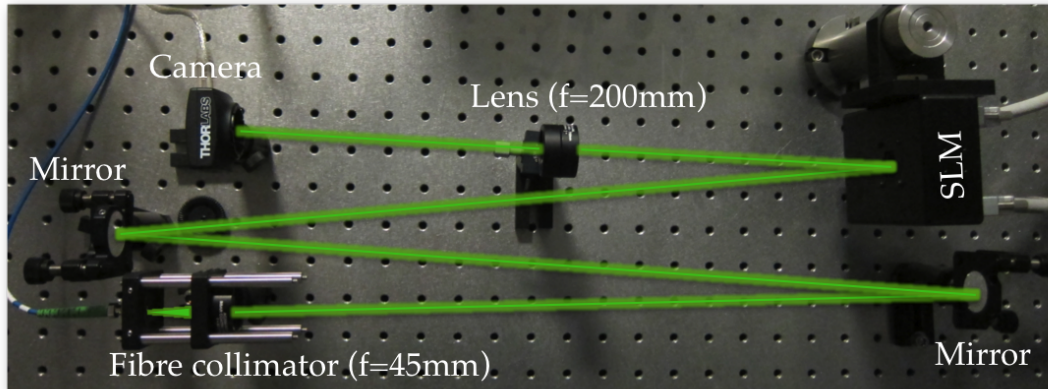


Figure C.1: SLM trial setup. Shown are the fibre output collimator (bottom left), steering mirrors, SLM head, Fourier lens and CCD camera. The light is derived from our 532nm diode-pumped solid-state (DPSS) laser.

Phase patterns, also known as kinoforms, are sent to the device in the form of a 600×800 array of 8-bit values ($0 \rightarrow 255$), corresponding to a phase shift of approximately $0 \rightarrow 2\pi$ at the desired wavelength⁵. The field incident on the SLM acquires this phase shift and is therefore multiplied by the factor, $P(x, y) =$

¹ Thorlabs, PM460-HP

² Thorlabs, AC254-045-A-ML

³ Thorlabs, LA1708-A

⁴ Thorlabs, DCC1545M CMOS

⁵ In practice the precise pixel value corresponding to a 2π phase shift is found empirically.

$e^{i\phi(x,y)}$, where $\phi(x,y)$ is the imprinted phase pattern, i.e.

$$E(\mathbf{r}, z_{\text{SLM}}) = \overbrace{E(\mathbf{r}, 0)}^{\text{incident}} \underbrace{e^{i\phi(x,y)}}_{\text{imprinted}} \quad (\text{SLM plane}) \quad (\text{C.1})$$

The field then passes through the so-called Fourier lens and is focussed in its focal plane. In order to find the final form of the field in the Fourier lens focal plane, we make use of the following:

1. Propagation of the *Fourier transform* of the field, \tilde{E} , from z_0 to z is accomplished by multiplication with a propagation phase factor:

$$\tilde{E}(\xi, z) = \tilde{E}(\xi, z_0) e^{ik(z-z_0)\sqrt{1-(\lambda\xi)^2}} \quad (\text{C.2})$$

2. Within the thin-lens approximation, the effect of an ideal lens of focal length f is simply to multiply the field by the phase factor,

$$E(\mathbf{r}, z) \rightarrow E(\mathbf{r}, z) e^{-ikr^2/2f}. \quad (\text{C.3})$$

3. The field in the lens focal plane can be found using the Fresnel diffraction formula:

$$E(\mathbf{r}', z) = \frac{e^{ikz}}{i\lambda z} e^{ikr'^2/2z} \int E(\mathbf{r}, 0) e^{ikr^2/2z} e^{-ik\mathbf{r}\cdot\mathbf{r}'/z} d^2\mathbf{r} \quad (\text{C.4})$$

Using the above we find that the field at the focal plane after the lens, $z = f$, is related, up to a global phase factor, to the field at a distance d before the lens, $z = -d$ by

$$E(\mathbf{r}', f) = \frac{e^{i\frac{kr'^2}{2f}(1-\frac{d}{f})}}{i\lambda f} \int E(\mathbf{r}, -d) e^{ik\mathbf{r}\cdot\mathbf{r}'/f} d^2\mathbf{r} \quad (\text{C.5})$$

In our experimental setup we have $z_{\text{SLM}} = -d = -f$. The phase factor preceding the above integral therefore vanishes, reducing the expression to a regular Fourier transform.

$$E(\mathbf{r}', f) = \frac{1}{i\lambda f} \int E(\mathbf{r}, z_{\text{SLM}}) e^{ik\mathbf{r}\cdot\mathbf{r}'/f} d^2\mathbf{r} \quad (\text{focal plane}) \quad (\text{C.6})$$

with $E(\mathbf{r}, z_{\text{SLM}})$ the field of equation C.1, including the imprinted phase pattern.

C.3 Trial 1: Laguerre-Gauss modes

A uniform trapping potential can be generated by replacing the harmonic confinement provided by a Gaussian beam with a potential consisting of a flat bottom with sharp outer walls. Laguerre-Gauss (LG) modes are the solutions to the paraxial Helmholtz equation¹ in the case of cylindrical symmetry, and such a flat-bottomed potential can be provided by the annular $\text{LG}_{p=0}^{l \neq 0}$ modes, where l and p are the azimuthal and radial mode indices, respectively. LG_0^l beams can be generated by imprinting a phase winding of the form

$$\phi(x, y) = l\theta \quad (\text{C.7})$$

onto an incident Gaussian beam, where θ is the polar angle in the xy plane and l is an integer, often called the *charge* or *winding number*. Beams generated using this method have attracted much attention recently since their photons each possess $L = l\hbar$ of orbital angular momentum which can be transferred to the particles with which they interact [286, 287, 288]. Therefore, in addition to enabling studies of gases confined in uniform potentials, the ability to easily and dynamically change the charge of the LG beams also lends itself to use in experiments studying the rotational properties of BECs such as vortex nucleation [289] and superfluidity measurements (see [290] and subsection C.7 below).

Figure C.2 shows some example kinoforms used for imprinting such phase windings, together with their resulting intensity profiles, which can be obtained as follows: For an incident Gaussian beam of wavelength λ and waist ω , passing through the ‘phaseplate’ of equation C.7, the field at the focus of a subsequent Fourier lens of focal length f is given by equation C.6 using cylindrical coordinates

$$E(r', \theta') = \frac{\sqrt{I_0}}{\lambda f} \int dr d\theta r e^{i\mathbf{k}\mathbf{r}\cdot\mathbf{r}'/f} e^{-r^2/\omega^2} e^{il\theta} \quad (\text{C.8})$$

where the field immediately before the phaseplate is taken to be $E(r, \theta) = \sqrt{I_0} e^{-r^2/\omega^2}$. The Fourier term can be decomposed in terms of Bessel functions of the first kind, $J_m(z)$, using the identity

$$e^{iz \cos \phi} = \sum_{m=-\infty}^{\infty} i^m J_m(z) e^{-im\phi} \quad (\text{C.9})$$

¹ Helmholtz equation: $\nabla^2 \psi + k^2 \psi = 0$. The paraxial (small-angle) approximation neglects second-order variations of amplitude along direction of propagation.

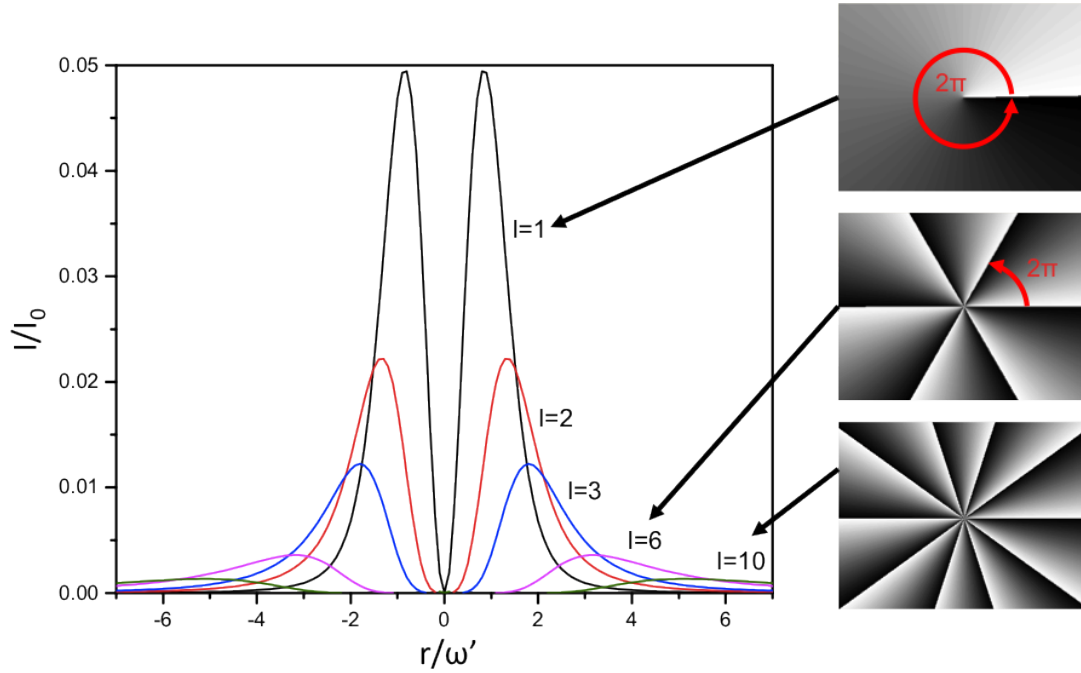


Figure C.2: Radial cross-section through the intensity distribution for LG_0^l beams of winding number $l = 1, 2, 3, 6, 10$. Shown on the right are the phase patterns used for the $l = 1, 6$ and 10 beams.

and hence

$$e^{ik\mathbf{r}\cdot\mathbf{r}'/f} = e^{ikrr'\cos(\theta-\theta')/f} = \sum_{m=-\infty}^{\infty} i^m J_m(krr'/f) e^{-im(\theta-\theta')} \quad (\text{C.10})$$

Inserting equation C.10 into equation C.8 and noting that only the term for which $l = m$ will survive the integral over θ , results in the following expression for the field

$$E(r', \theta') = i^l \sqrt{I_0} e^{il\theta'} \int_0^{\infty} du u J_l(2ur'/\omega') e^{-u^2} \quad (\text{C.11})$$

where the substitution $u = r/\omega$ has been made and $\omega' = \lambda f/\pi\omega$ is the waist at the lens focus. The intensity is obtained as $I(r', \theta') = |E(r', \theta')|^2$. Near the optical axis, for $r' \ll l\omega'$, the Bessel function's small-argument approximation $J_l(2ur'/\omega') \sim (ur'\omega')^l/l!$ can be used to obtain

$$I(r') \propto I_0 \left(\frac{r'}{\omega'} \right)^{2l} \quad \text{for} \quad r' \ll l\omega' \quad (\text{C.12})$$

It can be shown [291] that for large radii, the intensity falls as $I(r') \propto \sqrt{I_0} l^2 r'^{-4}$, with the radial dependence, $I(r') \propto 1/r'^4$, independent of the charge, l . The l^2 -

dependence is responsible for transferring large fractions of the beam power into the wings and explains the large difference between the peak heights in figure C.2. Figure C.3 shows LG beams recorded using the setup of figure C.1 using the winding numbers $l = 1, 3, 5, 11, 13, 15, 17, 19, 25, 30, 35, 45$. We note that the images of figure C.3 were taken after correcting for aberrations in the optical path using the Shack-Hartmann algorithm [292] and applying an annular aperture to the SLM pattern which suppresses the fringes normally present outside the main LG ring.

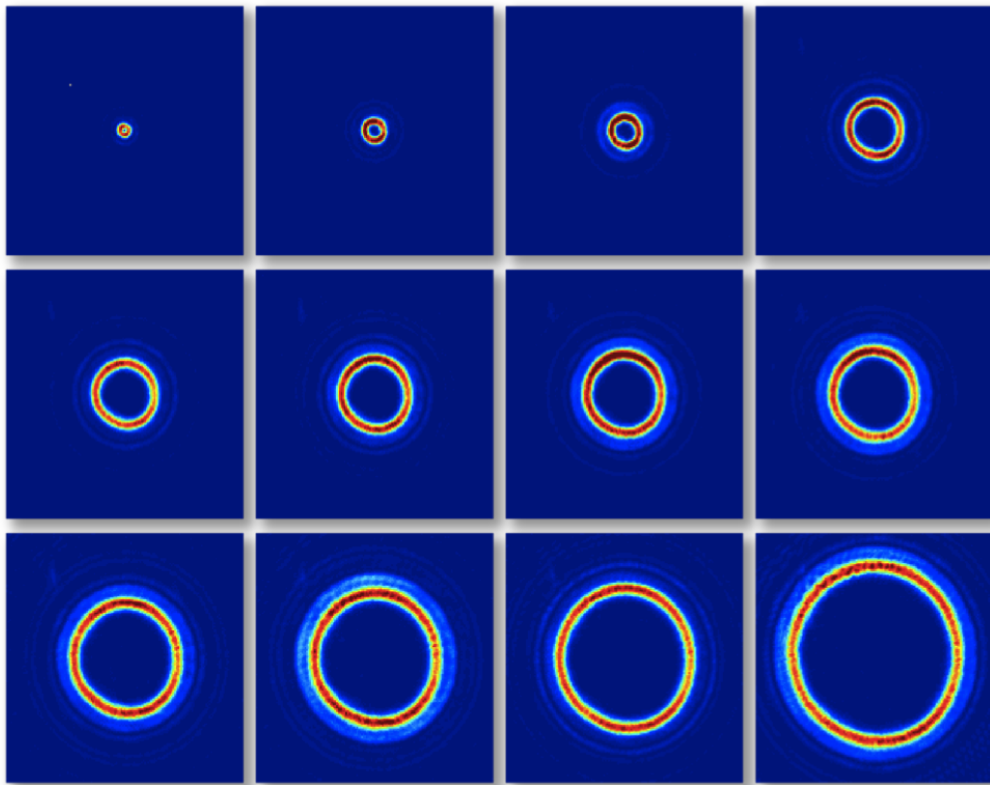


Figure C.3: Measured profiles of beams with $l = 1, 3, 5, 11, 13, 15, 17, 19, 25, 30, 35, 45$ (top-left to bottom-right). The field of view in each image is $d = 0.78 \times 0.78\text{mm}$ (i.e. 150×150 pixels). The colorscale of each image is scaled to the image's maximal and minimal values.

C.4 Trial 2: 2D confinement and the 2D-3D crossover

Phase gradients are used to produce a uniform translation of the field in the image plane, as can be easily understood by observing that insertion of the factor $P(x, y) = e^{\pm ipx}$ into equation C.6 is equivalent to a straightforward translation by $\pm p$ in the Fourier domain. These gradients can of course be superposed to translate the field in both directions, as illustrated in figure C.4.

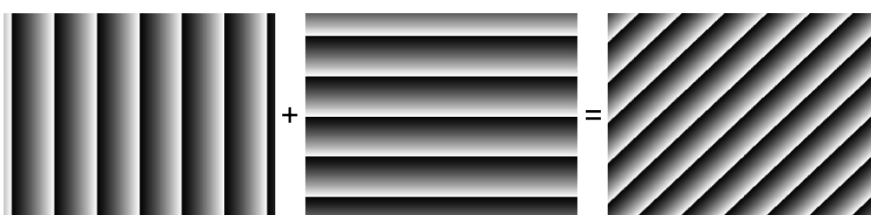


Figure C.4: ‘Translation gradients’ are used to uniformly translate the field profile in the image plane. Horizontal (left) gradients are superposed with vertical gradients (middle) to translate diagonally. The higher the gradient, the larger the translation.

Such gradients are commonly used in order to separate the modulated light diffracted from the SLM from the light undergoing specular reflection from its surface, which contributes an unwanted signal in the image plane. However, with only a slight modification, similar gradients can also be used to provide a useful potential for exploring the 2D-3D crossover regime. Figure C.5 shows a phase pattern consisting of opposing linear gradients centred on the horizontal axis. This phase pattern produces an intensity profile consisting of two vertically-spaced thin ‘light sheets’ (*aka lids*), whose spacing grows with the phase gradient.

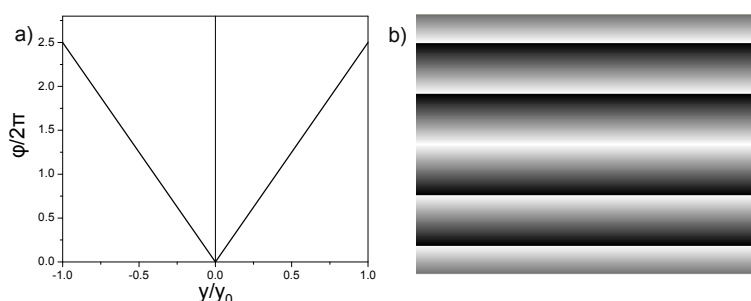


Figure C.5: ‘Splitting gradients’ can be used to produce two thin light sheets for exploring the transition between the 2D and 3D confinement regimes. In this example, the gradient is $p = 5\pi/y_0$

The formation of this profile can be intuitively understood by considering illumination of the SLM by a plane wave. The phase pattern of figure C.5 has the form

$$P(x, y) = \begin{cases} e^{-ipy} & \text{if } y \in [-y_0, 0] \\ e^{ipy} & \text{if } y \in [0, y_0] \end{cases} \quad (\text{C.13})$$

where y_0 is the distance from the horizontal axis to the top of the SLM. The amplitude in the image plane therefore takes the form

$$E(x', y') \propto \int_{-y_0}^0 e^{i(-p+k)y} dy + \int_0^{y_0} e^{i(p+k)y} dy \quad (\text{C.14})$$

$$\propto \left[\frac{e^{i(-p+k)y}}{i(-p+k)} \right]_{-y_0}^0 + \left[\frac{e^{i(p+k)y}}{i(p+k)} \right]_0^{y_0} \quad (\text{C.15})$$

$$\propto e^{-i(-p+k)\frac{y_0}{2}} \left[\text{sinc}\left(\left(-p+k\right)\frac{y_0}{2}\right) \right] + e^{i(p+k)\frac{y_0}{2}} \left[\text{sinc}\left(\left(p+k\right)\frac{y_0}{2}\right) \right] \quad (\text{C.16})$$

i.e. a sum of two sinc functions. Assuming a Gaussian incident beam would lead to a convolution of a gaussian with each of the sinc peaks. For large enough y_0 and p , the cross term arising from taking the modulus of the amplitude can be neglected, producing two separated peaks.

The possibility of dynamically tightening the confinement into the 2D regime, may also be useful for gathering as high a number of atoms as possible into the trap, compared with current loading procedures, which simply turn on the final two-dimensional potential in its final form, incurring the loss of those atoms beyond its reach. We intend to explore this technique in future experiments. Figure C.6 shows a series of intensity profiles, taken with varying values of the ‘splitting gradient’.

C.5 Trial 3: Arbitrary potentials

It is clear that the ability to generate arbitrarily-shaped optical potentials would make available a hugely versatile toolbox for performing a wide range of experiments in micron-scale custom-designed systems. Several algorithms exist for performing the phase-retrieval task required for producing arbitrary field profiles, the

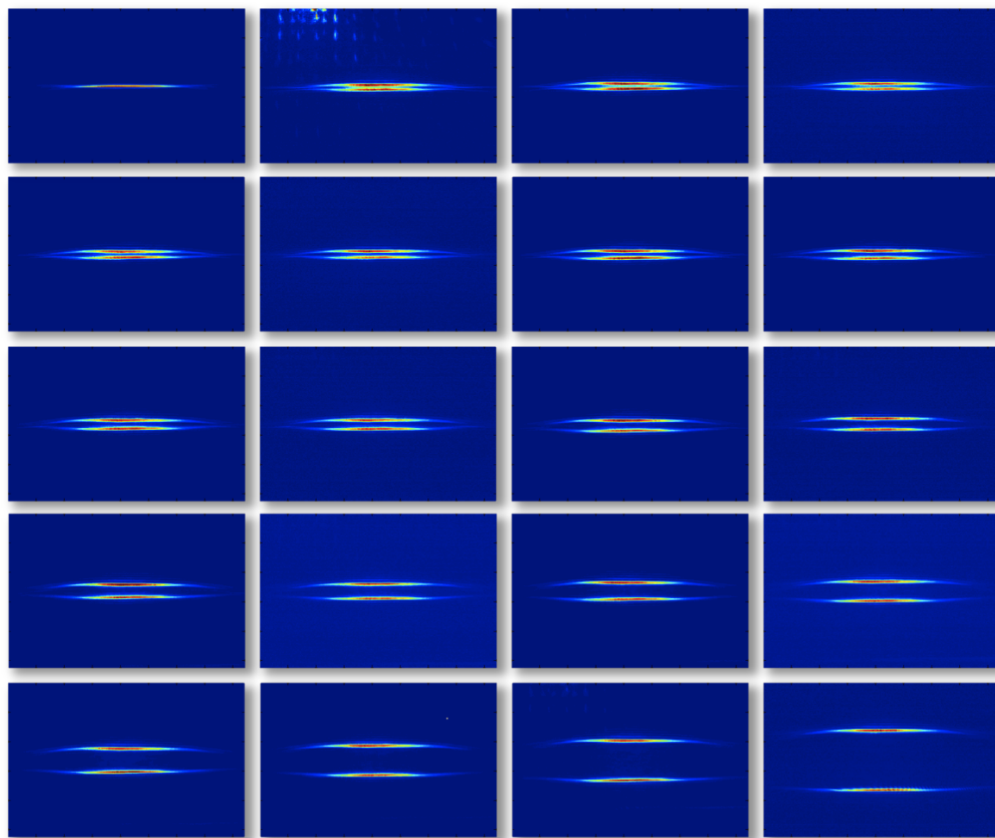


Figure C.6: Production of variably-spaced light sheets for studies of the 2D-3D crossover. The splitting gradient, p , was measured in terms of the number of SLM pixels per 2π phase shift. From top-left to bottom-right the images correspond to $p = 200, 190, \dots, 10$. Note that in these images, a cylindrical lens profile has also been added to the SLM in order to obtain the elongated aspect ratio shown.

most well-known of which is the Gerchberg-Saxton (GS) algorithm [293], which has been widely documented, implemented and investigated. The GS algorithm is an iterative algorithm for finding the phase pattern required to transform one intensity distribution into another, when both intensity distributions are known.

Although the GS algorithm is in wide use, it has been shown that its convergence is imperfect and often results in the production of numerous optical vortices in the resulting intensity profile. Following our initial use of the GS algorithm for making arbitrary profiles (see figure C.7), a project student (Alex Gaunt) conducted a theoretical, numerical and experimental investigation into these limitations and developed a method based on an extension of the mixed-region-amplitude-freedom (MRAF) algorithm of [294, 295, 296] for producing much smoother arbitrary potentials from which these optical vortices were also

practically eliminated. In addition, two further measures were implemented to improve the profile smoothness:

1. The Shack-Hartmann aberration correction algorithm [292] was used in order to compensate for aberrations present in the SLM panel and optical path.
2. A feedback algorithm was implemented to empirically compensate for irregularities in the final image by proportionally adjusting the target intensity profile fed to the phase-retrieval algorithm in response to the image recorded by the CCD camera.

Figure C.7 shows a rudimentary example of the improvements afforded by these techniques. For further details, see Alex Gaunt’s project report [297].

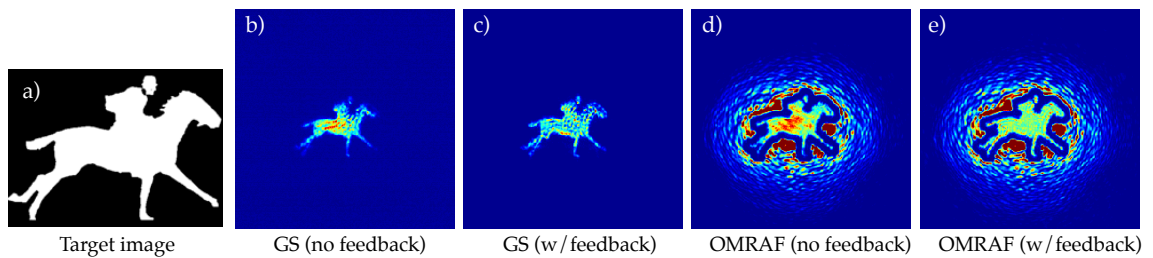


Figure C.7: Comparison of the Gerchberg-Saxton algorithm and the OMRAF algorithm developed by Alex Gaunt for producing smooth arbitrary potentials and removing optical vortices. The field of view in each image is approximately 1.6×1.6 mm. (a) Target image and images produced by (b) GS algorithm with no feedback, (c) GS algorithm with feedback, (d) OMRAF algorithm without feedback and (e) OMRAF algorithm with feedback.

Further applications involving the dynamic manipulation of optical potentials include mechanical stirring of condensed clouds [296] and the implementation of a lens with dynamically varying focal length for translation or compression of optical dipole potentials¹.

C.6 Home-made SLM

We have also briefly explored the possibility of constructing a home-made SLM using the LCD panel and control electronics found inside a simple commercial

¹ Note: the phase profile of a lens of focal length f is a quadratic: $\phi(\mathbf{r}) = -k\mathbf{r}^2/2f$

projector¹. The main motivation for this was the prospect of achieving comparable results to a commercial phase-only SLM for a roughly two-order-of-magnitude magnitude reduction in cost. Commercial LCD panels have already been used as intensity modulators to control the intensity of an array of optical dipole traps for manipulating a cold ^{85}Rb sample [298]. Figure C.8 shows the bare LCD panel connected to the control board, after the safety circuit controlling the projector's high-power light source was bypassed.

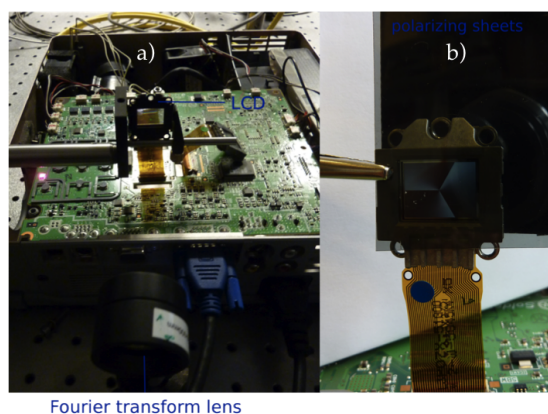


Figure C.8: (a) Home-made SLM using LCD panel and control electronics from commercial projector. (b) close-up of LCD panel between crossed polarizers showing the displayed ($l = 3$) phase pattern.

The main drawbacks of this approach, aside from the lack of robustness/rigidity of the setup, are:

- The transmissive nature of the device significantly reduces the diffraction efficiency. The commercial SLM operates reflectively and incorporates a dielectric mirror to maximize reflection over the desired wavelength range.
- The spaces between the panel's pixels give rise to a modulating envelope to the entire image and degrade its smoothness. The commercial SLM utilizes an LCOS panel, which operates in reflection and whose pixels are intrinsically much more closely spaced, reducing the effects of pixellation.
- Use of twisted nematic liquid crystals as opposed to parallel liquid crystals. Twisted nematics rotate the beam's polarization which has an unknown effect of the quality of the final image, relying as it does on interference of the beams emerging from each pixel. The commercial SLM utilizes a parallel-aligned nematic LCD which leaves the beam's polarization unaffected.

¹ Saville Audio Visual, TMX-1700XL. Cost: £150.

C.7 Current status and future plans

We are currently making use of a commercial SLM in experiments investigating the proliferation and non-equilibrium behaviour of vortices nucleated in a ^{87}Rb condensate using the LG_0^l beams described above. The techniques under development may also find application in direct measurements of the superfluid fraction of ultracold gases, as proposed in [290].

In addition, plans exist for a series of experiments on uniformly-confined clouds in both two and three dimensions, including the crossover between the two regimes.

Finally, another attempt at in-house construction of an SLM is also underway. We hope to improve on our previous efforts by making use of a commercially available LCOS panel instead of the conventional LCD display mentioned above in order to improve efficiency and reduce pixelation effects.

D

MOT and science cell properties

- Figure D.1 shows top and side views of the 316LN stainless steel MOT cell, as well a diagram of the quartz science cell with the dimensions in millimetres.
- Figure D.2 shows the single-surface reflectance spectrum at normal (0°) incidence (solid line).
- Figure D.3 shows the single-surface reflectance spectrum at 45° incidence. The upper, long-dashed line is the spectrum for s-polarized light and the lower, short-dashed line is the spectrum for p-polarized light. The solid line shows the mean for the two polarizations.
- Figure D.4 shows the transmittance spectrum at 45° incidence for an *entire* cell, with only the external surfaces coated. The upper, short-dashed line is the spectrum for p-polarized light and the lower, long-dashed line is the spectrum for s-polarized light. The solid line shows the mean for the two polarizations.

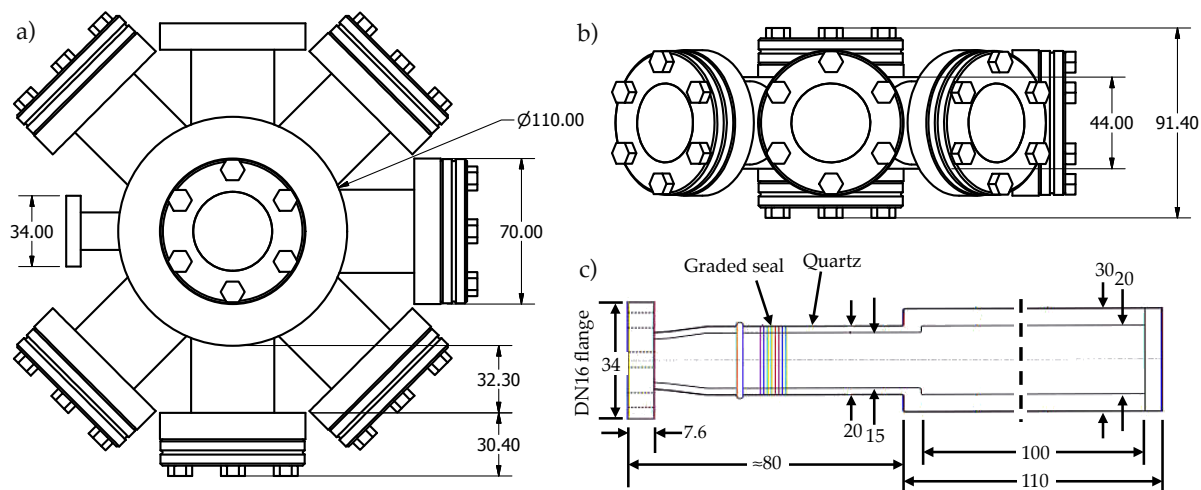


Figure D.1: Top (a) and side view (b) views of the MOT cell and a diagram of the science cell (c), including relevant dimensions (in mm).

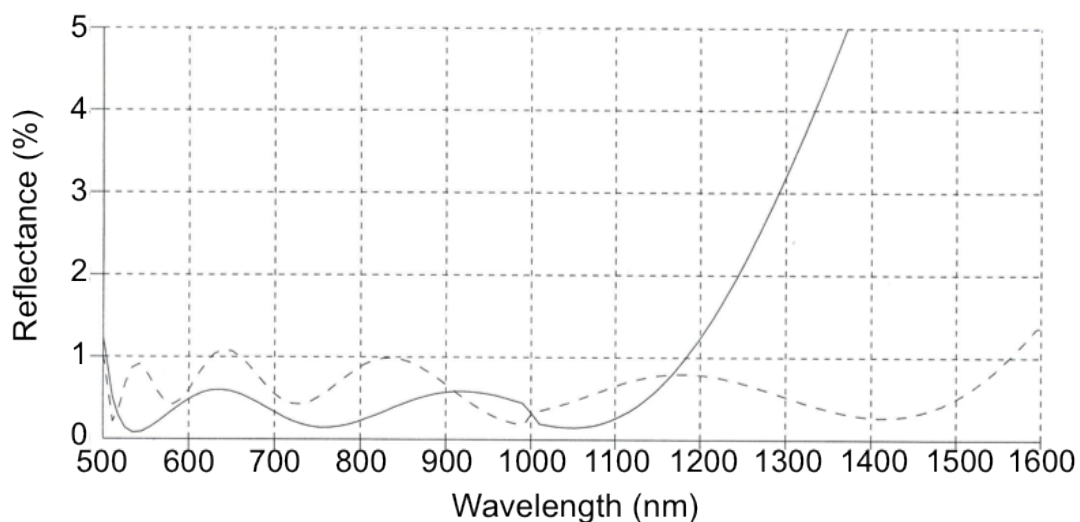


Figure D.2: Science cell BBAR coating. Single-surface reflectance spectrum at normal (0°) incidence (solid line). The dashed line shows an alternative coating offered by the manufacturer. Data provided by the manufacturer, Starna Scientific Ltd.

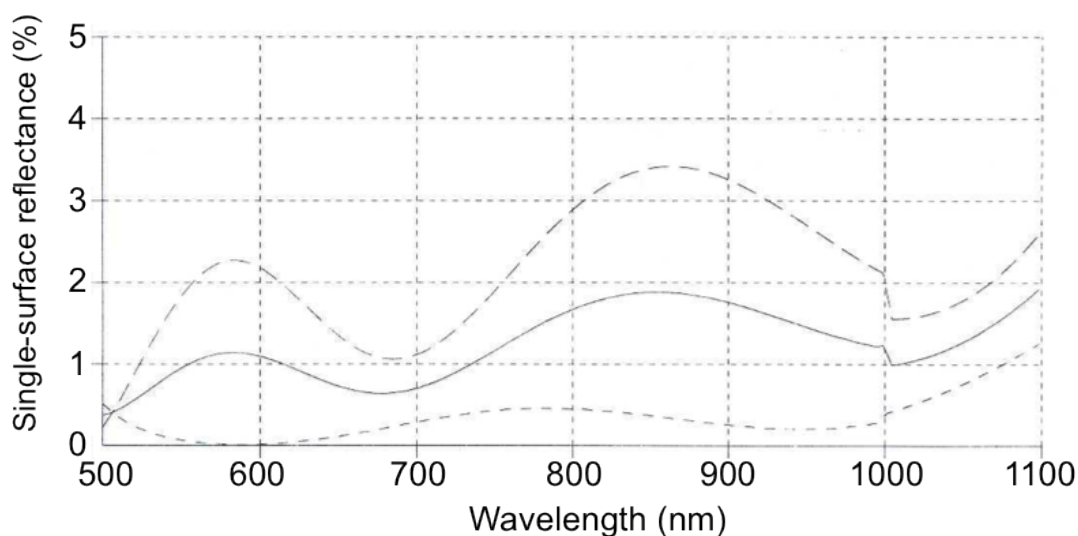


Figure D.3: Science cell BBAR coating. Single-surface reflectance spectrum at normal 45° incidence. Upper (long-dashed) line shows spectrum for s-polarized light and lower (short-dashed) line shows spectrum for p-polarized light. Solid line shows mean of both polarizations. Data provided by the manufacturer, Starna Scientific Ltd.

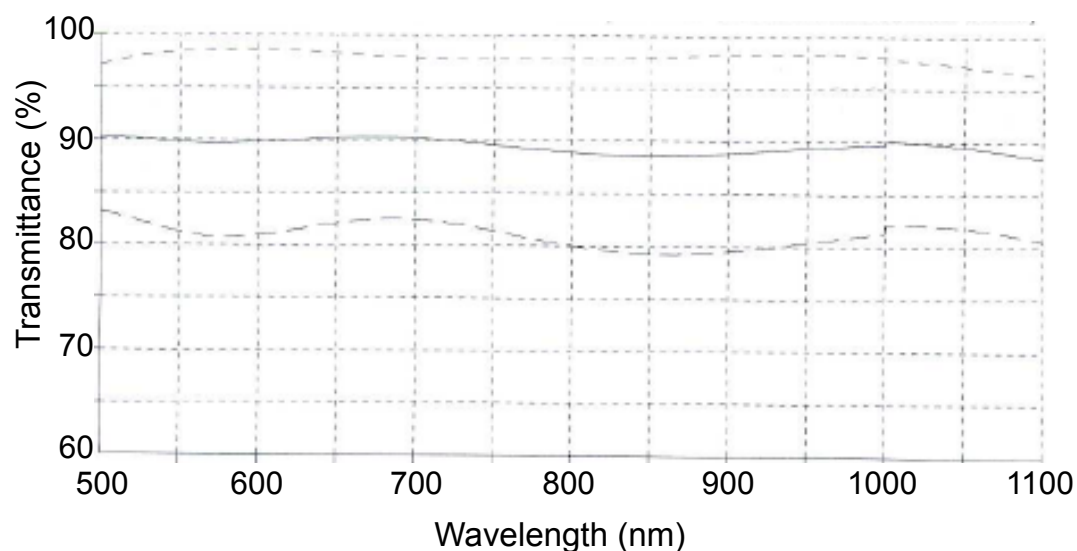


Figure D.4: Science cell BBAR coating. Transmittance through entire science cell at 45° incidence. Only external surfaces are coated. Upper (short-dashed) line shows spectrum for p-polarized light and lower (long-dashed) line shows spectrum for s-polarized light. Solid line shows mean of both polarizations. Data provided by the manufacturer, Starna Scientific Ltd.

E

Magnetic fields produced by current-carrying coils

E.1 Fields from circular coils

The axial and radial field components generated by loop of current I with radius R , displaced from the origin by a distance D (as illustrated in figure E.1a) are:

$$\begin{aligned} B_z &= \frac{\mu I}{2\pi} \frac{1}{\sqrt{(R+\rho)^2 + (z-D)^2}} \left[K(k^2) + \frac{R^2 - \rho^2 - (z-D)^2}{(R-\rho)^2 + (z-D)^2} E(k^2) \right] \\ B_\rho &= \frac{\mu I}{2\pi} \frac{1}{\rho} \frac{z-D}{\sqrt{(R+\rho)^2 + (z-D)^2}} \left[-K(k^2) + \frac{R^2 + \rho^2 - (z-D)^2}{(R-\rho)^2 + (z-D)^2} E(k^2) \right] \end{aligned} \quad (\text{E.1})$$

where

$$k^2 = \frac{4R\rho}{(R+\rho)^2 + (z-D)^2} \quad (\text{E.2})$$

and $K(k^2)$ and $E(k^2)$ are the complete elliptic integrals of the first and second kind, respectively¹.

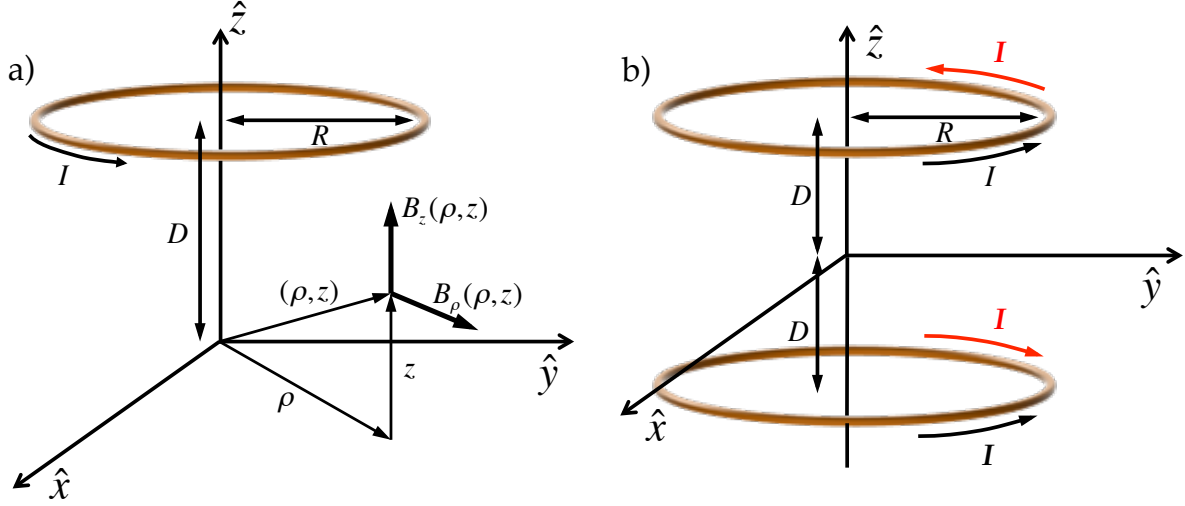


Figure E.1: Single-loop and coil-pair configuration. Figure (a) shows a thin loop of radius R and current I , mounted a distance D from the origin. Figure (b) shows a coil pair mounted a distance $d = 2D$ apart and operated in Helmholtz (black arrows) and Anti-Helmholtz (red arrows) configuration.

E.1.1 Near-origin approximation for circular current loops

Near the origin ($\rho = 0$, $z = 0$), the power series expansion for the field due to a single coil (see figure E.1a) to second order in ρ and z is:

$$\begin{aligned}
 B_z &= \mu I \frac{1}{2} \frac{R^2}{(D^2 + R^2)^{3/2}} + \underbrace{\mu I \frac{3}{2} \frac{DR^2}{(D^2 + R^2)^{5/2}} z}_{\text{axial field gradient}} + \underbrace{\mu I \frac{3}{4} \frac{R^2(4D^2 - R^2)}{(D^2 + R^2)^{7/2}} (z^2 - \rho^2/2)}_{\text{axial curvature}} + \dots \\
 B_\rho &= - \underbrace{\mu I \frac{3}{4} \frac{DR^2}{(D^2 + R^2)^{5/2}} \rho}_{\text{radial field gradient}} - \mu I \frac{3}{4} \frac{R^2(4D^2 - R^2)}{(D^2 + R^2)^{7/2}} z \rho + \dots
 \end{aligned} \tag{E.3}$$

E.1.2 Circular coil pairs

Figure E.1b shows a coil pair, operated in Helmholtz (black arrows) or Anti-Helmholtz (red arrows) configuration. The coils are a distance $d = 2D$ apart.

¹ These functions are implemented in *Mathematica* as `EllipticK[m]` and `EllipticE[m]`.

- For the **Helmholtz** configuration, the equations for the field near the origin to third order are

$$\begin{aligned}
 B_z &= \mu I \frac{R^2}{(D^2 + R^2)^{3/2}} + \mu I \frac{3 R^2 (4D^2 - R^2)}{2 (D^2 + R^2)^{7/2}} (z^2 - \rho^2/2) + \dots \\
 B_\rho &= -\mu I \frac{3 R^2 (4D^2 - R^2)}{2 (D^2 + R^2)^{7/2}} z \rho + \dots
 \end{aligned} \tag{E.4}$$

The next terms in this expansion are only fourth order in z and ρ . In the ideal Helmholtz case, when $R = 2D$ (i.e. coil *spacing* = coil *radius*), the second term in B_z and the first term in B_ρ vanish, leaving the uniform field

$$B_z = \mu I \frac{8}{5\sqrt{5}R} + \dots \tag{E.5}$$

$$B_\rho = 0 + \dots \tag{E.6}$$

- For the **Anti-Helmholtz** configuration, the equations for the field near the origin to third order are

$$\begin{aligned}
 B_z &= \mu I \cdot 3 \cdot \frac{DR^2}{(D^2 + R^2)^{5/2}} z + \mu I \frac{15 R^2 (4D^2 - 3R^2)}{24 (D^2 + R^2)^{9/2}} (4z^2 - 6\rho^2 z) + \dots \\
 B_\rho &= -\mu I \frac{3}{2} \frac{DR^2}{(D^2 + R^2)^{5/2}} \rho + \mu I \frac{15 R^2 (4D^2 - 3R^2)}{16 (D^2 + R^2)^{9/2}} (\rho^3 - 4\rho z^4) + \dots
 \end{aligned} \tag{E.7}$$

In this case, when $R = 2D$ the field gradient is maximized and is given by

$$\frac{dB_z}{dz} = \mu I \frac{48}{25\sqrt{5}R^2} = 2 \frac{dB_\rho}{d\rho} \tag{E.8}$$

It is also worth noting that the third order terms in both directions in both directions vanish when $R = \sqrt{4/3}D$.

Approximating the coil pairs in our experiments as stacked single pairs of increasing radius and separation we obtain a good estimate to the total field by summing the individual contribution of each pair according to the above equations using the appropriate spacings and radii. This was used in the design of our quadrupole, MOT compensation and Feshbach coils.

E.2 Fields from rectangular coils

Below are the expressions for the magnetic field produced by a thin rectangular loop of current, I lying in the xy plane¹. These were used in the design of the coil mount holding the rectangular Helmholtz coils mounted around the science cell and described in section 3.11. Figure E.2 shows the geometry under consideration.

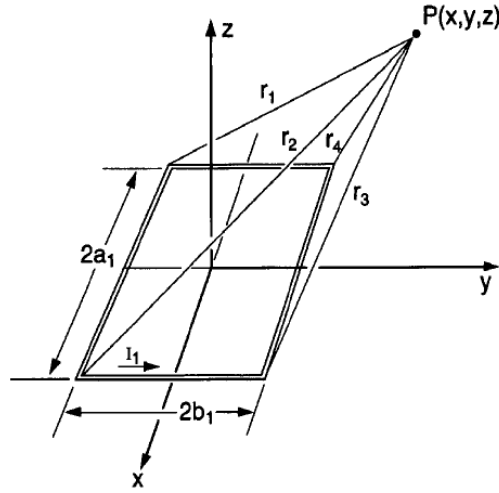


Figure E.2: Geometry for a single rectangular loop of wire with side dimensions $2 \times a_1$ by $2 \times b_1$ lying in the x - y plane. The field is evaluated at point $P(x, y, z)$.

The field is obtained from the vector potential using

$$B_x = -\frac{\partial A_y}{\partial z} \quad B_y = \frac{\partial A_x}{\partial z} \quad B_z = \frac{\partial A_y}{\partial x} - \frac{\partial A_x}{\partial y} \quad (\text{E.9})$$

The components of the vector potential are

$$A_x = \frac{\mu_0 I}{4\pi} \ln \left[\frac{(r_1 + a_1 + x)}{(r_2 - a_1 + x)} \cdot \frac{(r_3 - a_1 + x)}{(r_4 + a_1 + x)} \right]$$

$$A_y = \frac{\mu_0 I}{4\pi} \ln \left[\frac{(r_2 + b_1 + y)}{(r_3 - b_1 + y)} \cdot \frac{(r_4 - b_1 + y)}{(r_1 + b_1 + y)} \right] \quad (\text{E.10})$$

where r_1 , r_2 , r_3 and r_4 are the distances from the corners of the loop to the point $P(x, y, z)$ at which the field will be calculated (see figure E.2). The components

¹ Results reproduced from [299]

of the field at $P(x, y, z)$ are then

$$B_x = \frac{\mu_0 I}{4\pi} \sum_{\alpha=1}^4 \left[\frac{(-1)^{\alpha+1} z}{r_\alpha [r_\alpha + d_\alpha]} \right] \quad (\text{E.11})$$

$$B_y = \frac{\mu_0 I}{4\pi} \sum_{\alpha=1}^4 \left[\frac{(-1)^{\alpha+1} z}{r_\alpha [r_\alpha + (-1)^{\alpha+1} C_\alpha]} \right] \quad (\text{E.12})$$

$$B_z = \frac{\mu_0 I}{4\pi} \sum_{\alpha=1}^4 \left[\frac{(-1)^\alpha d_\alpha}{r_\alpha [r_\alpha + (-1)^\alpha C_\alpha]} - \frac{C_\alpha}{r_\alpha [r_\alpha + d_\alpha]} \right] \quad (\text{E.13})$$

where

$$\begin{aligned} C_1 = -C_4 = a_1 + x & & d_1 = d_2 = y + b_1 \\ C_2 = -C_3 = a_1 - x & & d_3 = d_4 = y - b_1 \end{aligned} \quad (\text{E.14})$$

$$\begin{aligned} r_1 &= \sqrt{(a_1 + x)^2 + (y + b_1)^2 + z^2} & r_2 &= \sqrt{(a_1 - x)^2 + (y + b_1)^2 + z^2} \\ r_3 &= \sqrt{(a_1 - x)^2 + (y - b_1)^2 + z^2} & r_4 &= \sqrt{(a_1 + x)^2 + (y - b_1)^2 + z^2} \end{aligned} \quad (\text{E.15})$$

Figure E.3 shows a screenshot from the Mathematica notebook used to obtain the total field and curvature of the rectangular Helmholtz coils used in our experiment. The predictions of this simulation are in excellent agreement with the measured field values reported in table 3.4.

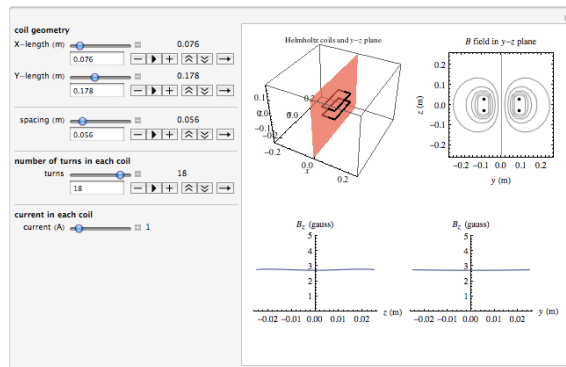


Figure E.3: Mathematica notebook. Includes a diagram of the specified coils (top left), a plot of the field contours in the y - z plane (top right) and B_z field profiles along the y and z axes, with the other two coordinates equal to zero (bottom right and left, respectively).

F

A tightly confining potential for studies of two-dimensional Bose gases

F.1 Introduction

A system's dimensionality plays a crucial role in determining its properties and the nature of its phase transitions. In general, ordered states are more robust in higher dimensions, while the effects of thermal and quantum fluctuations tend to destroy the ordering of the system in lower dimensions (see [300] and references therein).

The case of two dimensions is especially interesting since it displays 'marginal' behaviour: Although, as described by the Mermin-Wagner theorem, thermal fluctuations preclude true long-range order at any finite temperature in an infinite

ideal system, superfluidity is still possible in an interacting infinite system at finite temperature. The mechanism by which this superfluidity is established is named the Berezinskii-Kosterlitz-Thouless (BKT) transition, after those who first proposed its existence [301, 302].

In order to enter the 2D regime in the context of experiments on ultracold atoms a highly-anisotropic trap is required, possessing one spatial direction that is far more tightly-confining than the remaining two. The tightly-confining direction is ‘frozen out’ when the energy spacing, $\hbar\omega$, between the ground state and first excited state is much larger than both $k_{\text{B}}T$ and the mean-field interaction energy gn , where g is the coupling constant and n the particle density. Both of these quantities are typically on the order of a few kHz.

Our ability to fine-tune the interaction strength in our ^{39}K clouds opens the way for interesting experiments on the interplay between interactions and dimensionality in this system. The interaction strength in the 2D regime can be characterized by a dimensionless coupling constant, \tilde{g} , related to the 3D coupling strength, g via

$$g = \frac{\hbar^2}{m} \tilde{g} \quad (\text{F.1})$$

where m is the atomic mass. For a harmonically-confined gas, this can be rewritten as

$$\tilde{g} = \sqrt{8\pi} \frac{a}{a_{\text{ho}}} \quad (\text{harmonic trap}) \quad (\text{F.2})$$

where a is the scattering length and $a_{\text{ho}} = \sqrt{\hbar/m\bar{\omega}}$ is the oscillator length in the tightly-confining direction. As an example, assuming a trap frequency of 4kHz (see section F.3 below), the range of interaction strengths used in the experiments reported in this thesis ($a \approx 40 - 400a_0$), should allow us to span the interval $\tilde{g} = 0.04 - 0.4$. This compares to typical values of $\tilde{g} = 0.13$ in the Paris experiments [190, 303] and $\tilde{g} = 0.02$ in the NIST experiments of [304].

Furthermore, using the holographic techniques described in appendix C, novel geometries can be created for containing these two-dimensional ultracold clouds. These include, but are not limited to, uniform trapping potentials and non-simply-connected geometries such as toroidal traps. With these longer-term goals in mind, preliminary work was carried out on generating an optical potential possessing tight confinement along a single direction for studying two-dimensional clouds.

Several experimental methods have been employed in order to achieve 2D and

quasi-2D confinement of trapped clouds:

- A single red-detuned gaussian beam was used in conjunction with a tightly-focussing cylindrical lens to produce an attractive sheet trap. This was used in the first production of a gas in the quasi-2D regime [305] as well as in the experiments at NIST [304].
- Two interfering gaussian beams of wavelength λ , either perfectly counter-propagating or with a small angle, θ between them, can be used to produce a stack of adjacent 2D clouds separated by $\lambda/2$ or $\lambda/(2 \sin(\theta/2))$, respectively [306, 307, 308, 309, 310, 311, 312].
- Atoms can be tightly-confined against an evanescent wave in close proximity to a glass surface, with in-plane confinement being provided by an additional optical trap or magnetic field gradient [313, 314].
- 2D confinement has also been implemented using rf-dressed magnetic traps [315, 316, 317].
- Another technique involves the use of blue-detuned light in conjunction with a phaseplate to produce a potential consisting of two repulsive sheets, with the atoms confined in the dark plane and radial confinement provided by an additional optical or magnetic potential [318, 319, 320]

We have chosen to implement the last of these schemes following recent encouraging results from the ENS group. The principle behind generating the potential is identical to that described for spatial light modulators (SLMs) in appendix C, with the SLM surface replaced by a static optical element. These plates are made by spatially tailoring the thickness of an anti-reflection coating in order to produce the desired phase shift at the design wavelength. Below we describe this method in further detail and describe the results of our preliminary tests.

F.2 The $0-\pi$ phaseplate

The most convenient phase-pattern to produce a suitable tightly-confining potential is the $0-\pi$ plate, consisting of a π phase-shift for $Y < 0$ and no phase shift for $Y > 0$.

$$P(x, y) = \begin{cases} 0 & \text{if } y < 0 \\ \pi & \text{if } y > 0 \end{cases} \quad (\text{F.3})$$

This pattern produces a Hermite-Gaussian TEM_{01} -like mode at the focus of the

Fourier lens, which as usual is chosen to coincide with the position of the atoms. Figure F.1 shows the phase pattern, resulting intensity profile and a comparison to the unshifted Gaussian beam.

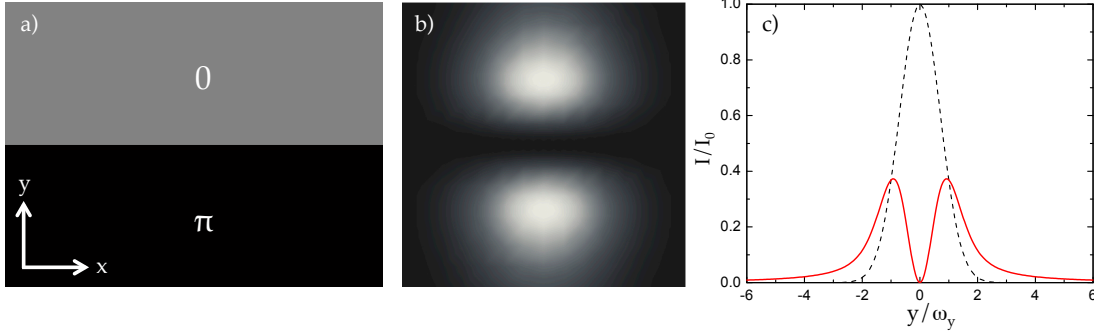


Figure F.1: Generating a 2D potential using a $0-\pi$ phaseplate. (a) The imprinted phase pattern, (b) the resulting intensity profile for a Gaussian input beam and (c) cross-sections through the intensity profiles of the shifted and unshifted beams, normalized to the peak intensity of the unshifted beam.

The field in the focal plane is given by (see equation C.6)

$$E(\mathbf{r}', f) = \frac{1}{i\lambda f} \int_{-\infty}^{\infty} dx \left(\int_0^{\infty} dy - \int_{-\infty}^0 dy \right) E(\mathbf{r}, 0) e^{ik\mathbf{r}\cdot\mathbf{r}'/f} \quad (\text{F.4})$$

where $r = \sqrt{x^2 + y^2}$, f is the Fourier lens focal length, $E(\mathbf{r}, 0)$ is the Gaussian field incident on the phaseplate and vertical centre of the phaseplate is at $y = 0$. For a Gaussian input beam of power P and waists ω_x, ω_y

$$E(\mathbf{r}, 0) = \sqrt{\frac{2P}{\pi\omega_x\omega_y}} \exp\left(-\frac{x^2}{\omega_x^2}\right) \exp\left(-\frac{y^2}{\omega_y^2}\right) \quad (\text{F.5})$$

the integral of equation F.4 can be evaluated analytically to give

$$E(\mathbf{r}', f) = \underbrace{\sqrt{\frac{2P}{\pi\omega'_x\omega'_y}} \exp\left(-\frac{x'^2}{\omega_x'^2}\right) \exp\left(-\frac{y'^2}{\omega_y'^2}\right)}_{\text{Focussed Gaussian}} \underbrace{\text{erfi}\left(\frac{y'}{\omega_y'}\right)}_{\text{modulation}} \quad (\text{F.6})$$

where $\omega'_{x,y} = \lambda f / \pi\omega_{x,y}$ is the usual focussed Gaussian waist and the imaginary error function, $\text{erfi}(z)$, is related to the error function by $\text{erfi}(z) = -i\text{erf}(iz)$, with $\text{erf}(z) = 2/\sqrt{\pi} \int_0^z \exp(-t^2) dt$. This has the form of a focussed Gaussian modulated by an error function and is shown in figure F.1c. Since the error

function is an odd function, the intensity profile vanishes along $y = 0$. This property is useful since it ensures the minimal photon scattering rate for the atoms confined at the centre of the potential. This is also an advantage of using blue- as opposed to red-detuned light. Furthermore, since blue-detuned light can be focussed down to smaller waists, it also enables the production of more tightly-confining traps than those using red-detuned light.

F.3 Estimating the trapping frequency and depth

The trapping frequency near the intensity minimum can be estimated by using the first-order approximation $\operatorname{erfi}(z) \approx (2/\sqrt{\pi})z + O(z^3)$. Inserting this into the expression for the intensity $I(\mathbf{r}', f) = |E(\mathbf{r}', f)|^2$ and using expression 2.47 for the potential produced by a far-detuned beam of detuning Δ

$$U_{\text{dip}}(\mathbf{r}) = \frac{3\pi c^2 \Gamma}{2\omega_0^3 \Delta} I(\mathbf{r}) \quad (\text{F.7})$$

gives a potential in the y -direction of the form $U_{\text{dip}}(y) = \frac{1}{2}m\Omega^2 y^2$ with the trapping frequency

$$\Omega^2 = \frac{24c^2 \Gamma P}{\pi m \omega_0^3 \omega_y'^3 \omega_x' \Delta} \quad (\text{F.8})$$

with Γ the natural linewidth, c the speed of light, m the atomic mass and ω_0 the transition frequency. Plugging in the constants for ^{39}K and 532nm light gives $\Omega^2 = \alpha P / \omega_y'^3 \omega_x'$, with $\alpha = 2.47 \times 10^{-11} \text{m}^4/\text{Js}$. Hence for a beam with *transverse* waist $\omega_x' = 150\mu\text{m}$ and *axial* waist $\omega_y' = 5\mu\text{m}$, this results in a vertical trapping frequency of $\Omega_y = 2\pi \times 5.77 \times \sqrt{P} \text{kHz}$, with the beam power P given in Watts.

By setting $dU_{\text{dip}}/dy = 0$, the distance, d , between the intensity maxima is found to be $d_y = 1.8483 \omega_y'$. Using this result, the trap depth is found to be 0.37 times the height of the unshifted Gaussian beam, i.e.

$$T = \frac{\Delta U}{k_B} = \frac{0.37 \cdot \alpha I_0}{k_B} = \frac{0.37 \cdot \alpha 2P}{\pi \omega_y' \omega_x' k_B} \quad (\text{F.9})$$

with $\alpha \approx 8.1 \times 10^{-37} \text{Jm}^2/\text{W}$ for both ^{39}K and ^{87}Rb . For the $5\mu\text{m}$ and $150\mu\text{m}$ waists above, this amounts to a depth of roughly $18\mu\text{K}/\text{W}$.

F.4 Experimental setup

Figure F.2 shows a schematic of the experimental setup designed for use in our apparatus. At the time of writing of this thesis this hardware has not yet been installed on the system but has undergone preliminary testing to ensure its suitability.

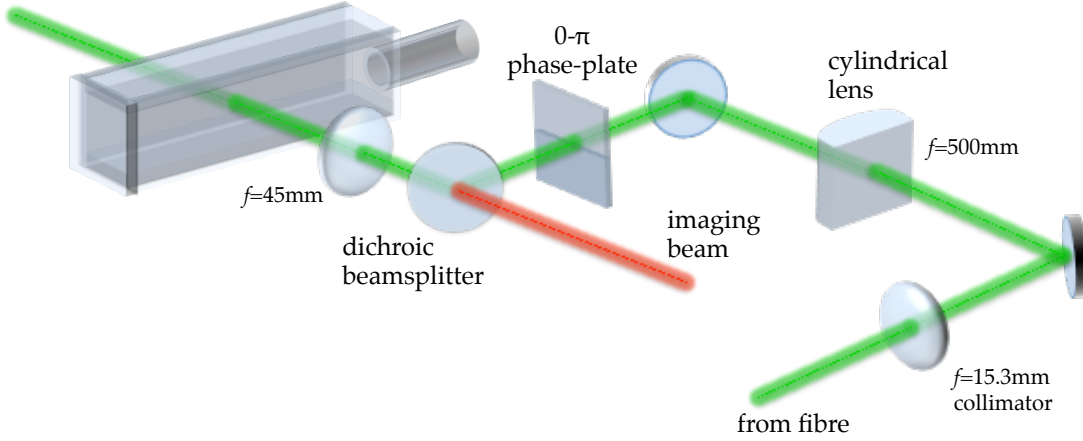


Figure F.2: Illustration of our setup for producing the 2D confining potential. In addition to being collimated and focussed to the desired waists, the trapping beam passes through the $0-\pi$ phaseplate. The trapping beam is overlapped with an imaging beam to aid alignment.

The main advantage of our configuration compared to those utilized by the Oxford and Paris groups lies in its simplicity, consisting in essence of three lenses and the $0-\pi$ phaseplate. By contrast, the Oxford setup contains seven lenses and the phaseplate, while the Paris setup uses four lenses in addition to the phaseplate. Our system is comparable in simplicity to that used by the Austin group, although they also include an aperture in the optical path. In addition, due to spatial limitations, the Paris group are constrained to use 2-inch optics along the entire beam path to avoid clipping of their 7mm-diameter beam. We are fortunate in being able to use a 45mm lens as the Fourier lens (compared to 100mm and 160mm for the Paris and Oxford groups, respectively) and hence achieve an equal spot size with a beam of less than half the diameter, allowing us to use only 1-inch optics. Figure F.3 shows a top and side view of the beam trajectory.

The trapping beam emerges from a polarization-maintaining (PM) single-mode fibre¹ and is collimated to a diameter of $d_{\text{init}} = 3\text{mm}$ by an $f = 15.3\text{mm}$ spherical

¹ Timbercon, Inc., PM-4630-0420-0420-008M

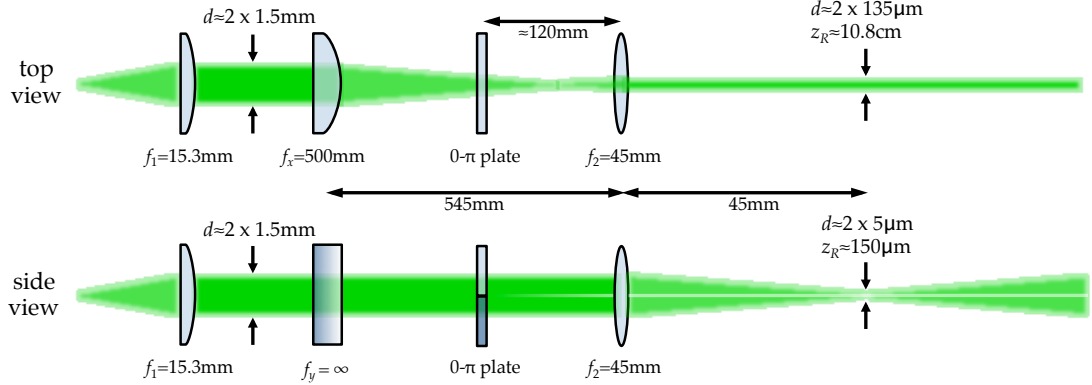


Figure F.3: Configuration for producing a tightly-confining optical potential. The blue-detuned (532nm) beam is collimated, and then telescoped transversely to a waist of $\omega'_x = 135\mu\text{m}$ while being focussed vertically to a waist of around $\omega'_y = 5\mu\text{m}$. On the way, it passes through the $0-\pi$ phaseplate which gives rise to the TEM_{01} -like mode in the focal plane.

lens¹. It then passes through an $f = 500\text{mm}$ cylindrical lens² which focusses the beam along the transverse (horizontal) direction and acts as the first lens of a two-lens telescope. The beam then passes through the $0-\pi$ phaseplate³, is reflected from a dichroic beamsplitter³ and is focussed on the atoms by the $f = 45\text{mm}$ spherical Fourier lens⁴. This lens collimates the beam transversely to a $1/e^2$ -waist of $\omega'_x = 135\mu\text{m}$ ⁵ and focusses the beam axially to a waist of $\omega'_y = 5\mu\text{m}$. The dichroic beamsplitter is chosen to reflect 532nm light while transmitting imaging light for both ^{87}Rb and ^{39}K in order to facilitate alignment of the 2D trap with the trapped atoms. These focal length values were chosen to provide sufficiently tight confinement, while possessing a Rayleigh range which was large enough to ensure a uniform potential (matching the CDT waist) without wasting beam power unnecessarily. Care was taken to match the transverse waist to the axial Rayleigh range in order to ensure a uniform aspect ratio for the trapped cloud.

The phaseplate is mounted in a rotation mount⁶ to allow for precise alignment of the trapping plane and this rotation mount is mounted onto an XY translation stage⁷ to enable precise alignment of the phaseplate centre line with the trapping

¹ Thorlabs, C260TME-A

² Thorlabs, LJ1144RM-A

³ Semrock Inc., LM01-552-25

⁴ Thorlabs, AC254-045-A-ML

⁵ Note: Changing the transverse waist simply requires changing the cylindrical lens focal length.

⁶ Thorlabs, CRM1

⁷ Thorlabs, ST1XY-D

beam. The $f = 45\text{mm}$ Fourier lens is mounted within a precision translation stage¹ to allow translation of the focal plane along the beam propagation axis for overlapping with the atoms. Since after passing through the phaseplate the beam is no longer Gaussian and will not retain its form during propagation, we endeavour to place the Fourier lens as close as possible to the phaseplate. To this end, the phaseplate, dichroic beamsplitter and Fourier lens, with their respective translation stages, are all mounted within a right-angle kinematic cage mount² to ensure their proximity and alignment. After passing through the science cell, the trapping beam is separated from the imaging beam by another beamsplitter³ and sent to a beam dump in order to avoid damage to the camera sensor.

Updated design

Subsequent to the design of this system, the waist of the CDT was increased from $100\mu\text{m}$ to $140\mu\text{m}$ in order to increase the number of loaded atoms. Consequently, the choice of focal lengths in the 2D setup should be modified in order to ensure a uniform axial confinement in this new trap. Using an aspheric collimating lens of focal length $f_1 = 15\text{mm}$ ⁴, a cylindrical lens of focal length $f_x = 400\text{mm}$ ⁵ and keeping the $f_2 = 45\text{mm}$ Fourier lens results in a transverse waist of $\omega'_x = 165\mu\text{m}$ (Rayleigh range: 16.3cm) and an axial waist of $\omega'_y = 5.2\mu\text{m}$ (Rayleigh range: $160\mu\text{m}$). This configuration maintains the good matching between the transverse waist and the axial Rayleigh range, and in addition does not affect our ability to use 1-inch optics throughout. The preliminary testing, described below, was performed using the original design.

F.4.1 Preliminary trials

We initially tested the setup *without* the cylindrical lens and using a $f_2 = 1000\text{mm}$ lens as the final Fourier lens in order to obtain a larger focussed waist for better visibility. The camera was placed in the lens focal plane and images were recorded with and without the phaseplate present. Figure F.4 shows cuts through these images, together with the theoretical profile predicted for the same peak intensity.

¹ Thorlabs, SM1Z

² Thorlabs, KCB1

³ This beamsplitter is mounted in a gimbal mount (Thorlabs, KC45D)

⁴ Thorlabs, AL1815-A

⁵ Thorlabs, LJ1363RM-A or LJ1363L1-A

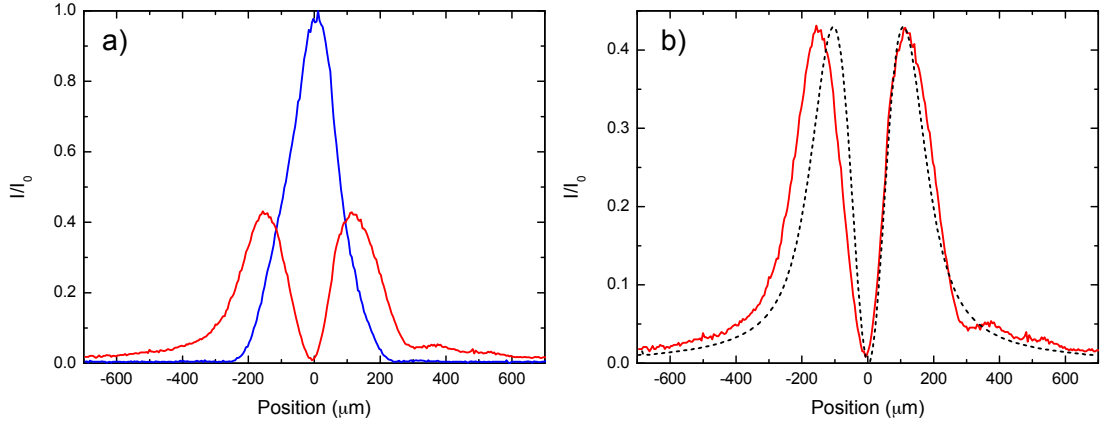


Figure F.4: (a) Intensity profile at the focus of a 1000mm Fourier lens with (red) and without (blue) the phaseplate in the beam path. (b) The profile with the phaseplate, together with the theoretical prediction for a beam of equal peak intensity.

We then made use of the custom ‘horizontal’ imaging objective described in section 3.14 to provide a higher spatial resolution. The profile with and without the phaseplate was recorded both in the presence and in the absence of the $f_x = 500\text{mm}$ cylindrical lens, using the $f_2 = 45\text{mm}$ lens as the Fourier lens. Figure F.5 shows the recorded profiles.

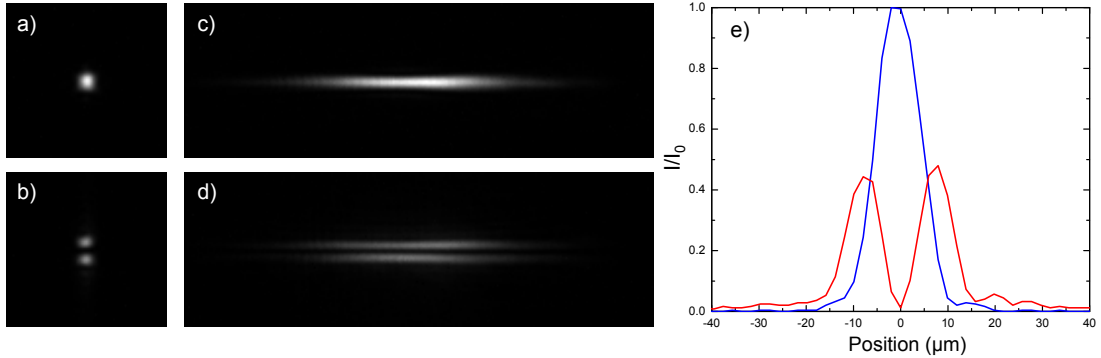


Figure F.5: Focal-plane intensity profiles with, ((b) and (d)), and without, ((a) and (c)), the phaseplate, in the presence, ((c) and (d)), and absence, ((a) and (b)), of the cylindrical lens. A 45mm lens was used as the Fourier lens. The field of view of the LHS images is $0.32 \times 0.26\text{mm}$ (H×W) and that of the RHS images is $0.37 \times 0.9\text{mm}$ (H×W). Figure (e) shows a vertical cut through the shifted (red) and unshifted (blue) profiles in the focal plane. The measured $1/e^2$ gaussian waist is $7.8\mu\text{m}$.

The magnification of the imaging system in this configuration was found to be $M = 2.35$ by focussing on a standard resolution chart (1951 USAF Resolution

Test Target¹). A Gaussian fit to the intensity profile yielded a waist in the focal plane of $7.8\mu\text{m}$, compared to the expected waist of $5.1\mu\text{m}$. In order to look into this discrepancy, we measured the profile of the beam after the first $f = 15.3\text{mm}$ collimating lens and found it to consist of only an approximate Gaussian, superposed with a sharper peak of roughly half the width.

We suspected that this might be due to clipping of the beam by the small diameter of the collimating lens (5mm) and in order to investigate this replaced it by a large-diameter, $f = 20\text{mm}$, asphere². This noticeably improved the gaussianity of the collimated beam and gave rise to a waist in the focal plane of the 45mm Fourier lens of $\omega'_y = 5.8\mu\text{m}$, implying a collimated waist of roughly 1.3mm, compared to the expected 1.97mm. This discrepancy may be due to an overestimate of the fibre's numerical aperture.

Loading procedure

The simplest protocol for transferring atoms into the 2D potential involves ramping up the 532nm beam in the presence of the CDT. In order to try and avoid heating, the Paris group ramp up their $\sim 3.6\text{kHz}$ trap over 1.5s ³, while the Oxford group ramp up their $\sim 2.2\text{kHz}$ trap over roughly 300ms. After this ramp-up, it is likely that some atoms will be trapped in the wings of the potential, within the CDT but outside the 2D plane. These atoms can be made invisible by transferring them to a state that does not interact with the imaging beam. This can be done using an RF sweep in the presence of a quadrupole magnetic field or, as in the Paris group, by selectively illuminating these atoms with $|F = 2\rangle \rightarrow |F' = 2\rangle$ pumping light to transfer them into the $|F = 1\rangle$ hyperfine state, which is not imaged. In order to transfer more atoms into the 2D potential, a preliminary stage can be added to the sequence, wherein a red-detuned gaussian sheet is first turned on in order to confine the atoms to a thin slab. The 2D potential can then be ramped up in order to provide the final tight confinement. An elaboration on this method was described in appendix C, whereby an SLM can be used to gradually decrease the distance between two initially well-separated blue-detuned sheets. See [291] and [321] for more details regarding the loading of atoms into the 2D potential.

¹ Thorlabs, R3L1S4P.

² Thorlabs, AL2520-A.

³ This ramp-up is carried out in the presence of an RF evaporation field and a magnetic TOP trap.

Bibliography

- [1] Onnes, H. K. The resistance of pure mercury at Helium temperatures. *Commun. Phys. Lab. Univ. Leiden* **12** (1911).
- [2] Allen, J. F. & Misener, A. D. Flow of liquid Helium II. *Nature* **141**, 75 (1938).
- [3] Kapitza, P. Viscosity of liquid Helium below the λ -point. *Nature* **141**, 74 (1938).
- [4] Allen, J. F. & Jones, H. New phenomena connected with heat flow in helium ii. *Nature* **141**, 243 (1938).
- [5] London, F. The λ -phenomenon of liquid Helium and the Bose–Einstein degeneracy. *Nature* **141**, 643 (1938).
- [6] Tisza, L. Transport phenomena in helium II. *Nature* **141**, 913 (1938).
- [7] Osheroff, D. D., Richardson, R. C. & Lee, D. M. Evidence for a new phase of solid He³. *Phys. Rev. Lett.* **28**, 885–888 (1972).
- [8] Osheroff, D. D., Gully, W. J., Richardson, R. C. & Lee, D. M. New magnetic phenomena in liquid He³ below 3 mK. *Phys. Rev. Lett.* **29**, 920–923 (1972).
- [9] Leggett, A. J. Interpretation of recent results on He³ below 3 mK: A new liquid phase? *Phys. Rev. Lett.* **29**, 1227–1230 (1972).
- [10] Nikuni, T., Oshikawa, M., Oosawa, A. & Tanaka, H. Bose-einstein condensation of dilute magnons in TlCuCl₃. *Phys. Rev. Lett.* **84**, 5868–5871 (2000).

-
- [11] Demokritov, S. O. *et al.* Bose–Einstein condensation of quasi-equilibrium magnons at room temperature under pumping. *Nature* **443**, 430–433 (2006).
- [12] Regal, C. A., Greiner, M. & Jin, D. S. Observation of resonance condensation of fermionic atom pairs. *Phys. Rev. Lett.* **92**, 040403 (2004).
- [13] Balili, R., Hartwell, V., Snoke, D., Pfeiffer, L. & West, K. Bose-Einstein condensation of microcavity polaritons in a trap. *Science* **316**, 1007–1010 (2007).
- [14] Kasprzak, J. *et al.* Bose-Einstein condensation of exciton polaritons. *Nature* **443**, 409–414 (2006).
- [15] URL http://www.nobelprize.org/nobel_prizes/physics/laureates/1997/.
- [16] URL http://www.nobelprize.org/nobel_prizes/physics/laureates/2001/.
- [17] URL http://www.nobelprize.org/nobel_prizes/physics/laureates/2005/.
- [18] Migdall, A. L., Prodan, J. V., Phillips, W. D., Bergeman, T. H. & Metcalf, H. J. First observation of magnetically trapped neutral atoms. *Phys. Rev. Lett.* **54**, 2596 (1985).
- [19] Raab, E. L., Prentiss, M., Cable, A., Chu, S. & Pritchard, D. E. Trapping of neutral Sodium with radiation pressure. *Phys. Rev. Lett.* **59**, 2631 (1987).
- [20] Hess, H. F. Evaporative cooling of magnetically trapped and compressed spin-polarized Hydrogen. *Phys. Rev. B* **34**, 3476 (1986).
- [21] Masuhara, N. *et al.* Evaporative cooling of spin-polarized atomic Hydrogen. *Phys. Rev. Lett.* **61**, 935 (1988).
- [22] Ketterle, W. & Druten, N. V. Evaporative cooling of trapped atoms. vol. 37 of *Advances In Atomic, Molecular, and Optical Physics*, 181–236 (Academic Press, 1996).
- [23] Anderson, M. H., Ensher, J. R., Matthews, M. R., Wieman, C. E. & Cornell, E. A. Observation of Bose-Einstein condensation in a dilute atomic vapor. *Science* **269**, 198 (1995).
- [24] Davis, K. B. *et al.* Bose-Einstein condensation in a gas of Sodium atoms. *Phys. Rev. Lett.* **75**, 3969 (1995).

-
- [25] Bradley, C. C., Sackett, C. A., Tollett, J. J. & Hulet, R. G. Evidence of Bose–Einstein condensation in an atomic gas with attractive interactions. *Phys. Rev. Lett.* **75**, 1687 (1995).
- [26] DeMarco, B. & Jin, D. D. Onset of Fermi degeneracy in a trapped atomic gas. *Science* **285**, 1703 (1999).
- [27] Truscott, A., Strecker, K., McAlexander, W., Partridge, G. & Hulet, R. G. Observation of Fermi pressure in a gas of trapped atoms. *Science* **291**, 2570 (2001).
- [28] Fried, D. G. *et al.* Bose–Einstein condensation of atomic Hydrogen. *Phys. Rev. Lett.* **81**, 3811 (1998).
- [29] Cornish, S. L., Claussen, N. R., Roberts, J. L., Cornell, E. A. & Wieman, C. E. Stable ^{85}Rb Bose–Einstein condensates with widely tunable interactions. *Phys. Rev. Lett.* **85**, 1795 (2000).
- [30] Robert, A. *et al.* A Bose–Einstein condensate of metastable atoms. *Science* **292**, 461–464 (2001).
- [31] Pereira Dos Santos, F. *et al.* Bose–Einstein condensation of metastable Helium. *Phys. Rev. Lett.* **86**, 3459–3462 (2001).
- [32] Modugno, G. *et al.* Bose–Einstein condensation of Potassium atoms by sympathetic cooling. *Science* **294**, 1320–1322 (2001).
- [33] Weber, T., Herbig, J., Mark, M., Nöcker, H.-C. & Grimm, R. Bose–Einstein condensation of Cesium. *Science* **299**, 232–235 (2003).
- [34] Takasu, Y. *et al.* Spin-singlet Bose–Einstein condensation of two-electron atoms. *Phys. Rev. Lett.* **91**, 040404 (2003).
- [35] Griesmaier, A., Werner, J., Hensler, S., Stuhler, J. & Pfau, T. Bose–Einstein condensation of Chromium. *Phys. Rev. Lett.* **94**, 160401 (2005).
- [36] Roati, G. *et al.* ^{39}K Bose–Einstein condensate with tunable interactions. *Phys. Rev. Lett.* **99**, 010403 (2007).
- [37] Kraft, S., Vogt, F., Appel, O., Riehle, F. & Sterr, U. Bose–Einstein condensation of alkaline earth atoms: ^{40}Ca . *Phys. Rev. Lett.* **103**, 130401 (2009).
- [38] Stellmer, S., Tey, M. K., Huang, B., Grimm, R. & Schreck, F. Bose–Einstein condensation of Strontium. *Phys. Rev. Lett.* **103**, 200401 (2009).

- [39] de Escobar, Y. N. M. *et al.* Bose-Einstein condensation of ^{84}Sr . *Phys. Rev. Lett.* **103**, 200402 (2009).
- [40] Stellmer, S., Tey, M. K., Grimm, R. & Schreck, F. Bose-Einstein condensation of ^{86}Sr . *Phys. Rev. A* **82**, 041602 (2010).
- [41] Lu, M., Burdick, N. Q., Youn, S. H. & Lev, B. L. Strongly dipolar Bose-Einstein condensate of Dysprosium. *Phys. Rev. Lett.* **107**, 190401 (2011).
- [42] Chin, C., Grimm, R., Julienne, P. & Tiesinga, E. Feshbach resonances in ultracold gases. *Rev. Mod. Phys.* **82**, 1225–1286 (2010).
- [43] Cornell, E. A. & Wieman, C. E. Nobel lecture: Bose-Einstein condensation in a dilute gas, the first 70 years and some recent experiments. *Rev. Mod. Phys.* **74**, 875–893 (2002).
- [44] Ketterle, W. Nobel lecture: When atoms behave as waves: Bose-Einstein condensation and the atom laser. *Rev. Mod. Phys.* **74**, 1131–1151 (2002).
- [45] Bloch, I., Dalibard, J. & Zwirger, W. Many-body physics with ultracold gases. *Rev. Mod. Phys.* **80**, 885 (2008).
- [46] Dalfovo, F., Giorgini, S., Pitaevskii, L. P. & Stringari, S. Theory of Bose-Einstein condensation in trapped gases. *Rev. Mod. Phys.* **71**, 463–512 (1999).
- [47] Williamson, R. S. I. & Walker, T. Magneto-optical trapping and ultracold collisions of Potassium atoms. *J. Opt. Soc. Am. B* **12**, 1393–1397 (1995).
- [48] Santos, M. S. *et al.* Simultaneous trapping of two different atomic species in a vapor cell MOT. *Phys. Rev. A* **52**, R4340 (1995).
- [49] Fort, C. *et al.* Cooling mechanisms in Potassium magneto-optical traps. *Eur. Phys. J. D* **3**, 113–118 (1998).
- [50] Santos, M. S. *et al.* Intensity dependence of the collisional loss rate for Potassium-39 atoms in a vapor cell MOT. *Laser Physics* **8**, 880–884 (1998).
- [51] Boesten, H. M. J. M., Vogels, J. M., Tempelaars, J. G. C. & Verhaar, B. J. Properties of cold collisions of ^{39}K atoms and of ^{41}K atoms in relation to Bose-Einstein condensation. *Phys. Rev. A* **54**, R3726 (1996).
- [52] Bohn, J. L. *et al.* Collisional properties of ultracold Potassium: Consequences for degenerate Bose and Fermi gases. *Phys. Rev. A* **59**, 3660–3664 (1999).

-
- [53] Prevedelli, M. *et al.* Trapping and cooling of Potassium isotopes in a double-magneto-optical-trap apparatus. *Phys. Rev. A* **59**, 886–888 (1999).
- [54] Ferrari, G. *et al.* Collisional properties of ultracold K-Rb mixtures. *Phys. Rev. Lett.* **89**, 053202 (2002).
- [55] G. Modugno *et al.* Comparative investigation of ^{39}K and ^{40}K trap loss rates: Alternative loss channel at low light intensities. *Eur. Phys. J. D* **23**, 409–413 (2003).
- [56] Banerjee, A. & Natarajan, V. Absolute-frequency measurements of the D_2 line and fine-structure interval in ^{39}K . *Phys. Rev. A* **70**, 052505 (2004).
- [57] Catani, J., Maioli, P., De Sarlo, L., Minardi, F. & Inguscio, M. Intense slow beams of bosonic Potassium isotopes. *Phys. Rev. A* **73**, 033415 (2006).
- [58] Ferlaino, F. *et al.* Feshbach spectroscopy of a K-Rb atomic mixture. *Phys. Rev. A* **73**, 040702 (2006).
- [59] De Sarlo, L. *et al.* Collisional properties of sympathetically cooled ^{39}K . *Phys. Rev. A* **75**, 022715 (2007).
- [60] D’Errico, C. *et al.* Feshbach resonances in ultracold ^{39}K . *New J. Phys.* **9**, 223 (2007).
- [61] Thalhammer, G. *et al.* Double species Bose-Einstein condensate with tunable interspecies interactions. *Phys. Rev. Lett.* **100**, 210402 (2008).
- [62] Thalhammer, G. *et al.* Collisional and molecular spectroscopy in an ultracold Bose-Bose mixture. *New J. Phys.* **11**, 055044 (2009).
- [63] Schreck, F. *et al.* Quasipure Bose-Einstein condensate immersed in a Fermi sea. *Phys. Rev. Lett.* **87**, 080403 (2001).
- [64] Tey, M. K., Stellmer, S., Grimm, R. & Schreck, F. Double-degenerate Bose-Fermi mixture of Strontium. *Phys. Rev. A* **82**, 011608 (2010).
- [65] Wu, C.-H., Santiago, I., Park, J. W., Ahmadi, P. & Zwierlein, M. W. Strongly interacting isotopic Bose-Fermi mixture immersed in a Fermi sea. *Phys. Rev. A* **84**, 011601 (2011).
- [66] Anderson, P. W. Absence of diffusion in certain random lattices. *Phys. Rev.* **109**, 1492–1505 (1958).
- [67] Roati, G. *et al.* Anderson localization of a non-interacting Bose-Einstein condensate. *Nature* **453**, 895–898 (2008).

- [68] Donley, E. A. *et al.* Dynamics of collapsing and exploding Bose–Einstein condensates. *Nature* **412**, 295 (2001).
- [69] Gerton, J., Strekalov, D., Prodan, I. & Hulet, R. G. Direct observation of growth and collapse of a Bose–Einstein condensate with attractive interactions. *Nature* **408**, 692–695 (2000).
- [70] Sackett, C. A., Gerton, J. M., Welling, M. & Hulet, R. G. Measurement of collective collapse in a Bose–Einstein condensate with attractive interactions. *Phys. Rev. Lett.* **82**, 876 (1999).
- [71] Müller, S. *et al.* Stability of a dipolar Bose–Einstein condensate in a one-dimensional lattice. *Phys. Rev. A* **84**, 053601 (2011).
- [72] Phillips, W. D. Nobel lecture: Laser cooling and trapping of neutral atoms. *Rev. Mod. Phys.* **70**, 721–741 (1998).
- [73] Cohen-Tannoudji, C. N. Nobel lecture: Manipulating atoms with photons. *Rev. Mod. Phys.* **70**, 707 (1998).
- [74] Chu, S. Nobel lecture: The manipulation of neutral particles. *Rev. Mod. Phys.* **70**, 685 (1998).
- [75] Maxwell, J. C. *A Treatise on Electricity and Magnetism* (Clarendon Press, Oxford, 1873).
- [76] Bartoli, A. *Sopra I Movimenti Prodotti dalla Luce e dal Calore* (Le Monnier, 1876).
- [77] Bartoli, A. Il calorico raggianti e il secondo principio di termodinamica. *Nuovo Cimento* **15**, 196–202 (1884).
- [78] Lebedev, P. Untersuchungen über die druckkräfte des lichtetes (the experimental study of the pressure of light). *Annalen der Physik* (1901).
- [79] Nichols, E. F. & Hull, G. F. A preliminary communication on the pressure of heat and light radiation. *Phys. Rev.* **13**, 307–320 (1901).
- [80] Nichols, E. F. & Hull, G. F. The pressure due to radiation. *The Astrophysical Journal* **17**, 315 (1903).
- [81] Einstein, A. Über die Entwicklung unserer Anschauungen über das Wesen und die Konstitution der Strahlung (On the Development of Our Views Concerning the Nature and Constitution of Radiation). *Physikalische Zeitschrift* **10**, 817–825 (1909).

- [82] Frisch, O. R. *Z. Phys.* **86** (1933).
- [83] Hänsch, T. W. & Schawlow, A. L. Cooling of gases by laser radiation. *Optics Comm.* **13**, 68 (1975).
- [84] Wineland, D. J. & Dehmelt, H. Proposed $10^{14}\delta\nu < \nu$ laser fluorescence spectroscopy on Ti^+ mono-ion oscillator III. *Bulletin of the American Physical Society* **20**, 637 (1975).
- [85] Ashkin, A. Trapping of atoms by resonance radiation pressure. *Phys. Rev. Lett.* **40**, 729–732 (1978).
- [86] Neuhauser, W., Hohenstatt, M., Toschek, P. & Dehmelt, H. Optical-sideband cooling of visible atom cloud confined in parabolic well. *Phys. Rev. Lett.* **41**, 223 (1978).
- [87] Andreev, S., Balykin, V., Letokhov, V. & Minogin, V. Radiative slowing and reduction of the energy spread of a beam of Sodium atoms to 1.5K in an oppositely directed laser beam. *JETP Lett.* **34**, 442 (1981).
- [88] Phillips, W. D. & Metcalf, H. J. Laser deceleration of an atomic beam. *Phys. Rev. Lett.* **48**, 596 (1982).
- [89] Metcalf, H. J. & Van der Straten, P. *Laser Cooling and Trapping* (Springer, 1999), illustrated edn.
- [90] Foot, C. J. *Atomic Physics* (Oxford University Press, 2005).
- [91] Letokhov, V. S. *Laser Control of Atoms and Molecules* (Oxford University Press, 2007).
- [92] Metcalf, H. J. & van der Straten, P. Laser cooling and trapping of atoms. *J. Opt. Soc. Am. B* **20**, 887–908 (2003).
- [93] Lett, P. D. *et al.* Observation of atoms laser cooled below the Doppler limit. *Phys. Rev. Lett.* **61**, 169 (1988).
- [94] Dalibard, J. & Cohen-Tannoudji, C. Laser cooling below the Doppler limit by polarization gradients: simple theoretical models. *J. Opt. Soc. Am. B* **6**, 2023 (1989).
- [95] Dalibard, J. & Cohen-Tannoudji, C. Dressed-atom approach to atomic motion in laser light: the dipole force revisited. *J. Opt. Soc. Am. B* **2**, 1707–1720 (1985).

- [96] Ungar, P. J., Weiss, D. S., Riis, E. & Chu, S. Optical molasses and multilevel atoms: Theory. *J. Opt. Soc. Am. B* **6**, 2058 (1989).
- [97] Weiss, D. S., Riis, E., Shevy, Y., Ungar, P. J. & Chu, S. Optical molasses and multilevel atoms: Experiment. *J. Opt. Soc. Am. B* **6**, 2072 (1989).
- [98] Castin, Y., Dalibard, J. & Cohen-Tannoudji, C. The limits of Sisyphus cooling. In Moi, L., Gozzini, S., Gabbanini, C., Arimondo, E. & Strumia, F. (eds.) *Proceedings of the workshop "Light-induced kinetic effects on atoms, ions and molecules", held in Elba Island, Italy* (ETS Editrice Pisa, 1990).
- [99] Bambini, A. & Agresti, A. Radiative cooling force in atoms with multiplet structure. *Phys. Rev. A* **56**, 3040–3055 (1997).
- [100] Steane, A. M. & Foot, C. J. Laser cooling below the Doppler limit in a magneto-optical trap. *Europhys. Lett.* **14**, 231 (1991).
- [101] Weidemüller, M. & Zimmermann, C. (eds.) *Cold Atoms and Molecules: Concepts, Experiments and Applications to Fundamental Physics* (Wiley-VCH, 2009).
- [102] Adams, C. & Riis, E. Laser cooling and trapping of neutral atoms. *Progress in Quantum Electronics* **21**, 1 – 79 (1997).
- [103] Kurosu, T. & Shimizu, F. Laser cooling and trapping of Calcium and Strontium. *Japanese Journal of Applied Physics* **29**, L2127–L2129 (1990).
- [104] Beverini, N. *et al.* Evidence for laser cooling in a Magnesium atomic beam. *Opt. Lett.* **14**, 350–352 (1989).
- [105] Xu, X., Loftus, T. H., Hall, J. L., Gallagher, A. & Ye, J. Cooling and trapping of atomic Strontium. *J. Opt. Soc. Am. B* **20**, 968–976 (2003).
- [106] Katori, H. & Shimizu, F. Laser cooling and trapping of Argon and Krypton using diode lasers. *Japanese Journal of Applied Physics* **29**, L2124–L2126 (1990).
- [107] Honda, K. *et al.* Magneto-optical trapping of Yb atoms and a limit on the branching ratio of the 1P_1 state. *Phys. Rev. A* **59**, R934–R937 (1999).
- [108] Lu, M., Youn, S. H. & Lev, B. L. Trapping ultracold Dysprosium: A highly magnetic gas for dipolar physics. *Phys. Rev. Lett.* **104**, 063001 (2010).
- [109] Youn, S. H., Lu, M., Ray, U. & Lev, B. L. Dysprosium magneto-optical traps. *Phys. Rev. A* **82**, 043425 (2010).

-
- [110] Steck, D. A. Rubidium-87 D-line data (2003). <http://steck.us/alkalidata/rubidium87numbers.1.6.pdf>.
- [111] Tiecke, T. Properties of potassium (2010). <http://staff.science.uva.nl/tgtiecke/PotassiumProperties.pdf>.
- [112] Williamson, R. S. I. *Magneto-optical trapping of potassium isotopes*. Ph.D. thesis, University of Wisconsin - Madison (1997).
- [113] Wang, H., Gould, P. L. & Stwalley, W. C. Photoassociative spectroscopy of ultracold ^{39}K atoms in a high-density vapor-cell magneto-optical trap. *Phys. Rev. A* **53**, R1216–1219 (1996).
- [114] Xu, X. *et al.* Single-stage sub-Doppler cooling of alkaline earth atoms. *Phys. Rev. Lett.* **90**, 193002 (2003).
- [115] Gokhroo, V., Rajalakshmi, G., Easwaran, R. K. & Unnikrishnan, C. S. Sub-Doppler deep-cooled bosonic and fermionic isotopes of Potassium in a compact 2D + -3D MOT set-up. *Journal of Physics B: Atomic, Molecular and Optical Physics* **44**, 115307 (2011).
- [116] Landini, M. *et al.* Sub-Doppler laser cooling of Potassium atoms. *Phys. Rev. A* **84**, 043432 (2011).
- [117] Breit, G. & Rabi, I. I. Measurement of nuclear spin. *Phys. Rev.* **38**, 2082–2083 (1931).
- [118] Majorana, E. Atomi orientati in campo magnetico variabile. *Nuovo Cimento* **9**, 43 (1932).
- [119] Schwinger, J. On nonadiabatic processes in inhomogeneous fields. *Phys. Rev.* **51**, 648 (1937).
- [120] McNicholl, T. B. P., Kycia, J., Metcalf, H. & Balazs, N. L. Quantized motion of atoms in a quadrupole magnetostatic trap. *J. Opt. Soc. Am. B* **6**, 2249 (1989).
- [121] Phillips, W. D., Prodan, J. V. & Metcalf, H. J. Laser cooling and electromagnetic trapping of neutral atoms. *J. Opt. Soc. Am. B* **2**, 1751 (1985).
- [122] Leanhardt, A. E. *et al.* Cooling Bose-Einstein condensates below 500 picokelvin. *Science* **301**, 1513–1515 (2003).
- [123] Pethick, C. & Smith, H. *Bose-Einstein Condensation in Dilute Gases* (Cambridge University Press, 2002).

- [124] Davis, K. B., Mewes, M.-O. & Ketterle, W. An analytical model for evaporative cooling of atoms. *Appl. Phys. B* **60**, 155 (1995).
- [125] Matsui, K. *et al.* Experimental study on evaporative cooling and Bose-Einstein condensation of Sodium atoms. *J. Phys. Soc. Japan* **78** (2009).
- [126] Yamashita, M. *et al.* Optimization of evaporative cooling towards a large number of Bose-Einstein-condensed atoms. *Phys. Rev. A* **67**, 023601 (2003).
- [127] Mukai, T. & Yamashita, M. Efficient rapid production of a Bose-Einstein condensate by overcoming serious three-body loss. *Phys. Rev. A* **70**, 013615 (2004).
- [128] Shobu, T., Yamaoka, H., Imai, H., Morinaga, A. & Yamashita, M. Optimized evaporative cooling for Sodium Bose-Einstein condensation against three-body loss. *Phys. Rev. A* **84**, 033626 (2011).
- [129] Myatt, C. J., Burt, E. A., Ghrist, R. W., Cornell, E. A. & Wieman, C. E. Production of two overlapping Bose-Einstein condensates by sympathetic cooling. *Phys. Rev. Lett.* **78**, 586–589 (1997).
- [130] Bloch, I., Greiner, M., Mandel, O., Hänsch, T. W. & Esslinger, T. Sympathetic cooling of ^{85}Rb and ^{87}Rb . *Phys. Rev. A* **64**, 021402 (2001).
- [131] Mudrich, M. *et al.* Sympathetic cooling with two atomic species in an optical trap. *Phys. Rev. Lett.* **88**, 253001 (2002).
- [132] Wang, H. *et al.* Ground-state scattering lengths for Potassium isotopes determined by double-resonance photoassociative spectroscopy of ultracold ^{39}K . *Phys. Rev. A* **62**, 052704 (2000).
- [133] Sakurai, J. J. *Modern Quantum Mechanics* (Addison-Wesley, Reading, Massachusetts, 1994).
- [134] Delannoy, G. *et al.* Understanding the production of dual Bose-Einstein condensation with sympathetic cooling. *Phys. Rev. A* **63**, 051602 (2001).
- [135] Grimm, R., Weidemüller, M. & Ovchinnikov, Y. B. Optical dipole traps for neutral atoms. vol. 42 of *Advances In Atomic, Molecular, and Optical Physics*, 95–170 (Academic Press, 2000).
- [136] Milloni, P. W. & Eberly, J. H. *Lasers* (John Wiley & Sons, 1988).
- [137] Chu, S., Bjorkholm, J. E., Ashkin, A. & Cable, A. Experimental observation of optically trapped atoms. *Phys. Rev. Lett.* **57**, 314 (1986).

- [138] Ashkin, A., Dziedzic, J. M., Bjorkholm, J. E. & Chu, S. Observation of a single-beam gradient force optical trap for dielectric particles. *Opt. Lett.* **11**, 288–290 (1986).
- [139] Jessen, P. & Deutsch, I. H. Optical lattices. *Adv. At. Mol. Opt. Phys.* **37**, 95–139 (1996).
- [140] Dalibard, J. Collisional dynamics of ultra-cold atomic gases. In Inguscio, M., Stringari, S. & Wieman, C. E. (eds.) *Proceedings of the International School of Physics Enrico Fermi, Course CXL*, 321 (IOS Press, 1999).
- [141] Modugno, G. Anderson localization in Bose-Einstein condensates. *Rep. Prog. Phys.* **73**, 102401 (2010).
- [142] Kondov, S. S., McGehee, W. R., Zirbel, J. J. & DeMarco, B. Three-dimensional Anderson localization of ultracold matter. *Science* **334**, 66–68 (2011).
- [143] Fattori, M. *et al.* Atom interferometry with a weakly interacting Bose-Einstein condensate. *Phys. Rev. Lett.* **100**, 080405 (2008).
- [144] Pitaevskii, L. & Stringari, S. *Bose-Einstein Condensation* (Oxford University Press, Oxford, 2003).
- [145] Ketterle, W., Durfee, D. & Stamper-Kurn, D. Making, probing and understanding Bose-Einstein condensates. In Inguscio, M., Stringari, S. & Wieman, C. E. (eds.) *Proceedings of the International School of Physics Enrico Fermi, Course CXL*, 67–176 (IOS Press, 1999).
- [146] Greiner, M., Bloch, I., Hänsch, T. & Esslinger, T. Magnetic transport of trapped cold atoms over a large distance. *Phys. Rev. A* **63**, 031401 (2001).
- [147] Chambers, A., Fitch, R. K. & Halliday, B. S. *Basic Vacuum Technology, 2nd edition* (Taylor & Francis, 1998).
- [148] Preston, D. W. Doppler-free saturated absorption: Laser spectroscopy. *Amer. J. of Phys.* **64**, 1432–1436 (1996).
- [149] Maguire, L. P., Szilagy, S. & Scholten, R. E. High performance laser shutter using a hard disk drive voice-coil actuator. *Rev. Sci. Instrum.* **75**, 3077 (2004).
- [150] Scholten, R. E. Enhanced laser shutter using a hard disk drive rotary voice-coil actuator. *Rev. Sci. Instrum.* **78** (2007).

- [151] Yu, J. *et al.* Effects of a static magnetic field on sub-Doppler molasses: manipulation of Cesium atoms. *Instrumentation and Measurement, IEEE Transactions on* **42**, 109–114 (1993).
- [152] Gustavson, T. L. *et al.* Transport of Bose-Einstein condensates with optical tweezers. *Phys. Rev. Lett.* **88**, 020401 (2001).
- [153] Zimmermann, B., Müller, T., Meineke, J., Esslinger, T. & Moritz, H. High-resolution imaging of ultracold fermions in microscopically tailored optical potentials. *New Journal of Physics* **13**, 043007 (2011).
- [154] Williamson, R. S. I., Voytas, P., Newell, R. & Walker, T. A magneto-optical trap loaded from a pyramidal funnel. *Opt. Express* **3**, 111–117 (1998).
- [155] Dieckmann, K., Spreuw, R. J. C., Weidemüller, M. & Walraven, J. T. M. Two-dimensional magneto-optical trap as a source of slow atoms. *Phys. Rev. A* **58**, 3891 (1998).
- [156] Arlt, J., MaragÃ, O., Webster, S., Hopkins, S. & Foot, C. A pyramidal magneto-optical trap as a source of slow atoms. *Optics Communications* **157**, 303 – 309 (1998).
- [157] Camposeo, A. *et al.* A cold Cesium atomic beam produced out of a pyramidal funnel. *Optics Communications* **200**, 231 – 239 (2001).
- [158] Uehlinger, T. *A 2D Magneto-Optical Trap as a High-Flux Source of Cold Potassium Atoms*. Master’s thesis, ETH - Zurich (2008).
- [159] Tiecke, T. G., Gensemer, S. D., Ludewig, A. & Walraven, J. T. M. High-flux two-dimensional magneto-optical-trap source for cold Lithium atoms. *Phys. Rev. A* **80**, 013409 (2009).
- [160] Battelier, B. *Gaz bidimensionnel de bosons ultra-froids: Nouvelle experience de condensation de Bose-Einstein*. Ph.D. thesis, Ecole Normale Supérieure (2007).
- [161] Lewandowski, H. J., Harber, D. M., Whitaker, D. L. & Cornell, E. A. Simplified system for creating a Bose-Einstein condensate. *Journal of Low Temperature Physics* **132**, 309–367 (2003). 10.1023/A:1024800600621.
- [162] Goldwin, J. M. *Quantum Degeneracy and Interactions in the ^{87}Rb - ^{40}K Bose-Fermi Mixture*. Ph.D. thesis, University of Wisconsin - Madison (1999).

- [163] Klempt, C. *et al.* Transport of a quantum degenerate heteronuclear Bose-Fermi mixture in a harmonic trap. *The European Physical Journal D - Atomic, Molecular, Optical and Plasma Physics* **48**, 121–126 (2008). 10.1140/epjd/e2008-00067-5.
- [164] White, M. R. *Ultracold atoms in a disordered optical lattice*. Ph.D. thesis, University of Illinois at Urbana-Champaign (2009).
- [165] Chikkatur, A. P. *Colliding and Moving Bose-Einstein Condensates: Studies of superfluidity and optical tweezers for condensate transport*. Ph.D. thesis, MIT (2002).
- [166] Lin, Y.-J., Perry, A. R., Compton, R. L., Spielman, I. B. & Porto, J. V. Rapid production of ^{87}Rb Bose-Einstein condensates in a combined magnetic and optical potential. *Phys. Rev. A* **79**, 063631 (2009).
- [167] van Kempen, E. G. M., Kokkelmans, S. J. J. M. F., Heinzen, D. J. & Verhaar, B. J. Interisotope determination of ultracold Rubidium interactions from three high-precision experiments. *Phys. Rev. Lett.* **88**, 093201 (2002).
- [168] Esslinger, T., Bloch, I. & Hänsch, T. W. Bose-Einstein condensation in a quadrupole-Ioffe-configuration trap. *Phys. Rev. A* **58**, R2664–R2667 (1998).
- [169] Pritchard, D. E. Cooling neutral atoms in a magnetic trap for precision spectroscopy. *Phys. Rev. Lett.* **51**, 1336 (1983).
- [170] Gotlibovych, I. *Microwave manipulation of ultracold atoms*. Master's thesis, University of Cambridge (2010).
- [171] Altin, P. A. *et al.* Collapse and three-body loss in a ^{85}Rb Bose-Einstein condensate. *Phys. Rev. A* **84**, 033632 (2011).
- [172] Kraus, J. D. & Marhefka, R. J. *Antennas for all Applications* (McGraw-Hill, 2002).
- [173] Balanis, C. A. *Antenna theory: analysis and design* (John Wiley, 2005).
- [174] Fedichev, P. O., Reynold, M. W. & Shlyapnikov, G. V. Three-body recombination of ultracold atoms to a weakly bound s-level. *Phys. Rev. Lett.* **77**, 2921 (1996).
- [175] Weber, T., Herbig, J., Mark, M., Nägerl, H.-C. & Grimm, R. Three-body recombination at large scattering lengths in an ultracold atomic gas. *Phys. Rev. Lett.* **91**, 123201 (2003).

- [176] Zaccanti, M. *et al.* Observation of an Efimov spectrum in an atomic system. *Nature Physics* **5**, 586–591 (2009).
- [177] Braaten, E. & Hammer, H.-W. Efimov physics in cold atoms. *Annals of Physics* **322**, 120 – 163 (2007).
- [178] Hara, K. M. O. *et al.* Measurement of the zero crossing in a Feshbach resonance of fermionic ${}^6\text{Li}$. *Phys. Rev. A* **66**, 041401 (2002).
- [179] Jochim, S. *et al.* Magnetic field control of elastic scattering in a cold gas of fermionic Lithium atoms. *Phys. Rev. Lett.* **89**, 273202 (2002).
- [180] Zaccanti, M. *et al.* Control of the interaction in a Fermi-Bose mixture. *Phys. Rev. A* **74**, 041605 (2006).
- [181] Inouye, S. *et al.* Observation of heteronuclear Feshbach resonances in a mixture of bosons and fermions. *Phys. Rev. Lett.* **93**, 183201 (2004).
- [182] Bradley, C. C., Sackett, C. A. & Hulet, R. G. Bose-Einstein condensation of Lithium: Observation of limited condensate number. *Phys. Rev. Lett.* **78**, 985 (1997).
- [183] Alt, W. An objective lens for efficient fluorescence detection of single atoms. *Optik* **113**, 142–144 (2002).
- [184] Dureau, A. *Optical devices for imaging, trapping and manipulating cold atoms*. Master’s thesis, University of Cambridge (2010).
- [185] Szczepkowski, J. *et al.* Analysis and calibration of absorptive images of Bose–Einstein condensate at nonzero temperatures. *Rev. Sci. Instrum.* **80**, 053103 (2009).
- [186] Gerbier, F. *et al.* Experimental study of the thermodynamics of an interacting trapped Bose–Einstein condensed gas. *Phys. Rev. A* **70**, 013607 (2004).
- [187] Einstein, A. Quantentheorie des einatomigen idealen gases. II. *Sitzungsberichte/Physikalische Klasse, Preussische Akademie der Wissenschaften* **1**, 3 (1925).
- [188] Huang, K. *Statistical Mechanics* (Wiley, New York, 1987).
- [189] Bagnato, V., Pritchard, D. E. & Kleppner, D. Bose-Einstein condensation in an external potential. *Phys. Rev. A* **35**, 4354 (1987).

-
- [190] Krüger, P., Hadzibabic, Z. & Dalibard, J. Critical point of an interacting two-dimensional atomic Bose gas. *Phys. Rev. Lett.* **99**, 040402 (2007).
- [191] Monroe, C. R., Cornell, E. A., Sackett, C. A., Myatt, C. J. & Wieman, C. E. Measurement of Cs-Cs elastic scattering at $T=30\ \mu\text{k}$. *Phys. Rev. Lett.* **70**, 414–417 (1993).
- [192] Wu, H., Arimondo, E. & Foot, C. J. Dynamics of evaporative cooling for Bose-Einstein condensation. *Phys. Rev. A* **56**, 560 (1997).
- [193] Wild, B. G. *The Hartree-Fock-Bogoliubov Theory of Bose-Einstein Condensates*. Ph.D. thesis, University of Otago (2011).
- [194] Griffin, A. Conserving and gapless approximations for an inhomogeneous Bose gas at finite temperatures. *Phys. Rev. B* **53**, 9341 (1996).
- [195] Shi, H. & Griffin, A. Finite-temperature excitations in a dilute Bose-condensed gas. *Physics Reports* **304**, 1 – 87 (1998).
- [196] Giorgini, S., Pitaevskii, L. P. & Stringari, S. Thermodynamics of a trapped Bose-condensed gas. *J. Low Temp. Phys.* **109**, 309 (1997).
- [197] Popov, V. N. *Functional Integrals and Collective Modes* (Cambridge University Press, Cambridge, 1987).
- [198] Giorgini, S., Pitaevskii, L. P. & Stringari, S. Condensate fraction and critical temperature of a trapped interacting Bose gas. *Phys. Rev. A* **54**, R4633 (1996).
- [199] Bogoliubov, N. N. On the theory of superfluidity. *J. Phys. (USSR)* **11**, 23 (1947).
- [200] Naraschewski, M. & Stamper-Kurn, D. M. Analytical description of a trapped semi-ideal Bose gas at finite temperature. *Phys. Rev. A* **58**, 2423 (1998).
- [201] Minguzzi, A., Conti, S. & Tosi, M. P. The internal energy and condensate fraction of a trapped interacting Bose gas. *J. Phys.: Condens. Matter* **9**, L33 (1997).
- [202] Dodd, R. J., Burnett, K., Edwards, M. & Clark, C. W. Two-gas description of dilute Bose-Einstein condensates at finite temperature. *Acta Physica Polonica* **93**, 45 (1998).
- [203] Giorgini, S., Pitaevskii, L. P. & Stringari, S. Scaling and thermodynamics of a trapped Bose-condensed gas. *Phys. Rev. Lett.* **78**, 3987–3990 (1997).

- [204] Grossmann, S. & Holthaus, M. On Bose-Einstein condensation in harmonic traps. *Physics Letters A* **208**, 188 (1995).
- [205] Grossman, S. & Holthaus, M. Bose-Einstein condensation and condensate tunneling. *Z. Naturforsch., A: Phys. Sci.* **50**, 323–326 (1995).
- [206] Ketterle, W. & van Druten, N. J. Bose-Einstein condensation of a finite number of particles trapped in one or three dimensions. *Phys. Rev. A* **54**, 656–660 (1996).
- [207] Kirsten, K. & Toms, D. J. Bose-Einstein condensation of atomic gases in a general harmonic-oscillator confining potential trap. *Phys. Rev. A* **54**, 4188 (1996).
- [208] Mewes, M.-O. *et al.* Bose-Einstein condensation in a tightly confining DC magnetic trap. *Phys. Rev. Lett.* **77**, 416 (1996).
- [209] Ensher, J. R., Jin, D. S., Matthews, M. R., Wieman, C. E. & Cornell, E. A. Bose-Einstein condensation in a dilute gas: Measurement of energy and ground-state occupation. *Phys. Rev. Lett.* **77**, 4984 (1996).
- [210] Han, D. J., Wynar, R. H., Courteille, P. & Heinzen, D. J. Bose-Einstein condensation of large numbers of atoms in a magnetic time-averaged orbiting potential trap. *Phys. Rev. A* **57**, R4114 (1998).
- [211] Anderson, B. P. & Kasevich, M. A. Spatial observation of Bose-Einstein condensation of ^{87}Rb in a confining potential. *Phys. Rev. A* **59**, R938–R941 (1999).
- [212] Maragó, O. M., Hechenblaikner, G., Hodby, E. & Foot, C. J. Temperature dependence and frequency shifts of the scissors mode of a trapped Bose-Einstein condensate. *Phys. Rev. Lett.* **86**, 3938 (2001).
- [213] Busch, B. D., Liu, C., Dutton, Z., Behroozi, C. H. & Hau, L. V. Observation of interaction dynamics in finite-temperature Bose condensed atom clouds. *EPL (Europhysics Letters)* **51**, 485 (2000).
- [214] Trebbia, J.-B., Esteve, J., Westbrook, C. I. & Bouchoule, I. Experimental evidence for the breakdown of a Hartree-Fock approach in a weakly interacting Bose gas. *Phys. Rev. Lett.* **97**, 250403 (2006).
- [215] Erhard, M., Schmaljohann, H., Kronjäger, J., Bongs, K. & Sengstock, K. Bose-Einstein condensation at constant temperature. *Phys. Rev. A* **70**, 031602 (2004).

-
- [216] Klaers, J., Schmitt, J., Vewinger, F. & Weitz, M. Bose-Einstein condensation of photons in an optical microcavity. *Nature* **468**, 545–548 (2010).
- [217] Ho, T.-L. & Zhou, Q. Obtaining the phase diagram and thermodynamic quantities of bulk systems from the densities of trapped gases. *Nature Physics* **6**, 131–134 (2010).
- [218] Nascimbene, S., Navon, N., Jiang, K. J., Chevy, F. & Salomon, C. Exploring the thermodynamics of a universal Fermi gas. *Nature* **463**, 1057 (2010).
- [219] Navon, N., Nascimbène, S., Chevy, F. & Salomon, C. The equation of state of a low-temperature Fermi gas with tunable interactions. *Science* **328**, 729–732 (2010).
- [220] Navon, N. *et al.* Dynamics and thermodynamics of the low-temperature strongly interacting Bose gas. *Phys. Rev. Lett.* **107**, 135301 (2011).
- [221] Nascimbène, S., Navon, N., Chevy, F. & Salomon, C. The equation of state of ultracold Bose and Fermi gases: A few examples. *New Journal of Physics* **12**, 103026 (2010).
- [222] Lee, T. D. & Yang, C. N. Many-body problem in quantum mechanics and quantum statistical mechanics. *Phys. Rev.* **105**, 1119–1120 (1957).
- [223] Lee, T. D. & Yang, C. N. Low-temperature behavior of a dilute Bose system of hard spheres. I. Equilibrium properties. *Phys. Rev.* **112**, 1419–1429 (1958).
- [224] Arnold, P. & Moore, G. BEC transition temperature of a dilute homogeneous imperfect Bose gas. *Phys. Rev. Lett.* **87**, 120401 (2001).
- [225] Baym, G., Blaizot, J.-P., Holzmann, M., Laloë, F. & Vautherin, D. Bose-Einstein transition in a dilute interacting gas. *Eur. Phys. J. B* **24**, 107–124 (2001).
- [226] Andersen, J. O. Theory of the weakly interacting Bose gas. *Rev. Mod. Phys.* **76**, 599–639 (2004).
- [227] Holzmann, M., Fuchs, J.-N., Baym, G. A., Blaizot, J.-P. & Laloë, F. Bose-Einstein transition temperature in a dilute repulsive gas. *C. R. Physique* **5**, 21 (2004).
- [228] Feynman, R. P. Atomic theory of the lambda-transition in Helium. *Phys. Rev.* **91**, 1291 (1953).

- [229] Glassgold, A. E., Kaufman, A. N. & Watson, K. M. Statistical mechanics for the nonideal Bose gas. *Phys. Rev.* **120**, 660–674 (1960).
- [230] Huang, K. Imperfect Bose gas. In de Boer, J. & Uhlenbeck, G. E. (eds.) *Studies in Statistical Mechanics*, vol. II, 3 (North-Holland, Amsterdam, 1964).
- [231] Fetter, A. L. & Walecka, J. D. *Quantum Theory of Many-Particle Systems* (McGraw-Hill, New York, 1971).
- [232] Toyoda, T. A microscopic theory of the lambda transition. *Annals of Physics* **141**, 154 – 178 (1982).
- [233] Stoof, H. T. C. Nucleation of Bose–Einstein condensation. *Phys. Rev. A* **45**, 8398 (1992).
- [234] Bijlsma, M. & Stoof, H. T. C. Renormalization group theory of the three-dimensional dilute Bose gas. *Phys. Rev. A* **54**, 5085 (1996).
- [235] Grüter, P., Ceperley, D. & Laloë, F. Critical temperature of Bose–Einstein condensation of hard-sphere gases. *Phys. Rev. Lett.* **79**, 3549 (1998).
- [236] Holzmann, M., Grüter, P. & Laloë, F. Bose-Einstein condensation in interacting gases. *Eur. Phys. J. B* **10**, 739–760 (1999).
- [237] Holzmann, M. & Krauth, W. Transition temperature of the homogeneous, weakly interacting Bose gas. *Phys. Rev. Lett.* **83**, 2687 (1999).
- [238] Baym, G., Blaizot, J.-P., Holzmann, M., Laloë, F. & Vautherin, D. The transition temperature of the dilute interacting Bose gas. *Phys. Rev. Lett.* **83**, 1703 (1999).
- [239] Huang, K. Transition temperature of a uniform imperfect Bose gas. *Phys. Rev. Lett.* **83**, 3770–3771 (1999).
- [240] Reppy, J. D. *et al.* Density dependence of the transition temperature in a homogeneous Bose-Einstein condensate. *Phys. Rev. Lett.* **84**, 2060–2063 (2000).
- [241] Kashurnikov, V. A., Prokof'ev, N. V. & Svistunov, B. V. Critical temperature shift in weakly interacting Bose gas. *Phys. Rev. Lett.* **87**, 120402 (2001).
- [242] Kleinert, H. Five-loop critical temperature shift in weakly interacting homogeneous Bose-Einstein condensate. *Modern Physics Letters B* **17**, 1011–1020 (2003).

- [243] Kastening, B. Bose-Einstein condensation temperature of a homogenous weakly interacting Bose gas in variational perturbation theory through seven loops. *Phys. Rev. A* **69**, 043613 (2004).
- [244] Nho, K. & Landau, D. P. Bose-Einstein condensation temperature of a homogeneous weakly interacting Bose gas: Path integral Monte Carlo study. *Phys. Rev. A* **70**, 053614 (2004).
- [245] Betz, V. & Ueltschi, D. Critical temperature of dilute Bose gases. *Phys. Rev. A* **81**, 023611 (2010).
- [246] Holzmann, M., Baym, G., Blaizot, J.-P. & Laloë, F. Nonanalytic dependence of the transition temperature of the homogeneous dilute Bose gas on scattering length. *Phys. Rev. Lett.* **87**, 120403 (2001).
- [247] Houbiers, M., Stoof, H. T. C. & Cornell, E. A. Critical temperature of a trapped Bose gas: Mean-field theory and fluctuations. *Phys. Rev. A* **56**, 2041 (1997).
- [248] Holzmann, M., Krauth, W. & Naraschewski, M. Precision Monte Carlo test of the Hartree-Fock approximation for a trapped Bose gas. *Phys. Rev. A* **59**, 2956–2961 (1999).
- [249] Arnold, P. & Tomášik, B. T_c for trapped dilute Bose gases: A second-order result. *Phys. Rev. A* **64**, 053609 (2001).
- [250] Davis, M. J. & Blakie, P. B. Critical temperature of a trapped Bose gas: Comparison of theory and experiment. *Phys. Rev. Lett.* **96**, 060404 (2006).
- [251] Zobay, O. Phase transition of trapped interacting Bose gases. *Laser Physics* **19**, 700–724 (2009).
- [252] Meppelink, R., Rozendaal, R. A., Koller, S. B., Vogels, J. M. & van der Straten, P. Thermodynamics of Bose-Einstein-condensed clouds using phase-contrast imaging. *Phys. Rev. A* **81**, 053632 (2010).
- [253] Gerbier, F. *et al.* Critical temperature of a trapped, weakly interacting Bose gas. *Phys. Rev. Lett.* **92**, 030405 (2004).
- [254] Smith, R. P., Tammuz, N., Campbell, R. L. D., Holzmann, M. & Hadzibabic, Z. Condensed fraction of an atomic Bose gas induced by critical correlations. *Phys. Rev. Lett.* **107**, 190403 (2011).
- [255] Campbell, R. L. D. *et al.* Efficient production of large ^{39}K Bose-Einstein condensates. *Phys. Rev. A* **82**, 063611 (2010).

- [256] Kawanaka, J., Shimizu, K. & Takuma, H. Decay rate measurement of Lithium in a magneto-optical trap. *Applied Physics B: Lasers and Optics* **57**, 113–118 (1993).
- [257] Marcassa, L. *et al.* Collisional loss rate in a magneto-optical trap for Sodium atoms: Light-intensity dependence. *Phys. Rev. A* **47**, R4563–R4566 (1993).
- [258] Ritchie, N. W. M. *et al.* Trap-loss collisions of ultracold Lithium atoms. *Phys. Rev. A* **51**, R890–R893 (1995).
- [259] Shaffer, J., Chalupczak, W. & Bigelow, N. Differential measurement of the ultracold Cs radiative escape and fine structure changing collision rates. *The European Physical Journal D - Atomic, Molecular, Optical and Plasma Physics* **7**, 323–330 (1999).
- [260] Mancini, M. W., Caires, A. R. L., Telles, G. D., Bagnato, V. S. & Marcassa, L. G. Trap loss rate for heteronuclear cold collisions in two species magneto-optical trap. *The European Physical Journal D - Atomic, Molecular, Optical and Plasma Physics* **30**, 105–116 (2004).
- [261] Burt, E. A. *et al.* Coherence, correlations, and collisions: What one learns about Bose–Einstein condensates from their decay. *Phys. Rev. Lett.* **79**, 337 (1997).
- [262] Novello, M., Visser, M. & Volovik, G. *Artificial Black Holes* (World Scientific, 2002).
- [263] Barceló, C., Liberati, S. & Visser, M. Analogue gravity from Bose-Einstein condensates. *Classical and Quantum Gravity* **18**, 1137 (2001).
- [264] Naik, D. S. & Raman, C. Optically plugged quadrupole trap for Bose-Einstein condensates. *Phys. Rev. A* **71**, 033617 (2005).
- [265] Heo, M.-S., Choi, J.-y. & Shin, Y.-i. Fast production of large ^{23}Na Bose-Einstein condensates in an optically plugged magnetic quadrupole trap. *Phys. Rev. A* **83**, 013622 (2011).
- [266] Cometa BEC group, Paris. URL <http://www-lpl.univ-paris13.fr/bec/>.
- [267] Du, S. *et al.* Atom-chip Bose-Einstein condensation in a portable vacuum cell. *Phys. Rev. A* **70**, 053606 (2004).
- [268] Altin, P. A. *et al.* ^{85}Rb tunable-interaction Bose-Einstein condensate machine. *Review of Scientific Instruments* **81**, 063103 (2010).

- [269] Farkas, D. M. *et al.* A compact, transportable, microchip-based system for high repetition rate production of Bose-Einstein condensates. *Applied Physics Letters* **96**, 093102 (2010).
- [270] ColdQuanta Inc. <http://www.coldquanta.com>.
- [271] Gozzini, A. *et al.* Light-induced ejection of alkali atoms in polysiloxane coated cells. *Il Nuovo Cimento D* **15**, 709–722 (1993).
- [272] Meucci, M., Mariotti, E., Bicchi, P., Marinelli, C. & Moi, L. Light-induced atom desorption. *EPL (Europhysics Letters)* **25**, 639 (1994).
- [273] Anderson, B. P. & Kasevich, M. A. Loading a vapor-cell magneto-optic trap using light-induced atom desorption. *Phys. Rev. A* **63**, 023404 (2001).
- [274] Alexandrov, E. B. *et al.* Light-induced desorption of alkali-metal atoms from paraffin coating. *Phys. Rev. A* **66**, 042903 (2002).
- [275] Atutov, S. N. *et al.* Fast and efficient loading of a Rb magneto-optical trap using light-induced atomic desorption. *Phys. Rev. A* **67**, 053401 (2003).
- [276] Aubin, S. *et al.* Trapping fermionic ^{40}K and bosonic ^{87}Rb on a chip. *Journal of Low Temperature Physics* **140**, 377–396 (2005).
- [277] Klempt, C. *et al.* Ultraviolet light-induced atom desorption for large Rubidium and Potassium magneto-optical traps. *Phys. Rev. A* **73**, 013410 (2006).
- [278] Kawalec, T. *et al.* Dynamics of laser-induced Cesium atom desorption from porous glass. *Chemical Physics Letters* **420**, 291 – 295 (2006).
- [279] Zhang, P. *et al.* Light-induced atom desorption for Cesium loading of a magneto-optical trap: Analysis and experimental investigations. *Phys. Rev. A* **80**, 053420 (2009).
- [280] Telles, G., Ishikawa, T., Gibbs, M. & Raman, C. Light-induced atomic desorption for loading a Sodium magneto-optical trap. *Phys. Rev. A* **81**, 032710 (2010).
- [281] Mimoun, E., Sarlo, L. D., Jacob, D., Dalibard, J. & Gerbier, F. Fast production of ultracold Sodium gases using light-induced desorption and optical trapping. *Phys. Rev. A* **81**, 023631 (2010).
- [282] Rei, T. T. *Atom sources for cold atoms experiments*. Master's thesis, National University of Singapore (2008/2009).

- [283] Billy, J. *et al.* Direct observation of Anderson localization of matter waves in a controlled disorder. *Nature* **453**, 891–894 (2008).
- [284] White, M. *et al.* Strongly interacting bosons in a disordered optical lattice. *Phys. Rev. Lett.* **102**, 055301 (2009).
- [285] Pasienski, M., McKay, D., White, M. & DeMarco, B. A disordered insulator in an optical lattice. *Nat Phys* **advance online publication**, – (2010).
- [286] Yao, A. M. & Padgett, M. J. Orbital angular momentum: origins, behavior and applications. *Adv. Opt. Photon.* **3**, 161–204 (2011).
- [287] Allen, L., Barnett, S. M. & Padgett, M. J. *Optical Angular Momentum* (Institute of Physics, 2003).
- [288] Torres, J. P. & Torner, L. (eds.) *Twisted Photons: Applications of Light with Orbital Angular Momentum* (Wiley-VCH, 2011).
- [289] Denschlag, J. *et al.* Generating solitons by phase engineering of a Bose-Einstein condensate. *Science* **287**, 97–101 (2000).
- [290] Cooper, N. R. & Hadzibabic, Z. Measuring the superfluid fraction of an ultracold atomic gas. *Phys. Rev. Lett.* **104**, 030401 (2010).
- [291] Rath, S. *Production and investigation of quasi-two-dimensional Bose gases*. Ph.D. thesis, Université Pierre et Marie Curie (2010). PhD thesis.
- [292] Bowman, R. W., Wright, A. J. & Padgett, M. J. An SLM-based Shack-Hartmann wavefront sensor for aberration correction in optical tweezers. *J. Opt.* **12**, 124004 (2010).
- [293] Gerchberg, R. W. & Saxton, W. O. A practical algorithm for the determination of the phase from image and diffraction plane pictures. *Optik* **35**, 237 (1972).
- [294] Aagedal, H., Schmid, M., Beth, T., Teiwes, S. & Wyrowski, F. Theory of speckles in diffractive optics and its application to beam shaping. *J. Mod. Opt.* **43**, 1409–1421 (1996).
- [295] Pasienski, M. & DeMarco, B. A high-accuracy algorithm for designing arbitrary holographic atom traps. *Optics Express* **16** (2008).
- [296] Bruce, G. D., Mayoh, J., Smirne, G., Torralbo-Campo, L. & Cassetari, D. A smooth, holographically generated ring trap for the investigation of superfluidity in ultracold atoms. *Physica Scripta* **2011**, 014008 (2011).

-
- [297] Gaunt, A. *Coherent Optical Sculpting for Manipulating and Probing Ultra-cold Atoms*. Master's thesis, University of Cambridge (2011).
- [298] Kruse, J., Gierl, C., Schlosser, M. & Birkl, G. Reconfigurable site-selective manipulation of atomic quantum systems in two-dimensional arrays of dipole traps. *Phys. Rev. A* **81**, 060308 (2010).
- [299] Misakian, M. Equations for the magnetic field produced by one or more rectangular loops of wire in the same plane. *Journal of Research of the National Institute of Standards and Technology* **105**, 557–564 (2000).
- [300] Hadzibabic, Z. & Dalibard, J. Two-dimensional Bose fluids: An atomic physics perspective. In Kaiser, R. & Wiersma, D. (eds.) *Nano optics and atomics: transport of light and matter waves*, vol. CLXXIII of *Proceedings of the International School of Physics Enrico Fermi, 2009* (IOS Press, 2010).
- [301] Berezinskii, V. L. Destruction of long-range order in one-dimensional and two-dimensional system possessing a continuous symmetry group - ii. quantum systems. *Soviet Physics JETP* **34**, 610 (1971).
- [302] Kosterlitz, J. M. & Thouless, D. J. Ordering, metastability and phase transitions in two dimensional systems. *J. Phys. C: Solid State Physics* **6**, 1181 (1973).
- [303] Hadzibabic, Z., Krüger, P., Cheneau, M., Battelier, B. & Dalibard, J. Berezinskii-Kosterlitz-Thouless crossover in a trapped atomic gas. *Nature* **441**, 1118–1121 (2006).
- [304] Cladé, P., Ryu, C., Ramanathan, A., Helmerson, K. & Phillips, W. D. Observation of a 2d Bose gas: From thermal to quasicondensate to superfluid. *Phys. Rev. Lett.* **102**, 170401 (2009).
- [305] Görlitz, A. *et al.* Realization of Bose–Einstein condensates in lower dimensions. *Phys. Rev. Lett.* **87**, 130402 (2001).
- [306] Orzel, C., Tuchmann, A. K., Fenselau, K., Yasuda, M. & Kasevich, M. A. Squeezed states in a Bose–Einstein condensate. *Science* **291**, 2386 (2001).
- [307] Burger, S. *et al.* Quasi-2D Bose–Einstein condensation in an optical lattice. *Europhys. Lett.* **57**, 1 (2002).
- [308] Köhl, M., Moritz, H., Stöferle, T., Schori, C. & Esslinger, T. Superfluid to Mott insulator transition in one, two, and three dimensions. *Journal of Low Temperature Physics* **138**, 635 (2005).

- [309] Morsch, O. & Oberthaler, M. Dynamics of Bose–Einstein condensates in optical lattices. *Rev. Mod. Phys.* **78**, 179 (2006).
- [310] Spielman, I. B., Phillips, W. D. & Porto, J. V. The Mott insulator transition in two dimensions. *Phys. Rev. Lett.* **98**, 080404 (2007).
- [311] Hadzibabic, Z., Stock, S., Battelier, B., Bretin, V. & Dalibard, J. Interference of an array of independent Bose–Einstein condensates. *Phys. Rev. Lett.* **93**, 180403 (2004).
- [312] Stock, S., Hadzibabic, Z., Battelier, B., Cheneau, M. & Dalibard, J. Observation of phase defects in quasi-two-dimensional Bose–Einstein condensates. *Phys. Rev. Lett.* **95**, 190403 (2005).
- [313] Rychtarik, D., Engeser, B., Nägerl, H.-C. & Grimm, R. Two-dimensional Bose–Einstein condensate in an optical surface trap. *Phys. Rev. Lett.* **92**, 173003 (2004).
- [314] Gillen, J. I. *et al.* Two-dimensional quantum gas in a hybrid surface trap. *Phys. Rev. A* **80**, 021602 (2009).
- [315] Zobay, O. & Garraway, B. M. Two-dimensional atom trapping in field-induced adiabatic potentials. *Phys. Rev. Lett.* **86**, 1195 (2001).
- [316] Colombe, Y. *et al.* Ultracold atoms confined in RF-induced two-dimensional trapping potentials. *Europhys. Lett.* **67**, 593 (2004).
- [317] Hofferberth, S., Lesanovsky, I., Fischer, B., Verdu, J. & Schmiedmayer, J. Radiofrequency-dressed-state potentials for neutral atoms. *Nature Physics* **2**, 710–716 (2006).
- [318] Smith, N. L., Heathcote, W. H., Hechenblaikner, G., Nugent, E. & Foot, C. J. Quasi-2D confinement of a BEC in a combined optical and magnetic potential. *Journal of Physics B* **38**, 223–235 (2005).
- [319] Meyrath, T., Schreck, F., Hanssen, J., Chuu, C. & Raizen, M. A high frequency optical trap for atoms using Hermite-Gaussian beams. *Opt. Express* **13**, 2843–2851 (2005).
- [320] Rath, S. P. *et al.* Equilibrium state of a trapped two-dimensional Bose gas. *Phys. Rev. A* **82**, 013609 (2010).
- [321] Smith, N. L. *The Tilting Mode and Two Dimensional Confinement of a Bose-Einstein Condensed Gas*. Ph.D. thesis, University of Oxford (2005).